

Synthesis, Characterization and Properties of Glass-free Vanadate based Ceramics for Microwave Circuit Applications

Thesis submitted to
UNIVERSITY OF CALICUT, KERALA
*for the partial fulfillment of the requirements
for the award of the degree of*
DOCTOR OF PHILOSOPHY IN PHYSICS
Under the Faculty of Science

by
Unnimaya A. N.

Under the Guidance of
Dr. R. Ratheesh



CENTRE FOR MATERIALS FOR ELECTRONICS TECHNOLOGY (C-MET)
SCIENTIFIC SOCIETY, MINISTRY OF ELECTRONICS AND INFORMATION TECHNOLOGY,
GOVERNMENT OF INDIA, SHORNUR ROAD, P.O MULAKUNNATHUKAVU, ATHANI,
THRISSUR- 680581, KERALA, INDIA

September 2017

*Synthesis, Characterization and Properties of Glass-free Vanadate based Ceramics
for Microwave Circuit Applications*

PhD Thesis

Submitted by

Unnimaya A. N
Avanoor House
M. G. Street, Thiroor
P.O. Mulakunnathukavu
Thrissur-680581
Kerala, India
e-mail: unnimayaan@gmail.com

Research Supervisor

Dr. R. Ratheesh
Scientist
Centre for Materials for Electronics Technology (C-MET), Hyderabad
e-mail: ratheesh@cmet.gov.in

September 2017



सेन्टर फॉर मैटेरियल्स फॉर इलेक्ट्रॉनिक्स टेक्नोलॉजी
(वैज्ञानिक संस्था, इलेक्ट्रॉनिकी और सूचना प्रौद्योगिकी मंत्रालय, भारत सरकार)
आई. डी. ए. फेज - III, चेरलापल्ली, हेच.सी.एल.डाकघर
हैदराबाद - ५०००५९. भारत

CENTRE FOR MATERIALS FOR ELECTRONICS TECHNOLOGY

(Scientific Society, Ministry of Electronics and Information Technology (MeitY), Govt. of India)

IDA PHASE-III, CHERLAPALLY, HCL (P.O.), HYDERABAD - 500 051, INDIA

Phone : +91-40-27265673

FAX : +91-40-27261658

EPABX : +91-40-27267006, 27265587.

E-mail : ratheesh@cmet.gov.in

Website: www.cmet.gov.in

Dr. R. Ratheesh

Director

Certificate

This is to certify that the thesis titled **Synthesis, Characterization and Properties of Glass-free Vanadate based Ceramics for Microwave Circuit Applications** submitted to University of Calicut in partial fulfillment of the requirements for the award of the degree of **Doctor of Philosophy in Physics** is a record of the authentic work carried out by Smt. Unnimaya A. N, at Microwave Materials Division, Centre for Materials for Electronics Technology, Thrissur, under my guidance. The work presented in this thesis has not been included in any other thesis submitted previously for the award of any degree.

Thrissur

Dr. R. Ratheesh
(Supervising Guide)



सेन्टर फॉर मैटेरियल्स फॉर इलेक्ट्रॉनिक्स टेक्नोलॉजी
(वैज्ञानिक संस्था, इलेक्ट्रॉनिकी और सूचना प्रौद्योगिकी मंत्रालय, भारत सरकार)
आई. डी. ए. फेज - III, चेरलापल्ली, हेच.सी.एल.डाकघर
हैदराबाद - ५०००५१. भारत

CENTRE FOR MATERIALS FOR ELECTRONICS TECHNOLOGY

(Scientific Society. Ministry of Electronics and Information Technology (MeitY), Govt. of India)

IDA PHASE-III, CHERLAPALLY, HCL (P.O.), HYDERABAD - 500 051, INDIA

Phone : +91-40-27265673

FAX : +91-40-27261658

EPABX : +91-40-27267006, 27265587.

E-mail : ratheesh@cmet.gov.in

Website: www.cmet.gov.in

Dr. R. Ratheesh

Director

TO WHOM IT MAY CONCERN

This is to certify that the corrections/suggestions received from the adjudicators have been incorporated at Chapter 5 of the thesis.

29.05.2018
Hyderabad

Dr. R. Ratheesh
Research Supervisor

DECLARATION

I hereby declare that the thesis entitled “**Synthesis, Characterization and Properties of Glass-free Vanadate based Ceramics for Microwave Circuit Applications**” submitted to University of Calicut, is based on the original work carried out by me under the guidance and supervision of Dr. R. Ratheesh, Scientist, Centre for Materials for Electronics Technology, Hyderabad. No part of this work has been presented for the award of any other degree from any other institution.

Place: Thrissur

Date:

Unnimaya A. N

Dedicated to my loving parents

Acknowledgement

First and foremost, thank God Almighty for all the blessings.

Let me acknowledge with endless gratitude to my research supervisor Dr. R. Ratheesh, Scientist, Centre for Materials for Electronics Technology (C-MET), for his immense guidance, ceaseless encouragement, honest criticism and continuous support throughout my research period. His advice and helpful discussions have been invaluable and helped me to pursue knowledge in the area of microwave ceramics and composites; it was such a pleasure to work with you.

I take this opportunity to express my sincere gratitude to former Director General of C-MET, Dr. D. P. Amalnerker, and former Director of C-MET, Dr. K. R. Dayas, for providing the experimental facilities to carry out my research work in C-MET. I would like to acknowledge Dr. N. R. Munirathnam, Director General of C-MET, Dr. N. Raghu, Director of C-MET, Thrissur for all the encouragement and valuable questions which helped me to think about my research work in a different perspective.

I sincerely thank Dr. S. N. Potty for his valuable support and care. I would also like to thank Dr. V. Kumar, Dr. N. C. Pramanik, Dr. A. Seema, Dr. Radhika, Dr. K. V. Baiju and Dr. Stanly Jacob for all the valuable suggestions and support throughout my research work. I also thank all the supporting staff of C-MET, Thrissur for their invariable support. I would like to thank Mr. T. K. Anilkumar, Administrative Officer, Mr. E. Ramadasan, Finance Officer and Administrative staff members of C-MET for their sincere help.

I am thankful to Dr. K. P. Murali for all the suggestions and advice given to me. I also take this opportunity to thank Mr. K. Prasad and Mr. Arun N. S for their sincere consideration towards me. I am deeply indebted to my seniors in the lab, Mr. Suresh E. K and Mr. Surjith A. for their marvelous friendship, enormous help for microwave measurements and the valuable suggestions given during my work. They always made positive atmosphere to work with. Thanks to Mrs. Dhanya Johnson for her sister like-concern and constant support throughout my research period.

I would like to express my sincere gratitude to my colleagues in microwave materials division, Mr. Freddy Sunny, Mr. Emil John, Mr. Anoop Chandran, Mr. R. Naveenraj and Mr. Basiludeen Azad for their care and support. My sincere gratitude to my lab mates Mr. Shakhil P. G, Mr. Sanaj T and Mr. Lijin Jose for the help given during the synthesis of polymer ceramic

composites. I extend my heart-felt thanks to Mr. Narayanan P. V for his valuable suggestions and help given for the simulation and fabrication of microstrip patch antenna. I am grateful to Mr. Albin Antony for the help given for SEM analysis. I also take this opportunity to thank the project students Mrs. Neethu Jose, Mrs. Drishya V, Mr. Kiranjith, Mr. Shiron, Mr. Varun V Pai, Ms. Biji Baby V. B, Ms. Anju Paulson, Ms. Sarika, Mrs. Reshma, Ms. Shereena Thomas, Ms. Roshni Rahulan for their care and affection.

I would like to thank Department of Science and Technology (DST), Government of India for providing me the research fellowship.

I express my deep sense of gratitude to Mr. I. Pakkja Selvam and Dr. S. Rajesh Kumar (C-MET, Hyderabad) for the XRD measurements. I also thank Mrs. V. Priyadarsini for TGA/DSC and Raman measurements.

My seniors and friends from different institutions always helped me with literature survey. I am deeply grateful to them; especially Dr. S. Rajesh, Dr. Nijesh K James, Dr. Rajani K V and Mr. Subin Joseph, for sparing time to collect literature admit their busy programmes.

At this point of time, I remember all my teachers at Vimala College, Thrissur and Cochin University of Science and Technology (CUSAT), Cochin especially Dr. Malini K. A. and Prof. M. R. Anantharaman, by whom I was motivated to do research.

I have no words to explain my profound love and gratitude to my parents for always believing and encouraging me to achieve my goals. My parents have always enlightened my path with valuable advices and support, without which this thesis could not be possible. I express my heart-felt gratitude to my dear brother Mr. Rajesh A. N for his immense support and endless care. I sincerely thank the love and inspiration I received from my husband Mr. Jithin P. S. It is by you my dearest daughter Devu by whom I get all the happiness and enthusiasm in my life. Last but not the least, I sincerely thank all those helped me in different ways for the successful completion of my research work.

Unnimaya A. N

Success is on the far side of failure
Thomas Watson

Preface

Microwave materials gained considerable attention because of the enormous developments in the area of advanced wireless communication systems such as mobile phones, satellite broadcasting, global positioning systems etc. The drive towards low cost, high volume and miniaturized microwave devices has led to the evolution of integration technologies. In this contest, Low temperature co-fired ceramics (LTCC) technology is in the forefront since it offers miniaturized multilayer ceramic substrates due to the buried passive components whereas the active devices can be mounted on the top of package. It has paved way for the fabrication of monolithic ceramic devices and modules with three dimensional integrated structures and System-in-packaging (SiP).

LTCC technology necessitates novel dielectric materials which can co-fire with metal electrodes since multilayer devices consist of alternating dielectric ceramics and internal metallic electrode layers. Traditionally, silver has been used as the metallic electrode layer because of its high conductivity and relatively low cost. Hence, the sintering temperature of the dielectric should be lower than the melting point of silver (961°C). It is generally known that the addition of glass additives and low melting oxides such as B_2O_3 , V_2O_5 and CuO reduce the sintering temperature of microwave dielectric ceramics through liquid phase sintering, though it deteriorates the microwave dielectric properties especially the intrinsic quality factor. This fueled the search for new microwave dielectric ceramics with low sintering temperature and excellent chemical compatibility. Even though large number of low temperature sinterable microwave dielectric ceramics are reported, the need for further lowering the sintering temperature of dielectric materials leads to the development of ultra-low temperature co-fired ceramics (ULTCC), wherein the ceramic material has to be sintered at temperatures less than 660°C, which is the melting point of Al electrode material. Only a few literature are available on the structure-property relationship of LTCC and ULTCC ceramic systems.

Chapter 1 gives a general introduction about microwave dielectrics including dielectric resonators, low temperature co-fired ceramics and ceramic filled polymer composites. It also discusses on the critical material requirements for LTCC technology and their application potential in the field of microwave circuit design. Chapter 2 presents a comprehensive description about the synthesis and

characterization of microwave ceramics and polymer ceramic composites. A brief account on the various characterization techniques used in the present work are also summarized in this chapter.

Detailed studies on the structure, microwave dielectric properties and chemical compatibility studies of alkaline earth metavanadates, AV_2O_6 ($A=Ba, Sr, Ca, Mg$ and Zn) ceramics are presented in Chapter 3. TGA-DSC studies confirm the phase formation of metavanadates in the ULTCC temperature range. XRD and Raman studies show that metavanadate compositions have single phase nature with vertex shared VO_4 tetrahedra in BaV_2O_6 and SrV_2O_6 , VO_5 trigonal bipyramid in CaV_2O_6 and VO_6 octahedra in MgV_2O_6 and ZnV_2O_6 . Among the metavanadates studied, only BaV_2O_6 and CaV_2O_6 exhibit microwave dielectric properties. BaV_2O_6 possesses a dielectric constant of 11.2, Q_{xf} of 42,790 GHz and τ_f of 28.2 ppm/ $^{\circ}C$ whereas CaV_2O_6 ceramic has a dielectric constant of 8.7, Q_{xf} of 60,310 GHz and τ_f of -50.7 ppm/ $^{\circ}C$. Barium and calcium metavanadates exhibit low coefficient of linear thermal expansion (α_L) of 10 and 9.7 ppm/ $^{\circ}C$ respectively, which are at par with commercial LTCC compositions. XRD and EDS studies show excellent chemical compatibility between calcium and barium metavanadates and Al electrode during co-firing. Owing to very low sintering temperature, excellent microwave dielectric properties, low coefficient of thermal expansion and good chemical compatibility with Al electrode, BaV_2O_6 and CaV_2O_6 ceramics can be used as ideal candidate materials for ULTCC applications.

The effect of vanadium substitution on the structure and microwave dielectric properties of $5BaO-2Nb_2O_5$ binary system is investigated in Chapter 4. $Ba_5Nb_4O_{15}$ is a classical high Q material with dielectric constant of ~ 40 , but sinter only at elevated temperature range ($>1400^{\circ}C$). Substitution of low melting oxides in the parent composition is one of the effective methods for the formation of low fired ceramics. Therefore, Nb^{5+} ions are substituted with V^{5+} ions in $Ba_5Nb_4O_{15}$ and their structural, microstructural and microwave dielectric properties are investigated in detail. Vanadium substituted $Ba_5Nb_{4-x}V_xO_{15}$ ceramics with $x=1-3$ are multiphase compounds with $Ba_3V_2O_8$ and $BaNb_2O_6$ as secondary phases, whereas the complete substitution of Nb^{5+} ions with V^{5+} ions results a multiphase composition comprising of hexagonal $Ba_3V_2O_8$ and triclinic $Ba_2V_2O_7$ phases. Raman spectroscopic studies also confirm the existence of $Ba_3V_2O_8$ and $Ba_2V_2O_7$ phases in the completely

vanadium replaced $5\text{BaO}-2\text{V}_2\text{O}_5$ composition. The sintering temperature and dielectric constant of $\text{Ba}_5\text{Nb}_{4-x}\text{V}_x\text{O}_{15}$ ($x=0-4$) ceramics decrease with increasing the vanadium content. The completely vanadium replaced ceramic exhibits a low dielectric constant of 12.1, reasonably good quality factor of 26,790 GHz and low τ_f of 7 ppm/°C. In addition to this, stoichiometrically weighed and mixed $\text{Ba}_3\text{V}_2\text{O}_8$ and $\text{Ba}_2\text{V}_2\text{O}_7$ ceramic mixtures sintered at 900°C for 1h exhibit a dielectric constant of 11.6, quality factor of 24,540 GHz and τ_f of 6 ppm/°C. Good chemical compatibility is obtained for $5\text{BaO}-2\text{V}_2\text{O}_5$ while co-firing with Ag electrode and hence can be used for LTCC applications.

The possibility of existence of alkaline earth oxovanadate ($\text{A}_4\text{V}_2\text{O}_9$) ceramics in the $\text{AO}-\text{V}_2\text{O}_5$ binary system, their structural resemblance with that of orthovanadates ($\text{A}_3\text{V}_2\text{O}_8$) and possible use of these materials for LTCC applications are reported in Chapter 5. Although structure papers are reported on $\text{A}_4\text{V}_2\text{O}_9$ (Ba, Sr, Ca and Zn) materials, available ICDD patterns suggest structural resemblance between oxovanadates and orthovanadates. Therefore, the structural resemblance of $\text{A}_4\text{V}_2\text{O}_9$ ceramics with that of alkaline orthovanadates, $\text{A}_3\text{V}_2\text{O}_8$ (A = Ba, Sr, Ca, Mg and Zn) ceramics are investigated extensively using X-ray diffraction and Raman spectroscopic studies. The XRD patterns of all the $\text{A}_4\text{V}_2\text{O}_9$ samples are different from that of orthovanadate samples and they exhibit single phase nature. Also, distinct structural differences are observed in the Raman spectra of both oxovanadate and orthovanadate ceramics with $(\text{VO}_4)^{3-}$ vibrational groups. Among $\text{A}_4\text{V}_2\text{O}_9$ ceramics, $\text{Mg}_4\text{V}_2\text{O}_9$ only exhibits resonance in the microwave frequency region with a dielectric constant of 6.3, Qxf of 37,263 GHz and a negative τ_f of -43.5 ppm/°C at optimum sintering temperature of 940°C for 1h. The XRD and EDS analyses reveal good chemical compatibility between $\text{Mg}_4\text{V}_2\text{O}_9$ and Ag electrode, hence can be used as a substrate material for LTCC applications.

The sixth chapter presents the effect of partial substitution of Bi^{3+} and R^{3+} (R= La, Nd, Y and Yb) ions on the structure and microwave dielectric properties of $\text{A}_4\text{V}_2\text{O}_9$ ceramics. Among these, $\text{Bi}_2\text{AV}_2\text{O}_9$ (A= Ba, Sr, Mg and Zn) and $\text{R}_2\text{AV}_2\text{O}_9$ (R= La, Nd, Y and Yb; A= Ba, Sr and Ca) ceramics are obtained as multiphase compounds. BiVO_4 and BiAVO_5 (A= Ba, Sr, Mg and Zn) phases are present in $\text{Bi}_2\text{AV}_2\text{O}_9$ whereas RVO_4 and RAVO_5 (R= La, Nd, Y and Yb; A= Ba, Sr and Ca) phases are present in $\text{R}_2\text{AV}_2\text{O}_9$ ceramics. Interestingly $\text{Bi}_2\text{CaV}_2\text{O}_9$ ceramic exhibits

single phase nature with a dielectric constant of 28.2 at 6.54065 GHz, Q_{xf} of 37,263 GHz together with a negative τ_f value of -46.1 ppm/°C. Single phase nature and ordering of the crystal structure could be the reasons for good microwave dielectric properties of $\text{Bi}_2\text{CaV}_2\text{O}_9$ ceramic. $\text{Bi}_2\text{CaV}_2\text{O}_9$ reacts with silver electrode during co-firing and hence it is not suitable for LTCC applications.

Preparation of $\text{Ba}_3\text{V}_2\text{O}_8$ ceramic filled HDPE composites, their thermal and microwave dielectric property evaluation, simulation studies of rectangular microstrip patch antenna using High Frequency Structure Simulator (HFSS), fabrication of the patch antenna through photolithography technique and microwave property evaluation of the same are discussed in Chapter 7. Dielectric, thermal and mechanical properties of HDPE/ $\text{Ba}_3\text{V}_2\text{O}_8$ composites are also studied as a function of filler fraction. HDPE/ $\text{Ba}_3\text{V}_2\text{O}_8$ composite has a dielectric constant of 6.3, loss tangent of 0.004 at 9.32 GHz, temperature variation of dielectric constant (τ_{ϵ_r}) of -498 ppm/°C, coefficient of thermal expansion of 138 ppm/°C and ultimate tensile strength of 5.5 MPa at optimum filler loading of 54 vol%. Because of the reasonably good dielectric, thermal and mechanical properties, HDPE/ $\text{Ba}_3\text{V}_2\text{O}_8$ composites can be used as base substrate for microwave circuit fabrication. Microstrip patch antennas are fabricated out of copper cladded HDPE/ $\text{Ba}_3\text{V}_2\text{O}_8$ laminates using photolithographic technique and the antenna performance is evaluated using vector network analyzer. Measured results of the microstrip patch antennas are in good agreement with simulated data.

The conclusions drawn from the previous chapters are summarized in Chapter 8. The major achievements of the work presented in the thesis and the scope for future work are highlighted.

LIST OF PAPERS PUBLISHED IN INTERNATIONAL JOURNALS

- [1] **A. N. Unnimaya**, E. K. Suresh, R. Ratheesh, Crystal structure and microwave dielectric properties of new alkaline earth vanadate $A_4V_2O_9$ (A= Ba, Sr, Ca, Mg and Zn) ceramics for LTCC applications, Mater. Res. Bull., 88 (2017) 174-181.
- [2] **A. N. Unnimaya**, E. K. Suresh, R. Ratheesh, Structure and microwave dielectric properties of ultra-low temperature co-firable BaV_2O_6 ceramics, Eur. J. Inorg. Chem., 2015 [2] (2015) 305-310.
- [3] **A. N. Unnimaya**, E. K. Suresh, J. Dhanya, R. Ratheesh, Structure and microwave dielectric properties of $5BaO-2V_2O_5$ binary ceramic system, J. Mater Sci: Mater Electron., 25 [2] (2014) 1127-1131.
- [4] E. K. Suresh, **A. N. Unnimaya**, R. Ratheesh, Microwave dielectric properties of ultralow-temperature co-firable $Ba_3V_4O_{13}$ ceramics, J. Am. Ceram. Soc., 97 [5] (2014) 1530-1533.
- [5] E. K. Suresh, **A. N. Unnimaya**, A. Surjith, R. Ratheesh, New vanadium based $Ba_3MV_4O_{15}$ (M=Ti & Zr) high Q ceramics for LTCC applications, Ceram. Inter., 39 [4] (2013) 3635-3639.
- [6] V. Drishya, **A. N. Unnimaya**, R. Naveenraj, E. K. Suresh, R. Ratheesh, Preparation, characterization and dielectric properties of PP/ $CaTiO_3$ composites for microwave substrate applications, Int. J. Appl. Ceram. Technol., 13 [5] (2016) 810-815.
- [7] J. Dhanya, **A. N. Unnimaya**, R. Ratheesh, Dielectric resonators with complex crystal structures in the $La_2O_3-Al_2O_3-TiO_2$ system for microwave applications, J Mater Sci: Mater Electron., 25 [10] (2014) 4617-4622.
- [8] **A. N. Unnimaya**, E K Suresh, R Naveenraj, R Ratheesh, Structure and microwave dielectric properties of double vanadate $Ca_9A(VO_4)_7$ (A= La, Pr, Nd and Sm) ceramics for LTCC applications, J. Electron. Mater. (Under Revision)

List of conference proceedings

- [1] **A. N. Unnimaya**, Basiluddeen Azad V, R. Ratheesh, “Structure and Microwave Dielectric Properties of CaV_2O_6 ULTCC Ceramic”, 2nd International Symposium on Physics and Technology of Sensors (ISPTS), Pune, 7-10 March, 2015.
- [2] Drishya V, **A. N. Unnimaya**, K. Prasad, R. Ratheesh, “Preparation, characterization and dielectric properties of CaTiO_3 filled PP composites for microwave substrate applications”, 14th Biennial International Symposium on Antennas and Propagation (APSYM), Cochin, 17-19 December, 2014.

Contents

List of Figures

List of Tables

Chapter 1 Introduction

1.1	Introduction -----	2
1.2	Microwave ceramics-----	3
1.2.1	Dielectric resonators-----	4
1.2.2	Microwave resonance -----	5
1.2.3	Modes of a dielectric resonator -----	7
1.3	Physics of microwave dielectrics -----	9
1.3.1	Polarization mechanisms in dielectrics -----	9
1.3.2	Clausius-Mossotti equation -----	12
1.4	Material requirements for dielectric resonator applications -----	13
1.4.1	Stable dielectric constant -----	13
1.4.2	Temperature dependence of dielectric constant -----	14
1.4.3	Quality factor -----	17
1.5	Multilayer co-fired ceramics -----	20
1.5.1	Introduction -----	20
1.5.2	High Temperature Co-fired Ceramics (HTCC) -----	21
1.5.3	Low Temperature Co-fired Ceramics (LTCC) -----	21
1.5.4	Manufacturing of LTCC -----	24
1.6	Material requirements for LTCC -----	25
1.6.1	Densification temperature -----	25
1.6.2	Dielectric properties -----	26
1.6.3	Thermomechanical properties-----	27
1.6.4	Chemical compatibility with metal electrode -----	27
1.7	LTCC material systems -----	28
1.7.1	Glass-Ceramic systems -----	28
1.7.2	Glass free ceramic systems -----	29
1.8	Ultra-low Temperature Co-fired Ceramics (ULTCC)-----	33
1.8.1	Introduction -----	33
1.8.2	ULTCC Material systems -----	35
1.9	Microwave substrates -----	36

1.9.1	Polymer ceramic composites -----	36
1.9.2	Connectivity -----	37
1.10	Objectives of the present work-----	38

Chapter 2 Experimental Techniques

2.1	Synthesis of microwave ceramic materials -----	49
2.1.1	Solid state ceramic route -----	49
2.1.1.1	Stoichiometric weighing and mixing of raw materials -----	50
2.1.1.2	Calcination -----	50
2.1.1.3	Pellet preparation -----	52
2.1.1.4	Sintering-----	52
2.2	Synthesis of polymer ceramic composites -----	56
2.3	Thermal characterization -----	56
2.3.1	Thermogravimetric Analysis (TGA) and Differential Scanning Calorimetry (DSC) -----	56
2.3.2	Thermomechanical Analysis (TMA) -----	57
2.3.2.1	Shrinkage behavior -----	58
2.3.2.2	Coefficient of thermal expansion (CTE) -----	58
2.4	Crystal structure characterization techniques -----	59
2.4.1	X- ray diffraction-----	59
2.4.2	Raman spectroscopy-----	60
2.5	Scanning Electron Microscopy (SEM) -----	61
2.6	Dielectric characterization-----	62
2.6.1	Low frequency measurements-----	62
2.6.2	Microwave dielectric characterization -----	63
2.6.2.1	Measurement of relative permittivity (ϵ_r) -----	64
2.6.2.2	Measurement of unloaded quality factor (Q_u) -----	66
2.6.2.3	Waveguide cavity perturbation technique -----	68
2.6.2.4	Measurement of temperature coefficient of resonant frequency (τ_f)-----	69
2.7	Mechanical strength measurement -----	70

Chapter 3 Structure and Microwave Dielectric Properties of Ultra-low Temperature Co-firable AV_2O_6 (A= Ba,Sr,Ca,Mg and Zn) Ceramics

3.1	Introduction	74
3.2	Experimental techniques	79
3.3	Results and discussion	80
3.3.1	TGA/DSC studies	80
3.3.2	X-ray diffraction studies	83
3.3.3	Raman spectroscopic studies	84
3.3.4	Morphological and dielectric studies	88
3.3.5	Compatibility studies	92
3.4	Conclusions	97

Chapter 4 Effect of Vanadium Substitution on the Structure and Microwave Dielectric Properties of $5BaO-2Nb_2O_5$ Binary Ceramic System

4.1	Introduction	103
4.2	Experimental techniques	105
4.3	Results and discussion	107
4.3.1	X-ray diffraction studies	107
4.3.2	Raman spectroscopic studies	111
4.3.3	Morphological and dielectric studies	115
4.3.4	Compatibility studies	121
4.4	Conclusions	123

Chapter 5 Crystal Structure and Microwave Dielectric Properties of New Alkaline Earth Vanadate $A_4V_2O_9$ (A= Ba,Sr,Ca,Mg and Zn) Ceramics

5.1	Introduction	129
5.2	Experimental techniques	132
5.3	Results and discussion	133
5.3.1	X-ray diffraction studies	133
5.3.2	Raman spectroscopic studies	136
5.3.3	Morphological and dielectric studies	142

5.3.4	Compatibility studies -----	145
5.4	Conclusions -----	148

Chapter 6 Effect of A site modification on the structure and microwave dielectric properties of $A_4V_2O_9$ ceramics

6.1	Introduction -----	152
6.2	Experimental techniques -----	153
6.3	Results and discussion -----	154
6.3.1	X-ray diffraction studies -----	154
6.3.2	Raman spectroscopic studies -----	158
6.3.3	Morphological and thermal studies -----	161
6.3.4	Dielectric studies -----	163
6.4	Conclusions -----	166

Chapter 7 Preparation and Characterization of $Ba_3V_2O_8$ filled HDPE Composites and Design of Microstrip Patch Antennas

7.1	Introduction -----	170
7.2	Experimental techniques -----	173
7.2.1	Preparation of phase pure $Ba_3V_2O_8$ filler -----	173
7.2.2	Fabrication of HDPE/ $Ba_3V_2O_8$ composites -----	173
7.2.3	Theoretical modeling -----	173
7.2.4	Fabrication of microstrip patch antenna -----	175
7.2.5	Characterization techniques -----	177
7.3	Results and discussion -----	178
7.3.1	X-ray diffraction studies of HDPE/ $Ba_3V_2O_8$ composites ----	178
7.3.2	Density and dielectric properties of the composites -----	179
7.3.3	Morphology of the composites -----	185
7.3.4	Coefficient of linear thermal expansion (CTE) -----	186
7.3.5	Ultimate tensile strength (UTS) -----	187
7.3.6	Microstrip patch antenna measurements -----	188
7.4	Conclusions -----	193

Chapter 8 Summary and Scope of Future Work

8.1	Summary -----	198
	8.1.1 Alkaline earth vanadate systems -----	198
	8.1.2 Microstrip patch antenna -----	202
8.1	Future work -----	202

List of Figures

<i>Figure No.</i>	<i>Caption</i>	<i>Page No</i>
Figure 1.1	The electromagnetic spectrum and IEEE microwave frequency bands-----	3
Figure 1.2	(a) Interaction of electric and magnetic field lines with a cylindrical resonator (b) Total multiple internal reflections in dielectric resonator -----	6
Figure 1.3	Magnetic wall boundary condition approximation and distribution of H_z versus z for $\rho=0$ of the first mode of the cylindrical dielectric resonator -----	8
Figure 1.4	Schematic of polarization mechanisms in dielectric materials -----	10
Figure 1.5	Variation of real and imaginary parts of dielectric constant with frequency -----	11
Figure 1.6	Temperature coefficient of dielectric constant verses dielectric constant plot for various materials -----	17
Figure 1.7	Schematic of a resonant peak -----	18
Figure 1.8	Cross sectional view of a LTCC module-----	24
Figure 1.9	Typical multilayer ceramic substrate manufacturing process --	25
Figure 1.10	Schematic representations of all possible interactions in the LTCC module with one, two and three types of tapes -----	30
Figure 1.11	Sheet resistance values of each type of conductive paste-----	34
Figure 1.12	Ten connectivity patterns for a diphasic solid-----	38
Figure 2.1	Reaction between two kinds of particles to form a product at the points of contact-----	50
Figure 2.2	Schematic representation of solid state ceramic route -----	51
Figure 2.3	Different stages of solid state sintering-----	54
Figure 2.4	Different stages of liquid phase sintering -----	55
Figure 2.5	Thermomechanical analyzer for shrinkage and CTE measurements -----	58
Figure 2.6	Schematic of (a) Bragg diffraction (b) X-ray diffractometer---	60
Figure 2.7	(a) Energy level diagram of Raman and Rayleigh scattering (b) Schematic of Raman spectrometer-----	61
Figure 2.8	Temperature coefficient of dielectric constant ($\tau_{\epsilon r}$) measurement setup -----	63

Figure 2.9	Schematic design of the Hakki and Coleman setup used for measuring the dielectric constant under end shorted condition -----	65
Figure 2.10	(a) Mode chart (b) Frequency response of the TE ₀₁₁ mode of a dielectric resonator with $\epsilon_r = 38$ -----	66
Figure 2.11	Cavity setup for the measurement of Q-factor -----	67
Figure 2.12	Microwave resonance spectra of BMT ($\epsilon_r = 24$) in the (a) reflection and (b) transmission configuration -----	68
Figure 2.13	(a) Schematic representation of X-band waveguide cavity (b) Shift in the resonant frequency with the introduction of the sample inside the cavity -----	69
Figure 3.1	Equilibrium diagram of the BaO-V ₂ O ₅ system: (1) Thermographic and (2) Thermo-optical results -----	75
Figure 3.2	Schematic views of the crystal structures of (a) ZnV ₂ O ₆ and (b) MgV ₂ O ₆ -----	78
Figure 3.3	(a) The schematic view of CaV ₂ O ₆ structure along <i>b</i> -direction (b) the VO ₅ chains along [010] axis -----	78
Figure 3.4	(a) The crystal structure of BaV ₂ O ₆ and (b) infinite chains formed by shared-corners of VO ₄ tetrahedra -----	79
Figure 3.5	TGA results of AO-V ₂ O ₅ (A= Ba, Sr, Ca, Mg and Zn) compositions -----	81
Figure 3.6	DSC results of AO-V ₂ O ₅ (A= Ba, Sr, Ca, Mg and Zn) compositions -----	82
Figure 3.7	TGA/DSC results of the as-received MgO powder -----	82
Figure 3.8	X-ray diffraction patterns of AV ₂ O ₆ (A= Ba, Sr, Ca, Mg and Zn) ceramics -----	83
Figure 3.9	Raman spectra of AV ₂ O ₆ ceramics with (a) Ba (b)Sr (c)Ca (d)Mg and (e)Zn -----	85
Figure 3.10	SEM pictures of AV ₂ O ₆ ceramics with (a) Ba (b) Sr (c) Ca and (d) Zn sintered at optimum sintering temperatures for 1h -----	88
Figure 3.11	Shrinkage behavior of (a) BaV ₂ O ₆ and (b) CaV ₂ O ₆ ceramics ----	89
Figure 3.12	CTE curves of BaV ₂ O ₆ and CaV ₂ O ₆ ceramics -----	89
Figure 3.13	Variation of density and dielectric constant of BaV ₂ O ₆ ceramic as a function of sintering temperature at GHz -----	91
Figure 3.14	Variation of density and dielectric constant of CaV ₂ O ₆ ceramic as a function of sintering temperature at GHz -----	91
Figure 3.15	Variation of resonant frequency of (a) BaV ₂ O ₆ and (b) CaV ₂ O ₆ ceramics as a function of temperature at GHz -----	92

Figure 3.16	X-ray diffraction pattern of BaV ₂ O ₆ ceramic co-fired with 20 wt% Al powder sintered at 550°C for 1h -----	93
Figure 3.17	X-ray diffraction pattern of CaV ₂ O ₆ ceramic co-fired with 20 wt% Al powder sintered at 660°C for 1h -----	94
Figure 3.18	(a) SEM image of BaV ₂ O ₆ ceramic co-fired with 20 wt% Al powder sintered at 550°C for 1h (b) EDS spectrum of Spot 1 (c) EDS spectrum of Spot 2 -----	94
Figure 3.19	X-ray dot mapping image of BaV ₂ O ₆ ceramic co-fired with 20 wt% Al powder sintered at 550°C for 1h [(a) Overlay on secondary electron image (b-e) elemental images (f) Overlay image]-----	95
Figure 3.20	(a) Backscattered SEM image of CaV ₂ O ₆ ceramic co-fired with 20 wt% Al sintered at 660°C for 1h (b) EDS spectrum of Spot 1 (c) EDS spectrum of spot 2-----	95
Figure 3.21	X-ray dot mapping image of CaV ₂ O ₆ ceramic co-fired with 20wt% Al sintered at 660°C for 1h [(a) Overlay on secondary electron image (b-e) elemental images (f) Overlay image]-----	96
Figure 3.22	EDS line scan image of BaV ₂ O ₆ ceramic co-fired with 20 wt%Al -----	96
Figure 3.23	EDS line scan image of CaV ₂ O ₆ ceramic co-fired with 20 wt%Al -----	97
Figure 4.1	Linkage of the [Cd(2)Cd(3)O ₈] zig zag chains by V(3)O ₄ tetrahedra (close hatching) and V ₂ O ₇ tetrahedron dough (Black, formed from V (1) and V (2))-----	105
Figure 4.2	X-ray diffraction patterns of Ba ₅ Nb _{4-x} V _x O ₁₅ (x = 0-4) ceramics-----	108
Figure 4.3	X-ray diffraction patterns of 5BaO-2V ₂ O ₅ ceramic fired at (a) 300°C (b) 400°C (c) 500°C (d) 600°C and (e) 700°C for 1h-----	109
Figure 4.4	X-ray diffraction pattern of Ba ₃ V ₂ O ₈ -Ba ₂ V ₂ O ₇ mixtures sintered at 900°C for 1h-----	110
Figure 4.5	Raman spectra of Ba ₅ Nb _{4-x} V _x O ₁₅ (x= 0-4) ceramics -----	111
Figure 4.6	Raman spectra of (a) BV4 (b) Ba ₃ V ₂ O ₈ and (c) Ba ₂ V ₂ O ₇ ceramics-----	114
Figure 4.7	SEM pictures of (a) BN4 (b) BN3V (c) BN2V2 (d) BNV3 (e) backscattered SEM image of BV4 ceramic (f) EDS spot analysis result and (g) EDS mapping of BV4 ceramic sintered at optimum temperature -----	116
Figure 4.8	Shrinkage behavior of BV4 ceramic -----	117

Figure 4.9	Variation of density and dielectric constant of $Ba_5Nb_{4-x}V_xO_{15}$ ceramics with respect to vanadium content (x) at 1MHz-----	118
Figure 4.10	Variation of density and dielectric constant with sintering temperature of BV4 ceramic -----	120
Figure 4.11	X-ray diffraction pattern of BV4 ceramic co-fired with 20 wt% Ag powder sintered at 900°C for 1h -----	122
Figure 4.12	(a) SEM image of BV4 ceramic co-fired with 20 wt% Ag powder sintered at 900°C for 1h (b) EDS spectrum of Spot 1 (c) EDS spectrum of Spot 2 -----	122
Figure 4.13	X-ray dot mapping image of BV4 ceramic co-fired with 20 wt% Ag powder sintered at 900°C for 1h [(a) Overlay on secondary electron image (b-e) elemental images (f) Overlay image]-----	123
Figure 4.14	EDS line scan image of BV4 ceramic co-fired with 20 wt% Ag powder sintered at 900°C for 1h -----	123
Figure 5.1	The ZnO- V_2O_5 phase diagram-----	130
Figure 5.2	Schematic representation of the atomic order of $Zn_4V_2O_9$ along [001] -----	130
Figure 5.3	The SrO- V_2O_5 phase diagram -----	131
Figure 5.4	XRD patterns of $A_4V_2O_9$ (A= Ba, Sr, Ca, Mg and Zn) ceramics-----	134
Figure 5.5	XRD patterns of $A_3V_2O_8$ (A= Ba, Sr, Ca, Mg and Zn) ceramics-----	135
Figure 5.6	Raman spectra of $A_4V_2O_9$ (A= Ba, Sr, Ca, Mg and Zn) ceramics-----	138
Figure 5.7	Raman spectra of $A_3V_2O_8$ (A= Ba, Sr, Ca, Mg and Zn) ceramics-----	139
Figure 5.8	SEM images of (a) $Ba_4V_2O_9$ (b) $Sr_4V_2O_9$ (c) $Mg_4V_2O_9$ and (d) $Zn_4V_2O_9$ at optimum sintering temperatures -----	142
Figure 5.9	Variation of density and dielectric constant of $Mg_4V_2O_9$ ceramic with sintering temperature -----	144
Figure 5.10	Temperature variation of resonant frequency of $Mg_4V_2O_9$ ceramic sintered at 940°C for 1h -----	144
Figure 5.11	XRD pattern of $Mg_4V_2O_9$ + 20 wt% Ag ceramic sintered at 940°C for 1h -----	146
Figure 5.12	(a) Backscattered image of $Mg_4V_2O_9$ ceramic co-fired with 20 wt% Ag (b) EDS spectrum of spot 1 and (c) EDS spectrum of spot 2 -----	146

Figure 5.13	X-ray dot mapping of $Mg_4V_2O_9$ ceramic co-fired with 20 wt% Ag [(a) Overlay on secondary electron image (b-e) elemental images (f) Overlay image]-----	147
Figure 5.14	EDS line scan of $Mg_4V_2O_9$ ceramic co-fired with 20 wt% Ag-----	147
Figure 6.1	Structure of $Bi_2CaV_2O_9$ -----	153
Figure 6.2	XRD patterns of $Bi_2AV_2O_9$ with A=Ba, Sr, Ca, Mg and Zn ceramics-----	155
Figure 6.3	XRD patterns of $R_2BaV_2O_9$ ceramics with R= La, Nd, Y and Yb -----	156
Figure 6.4	XRD patterns of $R_2SrV_2O_9$ ceramics with R=La, Nd, Y and Yb--	157
Figure 6.5	XRD patterns of $R_2CaV_2O_9$ ceramics with R=La, Nd, Y and Yb-	158
Figure 6.6	Raman spectra of $Bi_2AV_2O_9$ (A= Ba, Sr, Ca, Mg and Zn) ceramics-----	159
Figure 6.7	Backscattered SEM images of (a) $Bi_2BaV_2O_9$ (b) $Bi_2SrV_2O_9$ (c) $Bi_2CaV_2O_9$ (d) $Bi_2MgV_2O_9$ (e) $Bi_2ZnV_2O_9$ (f) EDS spectrum of $BiVO_4$ (g) $BiBaVO_5$ and (h) $Bi_2CaV_2O_9$ -----	162
Figure 6.8	TGA-DSC curves of Bi_2O_3 -CaO- V_2O_5 composition -----	163
Figure 6.9	Variation of density and dielectric constant of $Bi_2CaV_2O_9$ ceramic as a function of sintering temperature at GHz -----	164
Figure 6.10	Variation of resonant frequency of $Bi_2CaV_2O_9$ ceramic as a function of temperature -----	165
Figure 7.1	Photolithographic technique used for antenna fabrication-----	177
Figure 7.2	X-ray diffraction pattern of $Ba_3V_2O_8$ calcined at 1100°C for 1h	
Figure 7.3	X-ray diffraction patterns of (a) Pure HDPE (b) HDPE+20 vol% $Ba_3V_2O_8$ (c) HDPE+40 vol% $Ba_3V_2O_8$ and (d) HDPE+ 60 vol% $Ba_3V_2O_8$ -----	179
Figure 7.4	Variation of density and dielectric constant of HDPE/ $Ba_3V_2O_8$ as a function of filler loading. Fine tuning of density and dielectric constant of HDPE/ $Ba_3V_2O_8$ as a function of filler loading (Inset) -----	181
Figure 7.5	Variation of loss tangent of HDPE/ $Ba_3V_2O_8$ composites with filler loading at X-band -----	182
Figure 7.6	Comparison of dielectric constant of HDPE/ $Ba_3V_2O_8$ composites measured at X-band and 1MHz -----	183
Figure 7.7	Variation of temperature coefficient of dielectric constant with respect to filler loading -----	184
Figure 7.8	Comparison of experimental dielectric constant with different theoretical models -----	185

Figure 7.9	SEM micrographs of (a) $Ba_3V_2O_8$ filler (b) 52 vol% (c) 54 vol% (d) 56 vol% and (e) cross section of 54 vol% $Ba_3V_2O_8$ filled HDPE composites -----	186
Figure 7.10	Variation of CTE as a function of filler loading in HDPE/ $Ba_3V_2O_8$ composites-----	187
Figure 7.11	Variation of ultimate tensile strength of HDPE/ $Ba_3V_2O_8$ composites as a function of filler loading-----	188
Figure 7.12	Simulated structures of microstrip patch antennas with substrates of (a) 1.6 mm and (b) 0.8 mm thickness-----	189
Figure 7.13	(a) Microstrip patch antenna fabricated for (i) 2.45 GHz and (ii) 5 GHz (b) Measurement setup for microstrip patch antenna using vector network analyzer -----	190
Figure 7.14	(a) Simulated and (b) measured return loss characteristics of the patch antenna at 2.45 GHz for $\epsilon_r= 6.3$ and $\tan\delta= 0.004$ ---	191
Figure 7.15	(a) Simulated and (b) measured return loss characteristics of the patch antenna at 5 GHz for $\epsilon_r= 6.3$ and $\tan\delta= 0.004$ -----	192
Figure 8.1	Modified BaO- V_2O_5 phase diagram -----	200
Figure 8.2	Schematic of a substrate integrated waveguide (SIW) -----	203

List of Tables

<i>Table No.</i>	<i>Caption</i>	<i>Page No.</i>
Table 1.1	Typical material combinations of LTCC and HTCC -----	22
Table 1.2	Comparison between the dielectric properties of ceramic and organic materials -----	23
Table 1.3	Dielectric properties of commercial LTCCs -----	29
Table 1.4	Various molybdenum based compositions with their sintering temperature and microwave dielectric properties -----	31
Table 1.5	Vanadium based ceramics along with their microwave dielectric properties -----	32
Table 1.6	Electrical resistance and melting point of conductor metals -----	33
Table 3.1	Available crystal structure data of AV_2O_6 (A= Ba, Sr, Ca, Mg and Zn) compositions -----	79
Table 3.2	Comparison of lattice parameters of AV_2O_6 (A= Ba, Sr, Ca, Mg and Zn) ceramics -----	84
Table 3.3	Raman mode assignments for BaV_2O_6 and SrV_2O_6 ceramics-----	86
Table 3.4	Raman mode assignments for CaV_2O_6 , MgV_2O_6 and ZnV_2O_6 ceramics -----	87
Table 3.5	Sintering temperature, density and dielectric properties of AV_2O_6 (A= Ba, Sr, Ca, Mg and Zn) ceramics -----	92
Table 4.1	Raman mode assignments of BN_4 , BN_3V , BN_2V_2 , BNV_3 and BV_4 ceramics -----	113
Table 4.2	Raman mode assignments of $Ba_3V_2O_8$, $Ba_2V_2O_7$ and BV_4 ceramics -----	115
Table 4.3	Sintering temperature, density, dielectric constant, quality factor and temperature coefficient of resonant frequency of $Ba_5Nb_{4-x}V_xO_{15}(x=0-4)$, $Ba_2V_2O_7$ and $Ba_3V_2O_8$ ceramics -----	119
Table 5.1	Sintering temperature, density and dielectric properties of the stable compounds in the BaO- V_2O_5 phase diagram -----	129
Table 5.2	Comparison of the available structural details of the oxovanadate and orthovanadate ceramics -----	136
Table 5.3	Raman mode assignments of $A_4V_2O_9$ (A=Ba, Sr, Ca, Mg and Zn) ceramics -----	140

Table 5.4	Raman mode assignments of $A_3V_2O_8$ (A=Ba, Sr, Ca, Mg and Zn) ceramics -----	141
Table 5.5	Sintering temperature, density and dielectric properties of $A_4V_2O_9$ and $A_3V_2O_8$ (A=Ba, Sr, Ca, Mg, Zn) ceramics-----	143
Table 6.1	Raman mode assignments of $Bi_2AV_2O_9$ (A= Ba, Sr, Ca, Mg and Zn) ceramics -----	160
Table 6.2	Sintering temperature, density and dielectric properties of $Bi_2AV_2O_9$ (A=Ba, Sr, Ca, Mg, Zn) ceramics -----	165
Table 8.1	Identified LTCC and ULTCC single phase compositions in the AO- V_2O_5 (A=Ba, Sr, Ca, Mg and Zn) system-----	201

1

Introduction

- 1.1 Introduction
- 1.2 Microwave ceramics
- 1.3 Physics of microwave dielectrics
- 1.4 Material requirements for dielectric resonator applications
- 1.5 Multilayer co-fired ceramics
- 1.6 Material requirements for LTCC
- 1.7 LTCC material systems
- 1.8 Ultra-low Temperature Co-fired Ceramics (ULTCC)
- 1.9 Microwave substrates
- 1.10 Objectives of the present work

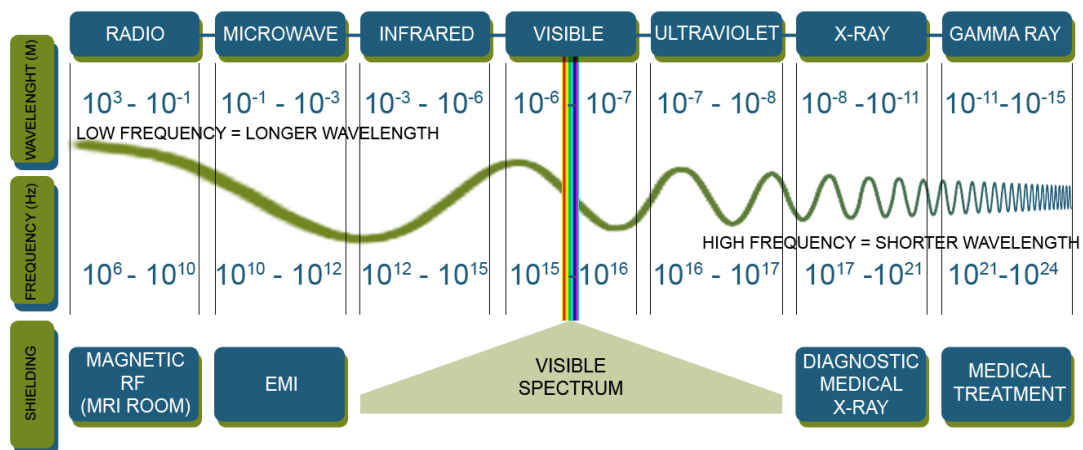
1.1 Introduction

With the recent revolution in wireless communication, the research and development in the miniaturization of microwave devices using advanced dielectric materials has been one of the biggest challenges in contemporary materials science. The advancement in the wireless communication devices and commercialization of the same demand miniaturized and multifunctional designs. Microwaves of higher frequency and smaller wavelength are preferred as carrier waves for wireless communication applications.

The electromagnetic spectrum can be divided into various frequency ranges of which radio frequencies range from 3 KHz to 300 GHz wherein microwaves range from 300 MHz to 300 GHz as shown in Figure 1.1 [1]. The microwave region can be further divided into ultra high frequency (UHF), super high frequency (SHF) and extremely high frequency (EHF) regions. The most explored microwave frequency region is 1-40 GHz because above this frequency long range communication becomes difficult due to high atmospheric absorption. Institute of Electrical and Electronic Engineers (IEEE) classified the microwave frequency spectrum into various bands such as L, S, C, X, K_u, K, K_a etc. and are used for specific applications. Each band has its own application areas for example C and X bands are for satellite communication, K and K_a bands are for military applications, K_u band for direct-broadcast satellite, V and W bands for millimeter wave radar applications etc.

Ceramics are generally classified into traditional and advanced ceramics. Traditional ceramics include bricks, tiles, white wares, pottery and is mainly based on clay and silica. While moving into advanced ceramics, this category describes solid articles made by inorganic non-metallic oxides. Advanced ceramics can be broadly classified into piezoelectric ceramics, laser host materials etc. and have superior mechanical, electrical, optical and magnetic properties. Ceramics were used for various applications from the first half of the twentieth century onwards because of their versatile nature and characteristic properties. More than half of the ceramic industry is mainly focused on the production of glass, while the rest concentrate on electroceramics, bioceramics, nanoceramics etc. Electroceramics is a technology

centered and application driven field, which includes both dielectric and conductive ceramics. Dielectric ceramics can be divided into linear and non-linear dielectrics with large number of materials. Conductive ceramics include conductors, semiconductors and superconductors including both ionically and electronically conductive ceramics. Electroceramics include BaTiO₃, PZT, AlN, ZnO etc. and are used for various applications like capacitors, varistors, micro-electro-mechanical systems (MEMS), substrates and packages for integrated circuits etc. [2].



Band designation	Frequency range (GHz)	Wavelength
Ultra high frequency (UHF)	0.3 – 1	1 m – 30 cm
L band	1 – 2	30 cm – 15 cm
S band	2 – 4	15 cm – 7.5 cm
C band	4 – 8	7.5 cm – 3.8 cm
X band	8 – 12	3.8 cm – 2.5 cm
Ku band	12 – 18	2.5 cm – 1.7 cm
K band	18 – 27	1.7 cm – 1.1 cm
Ka band	27 – 40	1.1 cm – 750 mm
V band	40 – 75	750 mm – 40 mm
W band	75 – 110	40 mm – 27 mm
Millimeter wave	110 – 300	27 mm – 10 mm

Figure 1.1 The electromagnetic spectrum and IEEE microwave frequency bands

1.2 Microwave ceramics

In the early stages, conventional ceramic materials were widely used for the production of microwave components such as filters and resonators but they became inadequate for the development in the area of high frequency applications. Microwave

dielectric ceramics are widely used for the confinement of electromagnetic waves in various microwave devices, which resulted rapid progress in the miniaturization of such circuitries. In high frequency electronic components, several kinds of ceramics with different dielectric constant are desirable for variety of applications. Low dielectric constant is preferred for high speed transmission of signals whereas high dielectric constant is needed for manufacturing miniaturized electronic devices since size is inversely proportional to square root of dielectric constant.

The recent developments in the wireless communication systems demand high volume and low cost fabrication along with good electrical performance, reliability, surface mounting techniques and circuit miniaturization. Among these, miniaturization of microwave devices has got paramount importance in wireless communication systems, which has led to the development of a new area of Low Temperature Co-fired Ceramics (LTCC) technology. In the present work, LTCC materials were prepared through solid state ceramic route and made in the form of dielectric resonators for microwave characterization. Hence, a brief account on the science behind dielectric resonators and their material requirements for practical applications are given in the forthcoming sections.

1.2.1 Dielectric resonators

Dielectric resonators are ceramic compacts which can confine electromagnetic energy in the air dielectric interface as a result of total internal reflection. The dielectric resonator concept was first introduced by Richtmyer in 1939 [3, 4]. Following this initial work, many research activities have been taken place on dielectric resonators but practically nothing happened for more than two decades. Compared to conventional metallic cavities, dielectric resonators are small in size, weight and cost and can be easily integrated in MICs and coupled to planar transmission lines. TiO₂ (Rutile) was the first dielectric resonator reported in the literature with high dielectric constant of ~ 100 and low dielectric loss of $\sim 6 \times 10^{-5}$ at 3 GHz [5]. But, the poor temperature coefficient of resonant frequency ($\sim +400$ ppm/°C) prevented its wider usage in microwave devices [6-8]. Later, a detailed analysis of the resonator modes in anisotropic dielectric, identification of various modes of oscillation and their respective resonant frequencies were carried out by

Cohn et al. [6]. According to previous reports, modes can be of two types: one resembles an electric dipole (E mode) and the other a magnetic dipole (H mode) field [6, 9]. Later in 1971, Masse et al. developed the first temperature stable low loss BaTi₄O₉ resonator [10]. A real breakthrough occurred when Murata Manufacturing Company, Japan developed (Zr,Sn)TiO₄ ceramics for microwave circuit applications. Afterwards, extensive work has been carried out in microwave dielectric resonators area by many researchers and came out with a host of materials suitable for all bands of microwave applications.

1.2.2 Microwave resonance

Resonant structures can be divided into two: transmission type, which is made from transmission structures such as rectangular, cylindrical, coaxial and microstrip resonators and non-transmission type, such as ring resonators and sphere resonators. Cylindrical dielectric resonators are widely used in microwave circuits and materials property characterization. Dielectric resonator exhibits maximum confinement of electromagnetic field at specific resonant frequencies due to multiple total internal reflections at the dielectric and air boundary (Figure 1.2). The confined electromagnetic wave form standing waves to generate resonance. A dielectric material must have sufficiently high dielectric constant to confine electromagnetic waves within itself by total internal reflection at the air dielectric interface [11, 12]. The air dielectric interface will act as a perfect reflector of microwaves, if the angle of incidence is greater than the critical angle θ_c and is expressed as

$$\theta_c = \sin^{-1} \left(\frac{1}{\sqrt{\epsilon_r}} \right) \quad (1.1)$$

For large values of dielectric constant ϵ_r , the waves are internally reflected and the reflection coefficient approaches unity. Therefore, the dielectric boundary of a high dielectric constant material can be considered as a perfect magnetic conductor [13]. If the transverse dimensions of the dielectrics are comparable to the wavelength of microwaves, then certain field distributions will satisfy Maxwell's equations and boundary conditions. The modes satisfying this condition only will be excited and the corresponding resonating frequency depends on the dimensions and relative permittivity of the dielectric specimen.

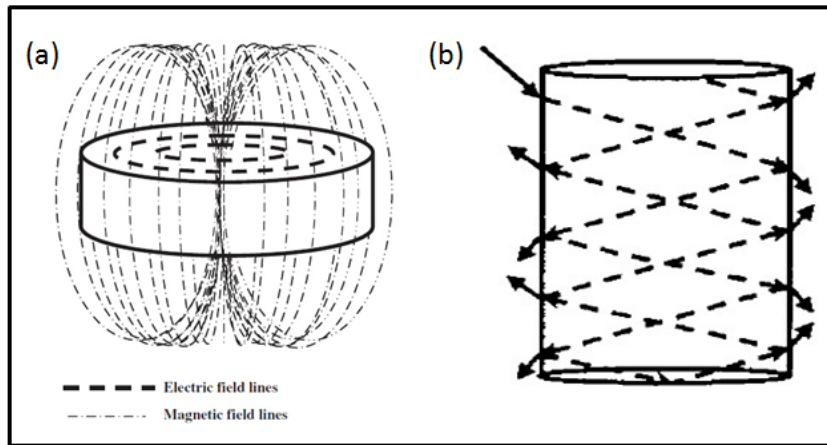


Figure 1.2 (a) Interaction of electric and magnetic field lines with a cylindrical resonator (b) Total multiple internal reflections in dielectric resonator

In terms of energy exchange, resonance can be considered as a phenomenon in which the electric and magnetic energy can be totally changed from one to the other in a periodic manner. Resonant frequency (f_o) is the frequency at which the electric energy can be totally changed to magnetic energy and vice versa. If the resonance is lossless, then the total energy (which is a sum of electric and magnetic energy) does not change with time.

$$W_e(t) + W_m(t) = W_0 \quad (1.2)$$

The electric and magnetic energy can be calculated from the field distributions in the resonator by solving the wave functions given below with certain boundary conditions.

$$\nabla^2 E + k^2 E = 0 \quad (1.3)$$

$$\nabla^2 H + k^2 H = 0 \quad (1.4)$$

where, $k^2 = \omega^2 \epsilon \mu$, ϵ and μ are the permittivity and permeability of the medium inside the resonator. For an ideal lossless resonator, k is a series of discrete real numbers like k_1, k_2, \dots , and are called as the Eigen values of the above wave equations. Therefore the resonant frequencies can be calculated from these Eigen values.

$$f_i = \frac{c}{2\pi} k_i \quad (i = 1, 2, 3 \dots) \quad (1.5)$$

where, c is the velocity of light in free space. At resonance, the total stored energy is equal to the maximum electric energy or maximum magnetic energy,

$$W = W_{e,max} = \frac{\epsilon}{2} \iiint |E^2| dV \quad (1.6)$$

$$= \frac{\mu}{2} \iiint |H^2| dV = W_{m,max} \quad (1.7)$$

The energy storage and the energy dissipation can be related by the factor called attenuation parameter (α), which is the attenuation rate of the resonator after the source is removed. By definition we have

$$E = E_0 e^{-\alpha t} \quad (1.8)$$

$$W = W_0 e^{-2\alpha t} \quad (1.9)$$

So the energy dissipation $P_L = \frac{-dW}{dt} = 2\alpha W$

$$\therefore \alpha = \frac{P_L}{2W} = \frac{\omega_0}{2Q_0} \quad (1.10)$$

where, $Q_0 = \frac{\omega_0 W}{P_L}$ is the quality factor. Therefore the total energy storage becomes

$$W = W_0 e^{-\frac{\omega_0}{Q_0} t} \quad (1.11)$$

The above equation indicates that higher the quality factor, the lower the resonance attenuation [11].

1.2.3 Modes of a dielectric resonator

There are many possible resonant modes in a dielectric resonator which can be excited by the applied field. They can be divided into three categories viz. transverse electric (TE), transverse magnetic (TM) and hybrid electromagnetic (HEM) modes. Each of these groups has infinite number of individual modes. Dimensions of the dielectric resonator are very important for the separation of the modes, and the aspect ratio (Diameter/Length) should be in between 1.5 to 2. The length L of the dielectric resonator is less than its diameter ($D = 2a$, a is the radius) for most of the practical applications. With this shape, the lowest frequency resonant mode has a circular electric field distribution and the magnetic field is strongest on the axis of the disk and at a sufficient distance outside the disk it resembles to that of

an axial magnetic dipole. For $L > D$, the fundamental mode has an equivalent magnetic dipole moment transverse to the axis. The traditionally used mode for a cylindrical dielectric resonator is $TE_{01\delta}$ and is the analogue of TE_{011} mode of a circular metallic cavity. The lowest order TE mode is TE_{01} which is similar to TM_{01} mode of a circular metallic waveguide. The resonant length for the $TE_{01\delta}$ mode is less than $\lambda_g/2$ (where λ_g is the guide wavelength of the TE_{01} dielectric waveguide mode), the symbol $\delta = 2L/\lambda_g < 1$ is used to denote the z variation of the resonant mode. Because of the high dielectric constant of the dielectric material compared to free space, propagation of the electromagnetic field along z direction (considering cylindrical coordinate system) can occur inside the dielectric at resonant frequency. But in the air region around the dielectric medium, the field will be zero. The distribution of H_z field distribution in a dielectric resonator is given in Figure 1.3 and the higher modes have more variation in the z direction inside the resonator [1, 13].

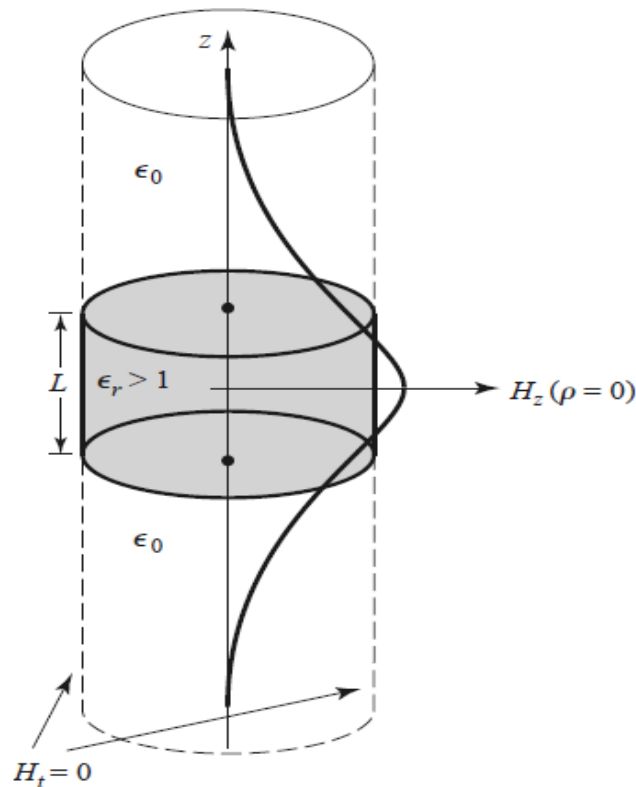


Figure 1.3 Magnetic wall boundary condition approximation and distribution of H_z versus z for $\rho=0$ of the first mode of the cylindrical dielectric resonator [Ref. 1]

1.3 Physics of Microwave Dielectrics

1.3.1 Polarization mechanisms in dielectrics

When an electric field is applied to a material having positive and negative charges, the positive charges displace in the direction of the applied field whereas the negative charges displace in the opposite direction. This displacement induces dipoles in the material. The dipole moment per unit volume of the material is the sum of all the individual dipole moments within that volume and is called as polarization (P) of the material. As polarization measures the additional electric flux density due to material present, it has the same unit as electric flux density ($D = \epsilon E$) and can be written as

$$D = \epsilon_0 E + P \quad (1.12)$$

$$\text{Therefore polarization } P \text{ is, } P = \epsilon_0 (\epsilon_r - 1)E \quad (1.13)$$

where, E is the electric field strength in units of N/C, ϵ_0 is the permittivity of free space and ϵ_r is the relative permittivity of the material. Relative permittivity is one for free space and greater than one for all other materials. Relative permittivity can be measured using parallel plate capacitor method where capacitance C of the capacitor is

$$C = \epsilon_0 \epsilon_r A/d \quad (1.14)$$

where, A is the area of the sample and d is the distance between the plates.

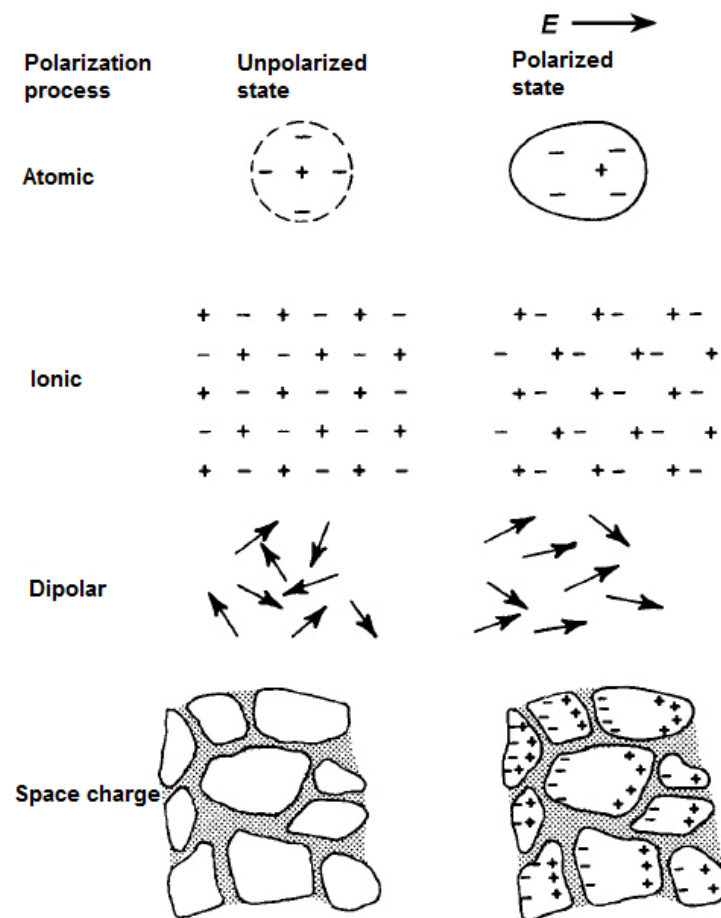


Figure 1.4 Schematic of polarization mechanisms in dielectric materials [Ref. 15]

Based on the formation mechanisms, polarization can be classified into four types viz. electronic, ionic, orientation and space charge polarizations (Figure 1.4). Electronic polarization is due to the displacement of positively charged nucleus and negatively charged electron cloud in opposite directions under the applied electric field. Electronic polarization is extremely rapid when voltage is applied. This occurs at optical frequency range (10^{15} GHz) and hence also called as optical polarization. Ionic polarization involves the displacement of positive and negative ions from their equilibrium positions under the influence of an electric field and thus results dipoles. Ionic polarization is slower than electronic polarization, since it involves the movement of heavier ions than electrons. This is essentially the distortion of the normal lattice vibration and the frequency corresponding to this is in the order of $\sim 10^9$ - 10^{13} Hz. The third type is orientation polarization which occurs only in molecules with permanent dipole moments. When an electric field is applied, these

dipoles orient themselves and thus induce polarization of the material. This type of polarization mainly takes place in ferroelectric materials. Finally the fourth type, space charge polarization occurs due to the accumulation of charge carriers at the electrodes or at the interface or grain boundary of a material. The ions diffuse over considerable distances in response to the applied electric field and results in the redistribution of charges in the dielectric medium [14-16]. The frequency dependence of different polarization mechanisms is given in Figure 1.5.

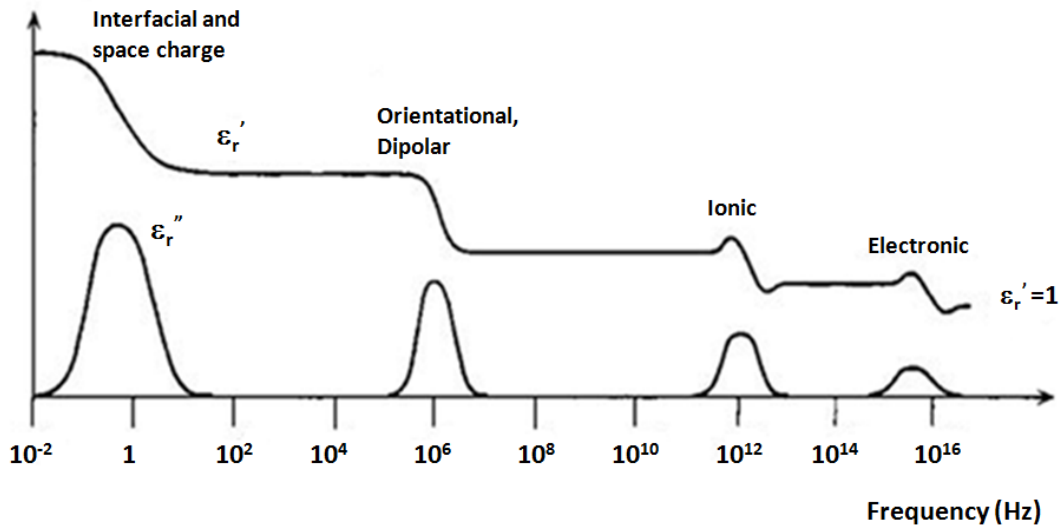


Figure 1.5 Variation of real and imaginary parts of dielectric constant with frequency

According to Debye model, electronic and ionic polarizations occur instantaneously, followed by the slower polarization mechanisms. The time dependence of polarization is expressed as

$$\dot{P} = \frac{1}{\tau} \{P_s - P(t)\} \quad (1.15)$$

$$P(t) = P_s \left\{ 1 - \exp\left(-\frac{t}{\tau}\right) \right\} \quad (1.16)$$

where, τ is the relaxation time. By substitution, the equation becomes

$$P = \frac{1}{\tau} \{(\epsilon_s' - \epsilon_\infty') \epsilon_0 E - P(t)\} \quad (1.17)$$

Integration followed by equating the real and imaginary parts of permittivity gives the Debye expressions for the relaxation mechanisms and are given by

$$\epsilon = \epsilon_\infty + \frac{\epsilon_s - \epsilon_\infty}{1 + \omega^2 \tau^2} \quad (1.18)$$

$$\varepsilon'' = \frac{(\varepsilon_s - \varepsilon_\infty)\omega\tau}{1 + \omega^2\tau^2} \quad (1.19)$$

where, ε_s is the low frequency dielectric constant (static dielectric constant), ε_∞ is the dielectric constant at very high frequency and τ is the relaxation time [17-20].

1.3.2 Clausius - Mossotti Equation

Consider a solid consists of identifiable polarizable entities on the atomic scale such that the electric field experienced by a single entity is called as the local field E_L which can be calculated by considering a spherical region within the dielectric and local field is given by

$$E_L = E_m + \gamma P \quad (1.20)$$

where, $\gamma = 1/3\varepsilon_0$ is the internal field constant. If all the entities of the dielectric are of the same type and have density N , then polarization

$$P = Np = N\alpha(E_m + \gamma P) \quad (1.21)$$

where, $p = \alpha E_L$ is the dipole moment induced in the entity.

$$\frac{P}{\varepsilon_0 E_m} = \chi_e = \frac{(N\alpha/\varepsilon_0)}{1 - N\alpha\gamma} \quad (1.22)$$

For $\gamma = 1/3\varepsilon_0$, the above equation leads to the famous Clausius-Mossotti relation (in SI units),

$$\frac{\varepsilon_r - 1}{\varepsilon_r + 2} = \frac{N\alpha}{3\varepsilon_0} \quad (1.23)$$

This equation is valid for high symmetry ionic structures that are non-polar and non-conductive in nature. In CGS system, the above equation becomes

$$\frac{\varepsilon_r - 1}{\varepsilon_r + 2} = \frac{4\pi N\alpha_m}{3} \quad (1.24)$$

and $N = \frac{1}{V_m}$ where, V_m is the molecular volume and α_m the molecular polarizability in (\AA)³. Rearranging the above equation results

$$\varepsilon_r = \frac{3V_m + 8\pi\alpha}{3V_m - 4\pi\alpha} \quad (1.25)$$

Dielectric constant can be calculated using the above equation by knowing the molar volume in (\AA)³ and total molecular polarizability by using Shannon's dielectric polarizability for individual ions [21, 22].

1.4 Material requirements for dielectric resonator applications

The main three parameters required for the application of dielectric resonators are their dielectric constant, temperature coefficient of resonant frequency and quality factor. Each application requires a specific set of values for these parameters.

1.4.1 Stable dielectric constant (ϵ_r)

When microwaves enter into a dielectric material, they are slowed down by a factor proportional to $(\epsilon_r)^{1/2}$ and can be mathematically expressed as

$$\lambda_d = \frac{\lambda_0}{(\epsilon_r)^{1/2}} \quad (1.26)$$

which indicates that the wavelength decreases while frequency remains the same, where λ_0 and λ_d are the wavelengths of the electromagnetic waves in the air and dielectric medium. Therefore, high ϵ_r reduces the wavelength in the microwave region, which is useful for miniaturization. High ϵ_r materials ($\epsilon_r > 50$) are mainly used in mobile phones where miniaturization of the hand set is very important whereas medium ϵ_r ceramics ($\epsilon_r = 25-50$) are used for satellite communications and mobile base stations. Low dielectric ceramics ($\epsilon_r < 25$) are used for millimeter wave communication and as substrates for integrated circuits. In the millimeter wave range, temperature stable, low ϵ_r and high Q ceramics are used for high speed signal transmission with minimum attenuation. High Q reduces the circuit insertion losses which are suitable for filter applications, and it also suppresses electrical noises in oscillators. According to Clausius-Mossotti equation, dielectric constant of a material can be tailored by the selection of various cations depending on their ionic polarizability, effective ionic radii and the filled 3d electron shells in the case of transition metals such as Ti^{4+} , Nb^{5+} and Ta^{5+} . The value of polarizability is constant for ceramics; therefore, the dielectric constant can be tailored by changing the polarizability per unit volume. Hence, higher values of dielectric constant are mainly due to the collective polar displacement of the metal ions with respect to the oxygen

sub lattice [23]. This was clearly observed in BaTiO₃ ceramic, where the replacement of Ti by Zr increases the B site polarizability and result an increase in dielectric constant [24]. According to Ohsato, the origin of ϵ_r is due to the octahedral tilt transitions in the dielectrics. The presence of covalent bonding in dielectrics increases the bond strength and thereby causes a decrease in the volume of the octahedra which lowers the dielectric constant [25].

1.4.2 Temperature dependence of dielectric constant

In order to obtain temperature stable resonators and filters for various applications, it is necessary that the resonant frequency of the resonator should be almost stable as the temperature changes. This means that the temperature coefficient of resonant frequency (τ_f) should be approximately zero.

$$\text{ie, } \tau_f = \frac{1}{f_r} \frac{\partial f_r}{\partial T} \cong \frac{1}{f_r} \frac{\Delta f_r}{\Delta T} \cong 0 \quad (1.27)$$

where, f_r is the resonant frequency of the dielectric resonator and T is the absolute temperature. Temperature coefficient of resonant frequency (τ_f) indicates the drift in resonant frequency as the temperature changes. For practical applications, the resonant frequency of a dielectric resonator should not change with change in temperature. The origin of τ_f is related to the linear coefficient of thermal expansion (α_l), which affects the resonator dimensions and its dielectric constant variation with temperature and can be mathematically represented by Eq. 1.28 [12]. In practice, τ_f should be nearly zero for an ideal resonator [26]. Since the resonant frequency f_r depends on both size and dielectric constant (ϵ_r) of the dielectric resonator,

$$\tau_f = \frac{-\tau_{\epsilon r}}{2} - \alpha_l \quad (1.28)$$

where α_l is the linear coefficient of thermal expansion. When $\tau_f \cong 0$ results

$$\tau_{\epsilon r} = -2\alpha_l \quad (1.29)$$

Harrop differentiated the Clausius-Mossotti equation and obtained the following relations

$$\tau_c = -\alpha_L \epsilon_r \quad (1.30)$$

$$\tau_{\varepsilon r} \propto -\alpha\varepsilon_r \quad (1.31)$$

As per the above equations and by Clausius-Mossotti equation, small values of α_L or large values of $\tau_{\varepsilon r}$ control the value of τ_f . Also the influence of phase transitions on the microwave dielectric properties of Ba and Sr based complex perovskites revealed that the onset of octahedral tilt transitions have a major influence on τ_f [27]. This tilt transitions are due to the rotation of corner shared octahedra either in phase or anti-phase around the major axis of the perovskite structure. Also, the changes in the tolerance factor in complex perovskites leads to the structural phase transitions, which changes the value of $\tau_{\varepsilon r}$. Later, Reaney et al. postulated that the tolerance factor controls the temperature of the onset of tilt transitions and there by τ_f values [28]. The differential form of Clausius - Mossotti gives the temperature dependence of dielectric constant and the differential equation is

$$\begin{aligned} & \frac{1}{(\varepsilon_r - 1)(\varepsilon_r + 2)} \left(\frac{\partial \varepsilon_r}{\partial T} \right)_p \\ &= -\frac{1}{3V} \left(\frac{\partial V}{\partial T} \right)_p + \frac{V}{\alpha_m} \left(\frac{\partial \alpha_m}{\partial V} \right)_T \times \frac{1}{3V} \left(\frac{\partial V}{\partial T} \right)_p + \frac{1}{3\alpha_m} \left(\frac{\partial \alpha_m}{\partial T} \right)_V \\ &= A + B + C \end{aligned} \quad (1.32)$$

where the terms A, B and C are:

- A: The decrease in the number of polarizable particles per unit volume as the temperature increases, the direct effect of volume expansion
- B: An increase of the polarizability of a constant number of particles as the temperature increases
- C: Dependence of polarizability on temperature, the volume remaining constant. Here, the sum of A and B which describes the total effect of volume expansion, can be written as

$$A + B = \frac{1}{(\varepsilon_r - 1)(\varepsilon_r + 2)} \left(\frac{\partial \varepsilon_r}{\partial V} \right)_T \left(\frac{\partial V}{\partial T} \right)_p = \frac{1}{(\varepsilon_r - 1)(\varepsilon_r + 2)} \left(\frac{\partial \varepsilon_r}{\partial P} \right)_T \left[\frac{\frac{1}{V} \left(\frac{\partial V}{\partial T} \right)_p}{\frac{1}{V} \left(\frac{\partial V}{\partial P} \right)_T} \right] \quad (1.33)$$

The above equation can be derived by differentiating with respect to volume at constant temperature [29]. In the similar manner, differentiation with respect to temperature at constant volume gives:

$$C = \frac{1}{(\varepsilon_r - 1)(\varepsilon_r + 2)} \left(\frac{\partial \varepsilon_r}{\partial T} \right)_V \quad (1.34)$$

Therefore, three effects contribute to the temperature dependence of dielectric constant (τ_{ε_r}):

1. The decrease in the number of polarizable particles per unit volume as temperature increases (A), which is a direct result of volume expansion
2. The increase of the macroscopic polarizability (α_m) due to volume expansion (B).
3. The temperature dependence of the macroscopic polarizability (α_m) at constant volume (C).

Experimentally it is found that the volume dependent contribution (A+B) is always positive and there is always a decrease in this value from compounds with low ε_r to compounds with high ε_r whereas the direct temperature dependent term (C) can be either positive or negative value. The C value is negative for compounds with $\varepsilon_r > 10$ and positive for $\varepsilon_r < 10$. On simplification of Equation 1.34, we get the expression for the temperature dependence of dielectric constant and can be written as

$$\tau_{\varepsilon_r} = \frac{(\varepsilon_r - 1)(\varepsilon_r + 2)}{\varepsilon_r} \left[\frac{V}{\alpha_m} \left(\frac{\partial \alpha_m}{\partial v} \right)_T \alpha_l + \frac{1}{3\alpha_m} \left(\frac{\partial \alpha_m}{\partial T} \right)_v - \alpha_l \right] \quad (1.35)$$

Figure 1.6 shows the relation between ε_r and τ_{ε_r} of a number of materials having ε_r less than 100 [29-31].

From Figure 1.6, diatomic alkali halides show positive τ_{ε_r} due to strong increase of ionic polarizability (α_i) and by the large thermal expansion (α_l). Here, the second term in the above equation is small and negative because of the anharmonic part of the lattice potential and results positive value for τ_{ε_r} . With decreasing the ionicity of the material, both $\left(\frac{\partial \alpha_m}{\partial v} \right)$ and α_l decreases, which results a decrease in τ_{ε_r} value (ionic inorganics). For materials with more complicated structures, the additional ionic polarizability increases the dielectric constant (ε_r) and at the same time shifts τ_{ε_r} to negative values. Here, both electronic and ionic

polarizabilities lead to the softening of the lattice modes, which increases the anharmonic part $\left(\frac{\partial\alpha_m}{\partial T}\right)$ in equation (1.35) and makes τ_{er} even more negative [28- 32].

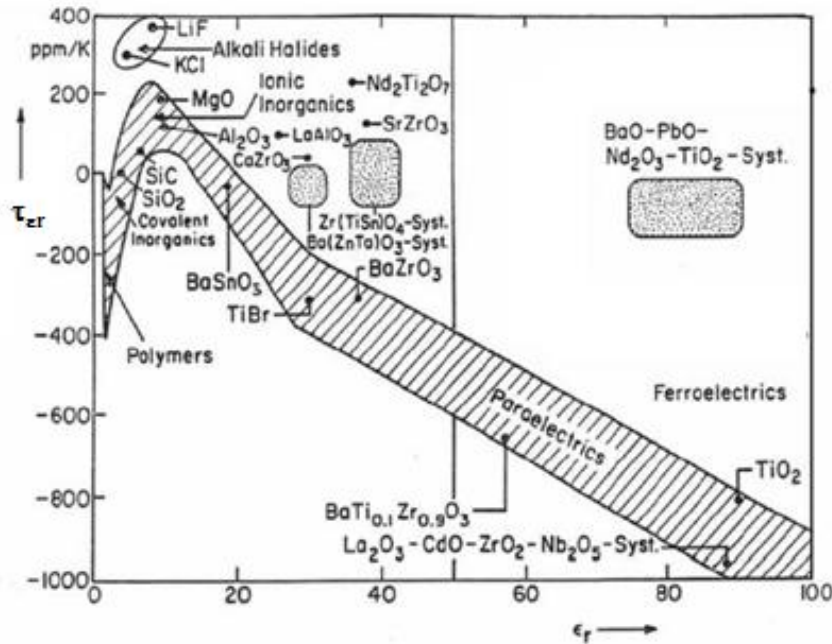


Figure 1.6 Temperature coefficient of dielectric constant versus dielectric constant plot for various materials [Ref: 32]

1.4.3 Quality factor

Quality factor of a dielectric resonator is the measure of the energy dissipated per cycle as compared to the energy stored per cycle inside the resonator. Q factor is defined by

$$Q = 2\pi \left[\frac{\text{maximum energy stored per cycle}}{\text{average energy dissipated per cycle}} \right] = \frac{2\pi W_o}{PT} = \frac{\omega_o W_o}{P} \quad (1.36)$$

where, W_o is the stored energy, P is the power dissipation, ω_o the resonant radian frequency and T is the time period equal to $2\pi/\omega_o$. The approximate band width is given by the expression

$$B = \Delta\omega = |\omega_1 - \omega_2| \cong \frac{\omega_o}{Q} \quad (1.37)$$

Hence, quality factor is given by

$$Q = \frac{\omega_o}{\Delta\omega} = \frac{f_o}{\Delta f_o} \quad (1.38)$$

where f_0 is the resonant frequency and Δf_0 is the bandwidth measured at 3dB below the maximum height at resonance (Figure 1.7). Since the resonator bandwidth is inversely proportional to the Q factor, resonators with high Q have narrow bandwidth [15]. Quality factor decreases with increasing frequency (f_0) and the theoretical relationship between the two is such that $Q \times f_0$ should be a constant for any given material. Higher Q value confirms the selection of required signals and removal of unwanted ones due to narrow bandwidth. It was reported that the ordering behavior of A/B site cations is responsible for high $Q \times f_0$ values [33].

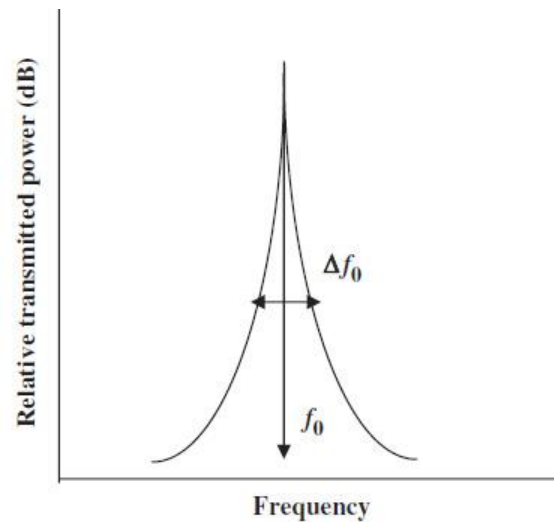


Figure 1.7 Schematic of a resonant peak

Dielectric resonators without any support are called isolated dielectric resonators [34, 35]. Isolated dielectric resonators are convenient for theoretical analysis. But in practice, dielectric resonators are supported or shielded by a cavity, and hence called shielded dielectric resonators. When a resonant circuit is used as a load in the microwave circuit, the possible quality factors are

- Unloaded quality factor, accounts for internal losses
- External quality factor, accounts for external losses
- Loaded quality factor, which includes internal and external losses

The unloaded quality factor is due to the internal losses, losses in the cavity or resonator itself. These intrinsic losses of the resonators depend on the crystal structure and can be described by the interaction of the phonon system with the ac

electric field. The applied ac electric field alters the equilibrium of the phonon system and the subsequent relaxation is associated with energy dissipation [32].

$$Q_o = \frac{\omega_o W}{P_o} \quad (1.39)$$

where P_o is the internal power dissipation. For cavity resonators, power loss due to conductors, dielectric filling factor and radiation can contribute to unloaded quality factor. If the conductor power loss is P_c , conductor quality factor Q_c is given by

$$Q_c = \frac{\omega_o W}{P_c} \quad (1.40)$$

The dielectric quality factor for a homogeneous dielectric is

$$Q_d = \frac{\omega_o W}{P_d} = \frac{\omega_o \varepsilon \int |E^2| dV}{\sigma \int |E^2| dV} = \frac{\omega_o \varepsilon}{\sigma} = \frac{1}{\tan \delta} \quad (1.41)$$

The loss tangent is the reciprocal of Q_d . The radiation quality factor Q_r is related to the radiated power from the cavity. For a closed cavity with conducting walls, radiation quality factor becomes infinity. But for a cavity with an aperture, radiation will occur and the radiation quality factor becomes

$$Q_r = \frac{\omega_o W}{P_r} \quad (1.42)$$

Therefore the total unloaded quality factor becomes

$$Q_o = Q_c + Q_d + Q_r \quad (1.43)$$

$$Q_o = \frac{\omega_o W}{P_c + P_d + P_r} \quad (1.44)$$

The above equation shows that higher the power loss, lower the quality factor. In practice, a cavity or a resonator must deliver power to an external circuit, which results in the external quality factor Q_e and written as

$$Q_e = \frac{\omega W}{P_e} \quad (1.45)$$

So the loaded quality factor which is due to the total effect of unloaded and external quality factor is given by

$$Q_L = Q_o + Q_e \quad (1.46)$$

The loaded quality factor Q_L and the unloaded quality factor Q_0 are related by the coupling coefficient $k = P_e/P_o$ and the relationship is given by

$$Q_L = \frac{Q_0}{1+k} \quad (1.47)$$

1.5 Multilayer co-fired ceramics

1.5.1 Introduction

Generally, a simple microelectronic package can be imagined as a planar substrate along with cases for discrete ICs, where the circuits are bonded to a base layer, which is previously printed with electronic components for circuit wiring. Such type of packaging where multiple ICs and components are confined into a single layer is called as a simple microelectronic module (MCM) [36]. This MCM can be again classified in to MCM-L, MCM-C and MCM-D where L stands for laminates, C for ceramic and D for deposits on the base substrates using thin film technology [37, 38]. Among these, ceramics exhibit preferred thermal and electrical characteristics compared to laminates [39]. On the other hand, advanced electronic packages are based on the integration of active and passive electronic components such as filters, RLC components (where R-resistor, L-inductor and C-capacitor) etc. in to the multilayer ceramic module. The embedding of these active/passive components on to the surface layers results in the fabrication of monolithic structures with increased performance, functionality/size ratio and reliability. The communication between the integrated components is enhanced by the electrical vias, which increase the wiring density and decrease the signal path by intelligent design concepts. The transition from surface mount discrete components to passive components integrated into the substrate layer enhances the electrical performance, reliability and miniaturization of the devices. Furthermore, it is possible to incorporate low loss metals as a conductor medium and low loss dielectric ceramic allows the materials to be low loss compared to other materials such as resin and the like. The electronic packaging technology based on this concept is called Multilayer Ceramic Integrated Circuit (MCIC). This can be again classified into three sub groups such as Thick film, High temperature co-fired ceramic (HTCC) and Low

temperature co-fired ceramic (LTCC) technologies. Thick film ceramics are created by deposit and etch process followed by an additive process in which each layer is printed and then fired in a furnace. The main advantage of thick film ceramics is their low cost solid vias so that the conducting paste materials can be gold, copper or silver. Here, printed metal and dielectric layers can be used to create complex circuits and the main drawback is the narrowest printed line in thick films [40].

1.5.2 High Temperature Co-fired Ceramic (HTCC)

High Temperature Co-fired Ceramic (HTCC) is very common and used for a wide variety of applications such as microprocessor packages, transmit/receive modules, crystal packages, optical sensors etc. In high volumes, HTCC can be low cost compared to other techniques. Majority of HTCC was fabricated using alumina. Aluminium nitride (AlN) can also be used instead of alumina due to its high thermal conductivity.

Important characteristics of HTCC are

- HTCC can be fired at very high temperatures such as alumina at 1600°C and Aluminium nitride at 2000°C.
- HTCC can be fabricated by firing of multiple layers of materials in order to create a homogeneous substrate material.
- Due to high sintering temperature, refractory metals can co-fire with the ceramic material. Noble metals such as gold, silver and copper won't survive the high sintering temperature of ceramic material. For example, the melting point of gold is 1063°C, which is well below the processing temperature of HTCC. Commonly used refractory metals include tungsten (W) have melting temperature 3410°C and molybdenum (Mo) have melting temperature 2610°C. Even though these refractory metals have high melting point, their resistivity is comparable to gold or silver which were commonly used to plate the surface metallization in such transmission lines to improve the insertion loss [41, 42].

1.5.3 Low Temperature Co-fired Ceramic (LTCC)

Low Temperature Co-fired ceramic (LTCC) is a multilayer ceramic technology wherein a number of ceramic layers with printed conductors are laminated and co-fired

with metal electrode at low temperatures (<850°C) to form a multilayer interconnection circuit. The passive/active components were integrated/screen printed on the substrate material to get a multilayer structure. A typical LTCC module consists of dielectric tapes, conducting vias, conductors and passive components such as resistor (R), inductor (L) and capacitor (C). Since the normal electronic ceramics are fired at higher temperatures <1500°C, the circuit electrodes have to be made out of fire-resistant metals such as tungsten or molybdenum. This difficulty can be overcome by the use of LTCC materials having sintering temperature below 1000°C, which is relatively low, compared to the available classic ceramic substrate materials. LTCC is fired at a lower temperature than HTCC thus allows the usage of noble metals such as gold and silver as electrode materials. The commonly used metals for LTCC are those having low melting point, less than 1000°C and high electrical conductivity. Some examples are Ag (961°C), Au (1063°C), Cu (1083°C) and their alloys like Ag-Pd (961-1552°C), Ag-Pt (961-1769°C) etc. Out of these, Ag is usually used as the electrode material because of its high conductivity, low cost, low conductor loss and low electrical resistance at high frequencies, which means that the sintering temperature of the ceramic should be below its melting point (961°C). Ag/Pd is also a good conductor and by changing the Ag/Pd ratio, a wide range of melting temperatures can be used [42].

Table 1.1 Typical material combinations of LTCC and HTCC [Ref: 42]

	Ceramics		Conductors	
	Material	Firing (°C)	Material	Melting (°C)
LTCC	Glass/Ceramic composite	900 to 1000	Cu	1083
	Crystallized glass		Au	1063
	Crystallized Glass/Ceramic composites		Ag	961
	Liquid phase sintered ceramics		Ag-pd	961 to 1552
			Ag-Pt	961 to 1769
HTCC	Alumina ceramics	1600 to 1800	Mo	2610
			W	3410
			Mo-Mn	1246 to 1500

Since ceramic material has to be co-fired with the metal, it is necessary to keep the sintering temperature of the ceramic material below the melting point of the metal used. Different methods are employed to get low sintering temperature of the dielectrics and they include: (1) addition of low melting-temperature glass phases, (2) addition of low melting-point oxides such as V_2O_5 , B_2O_3 , Bi_2O_3 or CuO and (3) the use of chemical processing routes to attain smaller particle sizes. The first method is one of the effective approaches, but results in the degradation of microwave dielectric properties of the base ceramic composition. Also the selection of glass material is very important for the sintering of glass-ceramic composites since the liquefaction of glass takes the major role in the viscous flow mechanism during sintering [43]. The comparison of dielectric properties of ceramics and organic materials is given in Table 1.2. These co-fired ceramics are applied in electronic circuits to get a cost effective and modest substrate technology with arbitrary number of layers that can incorporate embedded passive components. Passive components buried between the LTCC tape layers minimize the length of interconnects and thereby improve the integration, and thus reduce circuit geometry. Typical cross-sectional view of a LTCC module is given in Figure 1.8. LTCC technology is extensively used for telecommunication fields like mobile phones (0.9-2GHz), Bluetooth (2.4GHz), GPS (1.6GHz) and broadband access connection system (5.8-40GHz) [42].

Table 1.2 Comparison between the dielectric properties of ceramic and organic materials [Ref: 42]

Material		Dielectric constant @ 2GHz	Loss tangent @ 2GHz
Ceramics	Soda-lime glass	6.8	0.01 [95]
	Borosilicate glass	4.5	0.006 [150]
	Silica glass	3.8	0.00016 [6,000]
	Alumina	9.0	0.0003 [3,000]
	LTCC (Alumina/Borosilicate glass)	5-8	0.005-0.0016 [200-600]
Organic material	Epoxy	3.1	0.03 [30]
	FR4 (Epoxy + E-Glass 60wt %)	4.3	0.015 [65]
	Polyimide	3.7	0.0037 [270]
	Teflon (PTFE)	2.0	0.0005 [2,000]

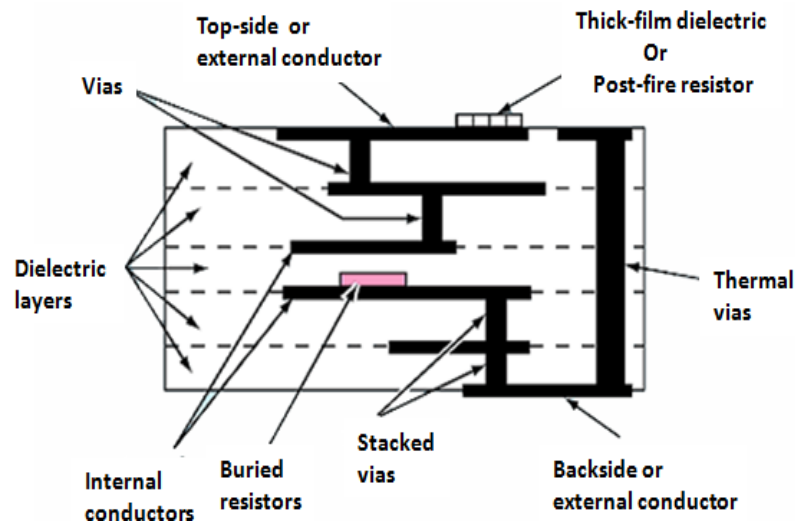


Figure 1.8 Cross sectional view of a LTCC module

1.5.4 Manufacturing of LTCC

The main steps for the manufacturing of LTCC include slurry preparation, tape casting, conductor pattern printing followed by stacking, co-firing and post processing. The first step in the process is the preparation of the ceramic slurry. The liquid slurry contains ceramic, glass, binding material and solvents to create the dielectric layers. The prepared slurry is mixed well to get a uniform distribution with specified particle size and then transferred into the tape casting machine, where the prepared slurry cast into green tapes of predefined thickness using doctor blades. The main aim of this process is to have green tape layers having dense and uniform distribution of material. The next step in the process is the punching of vias. Since each layer can have different via sizes and locations, each tape layer must be distinctly punched. The next step is the filling of the punched vias. The vias were filled and each layer was printed with metal pattern using screen printing technology. These layers are then stacked, pressed and co-fired to get the electronic package. For this process, the alignment of individual layers is important for maintaining an electrical connection. If any one of the layers is misaligned to the next, the vias for electrical connection may not line up properly. This difficulty can be avoided using via catch pads over the vias. This ensures the contact between via and the metal printed on the layer. The next step is the post processing where the fired ceramic sheets undergo an electrical testing and final assembly [41, 42].

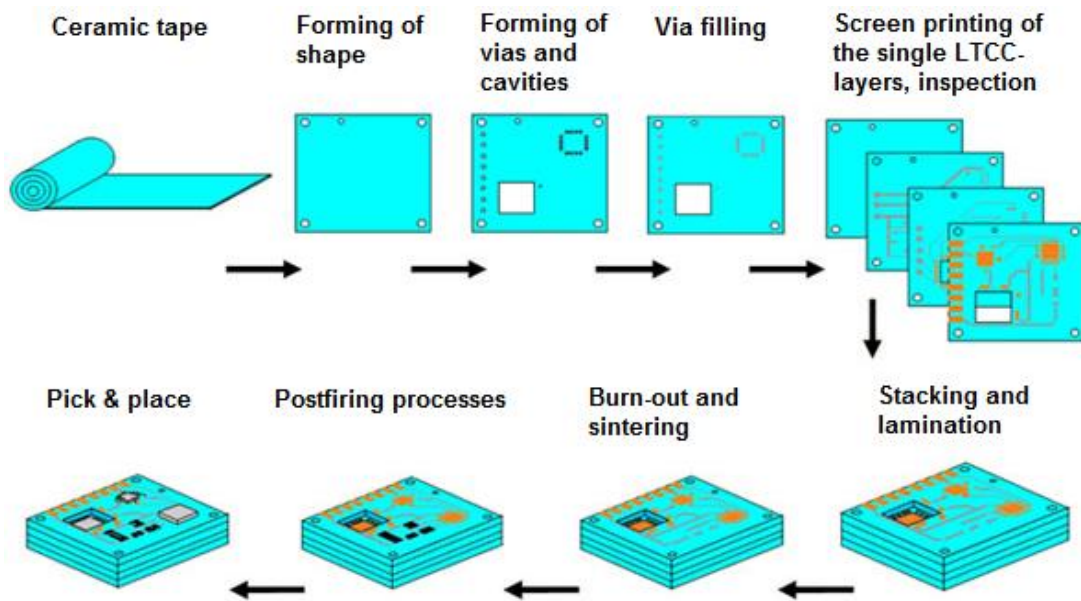


Figure 1.9 Typical multilayer ceramic substrate manufacturing process

1.6 Material requirements for LTCC

1.6.1 Densification temperature

Among the critical material requirements for LTCC applications, researchers mainly focused on the dielectric properties of the ceramic and its compatibility with the electrode material. The main difficulty in the development of new dielectric materials is not related to the dielectric properties but with the production cost, sintering temperature, thermo-mechanical properties and chemical compatibility with metal electrodes. The main characteristic of LTCC is that the common electrode materials introduced into the ceramic should have low sintering temperature of around 961°C so that it can be co-fired with these metals. LTCC ceramics are required to be fired at temperatures less than 961°C . In addition, the LTCC material should be chemically compatible with the metal electrode. Any mismatch in the dielectric, sintering behavior of the dielectrics and metal electrodes would result in the separation of conductive electrode patterns from the dielectric. Also, densification of the composition should not start at very low temperatures because this will prevent the evaporation of the organics and solvents used in the conductive pastes and dielectrics and thereby results residual carbon traces in the microstructure of the composition [44].

1.6.2 Dielectric properties

Determination of dielectric constant is very important for a dielectric material since it controls the functionality of the material. Materials with dielectric constant less than ten are commonly used for substrates and package layers while high dielectric constant materials for capacitors or resonating structures. Signal propagation is the most important factor for substrate applications, which can be directly determined from the dielectric constant of the substrate material by the equation given below.

$$t_d = \frac{l(\epsilon_r)^{1/2}}{c} \quad (1.48)$$

where, t_d is the propagation delay time, l is the length, ϵ_r is the dielectric constant of the substrate and c is the speed of the electromagnetic wave [23, 45]. In this equation, smaller the propagation delay time higher the transmission capacity. Dielectric constant values of commercial LTCC materials are in the range of 3-10 which very stable as a function of frequency (Table. 2). Instead, materials with too large dielectric constant create problems since they need narrow and accurate lines for proper impedance matching [46]. The preferred quality factor for high frequency applications is >1000 GHz or the loss tangent is $<10^{-3}$. In the case of LTCC materials, conductor losses play the major role than the dielectric losses at high frequencies [47]. From Table1.2, it can be seen that the dielectric loss values of commercial LTCCs are comparable with that of alumina.

Temperature variation of resonant frequency is another important factor for microwave components but it is not that important for substrate and packaging applications. The temperature coefficient of resonant frequency value of 10 ppm/°C causes a 0.11% shift of the resonant frequency within the temperature range from -30 to +80°C. Large variation of τ_f values requires additional mechanical structures or electrical circuits for temperature compensation [48, 49]. The temperature dependence of the resonance frequency is rarely reported for LTCCs, but for RF filter applications a value in between -10 to +10 ppm/°C is necessary for a stable frequency response of the component at its operational temperature. Novel LTCC materials with low τ_f

values are now commercially available [50, 51]. For example, Motorola T2000 based on alumina has a dielectric constant of 9.1 with near zero τ_f value [44].

1.6.3 Thermomechanical properties

Thermomechanical properties of the dielectric should be considered in the time of material development for better reliability of the designed components. In order to achieve this, the coefficient of linear thermal expansion (CTE) of the LTCCs should be closer to that of the mounting board. If LTCC is mounted on silicon, CTE should be 4 ppm/°C, for alumina it should be 7-9 ppm/°C and on PCBs it becomes 12-20 ppm/°C [52, 44].

1.6.4 Chemical compatibility with metal electrode

Compatibility between dielectric ceramic and conducting electrode material is the most decisive parameter for LTCC substrates for practical applications. For successful co-firing, the sintering profiles of all the materials present in the system must match with each other and also they should be chemically compatible. The only possible chemical reaction during co-firing is the recrystallization of the glassy phase and the products of the glassy phase must be chemically compatible with the entire material system. Therefore, it is necessary that during co-firing process the dielectric should not react with the electrode material. Also, the formation of extra phases in the dielectric should be minimized since their reaction with the conducting material can degrade the performance of the microwave modules. Thus, during the development of new dielectric materials it is necessary to take into account the reaction of dielectrics as well as the other additives with the conducting material [53, 44].

The advantages of LTCC are

- Very good dielectric properties including low loss tangent
- Integration of passive components such as resistors, inductors and capacitors
- Coefficient of thermal expansion (CTE) close to silicon (4 ppm/°C)
- High-density 3-D package
- Resistance against high temperature
- Mass production and cost effective manufacturing process

1.7 LTCC material systems

Multilayer microwave components have been developed in order to fabricate miniaturized devices to increase volume efficiency. This demands different types of ceramic materials with varying microwave dielectric properties. Recently extensive research has been carried out to cater such dielectric ceramics co-firable with metal electrodes for the miniaturization of microwave devices.

1.7.1 Glass-ceramic systems

In general, there are two methods to reduce the sintering temperature of the ceramics using glass additives. The first approach is via glass-ceramic route, which starts with a fully glass system that devitrifies during the sintering process. The starting materials used are cordierite, anorthite etc, which densifies first followed by crystallization. The physical properties of these systems depend on the degree of crystallization, which can be enhanced by the addition of a small amount of nucleating agent. During sintering, the glass recrystallizes and produces a low dielectric ceramic body. A typical example is Ferro A6M containing $\text{CaO-SiO}_2\text{-B}_2\text{O}_3$ glass [44].

The second approach is glass + ceramic route, which is simple and widely used method because of its ease in controlling the densification behavior. In this method, crystalline ceramic and a low-softening point glass are used as the starting materials. The densification is achieved through a three stage liquid phase sintering process by particle rearrangement, dissolution and precipitation and solid state sintering [54-56]. Here, the role of glass is not only to act as a bonding agent to hold the ceramic particles but also to react with ceramic filler at the sintering temperature to form a crystalline phase. During liquefaction, the glass penetrates into the 3D mesh structure formed by the ceramic particles, thereby wetting the surface of each ceramic particle. Therefore, to improve the density of the glass + ceramic composition, softening point of the glass as well as its volume and powder particle size have to be controlled to increase its fluidity [57-59]. Since the liquefaction of glass is a key process, the selection of glass material is also very important [43]. The properties of the final glass + ceramic compositions are controlled by the ratio of glass to ceramic and the

individual properties of the mixtures. Commercial LTCC tapes are low dielectric constant glass + ceramic compositions, with four or five phases and none of which react with the electrode. Typical examples are borosilicate glass + alumina system by Fujitsu and lead borosilicate glass + alumina system by DuPont.

Table 1.3 Dielectric properties of commercial LTCCs [Ref: 44]

LTCC supplier	Composition	ϵ_r	Q or $\tan \delta (f)$
Dupont951	$\text{Al}_2\text{O}_3 + \text{CaZrO}_3 + \text{glass}$	7.8	300 (3 GHz)
Motorola	T2000	9.1	0.003
Murata	BAS (Celsian) $\text{BaO} - \text{Al}_2\text{O}_3 - \text{SiO}_2$	6.1	300 (5 GHz)
Kyocera	JHB62 Pb-borosilicate glasses + $\text{Al}_2\text{O}_3 + \text{SiO}_2$	7.9	0.0002 (2 GHz)
NEC	MLS- 1000 ($\text{PbO} - \text{Al}_2\text{O}_3 - \text{SiO}_2$)	8	500 (2.4 GHz)
Alcoa	Borosilicate glass + $\text{SiO}_2 + \text{dopants}$	3.9-4.2	<0.003
Heraeus	CT2000	9.1	1000 (450 MHz)
Ferro	A6M	5.9	500 (3 GHz)
Toshiba	$\text{BaO} - \text{SnO}_2 - \text{TiO}_2 - \text{B}_2\text{O}_3$	7-13	0.0005-0.0008
Amkor	GCS 50	5	0.001 (10 GHz)
Hitachi	Pb-aluminoborosilicate + $\text{Al}_2\text{O}_3, \text{CaZrO}_3$	9-12	0.001-0.003

1.7.2 Glass free ceramic systems

Commercial LTCC modules are mainly based on low dielectric constant glass-ceramic composite substrates with four or five phases including the electrode material. The presence of so many phases will increase the possibility for chemical interaction between these phases with the metal electrode. This can be avoided by reducing the number of phases within the particular LTCC tape. In addition, the minimum number of phases within the tape cannot be reduced below two in the case of glass-ceramic composite tapes (Figure 1.10). The role of glass phase in these commercial tapes is mainly to enhance the sintering process through recrystallization, which results a LTCC composition with suitable dielectric properties. Also, the conductive losses in the strip-line circuitry and the losses in the glassy phase will reduce the quality factor of the glass-ceramic composite. Typically, the quality factor of such modules does not exceed 600 GHz. To avoid these

complexities, glass free systems have been considered. If glass free ceramic systems with suitable dielectric properties can be sintered in the required temperature range, the complexities imparted by the glass phase can be eliminated [60].

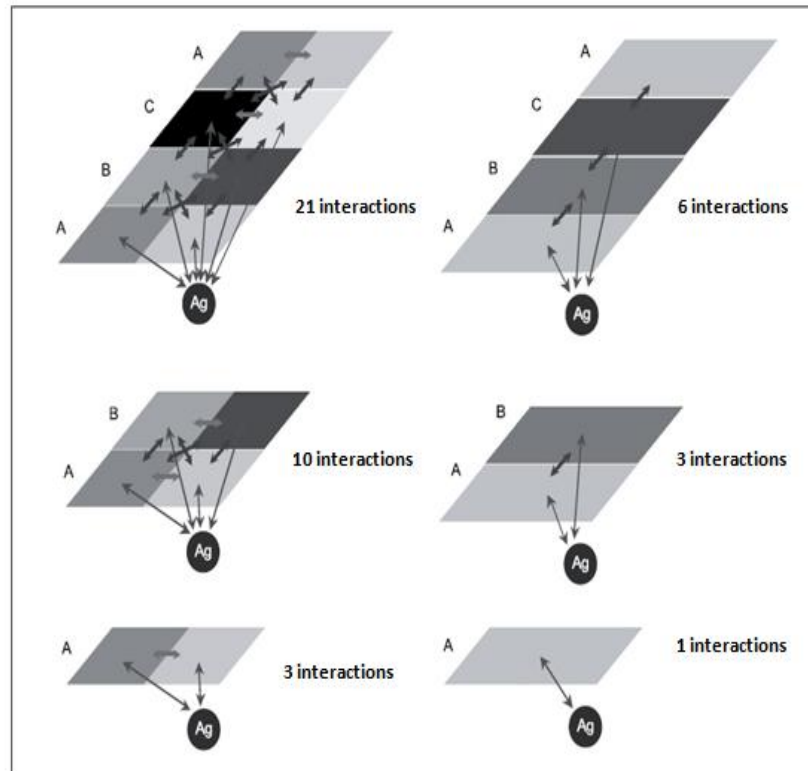


Figure 1.10 Schematic representations of all possible interactions in the LTCC module with one, two and three types of tapes [Ref. 60]

The new generation of glass free ceramic systems was realized when M. Valant and his co-workers explored the Bi_2O_3 based compounds, which include Bi eulytites, sillenites and $\delta\text{-Bi}_2\text{O}_3$ solid solution with Nb_2O_5 [60]. The main disadvantage of Bi_2O_3 based compounds is that their densification starts at a relatively high temperature $\sim 1100^\circ\text{C}$. Among the bismuth based ceramic systems, $\text{Bi}_2\text{O}_3\text{-ZnO-Nb}_2\text{O}_5$ ternary oxides received substantial attention with sintering temperature of $\sim 1000^\circ\text{C}$ [61]. Therefore, dopants like B_2O_3 , V_2O_5 and CuO etc. were used as sintering aids to lower the sintering temperature of these ceramics [62-64]. Later, tellurium based compounds were explored for LTCC applications because of their very low sintering temperature. Udovic and co-workers reported the first tellurium based material TiTe_3O_8 within the $\text{TiO}_2\text{-TeO}_2$ system, which has a dielectric constant of 50 at 5 GHz, Q_{xf} of 30,600 GHz and a τ_f of 113 ppm/ $^\circ\text{C}$ [65].

Similarly, $\text{Bi}_2\text{Te}_2\text{O}_8$ in the Bi_2O_3 - TeO_2 system with sintering temperature of 650°C exhibited a dielectric constant of 39, quality factor of 23,000 GHz and τ_f of -43 ppm/ $^\circ\text{C}$ [66]. Out of the single phase compounds in the BaO - TeO_2 system, BaTe_4O_9 exhibited a dielectric constant of 17.5, Qxf of 54,700 at 12 GHz, τ_f of -90 ppm/ $^\circ\text{C}$ at a sintering temperature of 550°C and shows good chemical compatibility with Al instead of Ag electrode during the co-firing process [67]. Also, all tellurium based compounds except TiTe_3O_8 have negative temperature coefficient of dielectric constant according to Harrop's diagram because of its high dielectric constant. The high cost and toxicity of TeO_2 limits its wider application and was replaced by MoO_3 based systems like Bi_2O_3 - MoO_3 , Li_2O - MoO_3 and K_2O - MoO_3 since the MoO_3 rich compounds showed low sintering temperature $<700^\circ\text{C}$ [68-70]. $\text{Bi}_2\text{Mo}_2\text{O}_9$ reported by Zhou et al. was well sintered at 620°C exhibited $\epsilon_r = 38$, Qxf=12,500 GHz and $\tau_f = 31$ ppm/ $^\circ\text{C}$ [71, 72]. In order to avoid the propagation delay due to high dielectric constant, low dielectric constant material like Li_2MoO_4 having a sintering temperature of 540°C together with $\epsilon_r = 5.5$, Qxf=46,000GHz and $\tau_f = -160$ ppm/ $^\circ\text{C}$ was developed [70]. Various molybdenum based compositions with their sintering temperature and microwave dielectric properties were given in Table 1.4. The main disadvantage of molybdenum based ceramics is their poor chemical compatibility with metal electrodes.

Table 1.4 Various molybdenum based compositions with their sintering temperature and microwave dielectric properties

Composition	Sintering Temp. ($^\circ\text{C}$)	ϵ_r	Qxf (GHz)	τ_f (ppm/ $^\circ\text{C}$)	Reference
$\text{BaCe}_2(\text{MoO}_4)_4$	835	12.3	24,730	-37	73
$\text{Bi}_3\text{FeMo}_2\text{O}_{12}$	825	27.2	14,500	-80	74
$\text{BaNd}_2(\text{MoO}_4)_4$	960	11.7	45,000	-41	75
$\text{BaSm}_2(\text{MoO}_4)_4$		11.8	20,000	-34	
AMoO_4 (Ba,Sr,Ca,Mg,Zn)	800-1100	7-11	49,000-89,000	-57 - -87	76
$\text{Nd}_2\text{Mo}_4\text{O}_{15}$	690	11.1	61,440	-44	77
$\text{Sm}_2\text{Mo}_4\text{O}_{15}$		10.7	63,360	-50	

In order to overcome the disadvantages of the above mentioned systems, Umemura et al. reported the first microwave dielectric material in the vanadate system, $Mg_3(VO_4)_2$ with orthorhombic crystal structure having $Cmca$ space group [78, 79]. The $Mg_3(VO_4)_2$ ceramic was well sintered at $1050^\circ C$ with a low dielectric constant of 9.1, highest Qxf of 64,000 GHz and τ_f of -93 ppm/ $^\circ C$. In order to reduce the sintering temperature of $Mg_3(VO_4)_2$, Mg was partially replaced with Co to form $Mg_{3-x}Co_x(VO_4)_2$, and there by reduced the temperature up to $850^\circ C$ due to the formation of $CoO-V_2O_5$ liquid phase. $Mg_{3-x}Co_x(VO_4)_2$ at $x=2$ was sintered at $900^\circ C$ for 5h with $\epsilon_r = 9.4$, $Qxf = 78,000$ GHz and $\tau_f = -95$ ppm/ $^\circ C$ [78]. $Ba_3(VO_4)_2$ was reported as a microwave material having a dielectric constant of 11, Qxf of 62,350 GHz and τ_f of 28.8 ppm/ $^\circ C$. But it requires 0.5 to 1wt% of B_2O_3 additives to reduce its sintering temperature to $950^\circ C/5h$ [80]. The reported vanadium based ceramics with their sintering temperature and microwave dielectric properties are compiled in Table 1.5.

Table 1.5 Vanadium based ceramics along with their microwave dielectric properties

Composition	Sintering temp ($^\circ C$)	ϵ_r	Q x f (GHz)	τ_f (ppm/ $^\circ C$)	Compatibility	Reference
$R_2V_2O_7$ (R=Ba, Sr, Ca)	600-700	10.4-12.1	15200-19520	-30.9 to -34.8	-	81
LaVO ₄	850/4	14.2	48,197	-37.9	-	82
CeVO ₄	950/4	12.3	41,460	-34.4	-	82
LiMgVO ₄	700/4	8.86	23,300	-140	-	83
LiCa ₃ ZnV ₃ O ₁₂	900	11.5	81,100	-72	Ag	84
LiCa ₃ MgV ₃ O ₁₂		10.5	74,700	-61	Ag	85
BaMg ₂ V ₂ O ₈	900	12	1,56,140	-36	-	86
NaCa ₂ Mg ₂ V ₃ O ₁₂	915	10	50600	-47	Ag	87
BiCu ₂ VO ₆	675	18.2	7775	-177.3	Ag	88
BiCa ₂ VO ₆	950	9.88	23,580	-71.4		
Ba ₃ TiV ₄ O ₁₅	800	13.6	31900-	10	Ag, Al	89
Ba ₃ ZrV ₄ O ₁₅		10.7	30640	-102		
Ba ₂ BiV ₃ O ₁₁	870/4	14.2	68,700	-81	-	90
Ca ₅ Zn ₄ (VO ₄) ₆	725	11.1	49,400	-83	-	91
Ca ₅ Mg ₄ (VO ₄) ₆	800	9.2	53,300	-50		

1.8 Ultra-low Temperature Co-fired Ceramics (ULTCC)

1.8.1 Introduction

Even though, there are plenty of reports on LTCC materials, present trend is to reduce the sintering temperature further which leads to a new class of materials called Ultra-low temperature co-fired ceramics. There are glass based ULTCC materials having low softening or sintering temperature, but are often multiphase in nature. Chen et al. reported the microwave dielectric properties of MO-B₂O₃-SiO₂ glasses (M= Ba, Sr, Ca) with low sintering temperature in the range 560-613°C, ϵ_r of 7.6 and high Qxf of 4100 GHz were obtained with M= Ba [92]. Similarly, 3ZnO-2B₂O₃, metal-boron-silica based glass-ceramic composites etc. are ultra-low temperature sinterable and co-firable with silver electrodes together with good microwave dielectric properties [93-95]. While moving to glass free ceramic systems, Valant and Suvorov were the first to report the microwave dielectric properties of glass free Bi₁₂PbO₁₉, having body centered cubic structure which was well sintered at 680°C with ϵ_r = 38.6, Qxf= 2900 GHz and τ_f = 84 ppm/°C [96].

Table 1.6 Electrical resistance and melting point of conductor metals [Ref: 42]

Metal	Electrical Resistance ($\mu\Omega.cm$)	Melting point (°C)
Cu	1.7	1083
Au	2.3	1063
Ag	1.6	961
Al	2.7	660
Pd	10.3	1552
Pt	10.6	1769
Ni	6.9	1455
W	5.5	3410
Mo	5.8	2610

During the manufacturing of LTCC, metal conductor patterning has to be done on ceramic green tapes by screen printing technique followed by co-firing. The conductive material is an important constituent and requires many characteristics like

low electrical resistance for low transmission loss at high-speed. As shown in Table 1.6, Cu, Au, Ag and Al have low electrical resistance compared to other metals. Usually metal powder was used as the conductive constituent and for inorganic additives low melting point glass and reactive oxides can be used.

Figure 1.11 shows the post-fired sheet resistance of different kinds of metal pastes used in thick film processing. Since the inorganic additives present in the conductive paste create voids inside the conductor during the sintering process which results in higher resistance than the specific resistance of the metal itself. By the way, sheet resistance is the bulk resistance of the conductive material divided by the nominal thickness (normally 0.0025 cm), and frequently used as a unit of resistance for thick film conductors. During the co-firing process, the conductor material is sintered and bonded to the ceramic layer below the melting point of the metallic conductor. As a result, the co-firing temperatures of most LTCC materials with Ag are below 961°C, which is the melting point of Ag. ULTCC ceramics with sintering temperature less than that of LTCC, Al is the suitable conductor material having melting point of 660°C and electrical resistance of 2.7 $\mu\Omega\cdot\text{cm}$ [49].

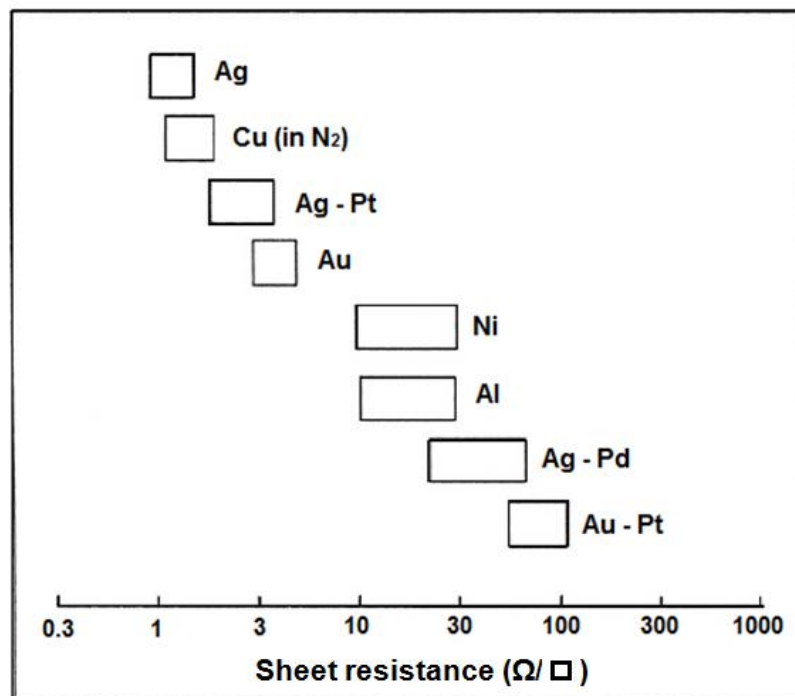


Figure 1.11 Sheet resistance values of each type of conductive paste [Ref: 42]

1.8.2 ULTCC Material systems

In the TeO₂ based ceramic systems like Bi₂O₃-TeO₂, BaO-TeO₂ etc., even if compounds have very low sintering temperature and reasonably good microwave dielectric properties, but these systems easily react with Ag because of the high reactivity of TeO₂ with Ag [67, 68, 97]. BaTe₄O₉ sintered at very low sintering temperature of 550°C was the first microwave ceramic which shows compatibility with Al electrode. At optimum sintering temperature, BaTe₄O₉ has a dielectric constant of 17.5, Qxf of 54,700 GHz and τ_f of -90 ppm/°C [68]. Among tungstates, Li₂WO₄ was well sintered in the temperature range of 640-660°C with ϵ_r = 5.5, Qxf= 62,000 GHz and τ_f = -146 ppm/°C [98]. In the PbO-WO₃ binary system, both PbWO₄ and Pb₂WO₅ are ULTCC compounds. PbWO₄ can be sintered at a low temperature of 520°C and possesses a relative permittivity of 16.4, Qxf of 14,800 GHz and τ_f of -90 ppm/°C whereas Pb₂WO₅ can be well sintered at 620°C with higher relative permittivity of 21.4, Qxf of 43,000 GHz and τ_f of -7 ppm/°C [99, 100]. All the aforementioned tungstate compositions show good compatibility with both Ag and Al electrodes. Among the compounds in the Bi₂O₃-MoO₃ system, Bi₂Mo₂O₉ has sintering temperature around 620°C with high relative permittivity of 38, Qxf of 12,500 GHz and τ_f of 31 ppm/°C. But Bi₂Mo₂O₉ exhibits reactivity with Ag to form a new phase of AgBi(MoO₄)₂ [71]. In the Na₂O-MoO₃ system, Na₂MoO₄, Na₂Mo₂O₇ and Na₆Mo₁₁O₃₆ have ultra-low sintering temperature in the range of 550-660°C, relative permittivity in the range of 4-13.4, Qxf up to 62,400GHz and τ_f in the range -57 to -115 ppm/°C [101]. Similarly in the K₂O-MoO₃ system, K₂Mo₂O₇ has the lowest sintering temperature of 460°C with relative permittivity of 7.5, Qxf of 22,000 GHz and τ_f of -63 ppm/°C among K₂Mo₂O₇, K₂Mo₃O₁₀ and K₂Mo₄O₁₃ compositions [70]. Recently some vanadium based compositions such as LiMgVO₄, Na₂BiMg₂V₃O₁₂ etc. have been reported as ULTCC ceramics [102, 103]. Recently, extensive work has been carried out by researchers to find out new ceramic materials having sintering temperature less than the melting point of Al electrode.

1.9 Microwave substrates

The rapid growth in the communication sector demands high speed data processing using microwaves, which demands high performance dielectric materials for packaging technology. Base substrate is the basic building block of any microwave circuitry. The essential features required for the base substrates are stable dielectric constant, low loss tangent, minimum porosity, good dimensional stability, low moisture absorption, high heat dissipation etc. [104]. Substrates can be generally classified in to two; hard and soft. Hard substrates are based on sintered ceramic oxides like alumina, magnesia, cordierite etc. whereas soft substrates are fabricated out of polymers or its composites. Compared to hard substrates, soft substrates have many advantages like ease of machinability, low cost conducting patterns, shock resistance, solvent resistance etc. [105]. Most commonly used base substrates are Alumina (99.6% pure), glass fiber filled epoxy (FR4) and filled thermoplastic materials. Since FR4 substrates are too lossy in the microwave frequency region, alternate materials having lower loss tangent than that of FR4 are preferred. Dielectric materials with high dielectric constant are required to reduce the size of the microwave devices since wavelength of the electromagnetic wave travelling through the medium is inversely proportional to the square root of dielectric constant. Also, high dielectric substrates result in narrow bandwidth. The main drawback of the existing high dielectric substrates is the lack of temperature stability of dielectric constant [106]. Therefore, substrates with low dielectric constant are preferred for better performance of the system. This leads to large bandwidth, better efficiency and radiation patterns [104, 107]. Even though many ceramic materials have the desired dielectric properties such as high dielectric constant and low loss, but they are brittle in nature. As a result of this, machining of ceramic substrates is difficult during circuit manufacturing. In addition, expensive conductive patterns have to be printed over the ceramic substrates for circuit realization. These difficulties can be circumvented by using polymer-ceramic composites of 0-3 connectivity.

1.9.1 Polymer ceramic composites

Microelectronic has witnessed revolutionary changes in the past few decades where circuit miniaturization and integration of multi components in a single module

are the major challenges. The recent trend in microwave materials research is mainly focused on small size, low cost and lightweight electronic circuits for aerospace and military applications. Hence, polymers with low density and adaptable properties offer design freedom, thinner products, reduction in material consumption and thereby cost [108]. Generally, composites are heterogeneous in nature and formed by the assembly of two or more components, one is particulate ceramic filler or a reinforcing agent and the other is a compatible matrix binder to obtain specific characteristics and properties. Dielectric constant, thermal conductivity, coefficient of thermal expansion and thermal stability are the major properties of a composite material. The reinforcing agent can be fibrous, inorganic, metallic or ceramic material. In a composite, the components as well as their interface can be physically identified and the properties of the interface control the properties of the composite [109]. The dielectric constant of the polymer and the volume fraction of the ceramic used in the composite are the most important factors to determine the effective dielectric constant of the composite. Apart from morphology, dispersion and interaction of different phases in a composite are also influence the effective dielectric properties. Among available polymer materials, PTFE is the most preferred polymer matrix because of its excellent microwave dielectric properties. But it has a downside of high linear coefficient of thermal expansion ($CTE > 100 \text{ ppm}/^\circ\text{C}$). Another major drawback of PTFE is the difficulty in processing. Unlike other polymers, PTFE cannot be processed through injection-molding or melt extrusion because of its high melt viscosity. Filled PTFE substrates have dielectric constant in the range of 2.2-10.2 and are commercially available under the trade name RT/Duroid [110, 111].

1.9.2 Connectivity

Connectivity is a key feature for multiphase composites since their physical properties can change in different order of magnitude by the manner in which connections are made. The concept of connectivity was first proposed by Newnham et al. where each phase in a composite can be connected in zero, one, two and three dimensions [112]. For a diphasic composite, using an orthogonal axis system there are ten possible connectivities: 0-0, 1-0, 2-0, 3-0, 1-1, 2-1, 3-1, 2-2, 3-2 and 3-3.

Using cube as a building block, the ten different connectivities can be illustrated as shown in Figure 1.12. Therefore, the possible number of connectivity patterns is $(n+3)!/3! n!$ for n phases.

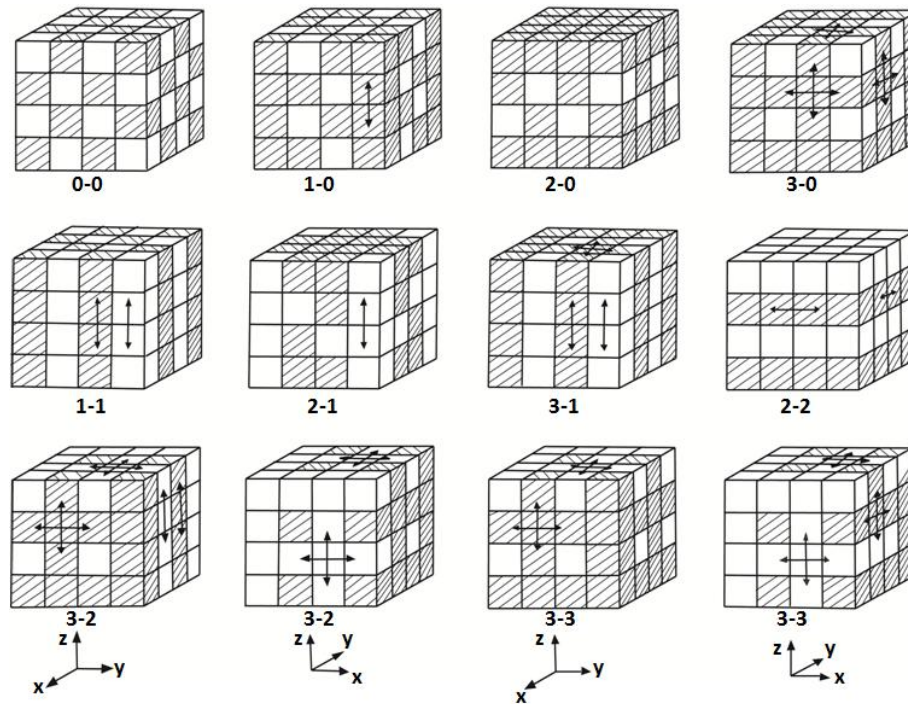


Figure 1.12 Ten connectivity patterns for a diphasic solid [Ref: 112]

In the 2-1 connectivity pattern, one phase is self-connected in two-dimensional layers and the other is self-connected in one dimensional layer or fibers. For 3-1 composites, one phase is three dimensionally and the other is one dimensionally connected. Out of the ten different connectivity patterns, the most complicated pattern is 3-3 connectivity where the two phases form interpenetrating three-dimensional networks. The simplest type of composite consists of polymer matrix loaded with ceramic powder where the ceramic powder is three dimensionally connected while the polymer is not in contact, making a 0-3 connectivity pattern [112, 113].

1.10 Objectives of the present work

The main objective of the present thesis work is to develop new LTCC and ULTCC materials for microwave circuit applications. Dielectric materials with low dielectric constant, low dielectric loss, low temperature coefficient of dielectric constant, low coefficient of linear thermal expansion, good chemical compatibility

with metal electrode and low cost are the critical parameters for electronic packaging applications. Most of the commercially available LTCC materials are based on glass-ceramic systems. The possible development of dielectric ceramic which can be sintered at low temperatures, i.e. less than the melting point of silver electrode, will lead to the possibility of elimination of glassy phases in the LTCC compositions and there by improve the processing as well as end properties of LTCC packages. In view of the above, compositions based on low melting oxides such as tellurium, molybdenum, bismuth etc. have been explored for LTCC and ULTCC applications. But each of these material systems have their own disadvantages like toxicity, non-compatibility, high cost etc.

V_2O_5 , with a low melting point of 691°C , is widely used for many technological applications including electrically conducting glasses, thermally activated electrical and optical switching devices etc. Recently it has been found that vanadium based dielectric ceramics are promising candidates for LTCC and ULTCC applications. As of now, only a few compounds based on alkaline earth vanadate have been reported. Most of these vanadate ceramics exhibit excellent microwave dielectric properties together with good chemical compatibility. Hence, low melting vanadate based dielectric ceramics have been extensively studied in the present thesis with an objective to derive new glass free LTCC and ULTCC compositions. In addition, vanadate ceramic filled polymer composite substrates have also been prepared and their microwave dielectric, thermal and mechanical properties were ascertained to exploit them for microwave circuit applications.

References

- [1] D. M. Pozar, *Microwave engineering*, John Wiley & Sons (1998).
- [2] N. Setter, *J. Eur. Ceram. Soc.*, 21 (2001) 1279-1293.
- [3] Rayleigh, *Phil. Mag.*, 43 [261] (1897) 125-132.
- [4] R. D. Richtmyer, *J. Appl. Phys.*, 10 [6] (1939) 391-398.
- [5] A. Okaya, L. F. Barash, *Proc. IRE.*, 50 [10] (1962) 2081-2092.
- [6] S. B. Cohn, *IEEE. Trans. Microw. Theory. Tech.*, 16 [4] (1968) 218-227.
- [7] S. B. Cohn, Microwave filters containing high-Q dielectric resonators, G-MTT Symposium Digest, DOI: 10.1109/GMTT.1965.1122473 (1965)
- [8] R. V. D'Aiello, H. J. Prager, *IEEE Trans. Microw. Theory. Tech. (Correspondence)*, 12 [5] (1964) 549-550.
- [9] J. C. Sethares, S. J. Naumann, *IEEE Trans. Microw. Theory. Tech.*, 14 [1] (1966) 2-7.
- [10] D. J. Masse, R. A. Pucel, D.W. Ready, E. A Maguire, C. P Hartwig, *Proc. IEEE.*, 59 [11] (1971) 1628-1629.
- [11] L. F. Chen, C. K. Ong, C. P. Neo, V. V. Varadan, V. K. Varadan, *Microwave electronics: measurement and materials characterization*, John Wiley & Sons (2004).
- [12] M. T. sebastian, *Dielectric materials for wireless communication*, Elsevier (2010).
- [13] D. Kajfez, P. Guillon, *Dielectric resonator*, Vector Fields (1998).
- [14] P. J. W. Debye, *Polar Molecules*, The Chemical Catalog Company, (Lancaster, 1992).
- [15] A. J. Moulson, J. M. Herbert, *Electroceramics: materials, properties and applications*, John Wiley & Sons (2003).
- [16] B. K. P. Scaife, *Principles of dielectrics*, OUP Oxford, (1998).
- [17] K. C. Kao, *Dielectric phenomena in solids*, Elsevier (2008).

- [18] S. O. Morgan, *J. Electrochem. Soc.*, 65 [1] (1934) 109-118.
- [19] A. K. Jonscher, *J. Phys. D: Appl. Phys.*, 32 (1999) R57-R70.
- [20] R. M. Hill, L.A. Dissado, *J. Phys. C: Solid State Phys.*, 18 (1985) 3829-3836.
- [21] R. D. Shannon, *J. Appl. Phys.*, 73 [1] (1993) 348-366.
- [22] R. D. Shannon, C. T. Prewitt, *Acta. Cryst.*, (1969) B25, 925-946.
- [23] R. Muhammad, Y. Iqbal, C. R. Rambo, H. Khan, *Int. J. Mater. Res.*, 105 [5] (2014) 431-439.
- [24] S. Mahajan, O. P. Thakur, C. Prakash, K. Sreenivas, *Bull. Mater. Sci.*, 34 [7] (2011) 1483-1489.
- [25] H. Ohsato, *J. Ceram. Soc. Jpn.*, 113 [11] (2005) 703-711.
- [26] M. P. Seabra, V. M. Ferreira, H. Zheng, I. M. Reaney, *J. Appl. Phys.*, 97 [3] (2005) 033525.
- [27] P. J. Haroop, *J. Mater. Sci.* 4 (1969) 370-374.
- [28] I. M. Reaney, P. Wise, R. Uvic, J. Breeze, N. McN. Alford, D. Iddles, D. Cannell, T. Price, *Philos. Mag.*, 81 [2] (2001) 501-510.
- [29] A. J. Bosman, E. E. Havinga, *Phy. Rev.*, 129 [4] (1963) 1593-1600.
- [30] B. C. H. Steele, *Electronic ceramics*, Elsevier Applied Science (1991) 67-119.
- [31] E. L. Colla, I. M. Reaney, N. Setter, *J. Appl. Phys.*, 74 [5] (1993) 3414-3425.
- [32] W. Worsing, *Curr. Opin. Solid State Mater. Sci.*, 1 [5] (1996) 715-731.
- [33] J. J. Bian, K. Yan, *J. Electroceram.*, 21 (2008) 132-136.
- [34] V. L. Gurevich, A. K. Tagantsev, *Sov. Phys. JETP* 64 (I), (1986) 142-151.
- [35] V. L. Gurevich, A. K. Tagantsev, *Adv. Phys.*, 40 (1991) 719-767.

- [36] S. Al-Taei, D. Haigh, G. Passiopoulos, Multilayer ceramic integrated circuits (MCICs) technology and passive circuit design, Proceedings of the London communication symposium 2001, 6th Annual London Conference on Communications, 139-142.
- [37] R. G. Loasby, *Handbook of Thick-film Technology*, Electrochemical Publications (1976).
- [38] M. Jackson, M. Pecht, S.B. Lee, P. Sandborn, Integral, embedded and buried passive technologies, From the archive of the Calce Electronics and Products Center (2003).
- [39] V.A. Chiriach, T.Y. T. Lee, IEEE Trans. Adv. Packag., 27 [3] (2004) 545-557.
- [40] R. L. Brown, A. A. Shapiro, P.W. Polinski, Inter. J. Micro. Electron. Packag., 16 [4] (1993) 328-338.
- [41] R. Sturdivant, *Microwave and Millimeter-wave Electronic Packaging*, Artech House (2014).
- [42] Y. Imanika, *Multilayered Low Temperature Co-fired Ceramics (LTCC) Technology*, Springer (2005).
- [43] M. T. Sebastian, R. Uvic, H. Jantunen, Inter. Mater. Rev., 60 [7] (2015) 392-412.
- [44] M. T. Sebastian, H. Jantunen, Inter. Mater. Rev., 53 [2] (2008) 57-90.
- [45] R. R. Tummala, J. Am. Ceram. Soc., 74 [5] (1991) 895-908.
- [46] R. Ludwig, P. Bogdanov, *RF circuit design: theory and applications*, Pearson (2000).
- [47] S. H. Hall, G. W. Hall, J. A. McCall, *A high speed digital system design: a hand book of interconnect theory and design practices*, John Wiley & Sons (2000).
- [48] C. Wang, K. A. Zaki, Proc. Int. IEEE MTT-S Microwave Symp. Digest, 3, (1993) 1041-1044.
- [49] H. Jantunen, T. Turnnen, US Patent 5302924 (1994).

- [50] H. Jantunen, A Novel Low Temperature Co-firing Ceramic (LTCC) Material for Telecommunication Devices, PhD thesis, University of Oulu, Finland (2001).
- [51] P. Barnwell, W. Zhang, J. Lebowitz, K. Jones, N. MacDonald, An Investigation of the Properties of LTCC Materials and Compatible Conductors for their use in Wireless Applications, International Symposium on Microelectronics (IMAPS) Boston, 4339 (2000) 659-664.
- [52] V. Gektin, A. Bar-Cohen, S. Witzman, IEEE Trans. Compon. Packag. Technol., Part A, 21 [4] (1998) 577-584.
- [53] M. Valant, D. Suvorov, J. Am. Ceram. Soc., 83 [11] (2000) 2721-2729.
- [54] O. H. Kwon, G. L. Messing, J. Am. Ceram. Soc., 73 [2] (1990) 275-281.
- [55] W. D. Kingery, E. Niki, M. D. Narasimhan, J. Am. Ceram. Soc., 44 [1] (1961) 29-35.
- [56] R. M. German, *Liquid Phase Sintering*, Springer (1985).
- [57] J. H. Jean, T. K. Gupta, J. Mater. Sci., 27 [6] (1992) 1575-1584.
- [58] J. H. Jean, T. K. Gupta, J. Mater. Sci., 27 [18] (1992) 4967-4973.
- [59] G. C. Kuczynski, I. Zaplatynskyj, J. Am. Ceram. Soc., 39 [10] (1956) 349-350.
- [60] M. Valant, D. Suvorov, J. Eur. Ceram. Soc., 24 [6] (2004) 1715-1719.
- [61] M.F. Yan, H. C. Ling, W. W. Rhodes, J. Am. Ceram. Soc., 73 [4] (1990) 1106-1107.
- [62] H. B. Hong, D. W. Kim, K. S. Hong, Jpn. J. Appl. Phys., 42 (2003) 5172-5175.
- [63] H. Wang, H. Du, Z. Peng, M. Zhang, X. Yao, Ceram. Int., 30 [7] (2004) 1225-1229.
- [64] D. W. Kim, K. H. Ko, K. S. Hong, J. Am. Ceram. Soc., 84 [6] (2001) 1286-1290.

- [65] M. Udovic, M. Valant, D. Suvorov, *J. Euro. Ceram. Soc.*, 21 (2001) 1735-1738
- [66] M. Udovic, M. Valant, D. Suvorov, *J. Am. Ceram. Soc.*, 87 [4] (2004) 591-597.
- [67] D. K. Kwon, M. T. Lanagan, T. R. Shrout, *J. Am. Ceram. Soc.*, 88 [12] (2005) 3419-3422.
- [68] D. Zhou, H. Wang, L.X. Pang, C. A. Randall, X. Yao, *J. Am. Ceram. Soc.*, 92 [10] (2009) 2242-2246
- [69] D. Zhou, C. A. Randall, H. Wang, L. X. Pang, X. Yao, *J. Am. Ceram. Soc.*, 93 [4] (2010) 1096-1100.
- [70] G. Q. Zhang, J. Guo, L. He, D. Zhou, H. Wang, J. Koruza, M. Kosec, *J. Am. Ceram. Soc.*, 97 [1] (2014) 241-245.
- [71] D. Zhou, H. Wang, X. Yao, L. X. Pang, *J Am. Ceram. Soc.*, 91 [10] (2008) 3419-3422.
- [72] D. Zhou, C. A. Randall, A. Baker, H. Wang, L. X. Pang, X. Yao, *J. Am. Ceram. Soc.*, 93 [5] (2010) 1443-1446.
- [73] N. K. James, R. Ratheesh, *J. Am. Ceram. Soc.*, 93 [3] (2010) 931-933.
- [74] D. Zhou, L. X. Pang, J. Guo, Y. Wu, G. Q. Zhang, H. Wang, X. Yao, *J. Adv. Dielectric.*, 1 [4] (2011) 379-382.
- [75] D. Zhou, L. X. Pang, J. Guo, Y. Wu, G. Q. Zhang, W. Dai, H. Wang, X. Yao, *J. Am. Ceram. Soc.*, 94 [9] (2011) 2800-2803.
- [76] G.K. Choi, J. R. Kim, S. H. Yoon, K. S. Hong, *J. Eur. Ceram. Soc.*, 27 (2007) 3063-3067.
- [77] A. Surjith, E. K. Suresh, S. Freddy, R. Ratheesh, *J. Mater.Sci: Mater. Electron.*, 24 [6] (2013) 1818-1822.
- [78] R. Umemura, H. Ogawa, H. Ohsato, A. Kan, A. Yokoi, *J. Eur. Ceram. Soc.*, 25 [12] (2005) 2865-2870.
- [79] N. Krishnamachari, C. Calco, *Can. J. Chem.*, 49 [10] (1971) 1629-1637.

- [80] R. Umemura, H. Ogawa, A. Yokoi, H. Ohsato, A. Kan, *J. Alloy. Compd.*, 424 (2006) 388-393.
- [81] M. R. Joung, J. S. Kim, M. E. Song, S. Nahm, J. H. Park, *J. Am. Ceram. Soc.*, 92 [12] (2009) 3092-3094.
- [82] Y. Wang, R. Zuo, C. Zhang, J. Zhang, T. Zhang, *J. Am. Ceram. Soc.*, 98 [1] (2015) 1-4.
- [83] G. G. Yao, X. S. Hu, X. L. Tian, P. Liu, J. G. Xu, *J Mater Sci: Mater. Electron.*, 26 [3] (2015) 1795–1798.
- [84] C. Su, L. Fang, Z. Wei, X. Kuang, H. Zhang, *Ceram. Int.*, 40 [3] (2014) 5015-5018.
- [85] L. Fang, C. Su, H. Zhou, Z. Wei, H. Zhang, *J. Am. Ceram. Soc.*, 96 [3] (2013) 688-690.
- [86] Y. Wang, R. Zuo, *J. Eur. Ceram. Soc.*, 36 [1] (2016) 247-251.
- [87] L. Fang, F. Xiang, C. Su, H. Zhang, *Ceram. Int.*, 39 [8] (2013) 9779-9783.
- [88] H. D. Xie, C. Chen, H. H. Xi, R. Tian, X. C. Wang, *Ceram. Int.*, 42 [1] (2016) 989-995.
- [89] E.K. Suresh, A. N. Unnimaya, R. Ratheesh, *Ceram. Int.*, 39 [4] (2013) 3635-3639.
- [90] J. Li, C. Li, Z. Wei, Y. Tang, C. Su, L. Fang, *J. Am. Ceram. Soc.*, 98 [3] (2015) 683-686.
- [91] G. G. Yao, P. Liu, H. W. Zhang, *J. Am. Ceram. Soc.*, 96 [6] (2013) 1691–1693.
- [92] C. C Chen, C. C. Chou, W. J. Shih, K. S. Liu, C. S. Chen, I. N. Lin, *Mater. Chem. Phys.*, 79 (2003) 129-134.
- [93] K. Ju, H. Yu, L. Ye, G. Xu, *J. Am. Ceram. Soc.*, 96 [11] (2013) 3563-3568.
- [94] H. Yu, K. Ju, K. Wang, *J. Am. Ceram. Soc.*, 97 [3] (2014) 704-707.

- [95] S. Rajesh, H. Jantunen, M. Letz, S. P. Willhelm, *Int. J. Appl. Ceram. Technol.*, 9 [1] (2012) 52-59.
- [96] M. Valant, D. Suvorov, *J. Am. Ceram. Soc.*, 84 [12] (2001) 2900-2904.
- [97] D. K. Kwon, M. T. Lanagan, T. R. Shrout, *Mater. Lett.*, 61 (2007) 1827-1831.
- [98] D. Zhou, C. A. Randall, L. X. Pang, H. Wang, J. Guo, G. Q. Zhang, X. G. Wu, L. Shui, X. Yao, *J. Am. Ceram. Soc.*, 94 [2] (2011) 348-350.
- [99] H. D. Xie, H. H. Xi, C. Chen, D. Zhou, *Ceram. Int.* 41 [8] (2015) 10287-11092.
- [100] M. T. Sebastian, H. Wang, H. Jantunen, *Curr. Opin. Solid State Mater. Sci.*, 20 [3] (2016) 151-170
- [101] G. Q. Zhang, H. Wang, J. Guo, L. He, D. D. Wei, Q. B. Yuan, *J. Am. Ceram. Soc.*, 98 [2] (2015) 528-533.
- [102] W. B. Li, H. H. Xi, D. Zhou, *Ceram. Int.*, 41 [7] (2015) 9063-9068.
- [103] H. Zhou, Y. Miao, J. Chen, X. Chen, F. He, D Ma, *J. Mater. Sci. Mater. Electron.*, 25 [6] (2014) 2470-2474.
- [104] L. S. Laverghetta, *Microwave materials and fabrication techniques*, Artech House, (2000).
- [105] L. M. Walpita, M. R. Ahern, *IEE. J. Microwaves Antennas Propag.*, 147 [4] (2000) 285-288.
- [106] D. J. Arthur, G. S. Swei, Ceramic filled flouropolymeric composite material. US patent No. 5024871 (1990).
- [107] P. Gonon, A. Sylvestre, J. Teyseyre, C. Prior, *J. Mater. Sci: Mater. Electron.*, 12 [2] (2001) 81-86.
- [108] J. A. Brydson, *Plastic Materials*, Elsevier, (1999).
- [109] G. Lubin, *Handbook of Composites*, Van Nostrand Reinhold Company (1981).

- [110] N. K. James, S. Rajesh, K. P. Murali, K. Stanly Jacob, R. Ratheesh, J. Mater. Sci: Mater. Electron., 21 [12] (2010) 1255-1261.
- [111] D. N. Light, J. R. Wilcox, IEEE Trans. Compon. Packag. Technol., 18 [1] (1995) 118-126.
- [112] R. E. Newnham, D. P. Skinner, L. E. Cross, Mat. Res. Bull., 13 [5] (1978) 525-536.
- [113] R. E. Newnham, A. Safari, J. Giniewicz, B. H. Fox, Ferroelectrics, 60 [1] (1984) 15-21.

2

Experimental Techniques

- 2.1 Synthesis of microwave ceramic materials
- 2.2 Synthesis of polymer ceramic composites
- 2.3 Thermal characterization
- 2.4 Crystal structure characterization techniques
- 2.5 Scanning Electron Microscopy (SEM)
- 2.6 Dielectric characterization
- 2.7 Mechanical strength measurement

2.1 Synthesis of microwave ceramic materials

Advanced ceramics have attracted increasing attention from many disciplines including chemistry, physics, metallurgy and materials science. The use of ceramics by man dates from the time of ancient civilizations. Advanced ceramics can be prepared through chemical and synthetic routes. Almost all ceramics are composed of electropositive and negative ions in the periodic table where the bonding is mainly ionic in nature. The main properties of these ceramics include high heat resistance, varying dielectric and magnetic properties, strong resistance to deformation, low toughness etc. Ceramics are polycrystalline in nature with definite crystal structure, grains, grain boundaries, impurities, pores and imperfections. Powder mixing, precipitation from solution and fusion are all conventional techniques used for the synthesis of advanced ceramics on both the laboratory and industrial scale. The material property is controlled not only by the composition but also by the grain size and porosity of the sintered ceramic body [1].

2.1.1 Solid state ceramic route

The most conventional and accurate method for the preparation of bulk ceramics is solid state ceramic route because it is the simplest, easiest and cost effective method compared to other preparation methods. The particle size of ceramic powders derived through solid state ceramic route is very fine and this makes lesser points of contact which is very important for the effective sintering of the ceramics [2, 3]. Conventional solid state ceramic route involves the heating of stoichiometric quantities of the raw materials to form a solid phase product. On the other hand, mechanical methods result smaller particles from larger ones by mechanical treatment but lacks the formation of phase pure ceramics, which is essential for the fabrication of dielectric resonators with optimum dielectric properties. The chemical methods like sol-gel, co-precipitation, hydrothermal and combustion methods are also used as preparation techniques [4, 5]. In the present work, conventional solid state ceramic route is employed for the fabrication of dielectric resonators. The solid state ceramic approach basically involves (a) intimate mixing of the raw materials using appropriate solvents (b) drying of the resultant slurry in a hot air oven (c) high temperature firing/calcination (d) intermediate grinding and (e) sintering. Calcination leads to the formation of a new material in order to reduce the free

energy at the points of contact through solid state diffusion (Figure 2.1). The new product layer acts as a potential barrier between two grains and thereby impeding further grain to grain material transport. This demands new points of contacts which can be achieved through grinding or ball milling [6, 7]. The schematic representation of main steps involved in the solid state synthesis is given in Figure 2.2.

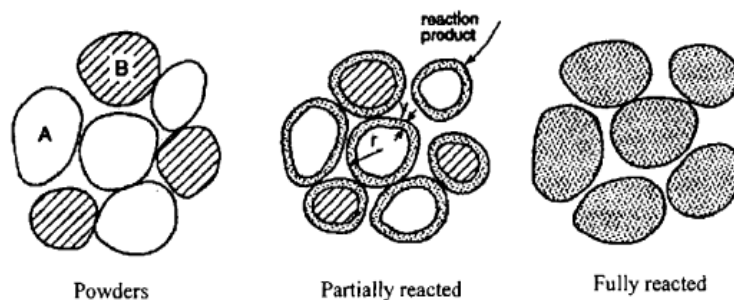


Figure 2.1 Reaction between two kinds of particles to form a product at the points of contact

2.1.1.1 Stoichiometric weighing and mixing of raw materials

The first step in the solid state ceramic route is the weighing of raw materials. Stoichiometric quantities of the raw materials were weighed using an electronic weighing balance (Accuracy- 0.001g). The purity of the initial raw materials is very important to have a phase pure compound. The presence of impurities in the raw materials affects the reactivity as well as dielectric property of sintered ceramics. The weighed reagents were then mixed well with the aid of double distilled water for one hour. Point to point contact between the particles can be achieved by this process. Mixing of the chemical reagents can be done through various methods like hand mixing, ball milling etc. Hand mixing of raw materials can be done using an agate mortar and pestle. The mixing of the reagents eliminates agglomeration and reduces the particle size. Presence of agglomerates leads to rapid densification followed by the formation of pores. This can be eliminated by the mixing process where agglomerates are broken and defects are introduced into the grains and thereby enhance the diffusion mechanism. The hand mixed composition was dried for one hour and again powdered.

2.1.1.2 Calcination

Calcination is an intermediate heat treatment process at a lower temperature prior to sintering in order to remove the volatile impurities like carbonates, nitrates

etc. Calcination leads to the interaction of the constituents by the inter-diffusion of their ions and thereby reduce the extend of diffusion during the sintering process in order to obtain a homogeneous body. One of the main uses of calcination is coarsening, that is, increasing the particle size of the powdered sample. The calcination conditions are very important factors for controlling the shrinkage during sintering. Calcination may not lead to the formation of the required final phase but the remaining chemical gradients may aid the sintering process [1, 7]. In some cases, when compounds are available in the powder form, the powders can be directly compacted and sintered without any intermediate calcination process. Alumina crucibles and lids with high melting point are usually used for calcination process.

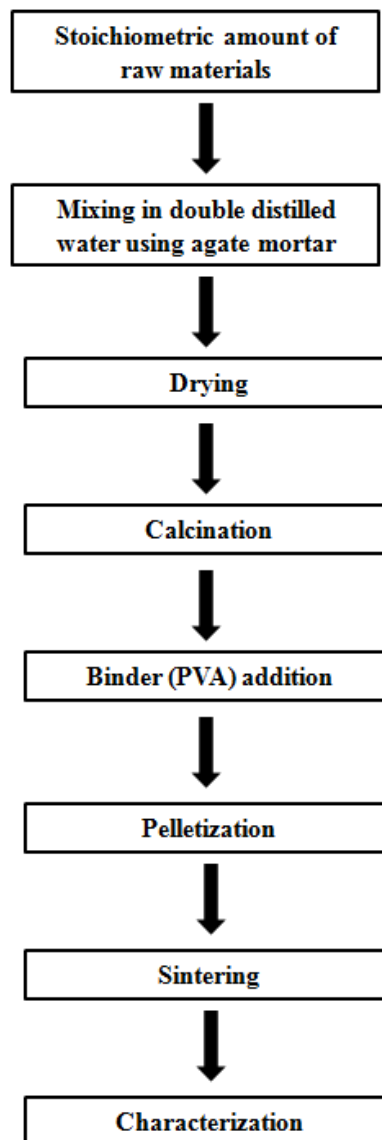


Figure 2.2 Schematic representation of solid state ceramic route

2.1.1.3 Pellet preparation

The next step is the preparation of green compacts for sintering. The calcined powder has to be well ground for removing agglomerates. The resultant powders with particle size around 1-10 μm are suitable for ceramic formation. If the ground powder is coarser, it results large inter-granular voids and low density after firing. Generally, ball milling or hand mixing using mortar with pestle is used for grinding. The resultant powder was mixed with binder and dried well for ceramic compact (pellet) formation. Binder is commonly used to form bridges between the ceramic grains. The binder allows the ceramic particles to be arranged in the closest possible packing by forming temporary bonds. The most accepted binder is polyvinyl alcohol (PVA). Available research studies suggest that around 5 wt% of PVA is ideal for fabrication of microwave dielectric ceramics. Binders provide appropriate elastic properties and shaping during the formation stage and influence the bulk density, flow rate and compaction behavior of the ceramic material. PVA provides high green strength without affecting the dielectric properties of the ceramic material and it decomposes at a low temperature of 600°C [8, 9]. In view of the above, PVA is used as the binder in the present study. The dried powders were again ground well and then pressed uniaxially in a 11 mm diameter tungsten carbide (WC) die by applying a pressure of 250 MPa in a hydraulic hand press.

2.1.1.4 Sintering

Sintering is generally a densification process, where the powder is converted into a dense solid body by heating near to the melting temperature of the packed particles. The main objective of sintering is to eliminate porosity. The vacant spaces between the compacted grains of ceramics are called “voids”, which differ from the isolated spaces called “pores” which happen during the final stage of sintering. The driving force for sintering is the decrease in the surface free energy of the powdered compact by replacing the solid–vapor interface with solid–solid interface. If Γ_{ss} is the energy of solid–solid interface and Γ_{sv} is the energy of solid–vapor interface then $\Gamma_{ss} > \Gamma_{sv}$. Sintering studies are generally carried out to understand how the microstructure is influenced by the processing variables such as temperature, applied pressure, particle size, particle packing, chemical composition, sintering atmosphere

etc. Sintering process occurs over a period of time, but it gets accelerated as the particles come close to their melting range. Sintering takes place at a faster rate as the particle size reduces since diffusion distances are shorter for small particles and the curvature stresses are larger. Sintering process is generally classified into four categories based on the composition being fired and the extent to which secondary phases are formed during the heat treatment [10]. They are solid state sintering, liquid phase sintering, vitrification and viscous flow sintering. In solid state sintering, no liquid phase is present and the atomic diffusion in the solid state leads to the joining of the particle and densification. On the other hand, in liquid phase sintering a small amount of liquid, less than a few volume percentage of the solid mixture is present. Since the volume of the liquid phase is not sufficient for densification, some additional processes are required for the complete densification of the materials. This is one of the important methods used in industrial production since the liquid phase enhances the densification at lower temperatures. In vitrification, the volume of liquid is sufficient ($> \sim 25\%$) to fill the volume of the pores. This method is mainly used for the production of ceramics from natural sources like clays. During viscous flow sintering, densification occurs by the viscous flow of consolidate mass of glass heated near to its softening point [11].

(a) Solid state sintering

The main driving force for solid state sintering is the reduction in the surface free energy of the sintered ceramic compact as a result of the elimination of the pores. According to microstructure, the sintering process can be divided into three stages, initial, intermediate and final stages. During the initial stage, the degree of atomic mobility increases followed by the formation of sharp concave necks between the individual particles. In this stage, the percentage of densification is only $\sim 5\%$ of the linear shrinkage. During the intermediate stage, the curvatures of the initial stage become moderated and this leads to the formation of continuous channel like pores. As a result, grain growth becomes significant in this stage. Around 90-95% of the densification occurs during the intermediate stage. The channel-like pores break down into isolated, closed voids in the final stage.

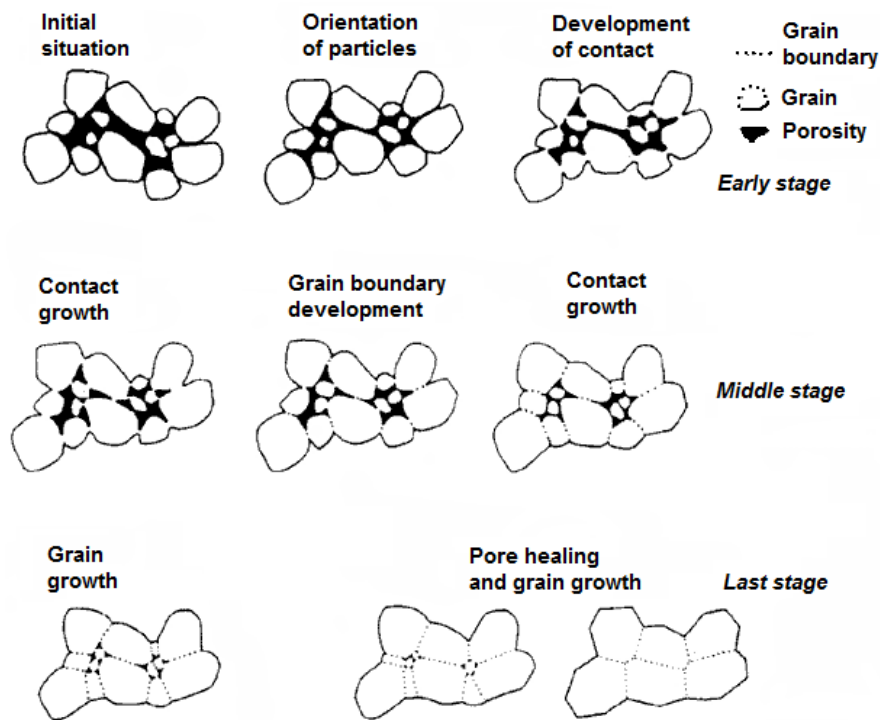


Figure 2.3 Different stages of solid state sintering

The major mechanisms during the sintering of crystalline materials are vapour transport such as evaporation/condensation, surface diffusion, lattice (volume) diffusion, grain boundary diffusion and dislocation motion. Among the above mentioned mechanisms, vapor transport, surface and lattice diffusion mechanisms take place from the particle surface to the neck leading to the neck growth and coarsening of the particles without any densification, whereas grain boundary diffusion and lattice diffusion from the grain boundary to the neck are the densification mechanisms. On the other hand, diffusion from the grain boundaries to the pores leads to neck growth as well as densification.

(b) Liquid phase sintering

In many of the sintering processes, the involvement of liquid phase enhances the densification rate and thereby accelerates the grain growth of the samples. Typically, a few volume percentage of the liquid phase is present. The main step in the liquid phase sintering is the melting of the liquid forming additive and the redistribution of the liquid. Later, the solution precipitation leads to the rearrangement of the solid phase by their shape accommodation and densification.

The final densification process in liquid phase sintering is driven by the residual porosity in the liquid phase.

Another process related to liquid phase sintering is activated sintering where small amounts of additives segregate to the grain boundary and enhance the grain boundary transport rates and thus accelerate the densification even below any eutectic temperatures in the additive/host system. In many cases, there may not be any clear difference between activated sintering and liquid phase sintering. But activated sintering involves the addition of less than 1% additive for which the resulting liquid grain boundary film can be difficult to detect [10-12].

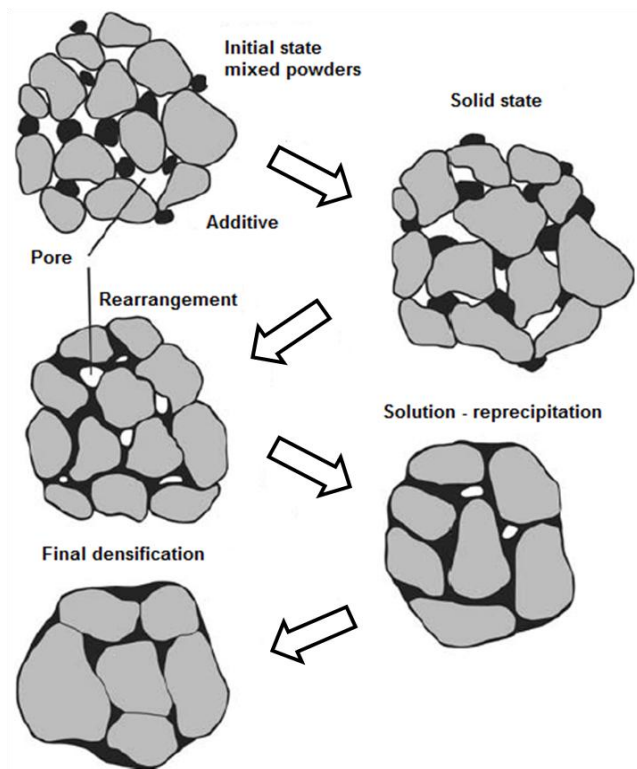


Figure 2.4 Different stages of liquid phase sintering

(c) Influence of processing parameters

The temperature where both reaction and densification occurs at the same rate, can be affected by factors like particle size, transport mechanisms involved in product formation, and also by the distribution of reactant particles. Starting particles with smaller size accelerate the densification with respect to reaction rates result higher sintered densities.

2.2 Synthesis of polymer ceramic composites

Composite materials play a decisive role in modern communication sector, especially in the area of advanced electronics. Also, ceramic filled polymer composites having low loss tangent has tremendous applications in the field of electronic packaging. There are different techniques including powder processing, melt mixing, molding etc. which are used for the fabrication of polymer ceramic composites. Powder processing method is mainly used for polymers having high melt viscosity and melting point like PTFE (327°C). Melt mixing is used for thermoplastic polymers with low viscosity during melting and have low melting points (< 300°C) compared to PTFE. Unlike other two methods, molding is mainly used for composite systems involving thermosetting polymers like epoxy resin.

2.3 Thermal characterization

2.3.1 Thermogravimetric Analysis (TGA) and Differential Scanning Calorimetry (DSC)

The thermal methods usually employed for the characterization of materials are Differential scanning calorimetry (DSC) and Thermogravimetric analysis (TGA) under identical experimental conditions. Thermogravimetric analysis deals with the change in mass of a substance as a function of temperature or time, when the sample is heated or cooled at a predetermined rate. It is used to determine the thermal stability of the material and its fraction of volatile components by monitoring the weight change while heating. During the thermal analysis, the mass of the material will be lost if the substance contains a volatile fraction. Differential scanning calorimetry (DSC) provides the information about the difference in heat flow to the sample against time/temperature. The reference used is an inert material such as alumina or platinum. During heating or cooling of the material, it may undergo changes such as reaction, oxidation, decomposition, fusion, expansion, contraction, crystallization or phase transition. DSC is used to monitor the energy released or absorbed via chemical reactions during the heating process. TGA/DSC is normally carried out in air and inert atmosphere at different heating rates. The rate of heating and the ambient atmosphere during analysis are very important factors to be

controlled during thermal analysis. TGA/DSC result will provide a clear understanding about the temperature at which material loses its weight and the onset of decomposition temperature. Also, it is possible to find out whether the decomposition of the material occurs in one or more stages [13-15].

2.3.2 Thermomechanical Analysis (TMA)

Thermomechanical analysis is a technique used to study the properties of materials as temperature changes. The basis of TMA is the dimensional change of the sample as a function of temperature. Thermomechanical analyzer consists of a furnace with accurate temperature measuring device, most commonly a thermocouple which couples to the sample and a sample holder. Normally quartz base is used to hold the sample, since quartz has a very low coefficient of thermal expansion (CTE) compared to other materials. Sample is placed on the quartz glass probe for measurements, which is integrated to an inductive position sensor. By heating the system at a controlled rate, the sample may expand or contracts and as a result the probe moves. The thermocouple close to the specimen measures the temperature changes. In thermomechanical analysis, the magnitude of penetration by probe into the sample is very important and is often less than 1mm. Such small changes can be measured using a Linear Variable Differential Transformer (LVDT) which converts the mechanical displacement into an electrical output. This mechanical change can be plotted against the temperature of the sample [16, 17]. The major advantage of TMA is that it is used to measure the glass transition temperature of polymers and polymer composites that are difficult to get by DSC, especially for highly cross linked thermosets.

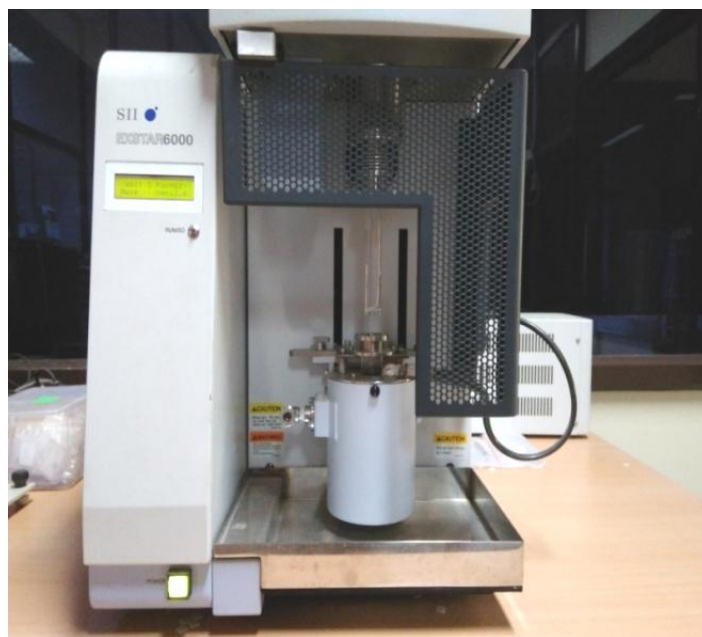


Figure 2.5 Thermomechanical analyzer for shrinkage and CTE measurements

2.3.2.1 Shrinkage behavior

For the shrinkage studies of ceramics, green pellets of 7mm diameter is placed on the quartz base. Temperature of the furnace increased with a specific rate which leads to the contraction of the sample. Shrinkage is obtained in percentage ($\Delta L/L$). The resultant $\Delta L/L$ plot gives information about the temperature at which the sample undergoes densification. The sintering temperature of the ceramic sample can be ascertained from these studies.

2.3.2.2 Coefficient of thermal expansion (CTE)

Coefficient of thermal expansion (CTE) of the dielectric ceramic as well as ceramic filled polymer composites can be accurately calculated by measuring the linear change of the sample length with respect to sample temperature using thermomechanical analyzer (TMA). Green pellets of 7 mm diameter and 1-2 mm thickness have been used in the present study for TMA measurements. For composites, samples with 8 mm length, 8mm width and 1-1.5 mm thickness have been used. TMA gives the percentage linear change (% LC) of the sample with respect to temperature and CTE can be calculated from the slope of the curve in

ppm/°C in the required temperature range and initial length of the sample using the equation given below.

$$CTE = \frac{L_{final} - L_{initial}}{L_{initial} (T_{final} - T_{initial})} \quad (2.1)$$

where, L_{final} , $L_{initial}$, T_{final} and $T_{initial}$ are the length and temperature of the sample at final and initial temperatures [16, 17].

2.4 Crystal structure characterization techniques

2.4.1 X- ray diffraction

A crystal consists of a regular array of atoms in such a way that each of which can scatter electromagnetic waves. When X-rays of wavelength λ strikes the crystalline sample, diffraction occurs in every possible orientation of 2θ and the interaction between the incident and diffracted rays produce constructive interference when the Bragg's law is satisfied (Equation 2.2). Bragg's law gives the relation between wavelength of the electromagnetic radiation λ , lattice spacing d in a crystalline sample, and diffraction angle θ and is given by

$$n\lambda = 2d\sin\theta \quad (2.2)$$

where, n is a positive integer. The diffracted beam was detected by electronic X-ray counters in order to accurately measure the intensities of the X-rays (Fig. 2.6). Every crystalline material gives X-ray diffraction pattern, the same substance always gives the same pattern and in a mixture of substances each produces its own patterns independently. Therefore, the X- ray diffraction pattern of a pure material is like a fingerprint of that material. Hence, X-ray diffraction method is widely used for the characterization of crystalline materials and yields information about the crystalline structure, unit cell dimensions, atomic site occupancy and many other physical properties.

In general, X-ray diffractometer has a sample holder, X-ray generator, goniometer and a fixed position detector to measure the diffraction patterns of unknown samples. X-rays generated from a high voltage source was applied to the X-ray tube within the diffractometer. X-ray produced when matter is irradiated with a beam of high-energy charged particles or photons. The energy associated with an

X-ray photon can be expressed as $E = hc/\lambda$ where h is Planck's constant (6.634×10^{-34} J.S) and c the speed of light (3×10^8 m/s). The diffractometer has a specific wavelength associated with them which depends on the metal used in the X-ray generator. For example, radiations from Cu includes $K_{\alpha 1}$ and $K_{\alpha 2}$ with typical wavelengths of 1.5406 Å and 1.5444 Å respectively. Other metals can also be used depending on the X-ray energy or wavelength needed. It is because certain samples give better diffraction intensities for different X-ray energies used in the diffractometer [18, 19].

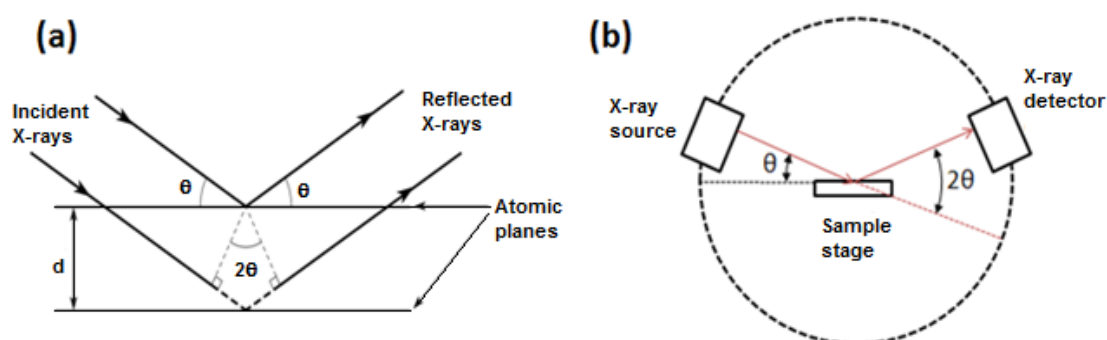


Figure 2.6 Schematic of (a) Bragg diffraction (b) X-ray diffractometer

2.4.2 Raman spectroscopy

Raman spectroscopy is an important spectroscopic technique used to investigate the rotational and vibrational spectra of molecules. Raman spectroscopy is based on the inelastic scattering of monochromatic light from molecules, which is known as the Raman Effect. When a sample is irradiated with a monochromatic light (usually a laser), most of the radiation is scattered by the sample at the same wavelength as that of the incoming laser radiation in a process known as Rayleigh scattering. On the other hand, a small portion of the incident radiation is scattered at a wavelength different from the incident wavelength which results inelastic scattering. The frequency of the re-emitted light can decrease (giving rise to Stokes lines in the spectrum) or increase (anti-Stokes lines), depending on whether the molecule exists in the ground state or an excited state (Figure 2.7). Since the initial population of the excited states is usually very small, the anti-Stokes lines are much weaker compared to the Stokes lines.

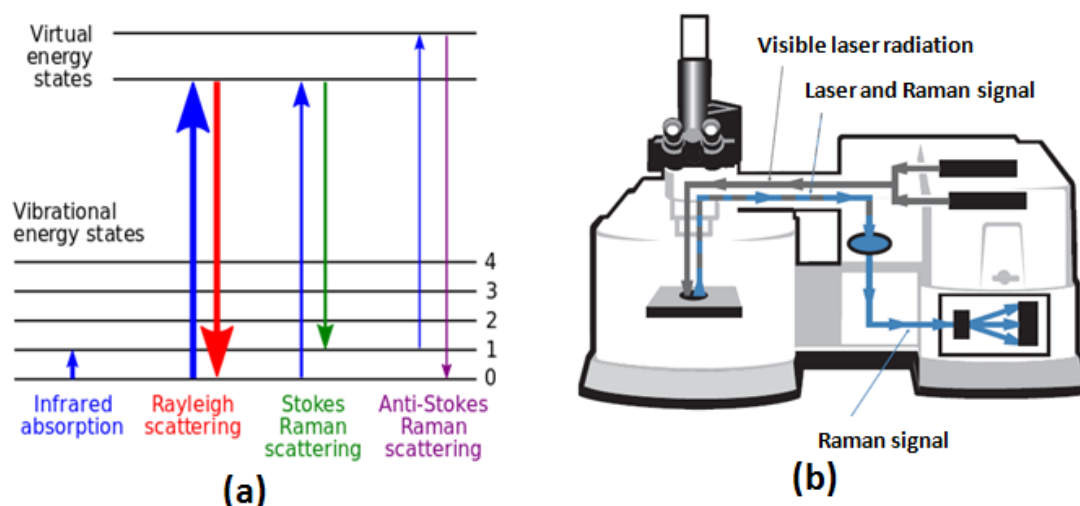


Figure 2.7 (a) Energy level diagram of Raman and Rayleigh scattering (b) Schematic of Raman spectrometer

The atoms of a molecule can vibrate in many ways and these vibrations are called normal modes of vibration. Since the normal modes have different excitation energies, the Raman spectrum will consist of more than one line. For a molecule with N number of nuclei, there will be $3N-6$ coordinates to account for the relative positions of the nuclei relative to each other for internal motions, and are called normal modes. Compared to other analytical techniques, Raman spectroscopy offers many advantages. The major advantage is that no two molecules give exactly the same Raman spectrum, which clearly gives the qualitative information about the molecule. There is no need to alter the physical or chemical structure of the sample for Raman spectroscopic analysis and it can also be used to investigate the physical properties of the sample such as crystallinity, phase transitions and polymorphism.

2.5 Scanning Electron Microscopy (SEM)

Scanning electron microscope is a type of electron microscope mainly used to understand the sample's surface morphology and composition. Scanning electron microscope produces images of the sample by scanning it with a focused beam of electrons due to the interaction between the electrons and the atoms in the sample. Since non-conductive specimens tend to charge when scanned by the electron beam causes scanning faults. In order to avoid this difficulty, specimens must be electrically conductive, at least at the surface, and electrically grounded to prevent the accumulation of electrostatic charge. Commonly used conductive materials include

gold, gold/palladium alloy, graphite etc. and an ultra-thin coating of the electrically conducting material on the sample can be done either by low-vacuum sputter coating or by high-vacuum evaporation. The different types of signals produced by a scanning electron microscope include secondary electrons (SE), reflected or backscattered electrons (BSE), photons of characteristic X-rays, light (cathodoluminescence) (CL), absorbed current (specimen current) and transmitted electrons. The most common and standard detection mode in SEM is secondary electron imaging, where the secondary electrons are emitted to the specimen surface from a very close distance. These electron beams interact with atoms of the sample at various depths and these interactions result signals. As a result, SEM can produce high resolution images of the sample surface and reveal details even less than 3 nm in size.

Reflected or Back-scattered electrons (BSE) are beam electrons that are reflected from the sample by means of elastic scattering. They emerge from deeper locations within the specimen and as a result the resolution of BSE images is generally not as good as that of SE images. Since heavy elements (having higher atomic number Z) backscatter electrons more strongly than light elements, and thus appear brighter in the image, BSE are used to detect contrast between areas with different chemical compositions. Since the intensity of the BSE signal is strongly related to the atomic number (Z) of the sample, it is often used in analytical SEMs along with the spectra made from the characteristic X-rays. These characteristic X-rays are emitted when the electron beam removes an inner shell electron from the sample, causing a higher-energy electron to fill the shell and release energy. Hence, these characteristic X-rays are used to identify the composition and measure the quantity of elements in the sample. As a result, BSE images can provide information about the distribution of different elements in the sample. The technique is known as Energy-Dispersive X-ray Spectroscopy (EDS) [20, 21].

2.6 Dielectric characterization

2.6.1 Low frequency measurements

The low frequency dielectric measurements of the ceramics and composites were carried out based on the parallel plate capacitor method using an impedance

analyzer (Agilent, 4294A, Malaysia) in the frequency range of 100 Hz to 13 MHz. This method involves the sandwiching of the dielectric material between two electrodes to form a parallel plate capacitor. The sintered body/composite sample was coated with silver paste on both sides, which act as the conductor plates. The parallel plate capacitor method consists of measuring the capacitance using an impedance analyzer from which dielectric constant can be calculated using the well known equation given below

$$\epsilon_r = \frac{cd}{A\epsilon_0} \quad (2.3)$$

where ϵ_0 is the permittivity of free space, ϵ_r is the relative permittivity or dielectric constant of the dielectric medium with respect to free space, A is the area of the sample and d is the distance between the plates. The temperature coefficient of dielectric constant can also be measured using an impedance analyzer coupled with a hot air oven (Figure 2.8) and can be calculated using the equation given below.

$$\tau_{\epsilon r} = \frac{\epsilon_{100} - \epsilon_{30}}{\epsilon_{30}(100 - 30)} \quad (2.4)$$

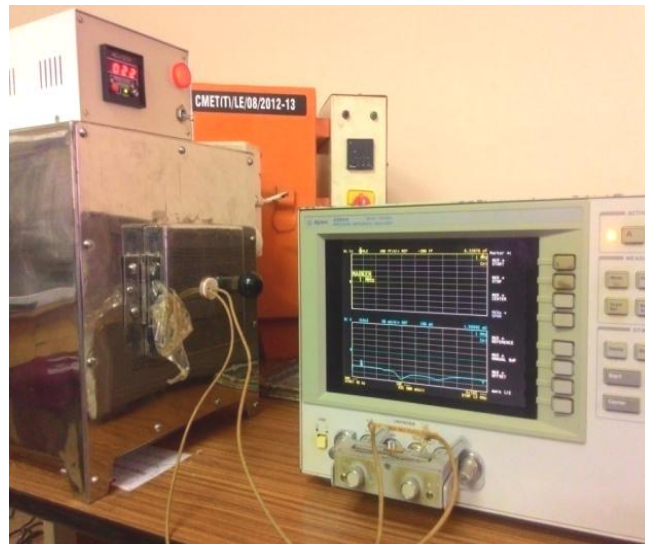


Figure 2.8 Temperature coefficient of dielectric constant ($\tau_{\epsilon r}$) measurement setup

2.6.2 Microwave dielectric characterization

The dielectric property measurement of materials at microwave frequencies can be generally classified into five categories: (a) perturbation methods (b) optical

methods (c) transmission line methods (d) reflection methods and (e) exact resonance methods. The choice of measurement mainly depends on the requirement of the measurement technique for the type of research, the accuracy required, availability of materials and material properties such as dielectric constant and loss factor. The perturbation methods are highly suitable for materials of small size and low dielectric constant since it does not alter the field configuration, while optical methods require large amount of material and applicable for wavelength less than one cm. Hence, both these methods are not suitable for dielectric resonator characterization. Moving to transmission and reflection methods, transmission line technique requires very small waveguides which leads to practical difficulties. In the case of reflection method, reflected waves from the dielectric were studied and if the dielectric constant of the material goes high, there occurs error due to complex voltage reflection coefficients. In exact resonance method, the exact resonant frequency of the dielectric sample was measured and from the resonant frequency value parameters such as dielectric constant, quality factor etc. can be determined [22-27]. Special techniques of exact resonance methods used in the present study are described below.

2.6.2.1 Measurement of relative permittivity (ϵ_r)

The relative permittivity of the dielectric resonator (DR) is measured by Hakki and Coleman method, modified by Courtney, in which DR in the form of a cylindrical puck is sandwiched between two conducting plates having diameter much larger than that of the DR (Figure 2.9) [28, 29]. The conducting plates are made up of well-polished copper plates coated with silver or gold. In order to carry out Hakki and Coleman measurement, the network analyzer (Model-Agilent PNA E8362B, Bayan Lepas, Malaysia) is set to the S_{12}/S_{21} mode. By tilting the top conducting plate, most of the modes will move to the right side except transverse electric mode (TE_{011} mode), which will move to the left side on further tilting the top plate. The TE_{011} mode is normally used to make the measurements since it propagate inside the DR sample but is evanescent outside the resonator sample. The azimuthal component of the electric field exists only for this mode and the error due to the air gap is practically eliminated [30, 31].

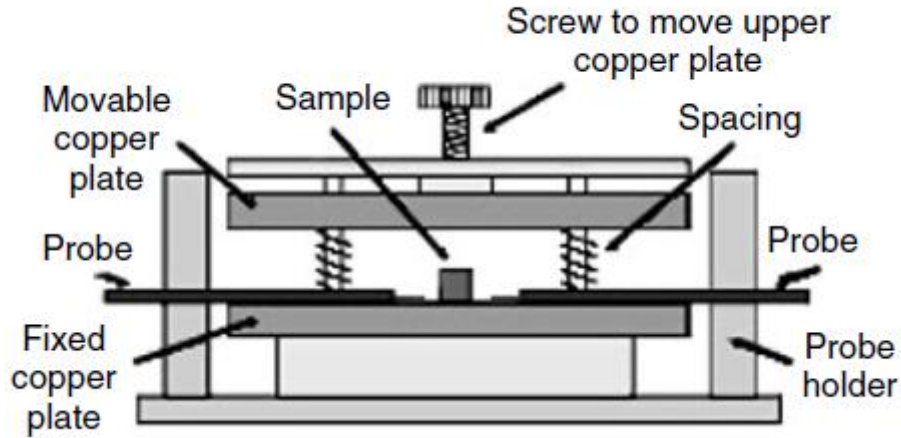


Figure 2.9 Schematic design of the Hakki and Coleman setup used for measuring the dielectric constant under end shorted condition [Ref. 29]

The diameter to thickness ratio of the DR should be between 1.5 to 2 to get wide mode separation so that the TE_{011} mode is not disturbed by other adjacent modes. For an isotropic dielectric material, the characteristic equation for the TE_{0ml} mode is given by

$$\alpha \frac{J_0(\alpha)}{J_1(\alpha)} = -\beta \frac{K_0(\beta)}{K_1(\beta)} \quad (2.5)$$

where $J_0(\alpha)$ and $J_1(\alpha)$ are the Bessel functions of first kind of order zero and one, $K_0(\beta)$ and $K_1(\beta)$ are the modified Bessel functions of second kind of order zero and one respectively. The α and β parameters depends on the geometry, resonant wavelength inside the dielectric resonator and the dielectric properties of the resonator, and can be calculated using the following equations.

$$\alpha = \frac{\pi D}{\lambda_0} \left[\epsilon_r - \left(\frac{l\lambda_0}{2L} \right)^2 \right]^{1/2} \quad (2.6)$$

$$\beta = \frac{\pi D}{\lambda_0} \left[\left(\frac{l\lambda_0}{2L} \right)^2 - 1 \right]^{1/2} \quad (2.7)$$

where, l is the longitudinal variation of the field along the axis, L is the length and D is the diameter of the dielectric resonator, λ_0 is the free space resonant wavelength. Hakki and Coleman provides a universal mode chart (Figure 2.10) which shows the variation of α as a function of β in such a way that for each value of β there is

infinite number of α_n that solves the characteristic equation [28, 31, 32]. Using the mode chart parameters, resonant frequency f and the dimensions of the dielectric resonator, the real part of the dielectric permittivity can be calculated using the following equation

$$\epsilon_r = 1 + \left[\frac{c}{\pi D f} \right]^2 (\alpha_1^2 + \beta_1^2) \quad (2.8)$$

If one can identify the transverse resonant modes other than TE_{011} , then dielectric constant can be measured at TE_{021} , TE_{031} and TE_{041} modes i.e., over a range of frequencies.

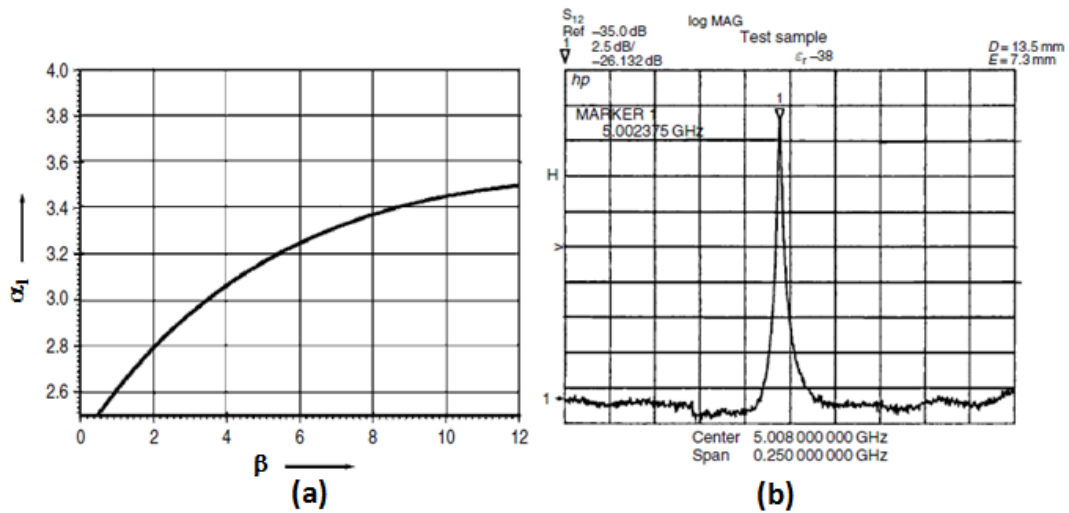


Figure 2.10 (a) Mode chart (b) Frequency response of the TE_{011} mode of a dielectric resonator with $\epsilon_r = 38$ [Ref. 32]

2.6.2.2 Measurement of unloaded quality factor (Q_u)

The unloaded quality factor can be measured using end shorted Hakki and Coleman or Courtney method. But the quality factor measured by this method will be affected by the radiation losses and conductor losses due to the conducting plates. These effects can be avoided by using cavity method in which the dielectric resonator is placed on low loss single crystal quartz or Teflon spacer inside a cavity usually made of copper and the inner surfaces are finely polished and coated with gold or silver (Figure 2.11). The cavity is designed in such a way that the diameter of the cavity is almost four times greater than that of the sample diameter in order to reduce the effect of cavity shielding. After loading the dielectric sample, the cavity is

closed with a lid and microwave is fed through loop coupling. The coupling should be adjusted to optimum, weak coupling for high Q_u and strong coupling for lossy samples [33].

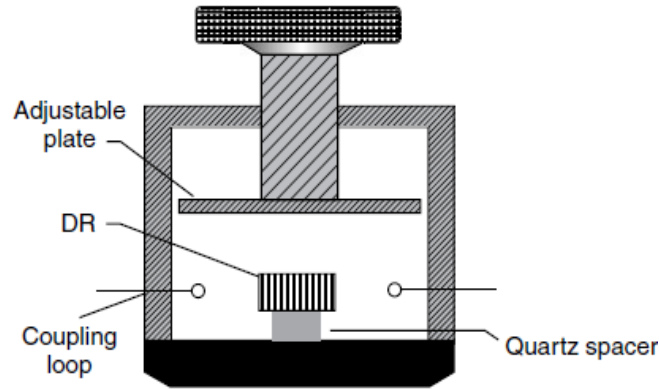


Figure 2.11 Cavity setup for the measurement of Q-factor

In general, the cavity has infinite number of modes, which can be excited with the applied microwave spectrum of frequencies. In the cavity method, TE_{011} mode is designated as $TE_{01\delta}$ mode because of the incomplete field confinement in the z direction. The cavity method using the $TE_{01\delta}$ mode has advantages like easy mode identification, small parasitic losses and lack of mode degeneracy. The quality factor measurement of dielectric resonators using a transmission mode cavity is proposed by J. Krupka [33], where the S_{21} or the transmission characteristics of the $TE_{01\delta}$ mode versus frequency is obtained. From the obtained $TE_{01\delta}$ mode frequency (f_0) and the 3dB bandwidth of the spectrum, quality factor can be calculated as

$$Q = \frac{f_0}{\Delta f} \quad (2.9)$$

The unloaded quality factor (Q_u) of the sample is calculated as

$$Q_u = \frac{Q}{1 - 10^{(-I_L/20)}} \quad (2.10)$$

where, I_L is the insertion loss of the resonance spectrum. The inverse of the unloaded quality factor is approximately equal to the dielectric loss tangent. The measured frequency depends upon the size and dielectric constant of the test samples [32, 33].

Figure 2.12 represents the typical resonance spectra of BMT ($\epsilon_r = 24$) in the reflection and transmission configuration.

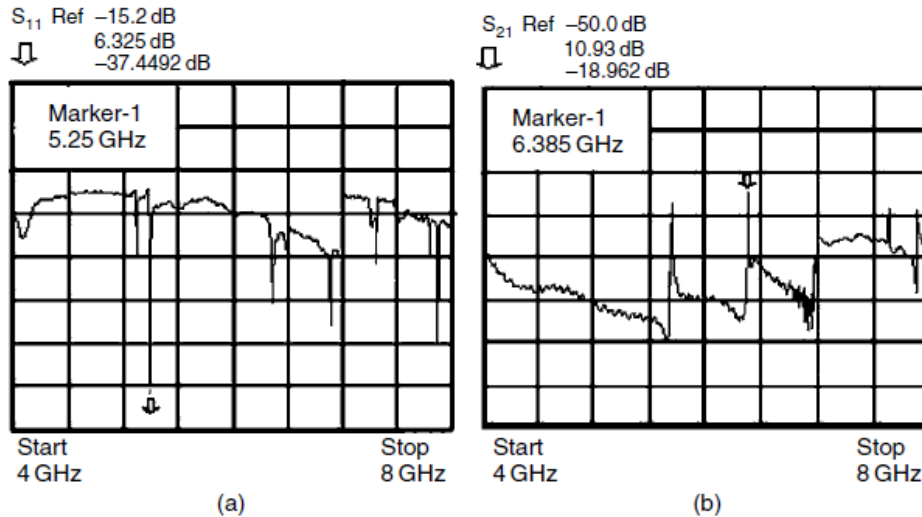


Figure 2.12 Microwave resonance spectra of BMT ($\epsilon_r = 24$) in the (a) reflection and (b) transmission configuration [Ref. 32]

2.6.2.3 Waveguide cavity perturbation technique

Waveguide cavity perturbation is used to measure the dielectric constant and loss tangent of composite samples. In the present work, X-band rectangular waveguide cavity as given in Figure 2.13 was fabricated out of a standard WR-90 brass waveguide of nearly 13.5 cm length. The upper broad wall of the waveguide has a thin slot of 4 cm length and 1 mm width. The conducting plate with an aperture of around 2 mm width on the either sides of the waveguide provides inductive coupling to the cavity. Thin samples in the form of strips of 2 mm width and around 0.8 mm thickness have been used for the measurement. Utilizing the sweep frequency capacity of the analyzer, the cavity was excited in five TE modes (TE_{105} - TE_{109}) and the corresponding five peaks are appeared on the screen of the network analyzer at 8.4 GHz, 9.1 GHz, 9.8 GHz, 10.6 GHz and 11.5 GHz. Before introducing the sample, resonant frequency of the cavity (f_c) has to be measured by connecting the cavity to a vector network analyzer. Sample is placed at the position of maximum intensity of the electric field position in the rectangular cavity and the resonant frequencies with the sample (f_s) is measured by noting the changes of the quality factor due to the presence of the sample [34].

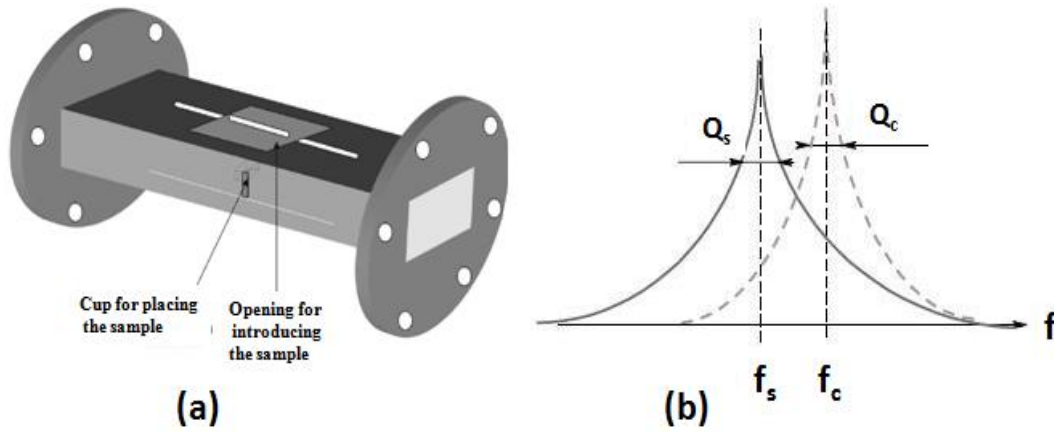


Figure 2.13 (a) Schematic representation of X-band waveguide cavity (b) Shift in the resonant frequency with the introduction of the sample inside the cavity

By assuming the dielectric material to be non-magnetic, the real and imaginary parts of the dielectric constant are given by the following equations.

$$\epsilon'_r = \left[\frac{f_c - f_s}{2f_s} \right] \frac{V_c}{V_s} + 1 \quad (2.11)$$

$$\epsilon''_r = \left[\frac{V_c}{4V_s} \right] \left[\frac{1}{Q_s} - \frac{1}{Q_u} \right] \quad (2.12)$$

$$Q_u = Q_c \left[1 + (\epsilon'_r - 1) \frac{V_s}{V_c} \right] \quad (2.13)$$

Where V_c and V_s are the cavity and sample volumes, Q_c and Q_s are the quality factors of the cavity with and without the sample respectively. Q_u is the theoretical quality factor and called as unloaded quality factor. According to the conventional cavity perturbation theory, the presence of the sample in the metal cavity would decrease the quality factor of the cavity due to the dielectric loss of the sample [34, 35]. The loss tangent of the sample is expressed as

$$\tan \delta = \frac{1}{Q_d} = \frac{\epsilon''}{\epsilon'} \quad (2.14)$$

2.6.2.4 Measurement of temperature coefficient of resonant frequency (τ_f)

Temperature coefficient of resonant frequency (τ_f) indicates the thermal stability of the resonator. Experimentally, τ_f is measured by noting the drift in the resonant frequency with varying temperature. The dielectric resonator is kept between two copper plates under Hakki and coleman set up and then the TE_{011} mode

is identified and the setup is heated in the temperature range 30-100°C. The shift in the resonant frequency due to the change in temperature is noted accurately using a vector network analyzer and the variation in the resonant frequency can be plotted as a function of temperature [32]. The value of τ_f can be calculated using the equation given below.

$$\tau_f = \frac{f_{100} - f_{30}}{f_{30}(100 - 30)} = \frac{1}{f} \frac{\Delta f}{\Delta T} \quad (2.15)$$

2.7 Mechanical strength measurement

Mechanical strength of the ceramic filled polymer composites in the present study is measured using a Universal Testing Machine (UTM, Shimadzu-1000G). A typical UTM consists of a testing frame, control and analysis software, test fixtures, devices to fix the sample and accessories. Load cells are used to measure force and extensometer for deformation. The specimen has to be placed in the machine between the grips and extensometer for measurements. The sample undergoes an elongation while applying load and breaks beyond the peak value of load. Ultimate tensile strength (UTS) is the maximum stress that a material can withstand while being stretched or pulled before breaking. Parameters like peak load, ultimate load, average load, distance at peak load and distance at break are obtained from the peel strength testing machine. By dividing the peak load (in N) with the cross sectional area (in mm²) of the sample will give the value of the tensile strength of the sample in MPa.

References

- [1] A. J. Moulson, J. M. Herbert, *Electroceramics: materials, properties and applications*, John Wiley & Sons (2003).
- [2] H. S. Nalwa, *Handbook of low and high dielectric constant materials and their applications: Materials and processing*, Academic Press (1999).
- [3] H. Schmalzried, *Solid state reactions*, Academic Press, New York (1974).
- [4] L. T. Fan, Y. Chen, *Powder Technol.*, 61 [3] (1990) 255-287.
- [5] M. Thirumal, P. Jain, A. K. Ganguli, *Mater. Chem. Phys.*, 70 [1] (2001) 7-11.
- [6] Y. Arai, *Chemistry of powder production*, Chapman & Hall (1996).
- [7] W. D. Kingery, H. K. Bowen, D. R. Uhlmann, *Introduction to ceramics*, John Wiley and Sons (1960).
- [8] G. Y. Onoda, L. L. Hench, *Ceramic Processing before Firing*, Wiley (1978).
- [9] N. M. Alford, X. Wang, S. J. Penn, M. Poole, A. Jones, *Br. Ceram. Trans.*, 99 [5] (2000) 212-214.
- [10] S. Somiya, *Handbook of advanced ceramics*, Elsevier (2003).
- [11] R. M. German, P. Suri, S. J. Park, *J. Mater. Sci.*, 44 [1] (2009) 1-39.
- [12] R. M. German, *Sintering: from empirical observations to scientific principles*, Elsevier (2014).
- [13] P. J. Haines, *Thermal Methods of Analysis: Principles, Applications and Problems*, Springer-Science + Business Media, (1995).
- [14] T. Hatakeyama, F. X. Quinn, *Thermal Analysis: Fundamentals and Applications to Polymer Science*, John Wiley & Sons (1994).
- [15] R. C. Mackenzie, *Differential Thermal Analysis*, Academic Press (1973).
- [16] B. A. Tonkin, M. W. Hosking, *J. Mater. Sci. Lett.*, 15 [23] (1996) 2030- 2032.
- [17] Z. Pluta, T. Hryniewicz, *J. Modern Phys.*, 3 (2012) 793-802.
- [18] B. D. Cullity S. R. Stock, *Elements of X-ray diffraction*, Prentice Hall (2001).

- [19] B. Fultz, J. Howe, *Transmission Electron Microscopy and Diffractometry of Materials*, Springer (2013).
- [20] D. McMullan, *Scanning.*, 17 [3] (1995) 175-185.
- [21] KCA Smith, C. W. Oatley, *Br. J. Appl. Phys.*, 6 [11] (1955) 391-399.
- [22] G. Birnbaum, J. Franeau, *J. Appl. Phys.*, 20 [8] (1949) 817-819.
- [23] J. Mussil, F. Zacek, *Microwave measurement of complex permittivity by free space methods and applications*, Elsevier (1986).
- [24] K. Leong, Precise measurements of surface resistance of HTS thin films using a novel method of Q-factor computations for sapphire dielectric resonators in the transmission mode, Ph.D thesis, James Cook University (2000).
- [25] K. Leong, J. Mazierska, *J. Supercond.*, 14 [1] (2001) 93-94.
- [26] D. Kajfez, *IEE Proc. Microw. Antennas Propag.*, 142 [5] (1995) 369-372.
- [27] K. Wakino, Proc. of the second Sendai Inter. Conference, YAGI Symposium on Advanced Technology Bridging the Gap between Light and Microwaves, (1990) 187-196.
- [28] B. W. Hakki, P.D. Coleman, *IRE Trans. Microw. Theory Tech.*, 8 [4] (1960) 402-410.
- [29] W. E. Courtney, *IEEE Trans. Microw. Theory Tech.*, 18 [8] (1970) 476- 485.
- [30] S. B. Cohn, K. C. Kelly, *IEEE Trans. Microw. Theory Tech.*, 14 [9] (1966) 406-410.
- [31] D. L. Rebsch, D. C. Webb, R. A. Moore, J. D. Cawlishaw, *IEEE Trans. Microw. Theory Tech.*, 13 [4] (1965) 468-469.
- [32] M. T. Sebastian, *Dielectric materials for wireless communication*, Elsevier (2010).
- [33] J. Krupka, *Meas. Sci. Technol.*, 17 [6] (2006) R55-R70.
- [34] D. C. Dube, M. T. Lanagan, J. H. Kim, S. J. Jang, *J. Appl. Phys.*, 63 [7] (1988) 2466-2468.
- [35] J. Sheen, *Meas.* 42 [1] (2009) 57–61

Structure and Microwave Dielectric Properties of Ultra-low Temperature Co-firable AV_2O_6 (A= Ba, Sr, Ca, Mg and Zn) Ceramics

- 3.1 Introduction
- 3.2 Experimental techniques
- 3.3 Results and discussion
- 3.4 Conclusions

Some of the contents of this chapter have published in

A. N. Unnimaya, E. K. Suresh, R. Ratheesh, Eur. J. Inorg. Chem., 2015 [2] (2015) 305-310

3.1 Introduction

The rapid growth in the area of communication systems such as mobile phones, antenna duplexers, global positioning systems etc. demand novel dielectric materials for the design of miniaturized microwave devices [1]. In general, the advanced dielectric material should have low dielectric constant to increase the signal speed, high quality factor for better frequency selectivity and stable temperature coefficient of resonant frequency to ensure the stability of resonant frequency. Moreover, the ceramics should be nontoxic, easily processable and in the same time cost effective. In this perspective, low temperature co-fired ceramics (LTCC) can satisfy most of the aforementioned requirements. Thus, the emergence of LTCC technology demands the development of new dielectric materials with low sintering temperature to enable its co-firing with metal electrodes.

A large number of dielectric ceramics including titanates and tantalates with stable dielectric constant, high quality factor and low temperature coefficient of resonant frequency have been reported and used as resonator materials since several years [2-4]. But most of them have very high sintering temperature $\geq 1300^\circ\text{C}$. Since silver has very high conductivity (6.3×10^7 S/m at 20°C) and reasonably low cost, it is generally used as the metallic electrode for LTCC technology, which has a melting point of 961°C [5]. Therefore, the sintering temperature of the dielectrics should be lower than the melting point of silver. However, reducing the sintering temperature without affecting the dielectric properties of the conventional microwave ceramic is difficult in LTCC materials research. Addition of low melting glasses or oxides such as B_2O_3 , CuO , Bi_2O_3 and V_2O_5 are commonly used as effective methods to reduce the sintering temperature of dielectric ceramics [6-9]. However, this approach has detrimental effects on the microwave properties of the dielectrics especially on the quality factor due to the formation of secondary phases. Thus, the preparation and characterization of new LTCC materials having high quality factor and near-zero temperature coefficient of resonant frequency, which can be sintered at less than 961°C without glass or oxide additives are essentially required for device fabrication.

Recently, low temperature sinterable dielectrics based on MoO_3 , Bi_2O_3 , TeO_2 and Li_2O_3 rich compounds have been reported by several authors [10-17]. In addition, V_2O_5 based single phase ceramic systems such as $\text{Ca}_5\text{A}_4(\text{VO}_4)_6$ ($\text{A}^{2+}=\text{Mg}$ and Zn), $\text{Mg}_3(\text{VO}_4)_2$, $\text{LiCa}_3\text{MgV}_3\text{O}_{12}$, $\text{Ba}_3\text{MV}_4\text{O}_{15}$ ($\text{M}=\text{Ti}$ and Zr) etc. have been

reported as low temperature sinterable microwave dielectric ceramics [18-21]. These ceramics not only have excellent microwave dielectric properties, but also exhibit chemical compatibility with metal electrodes. Even though large number of low temperature sinterable microwave dielectric ceramics are reported, the need for further lowering the sintering temperature of dielectric materials leads to a new category of ultra-low temperature co-fired ceramics (ULTCC), wherein the ceramic material has to be sintered at temperatures less than 660°C. As a result of this, the dielectric materials can be co-fired with Al electrode instead of Ag due to their ultra-low sintering temperature [22, 23]. BaTe₄O₉ was the first dielectric ceramic co-fired with Al electrode at 550°C by Kwon et al. [24]. Only very few literature are available on the structure and microwave dielectric properties of ULTCC ceramic systems.

The BaO-V₂O₅ binary system was first investigated by Kohemuller and Perrand and they found that three barium vanadate compositions namely BaV₂O₆, Ba₂V₂O₇ and Ba₃V₂O₈ exist in the BaO-V₂O₅ system [25]. Later, Fotiev et al. reinvestigated the BaO-V₂O₅ binary system using X-ray diffraction and thermo-optical studies [26]. They reported three new compounds Ba₃V₄O₁₃, BaV₁₂O₃₀ and BaV₈O_{21-x} along with the already known BaV₂O₆, Ba₂V₂O₇ and Ba₃V₂O₈ compositions. The equilibrium phase diagram of the BaO-V₂O₅ system based on the thermographic and thermo-optical methods is shown in Figure 3.1.

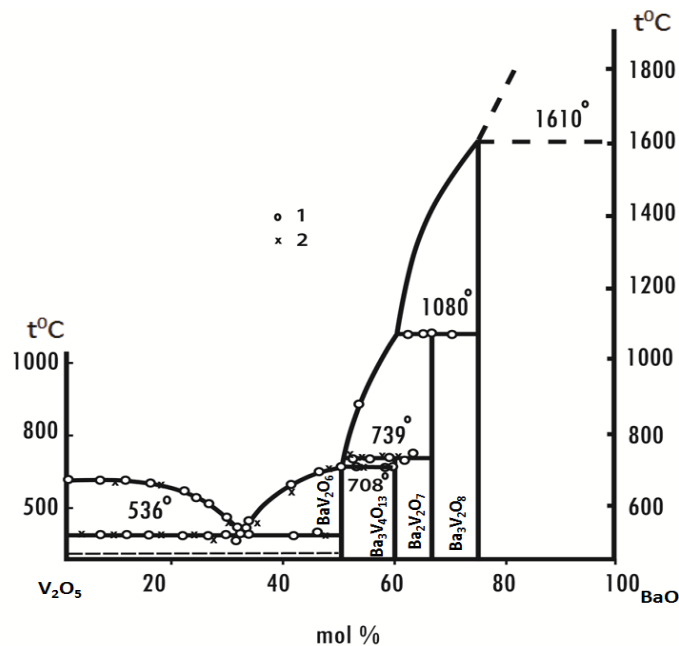


Figure 3.1 Equilibrium diagram of the BaO-V₂O₅ system: (1) Thermographic and (2) Thermo-optical results [Ref. 26]

According to Fotiev et al., BaV_2O_6 , $\text{Ba}_2\text{V}_2\text{O}_7$, $\text{Ba}_3\text{V}_2\text{O}_8$ and $\text{Ba}_3\text{V}_4\text{O}_{13}$ are stable and $\text{BaV}_{12}\text{O}_{30}$ and $\text{BaV}_8\text{O}_{21-x}$ are metastable compounds [26]. On heating, the stable BaV_2O_6 phase melts without any decomposition at 708°C and the other stable compounds $\text{Ba}_3\text{V}_4\text{O}_{13}$, $\text{Ba}_2\text{V}_2\text{O}_7$ and $\text{Ba}_3\text{V}_2\text{O}_8$ melt at 739°C , 1080°C and 1610°C respectively (Figure 3.1). On the other hand, the metastable compounds decompose on heating and result BaV_2O_6 and V_2O_5 [26]. Similar to barium, other alkali metal vanadates with general formula AV_2O_6 where $A = \text{Sr, Ca, Mg}$ and Zn also have low melting temperature among the stable compositions in the analogous $\text{AO-V}_2\text{O}_5$ binary system [27-29]. Since all aforementioned metavanadate compositions have lower melting temperature, they can be considered as a suitable system for both LTCC as well as ULTCC applications, where the ceramic should have a sintering temperature lower than that of the melting point of the respective metal electrodes such as Ag and Al .

The crystal structure of metavanadates with divalent metal atoms have the general formula AV_2O_6 ($A = \text{Ba, Sr, Ca, Mg}$ etc.) is well studied and are classified into Columbite, Rossite, Brannerite and NiV_2O_6 types [28]. These structures generally consist of frameworks of V-O polyhedra together with interstitial A^{2+} ions. Metavanadates usually crystallize in the Brannerite or Rossite structure. The Brannerite structure is derived from the mineral Brannerite (U, Ca, Y, Ce) $(\text{Ti, Fe})_2\text{O}_6$, which is monoclinic with space group $C2/m$ [30]. In general, the Brannerite structure consists of AO_6 and BO_6 octahedra. The BO_6 octahedra are edge-shared and form layers parallel to the (ab) plane whereas AO_6 octahedra form infinitely long edge-shared chains. In addition, the BO_6 and AO_6 octahedra are connected via corner linkage [30-33]. Rossite type structure has trigonal BO_5 bipyramids with an edge linkage in the direction of the b -axis whereas the AO_6 octahedra are in the $[010]$ direction, as in the case of the Brannerite type, connected to infinitely long chains via a corner linkage. Hence, these two structural modifications look similar. In the low temperature Brannerite form, vanadium ions have distorted octahedral coordination whereas in the high temperature Columbite structure vanadium ions form a well-defined trigonal bipyramid with the nearest five oxygen atoms [28, 34].

According to early reports, most of the divalent metavanadates crystallizes in the Brannerite-like structure consisting of zigzag chains of VO_5 square pyramids with sharing edges [35 - 37]. The divalent metal ions occupy the same site as U^{4+} in Brannerite, while the V^{5+} ions occupy a position corresponding to the Ti^{4+} sites [37]. The crystal structure of ZnV_2O_6 is a typical representative of AV_2O_6 compounds with Brannerite structure. The crystal structure of ZnV_2O_6 was first studied by Angenault et al. and later refined by Adreetti et al. [36, 38]. ZnV_2O_6 crystallizes in the monoclinic $C2/m$ space group, where the Zn^{2+} ions are octahedrally coordinated and the V^{5+} ions are having an irregular octahedral coordination. The VO_6 octahedra are linked by edges to form infinite anionic layers and the ZnO_6 octahedra are connected by the opposite edges form infinite rows along the b-axis and link the anionic layers [36, 39]. In the same way, MgV_2O_6 also has Brannerite structure, monoclinic $C2/m$ space group with distorted VO_6 octahedra. These distorted VO_6 octahedra share opposite corners forming chains running parallel to the b-axis and Mg^{2+} ions lie in the octahedral interstices sharing oxygen atoms with different V^{5+} ions [35, 40].

CaV_2O_6 belongs to monoclinic $C2/m$ space group with zigzag chains of VO_5 trigonal bipyramids and as a result possesses Rossite type structure [41]. The CaO_6 octahedra are in the same [010] direction as in the case of Brannerite type and connected to infinitely long chains through corner linkage. Basically, the vanadate modifications in CaV_2O_6 structure look similar to that in the Brannerite type, although it has linkages with various polyhedra [41].

On the other hand, metavanadates with larger divalent metal atoms ($\text{A}=\text{Ba}$ and Sr) adopt the structure with VO_4 tetrahedral units, where the V atoms lie in the tetrahedra of O atoms, and hence do not belongs to Brannerite and Rossite type structures. The corner shared VO_4 tetrahedra in these metavanadates lead to infinite chains as in the case of alkali metal vanadates MVO_3 ($\text{M}=\text{Li}, \text{Na}, \text{K}$ etc.) [42]. The crystal structure of BaV_2O_6 has already been studied in detail by Yao et al. and reported that BaV_2O_6 adopts orthorhombic crystal structure with the space group $C222$ (21) [42]. According to their report, the structure of BaV_2O_6 consists of infinite chains of vertex shared VO_4 tetrahedra running along the [120] directions

and Ba atoms located interstitially between the chains [42]. Recently, Li et al. carried out the structure refinement of both BaV_2O_6 and SrV_2O_6 and found that both of them crystallize in the orthorhombic crystal structure with space group $C222 (21)$ [43]. A comparison of the lattice parameters of these metavanadates based on A^{2+} cation sizes and their crystal structures are compiled in Table 3.1.

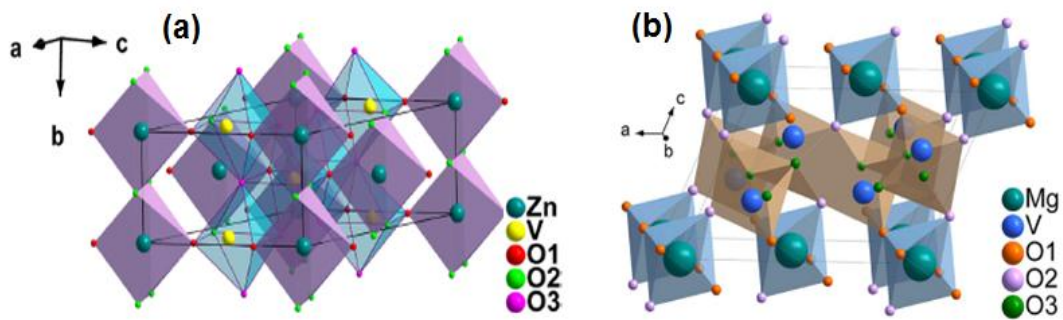


Figure 3.2 Schematic views of the crystal structures of (a) ZnV_2O_6 and (b) MgV_2O_6 [Ref. 39, 40]

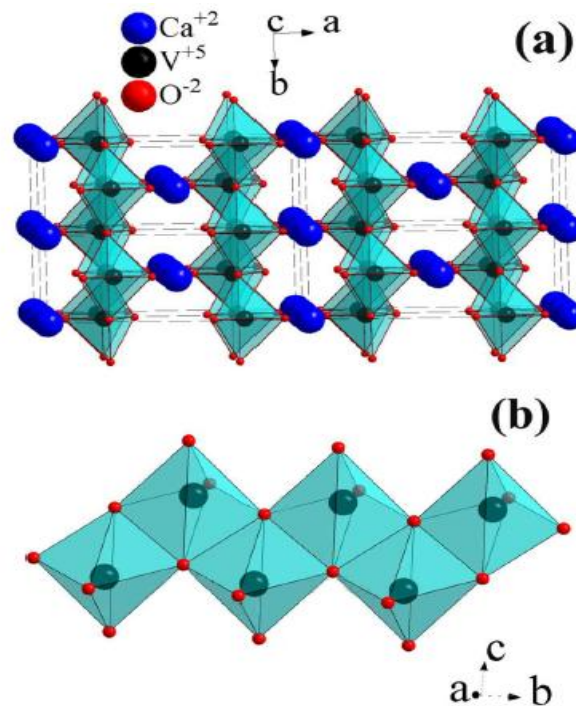


Figure 3.3 (a) The schematic view of CaV_2O_6 structure along b -direction (b) the VO_5 chains along $[010]$ axis [Ref. 41]

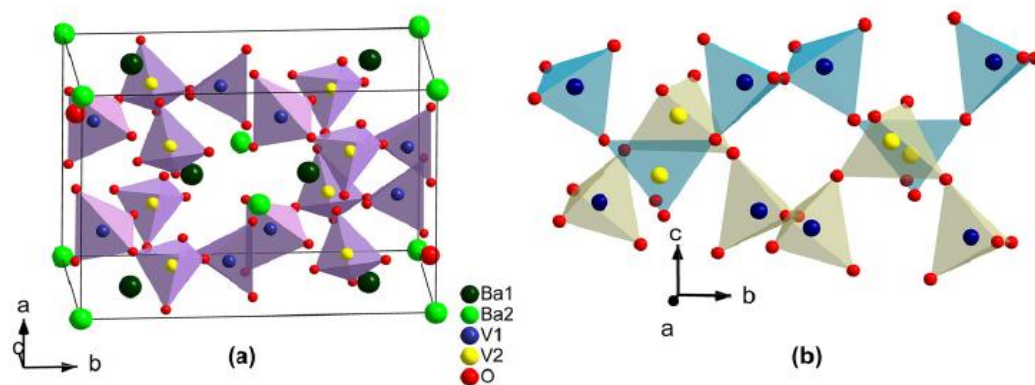


Figure 3.4 (a) The crystal structure of BaV_2O_6 and (b) infinite chains formed by shared-corners of VO_4 tetrahedra [Ref. 43]

Table 3.1 Available crystal structure data of AV_2O_6 (A= Ba, Sr, Ca, Mg and Zn) compositions

A^{2+} ion	Ionic radii of A^{2+} ions	Crystal structure	Space group	Z	References
Ba	1.36	Orthorhombic	$C222$	6	Ref. [42]
Sr	1.16	Orthorhombic	$C222$	6	Ref. [43]
Ca	1	Monoclinic	$C2/m$	2	Ref. [41]
Mg	0.72	Monoclinic	$C2/m$	2	Ref. [39]
Zn	0.74	Monoclinic	$C2/m$	2	Ref. [36]

In this chapter, a systematic study on the structure and microwave dielectric properties of AV_2O_6 (A= Ba, Sr, Ca, Mg and Zn) ceramics has been carried out. Detailed studies on their chemical compatibility with Al electrode have also been performed to ascertain their use for LTCC and ULTCC applications.

3.2 Experimental techniques

AV_2O_6 ceramics (A= Ba, Sr, Ca, Mg and Zn) were prepared by conventional solid state ceramic method. High purity BaCO_3 (Sigma Aldrich, 99%), SrCO_3 (Himedia, 99%), CaCO_3 (Sigma Aldrich, 99+%), MgO (Sigma Aldrich, 99+%), ZnO (Sigma Aldrich, 99%) and V_2O_5 (Sigma Aldrich, 99%) were used as starting materials. Stoichiometric amounts of the raw materials were weighed and wet mixed in distilled water for an hour in an agate mortar. The resultant slurry was dried at 100°C in a hot air oven, then ground well and calcined at 450°C for 1 hour. The calcined powders were ground again and then mixed with 5 wt% polyvinyl alcohol (PVA) as binder and the slurry was dried. The powders were again ground well and then pressed uniaxially in a

11 mm diameter tungsten carbide (WC) die by applying a pressure of 250 MPa in a hydraulic hand press. These cylindrical green compacts were sintered in a programmable furnace in the temperature range 500-700°C for an hour.

Phase purity of the AV_2O_6 samples was studied by powder X-ray diffraction (XRD) measurement using CuK_{α} radiation (Bruker 5005, Germany). The Raman spectra of the ceramic compositions were recorded using a Thermo Scientific DXR with Nd:YVO₄ DPSS laser of 532 nm. The surface morphology of the sintered samples was studied using scanning electron microscopy (Carl Zeiss, Model No: EVO18 Research, Germany). The low frequency measurements of the samples were carried out at 1 MHz using an impedance analyzer (Agilent, 4294A, Malaysia). The microwave dielectric properties were measured using a vector network analyzer (Agilent make PNA E8362B, Bayan Lepas, Malaysia). The dielectric constant and the unloaded quality factor of the samples were measured by Hakki and Coleman post resonator and resonant cavity methods respectively [44, 45]. The temperature coefficient of resonant frequency (τ_f) was also measured by noting the variation of TE₀₁₈ mode frequency with temperature in the range of 30-100°C.

3.3 Results and discussion

3.3.1 TGA/DSC studies

Thermogravimetric (TGA) and differential scanning calorimetric (DSC) studies of AO-V₂O₅ (A= Ba, Sr, Ca, Mg and Zn) compositions were carried out using stoichiometrically mixed oxides and carbonates of the raw materials inside platinum crucibles. The analyses were done at a heating rate of 5°C/min in nitrogen atmosphere to confirm the phase formation of AV_2O_6 ceramics and the results are given in Figures 3.5 and 3.6. TGA results show that the phase formation of AV_2O_6 ceramics was completed below 700°C. During the phase formation, total weight losses due to the evaporation of CO₂ are 12.2%, 14.2% and 16.4% for BaV₂O₆, SrV₂O₆ and CaV₂O₆ respectively, which are almost comparable with the theoretical weight losses. TGA of ZnO-V₂O₅ and CaO-V₂O₅ compositions exhibit weak endotherms below 200°C, which may be due to the decomposition of water molecules.

The TGA of MgO-V₂O₅ shows distinct endotherms below 400°C compared to other metavanadates. It is reported by our group that MgO is hydrophilic in nature and hence adsorbs water and form Mg(OH)₂ phase, which decomposes on heating at 361.88°C as shown in Figure 3.7 [46]. A total weight loss of about 3.4% is obtained at 600°C, which clearly indicates the release of hydroxyl groups adsorbed by MgO. Therefore, the endotherms observed below 400°C in TGA of MgO-V₂O₅ could be due to the decomposition of adsorbed hydroxyl groups.

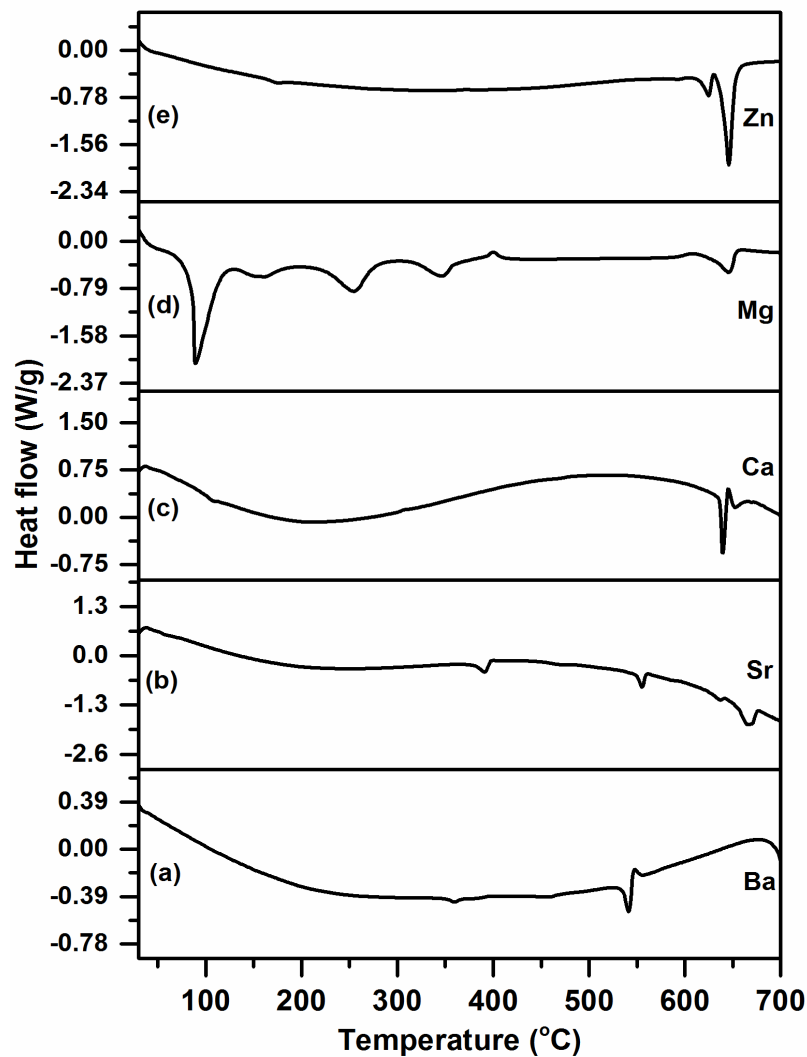


Figure 3.5 TGA results of AO-V₂O₅ (A= Ba, Sr, Ca, Mg and Zn) compositions

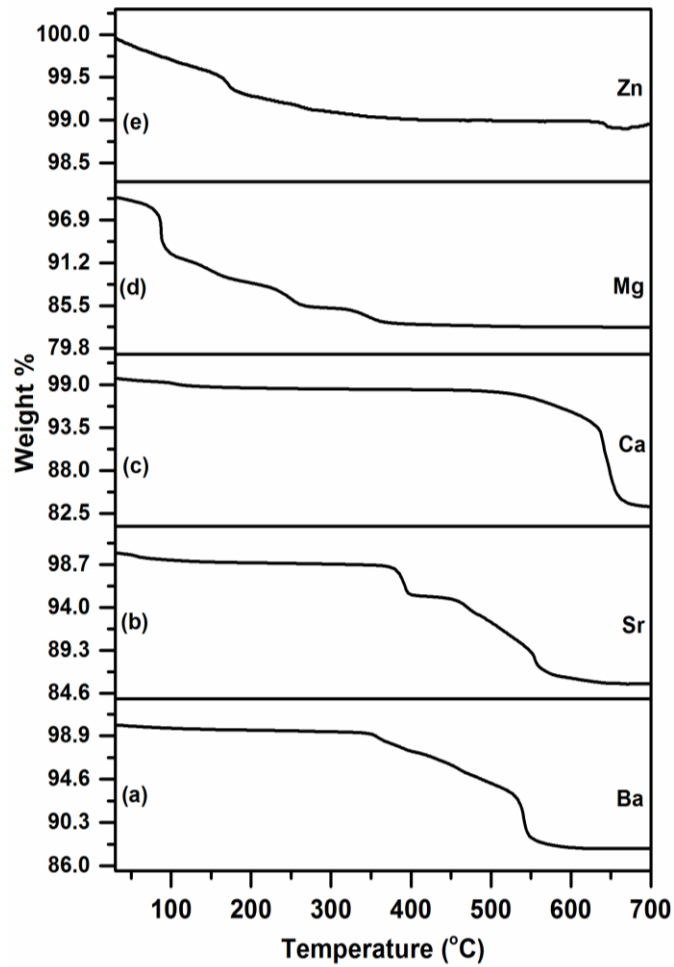


Figure 3.6 DSC results of AO-V₂O₅ (A= Ba, Sr, Ca, Mg and Zn) compositions

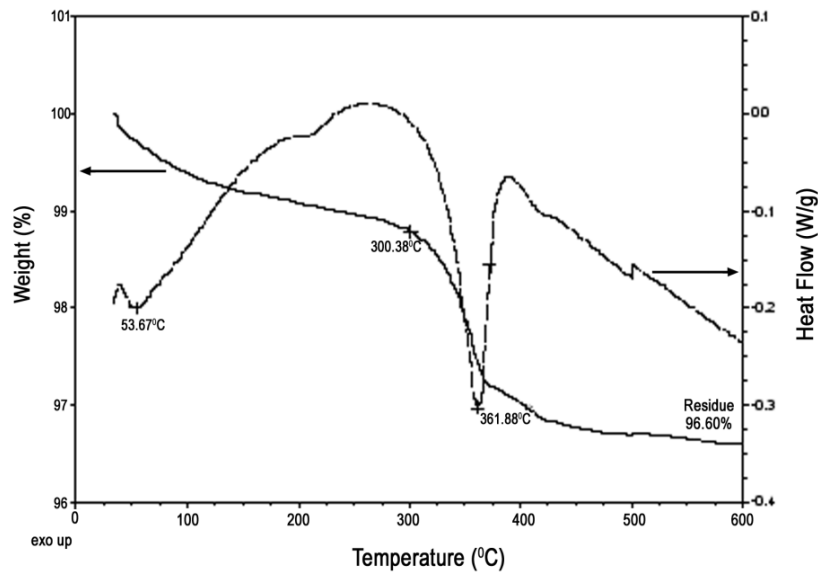


Figure 3.7 TGA/DSC results of the as-received MgO powder

3.3.2 X-ray diffraction studies

Figure 3.8 shows the X-ray diffraction patterns of AV_2O_6 samples with $A = Ba, Sr, Ca, Mg$ and Zn . As per the available ICDD patterns, both BaV_2O_6 (ICDD card No: 86-0240) and SrV_2O_6 (ICDD Card No: 27-1444) exhibit orthorhombic crystal structure. The XRD patterns of BaV_2O_6 and SrV_2O_6 obtained in the present study exactly match with the available ICDD patterns and indexed based on the same.

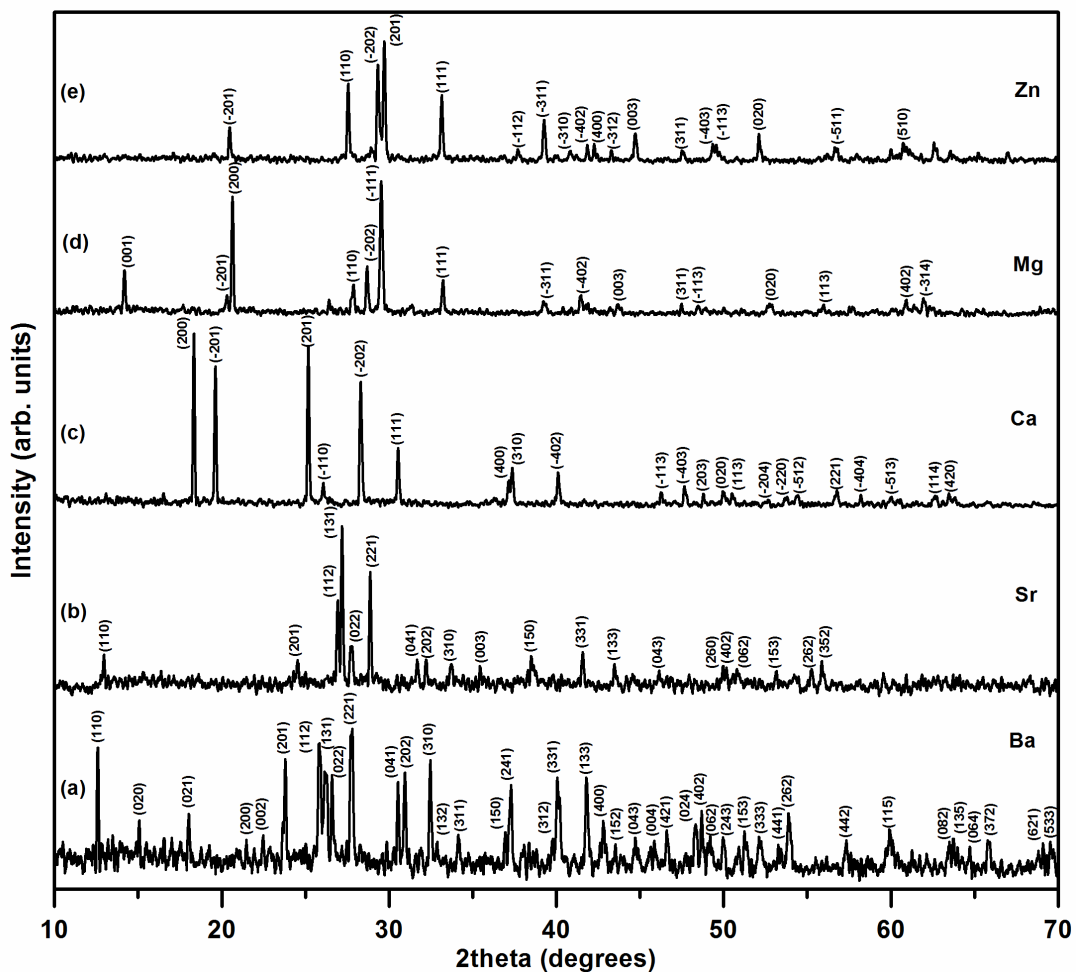


Figure 3.8 X-ray diffraction patterns of AV_2O_6 ($A = Ba, Sr, Ca, Mg$ and Zn) ceramics

On the other hand, AV_2O_6 compounds with $A = Ca, Mg$ and Zn (ICDD Card No: 23-0137, 45-1050 and 23-0757) belong to monoclinic crystal structure with $C2/m$ space group and show a decreasing trend for lattice parameters a, b and c while the A^{2+} ionic radii decreases from 1 to 0.72 Å. Rietveld refinement studies by Yu et al. also confirm the monoclinic structure for CaV_2O_6 [41]. The orthorhombic to monoclinic structural

transition can be due to the change in ionic radii of A type cations. The XRD patterns of AV_2O_6 samples with A= Ca, Mg and Zn obtained in the present study are compared with the available ICDD patterns and indexed accordingly. The calculated lattice parameters of the AV_2O_6 compounds in the present study are in good agreement with already reported data and are provided in Table 3.2.

Table 3.2 Comparison of lattice parameters of AV_2O_6 (A= Ba, Sr, Ca, Mg and Zn) ceramics

A^{2+} ion	Calculated lattice parameters (Å)			Reported lattice parameters (Å)			ICDD Card No.
	a	b	c	a	b	c	
Ba	8.532	12.583	7.554	8.482	12.611	7.961	86-0240
Sr	8.23	12.271	7.648	8.245	12.293	7.657	27-1444
Ca	9.986	3.65	6.637	10.06	3.673	7.038	23-0137
Mg	9.261	3.651	6.721	9.284	3.491	6.721	45-1050
Zn	9.238	3.526	6.563	9.242	3.526	6.574	23-0757

3.3.3 Raman spectroscopic studies

In order to study the crystal structure of AV_2O_6 ceramics in the molecular level, Raman spectroscopic studies have been carried out. Figure 3.9 shows the Raman spectra of AV_2O_6 ceramics and the corresponding band assignments are given in Tables 3.3 and 3.4. As per structural studies, VO_4 tetrahedra are present in the unit cell of barium and strontium metavanadates, VO_5 trigonal bipyramid for calcium metavanadate and distorted VO_6 octahedra for Mg and Zn metavanadates [36, 39, 40-43].

Six Raman bands are observed in the region $966-875\text{ cm}^{-1}$ for BaV_2O_6 whereas only three bands are observed for SrV_2O_6 and they can be assigned as the symmetric stretching vibrations of VO_4 tetrahedra. The higher number of bands observed in the symmetric stretching region of BaV_2O_6 can be attributed to the distortion of the VO_4 tetrahedra as reported in the crystal structural data, where the V-O distance vary between 1.636 and 1.784 Å in the case of V(1) VO_4 tetrahedron and between 1.653 and 1.812 Å in the case of V(2) VO_4 tetrahedron. The asymmetric

stretching vibrations of VO_4 tetrahedra result a weak band at 820 cm^{-1} for BaV_2O_6 which is observed at a lower wavenumber of 806 cm^{-1} for SrV_2O_6 . The symmetric bending vibrations are observed at 403 and 469 cm^{-1} for BaV_2O_6 and 399 and 475 cm^{-1} for SrV_2O_6 whereas the asymmetric bending vibrations are observed at 524 cm^{-1} for BaV_2O_6 and 528 cm^{-1} for SrV_2O_6 respectively. The more number of vibrational modes in the symmetric stretching region of BaV_2O_6 reveal that the distortion of VO_4 tetrahedra is more in BaV_2O_6 compared to SrV_2O_6 .

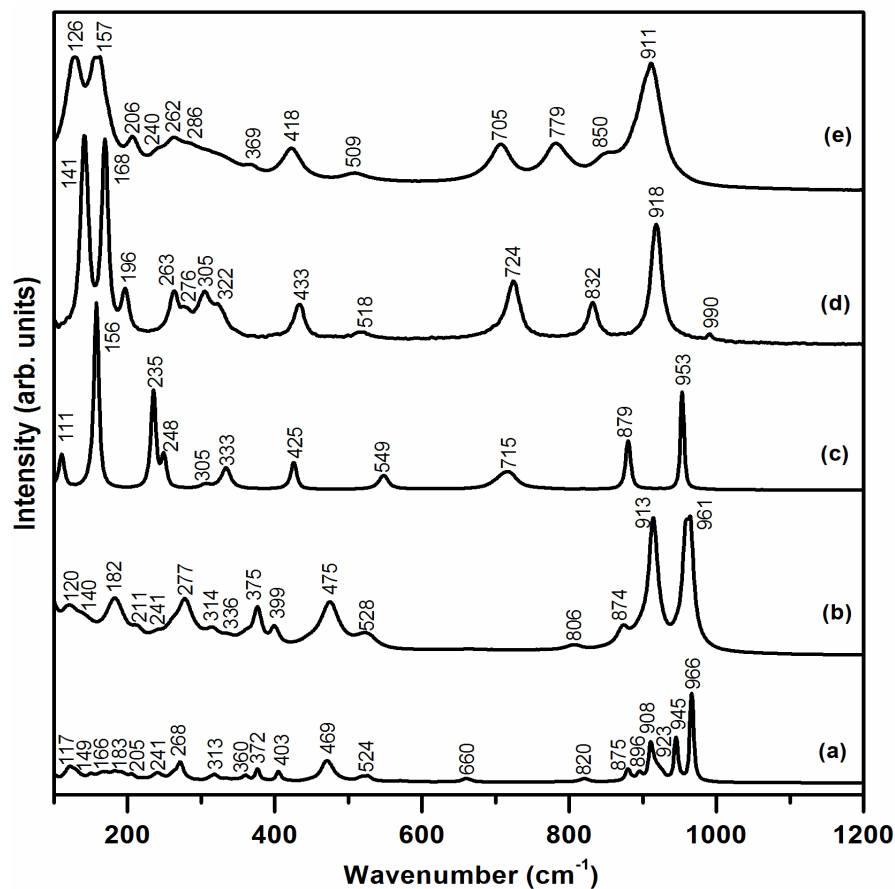


Figure 3.9 Raman spectra of AV_2O_6 ceramics with (a) Ba (b) Sr (c) Ca (d) Mg and (e) Zn

Table 3.3 Raman mode assignments for BaV₂O₆ and SrV₂O₆ ceramics

BaV ₂ O ₆	SrV ₂ O ₆	Assignments
966	961	ν_s VO ₄
945		
923		
908	913	
896		
875	874	
820	806	ν_{as} VO ₄
660		
524	528	δ_{as} VO ₄
469	475	δ_s VO ₄
403	399	
372	375	Lattice mode Vibrations
360	336	
313	314	
268	277	
241	241	
205	211	
183	182	
166		
149	140	
117	120	

ν_s – symmetric stretching, ν_{as} – asymmetric stretching, δ_{as} – asymmetric bending, δ_s – symmetric bending

CaV₂O₆ contains linked VO₅ trigonal bipyramids as the basic building blocks where each vanadium atom is surrounded by five O atoms, with double chains which are in turn linked by Ca²⁺ ions [41]. Hence, the Raman modes of CaV₂O₆ can be attributed to the vibrations of VO₅ polyhedra. The modes observed at 953 cm⁻¹ originate from the symmetric stretching vibrations of V-O bonds whereas the modes at 879 and 715 cm⁻¹ can be attributed to the asymmetric stretching vibrations. The symmetric bending vibrations of CaV₂O₆ are observed at 425 cm⁻¹ and the asymmetric bending mode at 549 cm⁻¹. The Raman bands appeared below 400 cm⁻¹ originates from lattice mode vibrations.

According to Busca et al., the crystal structure of MgV₂O₆ consists of both Mg²⁺ and V⁵⁺ ions in the octahedral coordination and three different types of oxygen atoms, each tri-coordinated to vanadium atom [47]. The three different types of oxygen

atoms include O(I) bonded to one V with short V-O bond (1.666 Å), O(II) bridges two atoms asymmetrically with one short V-O bond (1.671 Å) and one long V-O bond (2.671 Å) and O(III) triply bridges V atoms with intermediate V-O bond length. Hence, the zigzag chains of VO₆ octahedra along the [010] direction separates from each other. This results penta-coordinated V ions with two short terminal V-O bonds and three longer V-OV₂ bonds with O(III) atoms in the plane parallel to the [010] direction. Hence, the molecular vibrations of MgV₂O₆ can be associated with the VO₂ units with short V-O bonds and the motions of the O(III) atoms in the (V₂O₂)_n layers [47]. Raman spectrum of ZnV₂O₆ was already reported by Tang et al. [39]. These authors also assigned the stretching modes of ZnV₂O₆ with that of (V₂O₂)_n (generated by the edge-sharing between pairs of VO₆ octahedra) and V₃O (originating from the sharing of VO₆ octahedra between neighboring double chains).

Table 3.4 Raman mode assignments for CaV₂O₆, MgV₂O₆ and ZnV₂O₆ ceramics

CaV ₂ O ₆	Assignments	MgV ₂ O ₆	ZnV ₂ O ₆	Assignments
953	ν_s (V-O)	918 858	911 850	ν_s (VO ₂)
879 715	ν_{as} (V-O)	832		ν_{as} (VO ₂)
549	δ_{as} (V-O)	724 518	779 705 509	ν_s (V ₂ O ₂) _n + ν_s V ₃ O
425	δ_s (V-O)	433	418	δ (VO ₂)
333 305 248 235 156 111	Lattice mode vibrations	322 305 276 263 196 168 141	369 286 262 240 206 157 126	Lattice mode vibrations

ν_s – symmetric stretching, ν_{as} – asymmetric stretching, δ_{as} – asymmetric bending, δ_s – symmetric bending

Raman bands observed above 800 cm⁻¹ for metavanadates with A= Mg and Zn, are assigned to the stretching vibrations of the VO₂ units as reported by Busca et al. and

Tang et al. [47, 39]. The strong Raman bands observed at 918 and 858 cm^{-1} for MgV_2O_6 , vibrational modes at 911 and 850 cm^{-1} for ZnV_2O_6 are correspond to the symmetric stretching vibrations of V-O bonds of VO_2 units, while asymmetric stretching vibrations of VO_2 units are observed at 832 cm^{-1} for MgV_2O_6 , which is absent in ZnV_2O_6 . The vibrational modes observed at 724 and 518 cm^{-1} for MgV_2O_6 and 779, 705 and 509 cm^{-1} for ZnV_2O_6 are assigned to the stretching vibrations of the V_2O_2 network. Modes at 433 cm^{-1} for MgV_2O_6 and 418 cm^{-1} for ZnV_2O_6 can be assigned to the in-plane deformation modes of VO_2 units. An unambiguous assignment of Raman bands below 400 cm^{-1} is not possible due to lattice mode vibrations. The Raman spectra of MgV_2O_6 show an additional mode observed at 990 cm^{-1} , which is corresponding to the strong symmetric stretching vibration of V_2O_5 [48].

3.3.4 Morphological and dielectric studies

Figure 3.10 shows the SEM images of AV_2O_6 with A= Ba, Sr, Ca and Zn ceramics sintered at optimum temperatures. The SEM image of MgV_2O_6 could not record since the sample crumbles during sintering. Both BaV_2O_6 and CaV_2O_6 exhibit well defined dense microstructures whereas SrV_2O_6 has shown melted appearance. BaV_2O_6 shows polygonal grains with average grain size of 1-2 μm and CaV_2O_6 shows columnar grains with 12-20 μm size. On the other hand, ZnV_2O_6 exhibits polygonal grains together with needle like morphologies.

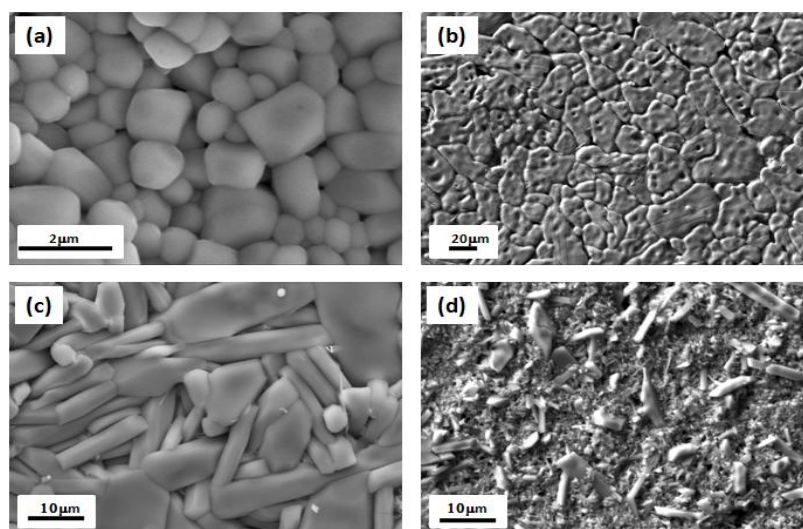


Figure 3.10 SEM pictures of AV_2O_6 ceramics with (a) Ba (b) Sr (c) Ca and (d) Zn sintered at optimum temperatures for 1h

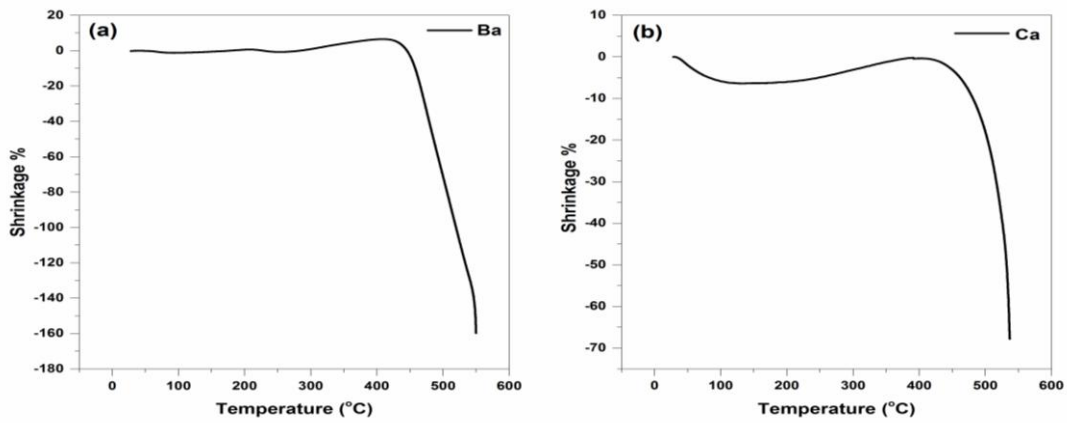


Figure 3.11 Shrinkage behavior of (a) BaV₂O₆ and (b) CaV₂O₆ ceramics

Figure 3.11 shows the shrinkage behavior of BaV₂O₆ and CaV₂O₆ ceramics. The shrinkage curves indicate that both BaV₂O₆ and CaV₂O₆ ceramics exhibit an onset of sintering <500°C.

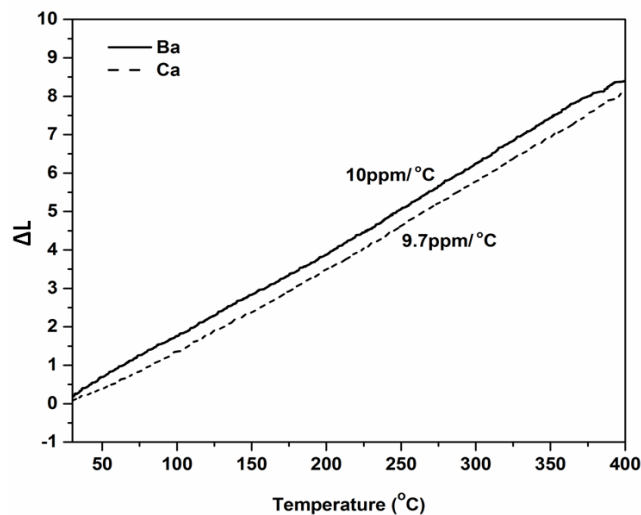


Figure 3.12 CTE curves of BaV₂O₆ and CaV₂O₆ ceramics

Figure 3.12 shows the coefficient of linear thermal expansion (CTE) curves of sintered BaV₂O₆ and CaV₂O₆ ceramics in the 30-400°C temperature range. The CTE results of both barium and calcium metavanadate ceramics show a linear variation with increase in temperature and the corresponding coefficient of thermal expansion (α_L) obtained is approximately 10 ppm/°C for barium and 9.7 ppm/°C for calcium respectively, which is comparable with that of commercial LTCC materials.

The AV_2O_6 (A= Ba, Sr, Ca, Mg and Zn) ceramics are sintered in the 500-700°C temperature range to get the optimum density. Table 3.5 shows the optimum sintering temperature, density and dielectric properties of AV_2O_6 ceramics. AV_2O_6 ceramics with A= Ba, Sr, Ca and Zn are well sintered below 700°C whereas MgV_2O_6 did not sinter well and obtained only an experimental density of 2.76 g/cc at 560°C. Beyond this temperature, MgV_2O_6 ceramic crumbles during sintering. Among AV_2O_6 ceramics, only BaV_2O_6 and CaV_2O_6 exhibit microwave dielectric properties while all others did not show resonance in the microwave frequency region due to relatively high loss tangent. Even though BaV_2O_6 and SrV_2O_6 belong to orthorhombic crystal structure, interestingly SrV_2O_6 did not show any resonance in the microwave frequency region.

The variation of density and dielectric constant of BaV_2O_6 and CaV_2O_6 ceramics as a function of sintering temperature is shown in Figures 3.13 and 3.14. The BaV_2O_6 samples sintered at an optimum temperature of 550°C for 1h exhibits a maximum experimental density of 3.68 g/cc, with dielectric constant of 11.2 and Q_{xf} of 42,790 GHz. Whereas CaV_2O_6 ceramic was well sintered at an optimum sintering temperature of 680°C for 1h exhibiting a maximum experimental density of 2.58 g/cc with dielectric constant of 8.7 and Q_{xf} of 60,310 GHz. Further increase in temperature deteriorates both density and dielectric constant of BaV_2O_6 and CaV_2O_6 ceramics. Interestingly, CaV_2O_6 ceramic exhibits relatively high quality factor value of 73,120 GHz at 660°C as a result of better structural ordering. Since metavanadates with A= Sr, Mg and Zn did not show resonance in the microwave frequency region, dielectric properties of these ceramics are measured at 1 MHz. The optimum sintering temperature, density, dielectric constant and loss tangent of AV_2O_6 samples at 1 MHz and GHz range are compiled in Table 3.5.

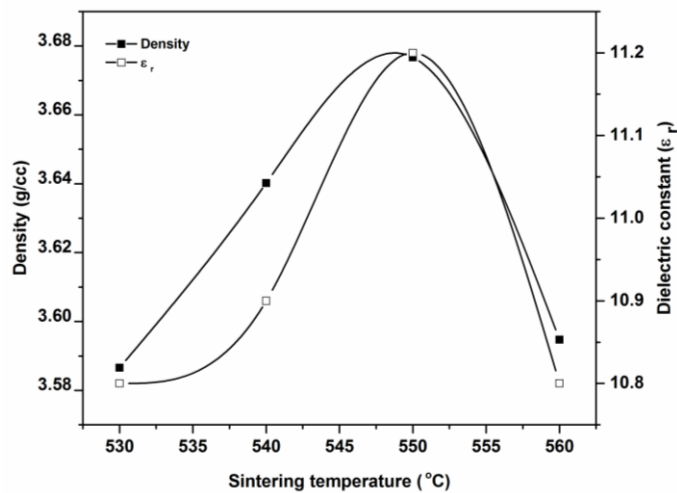


Figure 3.13 Variation of density and dielectric constant of BaV_2O_6 ceramic as a function of sintering temperature at GHz

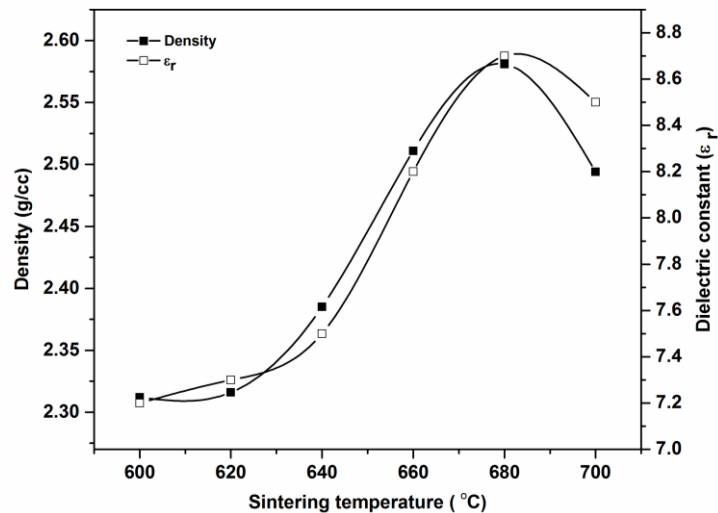


Figure 3.14 Variation of density and dielectric constant of CaV_2O_6 ceramic as a function of sintering temperature at GHz

Temperature variation of resonant frequency (τ_f) of BaV_2O_6 and CaV_2O_6 ceramics sintered at optimum sintering temperatures of 550°C and 680°C for 1h is calculated in the $30\text{-}100^\circ\text{C}$ region. Both BaV_2O_6 and CaV_2O_6 ceramics exhibited low τ_f of $28.2\text{ ppm}/^\circ\text{C}$ and $-50.7\text{ ppm}/^\circ\text{C}$ respectively (Figure 3.15).

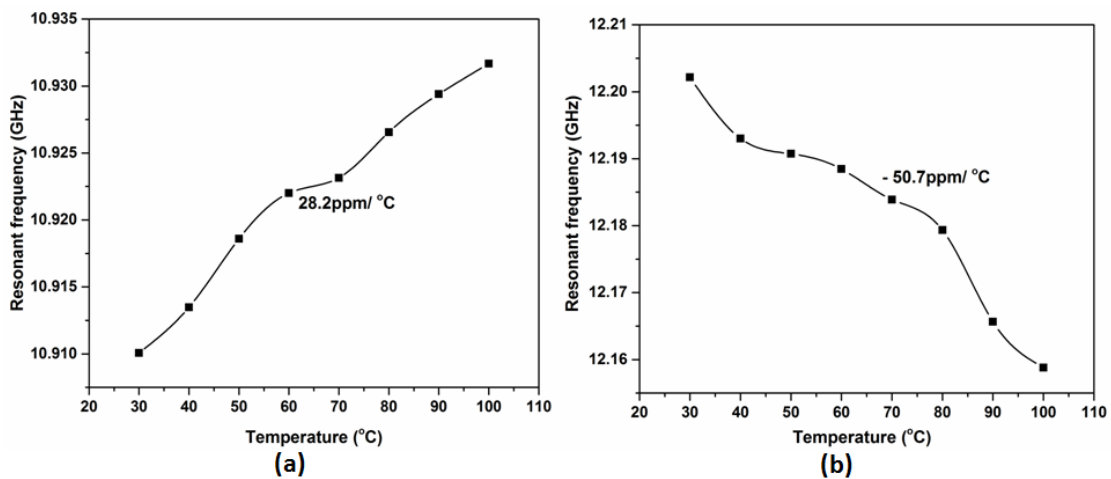


Figure 3.15 Variation of resonant frequency of (a) BaV₂O₆ and (b) CaV₂O₆ ceramics as a function of temperature at GHz

Table 3.5 Sintering temperature, density and dielectric properties of AV₂O₆ (A= Ba, Sr, Ca, Mg and Zn) ceramics

Compound	Sint. Temp. (°C/1h)	Density (g/cc)	Low frequency data (1MHz)		Microwave frequency data (GHz)			ϵ_{theo}
			ϵ_r	$\tan\delta$	ϵ_r	Qxf (GHz)	τ_f (ppm/°C)	
BaV ₂ O ₆	550	3.68	13.3	0.008	11.2	42,790	28.2	10.07
SrV ₂ O ₆	560	2.96	12.8	0.012	*	*	*	8.71
CaV ₂ O ₆	680	2.58	10.5	0.004	8.7	60,310	-50.7	7.16
MgV ₂ O ₆	560	2.76	#	#	*	*	*	10.62
ZnV ₂ O ₆	530	3.35	28.8	0.274	*	*	*	16.55

Measurement not possible, * No resonance

3.3.5 Compatibility studies

To evaluate the chemical compatibility of BaV₂O₆ and CaV₂O₆ ceramics with metal electrodes, BaV₂O₆ is co-fired with 20 wt% Al at 550°C for 1h and CaV₂O₆ is co-fired with 20 wt% Al at 660°C for 1h and the resultant samples are analyzed using X-ray diffraction and EDS analyses. The X-ray diffraction patterns of BaV₂O₆ and CaV₂O₆ ceramics co-fired with 20 wt% Al are given in Figures 3.16 and 3.17. The X-ray diffraction patterns do not show any secondary phase formation and the aluminium peaks are observed separately which are marked with ‘*’.

The planar SEM images of the BaV₂O₆ and CaV₂O₆ ceramics co-fired with Al at 550°C and 660°C are given in Figures 3.18 - 3.23. The SEM results also rule out

the possibility of chemical interaction/inter-diffusion between the metavanadates and Al. The EDS analysis is also performed on BaV_2O_6 , CaV_2O_6 and Al grains (Spot 1 and Spot 2). Spot1 in Figures 3.18 and 3.20 shows only the presence of Al whereas metavanadate ceramic without any inter-diffusion of Al is detected in Spot 2, which further confirms the chemical compatibility between metavanadates and Al electrode. The X-ray dot mapping of the co-fired BaV_2O_6 and CaV_2O_6 samples is also done to establish the non-reactivity of Al in the host matrix (Figures 3.19 and 3.21). The X-ray dot mapping result clearly shows the isolation of melted Al particles in deep red colour without any inter-diffusion complementing the XRD and spot analyses results. Further, the EDS line scan of the co-fired samples is also carried out to quantify the XRD and EDS results (Figures 3.22 and 3.23). From the EDS line scan analysis and element profile plot, it is clear that the Al profile decreases sharply at the interface, clearly indicating that Al does not diffuse into the ceramic during sintering. In view of the above results, it can be inferred that the BaV_2O_6 and CaV_2O_6 ceramics have excellent chemical compatibility with Al electrode together with relatively good microwave dielectric properties and hence can be used as candidate materials for ULTCC applications.

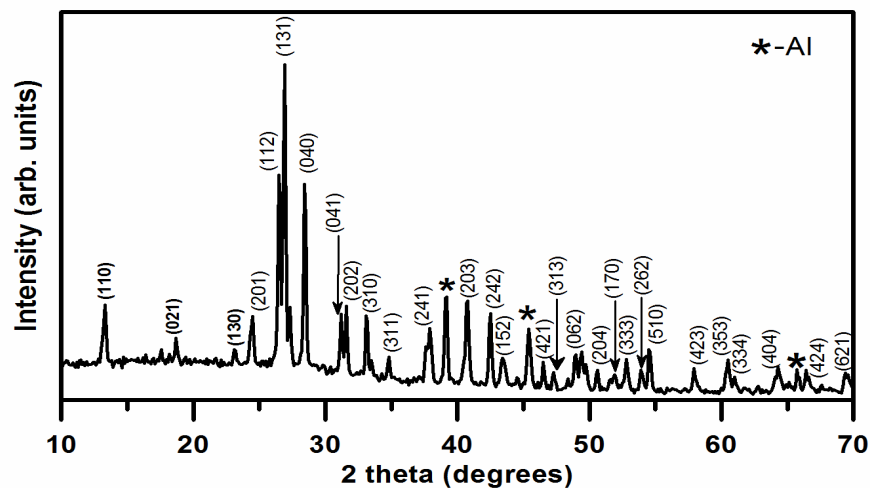


Figure 3.16 X-ray diffraction pattern of BaV_2O_6 ceramic co-fired with 20 wt% Al powder sintered at 550°C for 1h

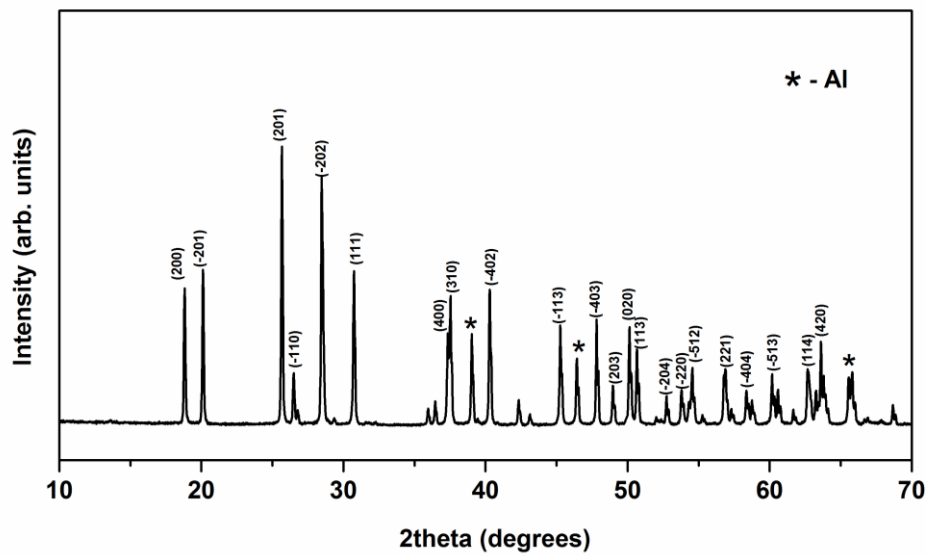


Figure 3.17 X-ray diffraction pattern of CaV_2O_6 ceramic co-fired with 20 wt% Al powder sintered at 660°C for 1h

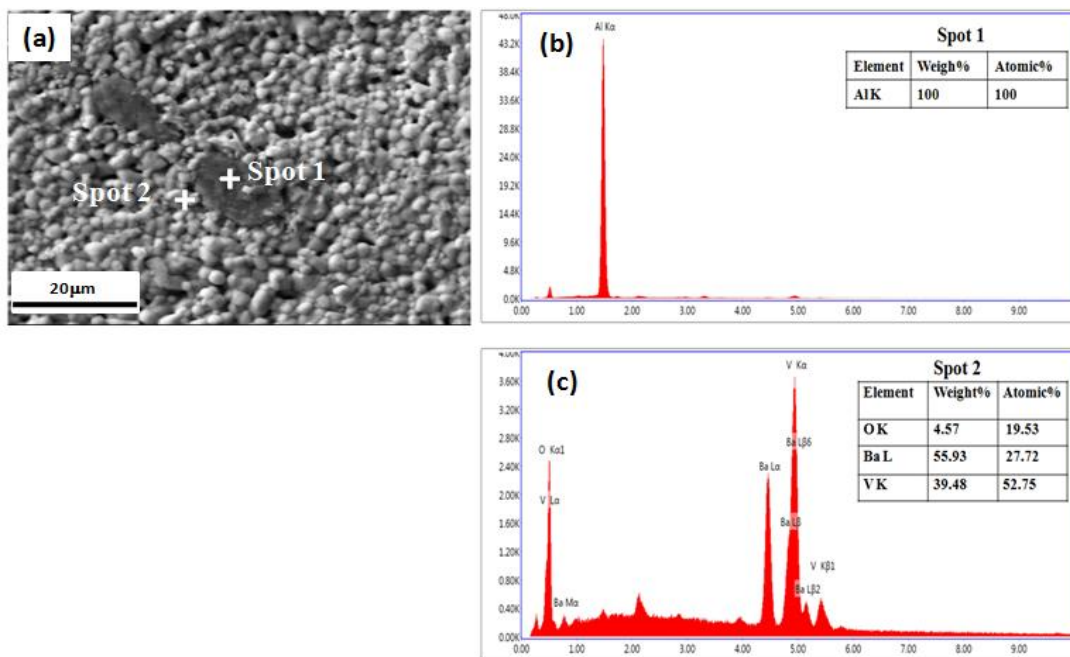


Figure 3.18 (a) SEM image of BaV_2O_6 ceramic co-fired with 20 wt% Al powder sintered at 550°C for 1h (b) EDS spectrum of Spot 1 (c) EDS spectrum of Spot 2

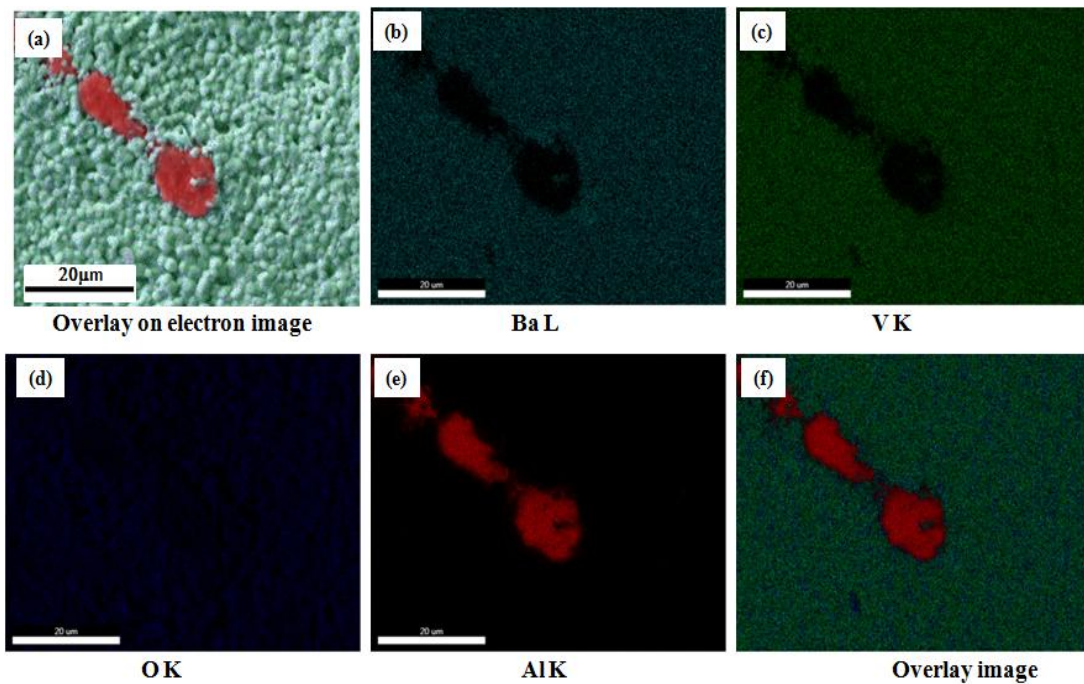


Figure 3.19 X-ray dot mapping image of BaV_2O_6 ceramic co-fired with 20 wt% Al powder sintered at 550°C for 1h [(a) Overlay on secondary electron image (b-e) elemental images (f) Overlay image]

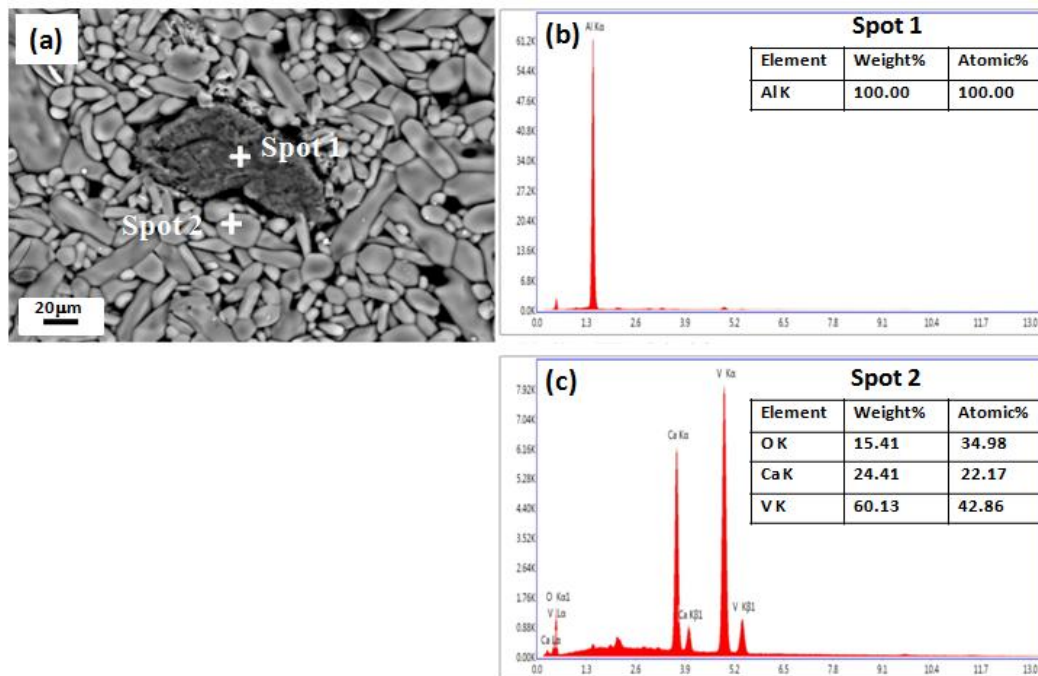


Figure 3.20 (a) Backscattered SEM image of CaV_2O_6 ceramic co-fired with 20 wt% Al sintered at 660°C for 1h (b) EDS spectrum of Spot 1 (c) EDS spectrum of Spot 2

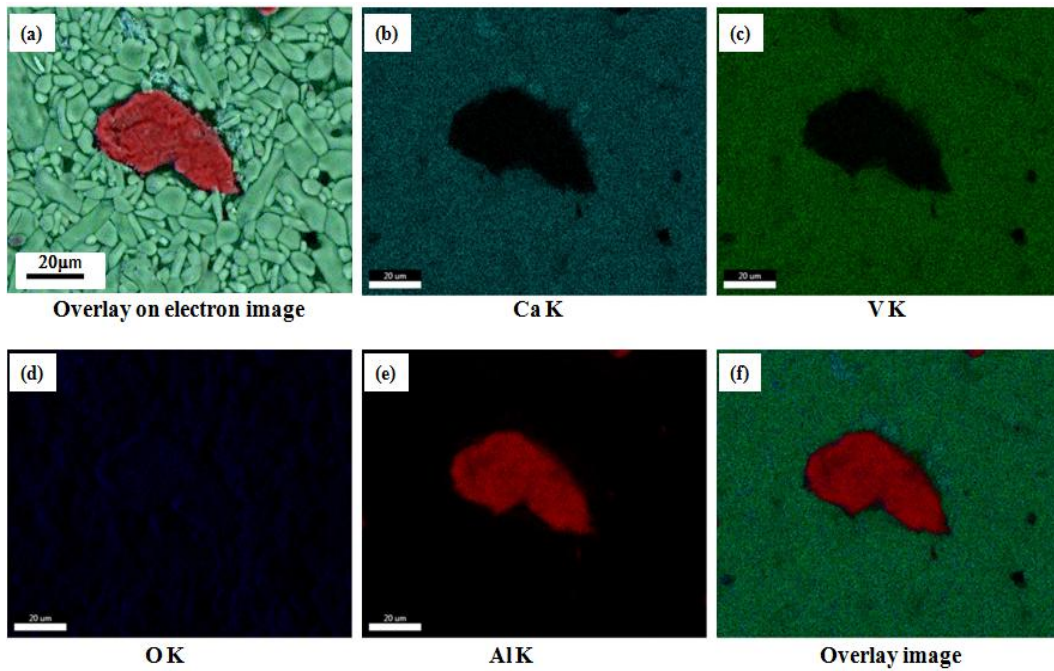


Figure 3.21 X-ray dot mapping image of CaV_2O_6 ceramic co-fired with 20 wt% Al sintered at 660°C for 1h [(a) Overlay on secondary electron image (b-e) elemental images (f) Overlay image]

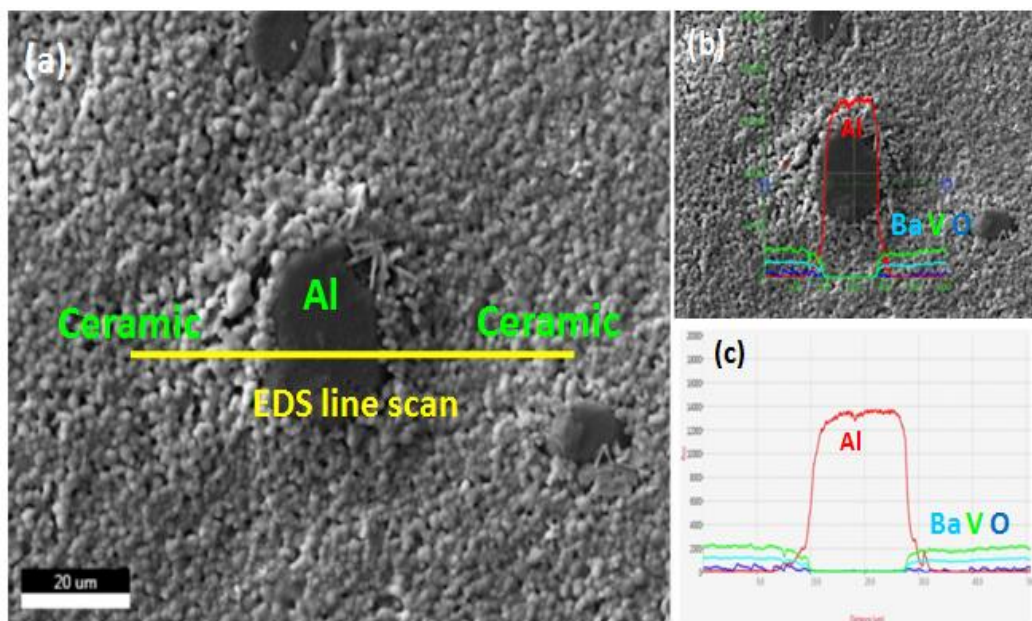


Figure 3.22 EDS line scan image of BaV_2O_6 ceramic co-fired with 20 wt% Al

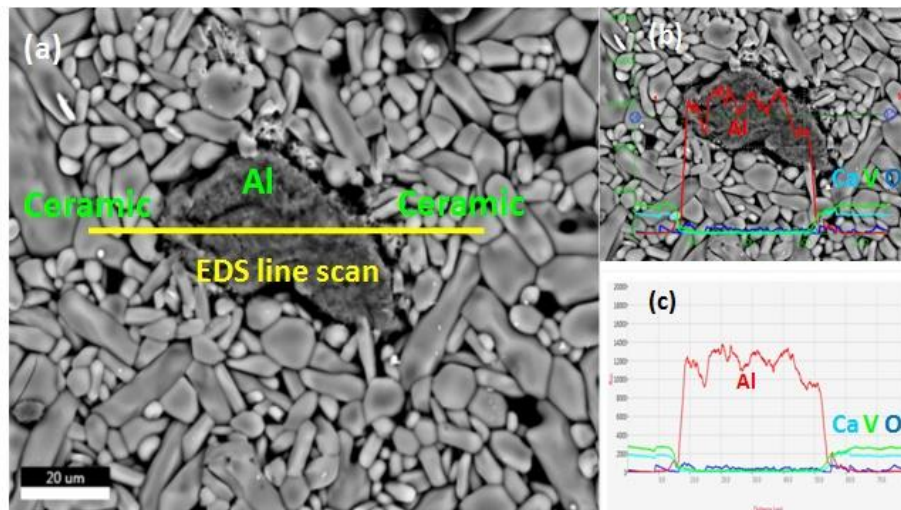


Figure 3.23 EDS line scan image of CaV_2O_6 ceramic co-fired with 20 wt% Al

3.4 Conclusions

AV_2O_6 (A= Ba, Sr, Ca, Mg, and Zn) ceramics are prepared through conventional solid state ceramic method. Thermogravimetric and differential scanning calorimetric analyses confirm the phase formation of AV_2O_6 compositions. The phase purity of the samples was confirmed using powder X-ray diffraction studies. Laser Raman studies confirm the existence of VO_4 tetrahedral units in BaV_2O_6 and SrV_2O_6 ceramics whereas VO_2 vibrational units exist in AV_2O_6 with A= Mg and Zn ceramics. The presence of VO_5 vibrational units is evident in the Raman spectrum of CaV_2O_6 . SEM images of sintered AV_2O_6 ceramic show pore-free microstructures for barium and calcium metavanadates. The shrinkage behavior studies show that both BaV_2O_6 and CaV_2O_6 ceramics can be well sintered at relatively low temperatures. BaV_2O_6 and CaV_2O_6 ceramics exhibit a low coefficient of thermal expansion of 10 and 9.7 ppm/ $^\circ\text{C}$ respectively at par with commercial LTCC materials. Although all AV_2O_6 ceramics sintered in the low temperature range, only BaV_2O_6 and CaV_2O_6 exhibit microwave dielectric properties. At optimum sintering temperature of 550°C for 1h, BaV_2O_6 ceramic exhibits a maximum experimental density of 3.68 g/cc, dielectric constant of 11.2, Qxf of 42,790 GHz and τ_f of 28.2 ppm/ $^\circ\text{C}$. Besides BaV_2O_6 , CaV_2O_6 phase was also well sintered at an optimum sintering temperature of 680°C for 1h and exhibits a maximum experimental density of 2.58 g/cc with dielectric constant of 8.7, Qxf of

60,310 GHz and τ_f of -50.7 ppm/°C. Interestingly, CaV₂O₆ ceramic exhibits relatively high quality factor value of 73,120 GHz at 660°C as a result of better structural ordering. XRD and EDS analyses show excellent chemical compatibility with Al metal electrode for both BaV₂O₆ and CaV₂O₆ ceramics. Based on the above studies it can be concluded that barium and calcium metavanadates are ideal candidate materials for ULTCC applications.

References

- [1] S. George, M. T. Sebastian, S. Raman, P. Mohanan, *Int. J. Appl. Ceram. Tech.*, 8[1] (2011) 172-179.
- [2] J. Takada, S. F. Wang, S. Yoshikawa, S. J. Jang, R. E. Newnham, *J. Am. Ceram. Soc.*, 77[9] (1994) 2485-2488.
- [3] Y. Fang, A. Hu, Y. Gu, Y. J. Oh, *J. Eur. Ceram. Soc.*, 23 [14] (2003) 2497-2502.
- [4] H. M. O'Bryan, J. Thomson, D. Linn, J. K. Plourde, *J. Am. Ceram. Soc.*, 57 [10] (1974) 450-453.
- [5] L. Fang, F. Xiang, H. Zhang, *Ceram. Int.*, 39 [8] (2013) 9779-9783.
- [6] C. L. Huang, K. H. Chiang, S. C. Chuang, *Mater. Res. Bull.*, 39 [4-5] (2004) 629-636.
- [7] D. W. Kim, J. R. Kim, S. H. Yoon, K. S. Hong, *J. Am. Ceram. Soc.*, 85[11] (2002) 2759-2762.
- [8] J. Y. Ha, J. W. Choi, S. J. Yoon, D. J. Choi, K. H. Yoon, H. J. Kim, *J. Eur. Ceram. Soc.*, 23 [14] (2003) 2413-2416.
- [9] C. L. Huang, R. J. Lin, H. Wang, *Jpn. J. Appl. Phys.*, 41 [1] (2002) 758-762.
- [10] D. Zhou, H. Wang, X. Yao, L. X. Pang, *J. Am. Ceram. Soc.*, 91[10] (2008) 3419-3422.
- [11] A. Feteira, D. C. Sinclair, *J. Am. Ceram. Soc.*, 91[4] (2008) 1338-1341.
- [12] D. K. Kwon, M. T. Lanagan, T. R. Shrout, *Mater. Lett.*, 61 [8-9] (2007) 1827-1831.
- [13] L. Fang, D. J. Chu, H. F. Zhou, X. L. Chen, Z. Yang, *J. Alloys Comp.*, 509 [5] (2011) 1880-1884.
- [14] D. Zhou, L. X. Pang, H. D. Xie, J. Guo, B. He, Z. M. Qi, T. Shao, X. Yao, C. A. Randall, *Eur. J. Inorg. Chem.*, 2014 [2] (2014) 296-301.
- [15] D. Zhou, W. B. Li, J. Guo, L. X. Pang, Z. M. Qi, T. Shao, H. D. Xie, Z. Yue, X. Yao, *Inorg. Chem.*, 53 [11] (2014) 5712-5716.
- [16] D. Zhou, L. X. Pang, Z. M. Qi, *Inorg. Chem.*, 53 [17] (2014) 9222-9227.
- [17] D. Zhou, L. X. Pang, Z. M. Qi, B. B. Jin, X. Yao, *Sci. Rep.*, 4: 5980 (2014) 1-4.

- [18] G. G. Yao, P. Liu, H. W Zhang, J. Am. Ceram. Soc., 96 [6] (2013) 1691-1693.
- [19] R. Umemura, H. Ogawa, H. Ohsato, A. Kan, A. Yokoi, J. Eur. Ceram. Soc., 25 [12] (2005) 2865-2870.
- [20] L. Fang, C. Su, H. Zhou, Z. Wei, H. Zhang, J. Am. Ceram. Soc., 96 [3] (2013) 688-690.
- [21] E. K. Suresh, A. N. Unnimaya, A. Surjith, R. Ratheesh, Ceram. Int., 39 [4] (2013) 3635-3639.
- [22] M. Valant, D. Suvorov, J. Am. Ceram. Soc., 83 [11] (2000) 2721-2729.
- [23] M. Udovic, M. Valant, D. Suvorov, J. Am. Ceram. Soc., 87 [4] (2004) 591-597.
- [24] D. K. Kwon, M. T. Lanagan, T. R. Shrout, J. Am. Ceram. Soc., 88 [2] (2005) 3419-3422.
- [25] R. Kohemuller, J. Perrand, Bull. Soc. Chim. France, (1964) 642.
- [26] A. A. Fotieva, V. V. Makarov, V. L. Volkov, L. L. Surat, Russ. J. Inorg. Chem., 14 [1] (1969) 144-146.
- [27] J. J. Brown Jr, J. Am. Ceram. Soc., 55 [10] (1972) 500-503.
- [28] K. Mocala, J. Ziolkowski, J. Solid State Chem., 69 [2] (1987) 299-311.
- [29] M. Kurzawa, I. R. Himmel, M. Bosocka, A. B. Tabero, J. Them. Anal. Cal., 64 [3] (2001) 1113-1119.
- [30] Hyun- Seup Ra, Structure chemical examinations to AB₂O₆ oxides and and examinations on photocatalytic activity of selected compounds of this type (A = Ba, Ca, Co, Cu, Eu, Fe, Mg, Mn, Ni, Pb, Sn, Sr), PhD Thesis, University of Saarland (2009).
- [31] H. P. Beck, Z. Kristallogr., 227 [12] (2012) 843-858.
- [32] H. P. Beck, Z. Kristallogr., 228 [6] (2013) 271-288.
- [33] R. Ruh, A. D. Wadsley, Acta. Cryst., 21 (1966) 974-978.
- [34] J. Bouloux, G. Perez, J. Galy, Bull. Soc. Fr. Mineral. Crystallogr., 95 (1972) 130-133.
- [35] H. N. Ng, C. Calvo, Can. J. Chem., 50 [22] (1972) 3619-3624.
- [36] G. D. Andreotti¹, G. Calestani¹, A. Montenero, M. Bettinelli, Zeit. Kristallogr., 168 [1-4] (1984) 53-58.

- [37] S. Hansen, J. Nilsson, *Acta Chem. Scand.*, 50 [6] (1996) 512-515.
- [38] J. Angenault, A. Rimsky, *CR Acad. Sci. Paris, Ser. C*, 267 (1968) 227-230.
- [39] R. Tang, Y. Li, N. Li, D. Han, H. Li, Y. Zhao, C. Gao, P. Zhu, X. Wang, *J. Phys. Chem. C*, 118 [20] (2014) 10560-10566.
- [40] R. Tang, Y. Li, S. Xie, N. Li, J. Chen, C. Gao, P. Zhu, X. Wang, *Sci. Rep.*, 6:38566 (2016) 1-9.
- [41] R. Yu, N. Xue, S. Huo, J. Li, J. Wang, *RSC Adv.*, 5 [78] (2015) 63502-63515.
- [42] T. Yao, Y. Oka, N. Yamamoto, *Inorg. Chim. Acta.*, 238 [1-2] (1995) 165-168.
- [43] Y. Li, R. Tang, N. Li, H. Li, X. Zhao, P. Zhu, X. Wang, *J. Appl. Phys.*, 118 [3] (2015) 035902.
- [44] B. W. Hakki, P. D. Coleman, *IRE Trans. Mircrow. Theory Tech.*, 8 [4] (1960) 402-410.
- [45] J. Mazierska, M. V. Jacob, A. Harring, J. Krupka, P. Barnwell, T. Sims, *J. Eur. Ceram. Soc.*, 23 [14] (2003) 2611-2615.
- [46] K.P. Murali, S. Rajesh, Om Prakash, A.R. Kulkarni, R. Ratheesh, *Mater. Chem. Phys.*, 122 [2-3] (2010) 317-320.
- [47] G. Busca, G. Ricchiardi, D. Siew H. Sam, *J. C. Volta, PJ. Chem. Soc. Faraday Trans.*, 90 [8] (1994) 1161-1170.
- [48] C. Sanchez, J. Livage, G. Lucazeau, *J. Raman Spec.*, 12 [1] (1982) 68-72.

4

Effect of Vanadium Substitution on the Structure and Microwave Dielectric Properties of 5BaO-2Nb₂O₅ Binary Ceramic System

- 4.1 Introduction
- 4.2 Experimental techniques
- 4.3 Results and discussion
- 4.4 Conclusions

Some of the contents of this chapter have published in

A. N. Unnimaya, E. K. Suresh, J. Dhanya, R. Ratheesh, J Mater Sci: Mater Electron., 25 [2] (2014) 1127–1131

4.1 Introduction

Recently, microwave communication has witnessed unprecedented growth with wide range of applications such as satellite communications, mobile phones, global positioning systems etc. This wide spread usage of microwave communication systems demands a new family of low temperature co-fired ceramics (LTCC) to realize miniaturized microwave devices suitable for high frequency applications [1]. Basically, ceramic compositions having low dielectric constant (ϵ_r), relatively high quality factor (Q_{xf}) and nearly zero temperature coefficient of resonant frequency (τ_f) are preferred for microwave LTCC applications. In addition, LTCC technology necessitates the co-firing of both metal electrodes and dielectric materials without inter-diffusion. High temperature sinterable ceramics cannot be co-fired with Ag since the melting temperature of Ag electrode is 961°C [2]. Therefore, the sintering temperature of dielectrics should be lower than the melting temperature of metal electrode. In addition, there should be good chemical compatibility between the LTCC material and the metal electrode [1, 3].

Generally, most of the commercial microwave dielectric materials such as $Ba(Mg_{1/3}Ta_{2/3})O_3$, $Ba_5Nb_4O_{15}$, $(Zr,Sn)TiO_4$, $Ba_2Ti_9O_{20}$ etc. have good microwave dielectric properties, but they sinter only at elevated temperatures [4-7]. Addition of sintering aids are effective in bringing down the sintering temperature of microwave dielectric ceramics but these additives deteriorate the microwave dielectric properties due to the formation of secondary phases [8-11]. Although $Ba(Mg_{1/3}Ta_{2/3})O_3$ is an archetypical high Q material, the sintering temperature of this material is extremely high (>1600°C) and their intrinsic quality factor is governed by the order-disorder effect and microstructural properties [12]. In this context, cation-deficient hexagonal perovskite, $Ba_5Nb_4O_{15}$ is an attractive microwave ceramic material suitable for tailor making LTCC composition by proper substitution owing to their excellent microwave dielectric properties, good sintering characteristics and ease of phase formation [13].

$Ba_5Nb_4O_{15}$ ceramic in the $A_5B_4O_{15}$ family crystallizes in the trigonal space group and it is one of the classic high Q ceramic materials, ideally suited for microwave communication applications. The structure and microwave dielectric

properties of $\text{Ba}_5\text{Nb}_4\text{O}_{15}$ were studied by many researchers and it is reported that $\text{Ba}_5\text{Nb}_4\text{O}_{15}$ can be sintered in the temperature range 1400-1450°C and exhibits a dielectric constant of 39, Qxf value of 23,700 GHz and τ_f of ~78 ppm/°C [14, 15]. The microwave dielectric properties of $\text{Ba}_5\text{Nb}_4\text{O}_{15}$ ceramic were accurately determined using Whispering Gallery Mode (WGM) by Ratheesh et al. [16]. $\text{Ba}_5\text{Nb}_4\text{O}_{15}$ powders synthesized by molten salt method with NaCl-KCl flux in the 1:1 ratio sintered at 1300°C for 2h exhibit good microwave dielectric properties with $\epsilon_r=39.2$, Qxf ~ 27,200 GHz and $\tau_f \sim 72$ ppm/°C [17].

Relatively high sintering temperature of ~1400°C is needed to get dense $\text{Ba}_5\text{Nb}_4\text{O}_{15}$ ceramics by conventional solid state ceramic route [15], although it was reported that 3wt% B_2O_3 addition to $\text{Ba}_5\text{Nb}_4\text{O}_{15}$ reduces the sintering temperature to 925°C with microwave dielectric properties of $\epsilon_r \sim 39$, Qxf ~18,700 GHz and $\tau_f \sim 0$ ppm/°C [18]. Also, the addition of small amount of B_2O_3 in to $\text{Ba}_5\text{Nb}_4\text{O}_{15}$ - BaNb_2O_6 mixtures significantly lowers the sintering temperature to 900°C [19]. The low fired 0.84 $\text{Ba}_5\text{Nb}_4\text{O}_{15}$ - 0.16 BaNb_2O_6 mixture possesses $\epsilon_r \sim 42$, Qxf ~19,500 GHz and $\tau_f \sim 0$ ppm/°C at microwave frequencies and hence suitable for low temperature co-fired ceramic (LTCC) applications [20]. The effect of tantalum substitution for niobium in the structure and microwave dielectric properties of $\text{Ba}_5\text{Nb}_4\text{O}_{15}$ ceramic was also reported [15]. Even though tantalum has larger ionic polarizability, $\text{Ba}_5\text{Ta}_4\text{O}_{15}$ has lower dielectric constant ($\epsilon_r=28$) than $\text{Ba}_5\text{Nb}_4\text{O}_{15}$. This is because of the lattice anharmonicity of $\text{Ba}_5\text{Nb}_4\text{O}_{15}$, which results relatively larger dielectric constant for $\text{Ba}_5\text{Nb}_4\text{O}_{15}$ ceramic [14, 15]. Recent literature [21] revealed the phase relations and microwave dielectric properties of vanadium modified $\text{Ba}_5\text{Nb}_4\text{O}_{15}$. It was found that the addition of vanadium reduces the sintering temperature of $\text{Ba}_5\text{Nb}_4\text{O}_{15}$ from 1450°C to 1100°C and $\text{Ba}_5\text{Nb}_{4-x}\text{V}_x\text{O}_{15}$ ($x=0-1$) compositions exhibit $\text{Ba}_3\text{V}_2\text{O}_8$ as secondary phase and the intensity of the peaks corresponding to $\text{Ba}_3\text{V}_2\text{O}_8$ phase increases with increasing vanadium content [21]. Recent studies on the crystal structure of single crystal $\text{Ba}_2\text{Cd}_3\text{V}_4\text{O}_{15}$ by Mertens et al. prompted us to see whether $5\text{BaO}-2\text{V}_2\text{O}_5$ phase will exist in the $\text{BaO}-\text{V}_2\text{O}_5$ binary system [22]. These authors identified the co-existence of $(\text{VO}_4)^{3-}$ and $(\text{V}_2\text{O}_7)^{4-}$ groups (Figure 4.1) together with

BaO₉ and BaO₁₂ polyhedra in Ba₂Cd₃V₄O₁₅, having an orthorhombic crystal structure with $P2_12_12_1$ space group with four number of molecules per unit cell [22].

Even though conventional methods such as low-melting glass addition, chemical processing and additives were found effective in lowering the sintering temperature, but are relatively expensive, time consuming and often deteriorates the microwave dielectric properties [8-10, 17, 23]. However, substitution of low melting oxides in the parent composition can be considered as an effective method for the formation of low fired ceramics [10, 21]. In the present study, Nb⁵⁺ ions in Ba₅Nb₄O₁₅ is substituted by V⁵⁺ ions and its structural, microstructural and microwave dielectric properties are investigated in detail.

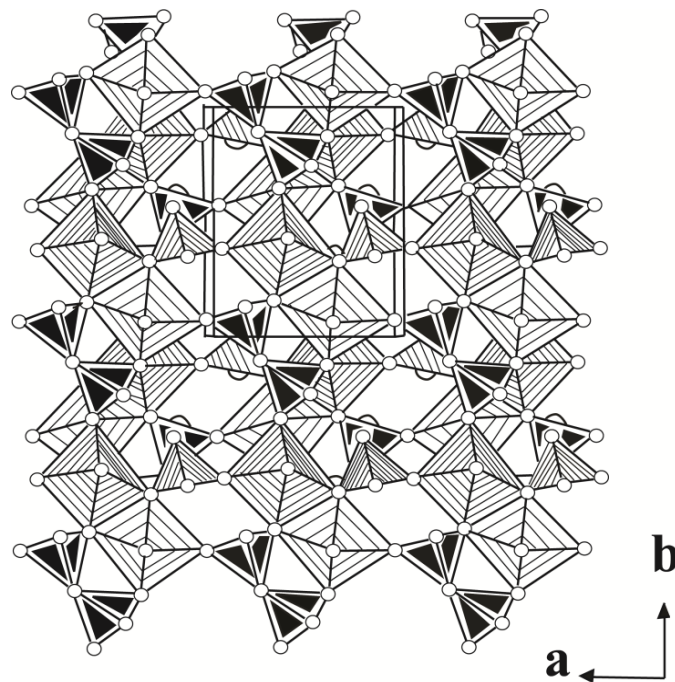


Figure 4.1 Linkage of the [Cd(2)Cd(3)O₈] zig zag chains by V(3)O₄ tetrahedra (close hatching) and V₂O₇ tetrahedron dough (Black, formed from V (1) and V (2)) [Ref: 22]

4.2 Experimental techniques

Ba₅Nb_{4-x}V_xO₁₅ (x=0-4) ceramics were prepared by conventional solid state ceramic method. High purity BaCO₃ (Sigma Aldrich, 99%), Nb₂O₅ (Aldrich, 99.9%) and V₂O₅ (Sigma Aldrich, 99%) were used as starting materials. Stoichiometric amounts of the raw materials were weighed and wet mixed in distilled water for an hour using agate mortar. The resultant slurry was dried at 100°C in hot air oven, then

ground well, and calcined at various temperatures. The calcined powders were ground again and then mixed with 5 wt% polyvinyl alcohol (PVA) as binder and the slurry was dried. The powders were again ground well and then pressed uniaxially in a tungsten carbide (WC) die of about 11 mm diameter by applying a pressure of 250 MPa in a hydraulic hand press. These cylindrical green compacts were sintered in a programmable furnace in the 900-1400°C temperature range for 1h. $Ba_3V_2O_8$ and $Ba_2V_2O_7$ ceramics were also prepared through solid state ceramic route and sintered in the 800-1300°C temperature range for 1h. The green pellets were initially fired at a rate of 8°C/min up to 600°C and then at a rate of 10°C/min up to the sintering temperature. An intermediate soaking was given at 600°C for 30 min to expel the binder.

Phase purity of the samples was studied by powder X-ray diffraction (XRD) measurement using CuK_{α} radiation (Bruker 5005, Germany). The Raman spectra of the ceramic compositions under study were recorded using a Thermo Scientific DXR with Nd:YVO₄ DPSS laser of 532 nm. The sintered samples were thermally etched for 30 min at a temperature of about 100°C below the sintering temperature, and the surface morphology was studied using a scanning electron microscope (Carl Zeiss, Model No: EVO18 Research, Germany). The shrinkage behavior of the $5BaO-2V_2O_5$ ceramic was studied in the temperature range 30-900°C using an EXSTAR 6000 model Thermo Mechanical Analyzer (SII Nano technology INC., Japan). The low frequency measurements of the samples were carried out at 1 MHz using an impedance analyzer (Agilent, 4294A, Malaysia). The microwave dielectric properties were measured using a vector network analyzer (Agilent make PNA E8362B, Bayan Lepas, Malaysia). The dielectric constant and the unloaded quality factor of the samples were measured by Hakki and Coleman post resonator [24] and cavity perturbation methods [25] respectively. The temperature coefficient of resonant frequency (τ_f) was measured by noting the variation of TE₀₁₈ mode frequency with temperature in the range of 30-100°C.

4.3 Results and discussion

4.3.1 X-ray diffraction studies

Figure 4.2 shows the X-ray diffraction patterns of $\text{Ba}_5\text{Nb}_{4-x}\text{V}_x\text{O}_{15}$ ($x=0-4$) ceramics (here after referred as BN4, BN3V, BN2V2, BNV3 and BV4). Figure 4.2a shows the X-ray diffraction pattern of sintered $\text{Ba}_5\text{Nb}_4\text{O}_{15}$ ceramic. $\text{Ba}_5\text{Nb}_4\text{O}_{15}$ crystallizes in the hexagonal system with space group $P\bar{3}m1$ having one formula unit per cell ($Z=1$) [26]. The XRD pattern of $\text{Ba}_5\text{Nb}_4\text{O}_{15}$ obtained in the present study is exactly matches with the available ICDD pattern (ICDD Card No: 14-0028) and hence indexed on the basis of the hexagonal symmetry of $\text{Ba}_5\text{Nb}_4\text{O}_{15}$ (indicated by I). The X-ray diffraction patterns of BN3V, BN2V2 and BNV3 obtained in the present study are compared with that of $\text{Ba}_5\text{Nb}_4\text{O}_{15}$ and those phases that are expected to occur in the solid solution. From Figure 4.2b-d, it can be observed that the intensities of the major diffraction peaks of $\text{Ba}_5\text{Nb}_4\text{O}_{15}$ phase decrease with increasing vanadium content (x) whereas the diffraction peaks of $\text{Ba}_3\text{V}_2\text{O}_8$ secondary phase increase steadily. It indicates that $\text{Ba}_3\text{V}_2\text{O}_8$ is formed as secondary phase as a result of vanadium substitution. Moreover, Figure 4.2b-d shows the occurrence of some weak peaks at 2θ angles $\sim 28.3^\circ$ and 29.7° (indicated by 'o' in Figure 4.2) clearly shows the presence of BaNb_2O_6 secondary phase (ICDD Card No: 32-0077) in BN3V, BN2V2 and BNV3 ceramics. This phenomenon has already been observed in B_2O_3 added $\text{Ba}_5\text{Nb}_4\text{O}_{15}$ ceramics reported by Kim et al. [18].

Recently, Zhao et al. made a comprehensive effort to study the effect of vanadium substitution on the structure and microwave dielectric properties of $\text{Ba}_5\text{Nb}_{4-x}\text{V}_x\text{O}_{15}$ ($x=0-1$) [21]. The objective of this study was to investigate the phase relations and microwave dielectric properties of vanadium modified $\text{Ba}_5\text{Nb}_4\text{O}_{15}$ as a function of vanadium content and sintering temperature. In this work, Zhao et al. reported the formation of $\text{Ba}_3\text{V}_2\text{O}_8$ secondary phase in samples with compositions of $x \geq 0.125$ and some weak peaks corresponding to BaNb_2O_6 secondary phase at $x \geq 0.5$. These authors suggested that majority of V^{5+} ions hardly substituted in place of Nb^{5+} ions in $\text{Ba}_5\text{Nb}_4\text{O}_{15}$ hexagonal perovskite, instead forming another compound

$\text{Ba}_3\text{V}_2\text{O}_8$. A hexagonal to orthorhombic phase transition for BaNb_2O_6 secondary phase is also reported by Zhao et al. [21].

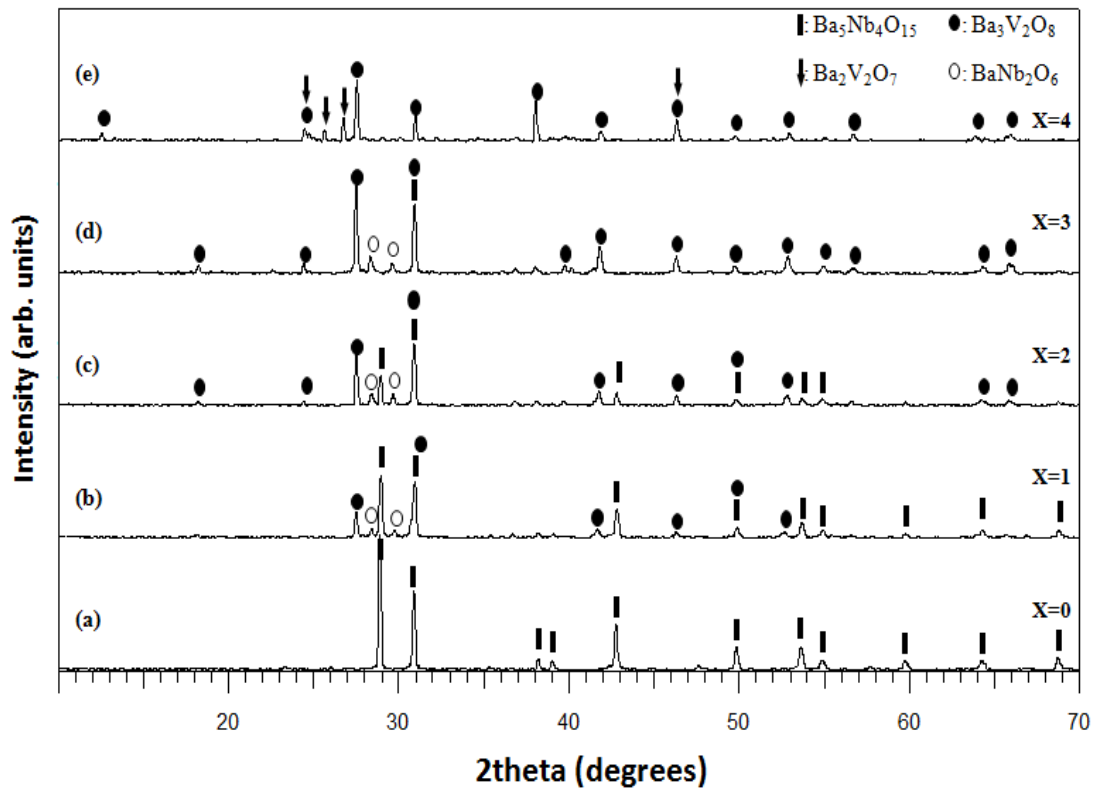


Figure 4.2 X-ray diffraction patterns of $\text{Ba}_5\text{Nb}_{4-x}\text{V}_x\text{O}_{15}$ ($x=0-4$) ceramics

The X-ray diffraction patterns of BN3V, BN2V2 and BNV3 ceramics obtained in the present study are also in agreement with the results reported by Zhao et al. Furthermore, it is found that the complete substitution of Nb^{5+} ions by V^{5+} ions in $\text{Ba}_5\text{Nb}_4\text{O}_{15}$ (at $x=4$) result $\text{Ba}_5\text{V}_4\text{O}_{15}$, as a multiphase composition comprising of hexagonal $\text{Ba}_3\text{V}_2\text{O}_8$ and triclinic $\text{Ba}_2\text{V}_2\text{O}_7$ (Figure 4.2). In order to understand the phase formation of BV4 composition, stoichiometric amounts of BaCO_3 and V_2O_5 were calcined at different temperatures for 1h (Figure 4.3). The specimen fired at 300°C and 400°C exhibited diffraction peaks corresponding to that of BaCO_3 and V_2O_5 , indicating that no reaction has taken place between BaCO_3 and V_2O_5 up to 400°C . The specimen heat treated at 500°C showed peaks of $\text{Ba}_2\text{V}_2\text{O}_7$ phase (ICDD Card No: 39-1432), as indicated by arrows in addition to BaCO_3 and V_2O_5 . When the calcination temperature exceeds 500°C , $\text{Ba}_3\text{V}_2\text{O}_8$ phase was formed due to the reaction of remaining BaCO_3 and V_2O_5 and the peaks are indexed on the basis of ICDD Card No: 29-0211. Both $\text{Ba}_3\text{V}_2\text{O}_8$ and $\text{Ba}_2\text{V}_2\text{O}_7$ phases coexist with a small amount of

BaCO₃ phase in the specimens fired at 600°C. Furthermore, the specimens fired at temperatures greater than 600°C show the coexistence of both Ba₃V₂O₈ and Ba₂V₂O₇ (ICDD Card No: 29-0211 and 39-1432) phases without the presence of BaCO₃ phase. Therefore, it can be inferred that BaCO₃ and V₂O₅ reacted together at temperatures in between 400-500°C and form Ba₂V₂O₇ phase and the reaction of remaining BaCO₃ and V₂O₅ resulted the formation of Ba₃V₂O₈ phase for specimens calcined above 500°C.

In order to further quantify the co-existence of both Ba₃V₂O₈ and Ba₂V₂O₇ phases in BV4, both Ba₃V₂O₈ and Ba₂V₂O₇ powders were individually prepared through conventional solid state ceramic route and calcined at 700°C for 1h. Calcined powders of Ba₃V₂O₈ and Ba₂V₂O₇ were taken stoichiometrically (1:1 ratio), mixed well and sintered at 900°C for 1h. The X-ray diffraction pattern of the sintered Ba₃V₂O₈-Ba₂V₂O₇ composite ceramic is given in Figure 4.4. The sintered Ba₃V₂O₈-Ba₂V₂O₇ mixture do not form single phase material and exactly resembled with the X-ray diffraction pattern of stoichiometrically prepared 5BaO-2V₂O₅ ceramic (Figure 4.3e). Hence the X-ray diffraction pattern is indexed on the basis of both hexagonal Ba₃V₂O₈ (ICDD Card No: 29-0211) and triclinic Ba₂V₂O₇ (ICDD Card No: 39-1432).

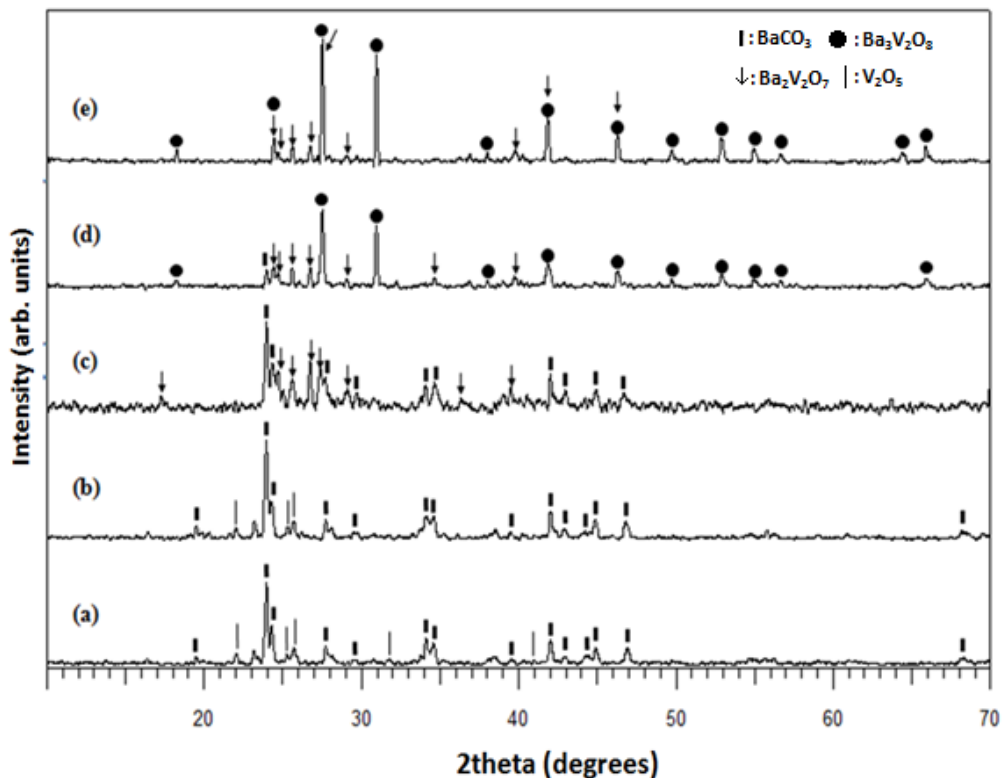


Figure 4.3 X-ray diffraction patterns of 5BaO-2V₂O₅ ceramic fired at (a) 300°C (b) 400°C (c) 500°C (d) 600°C and (e) 700°C for 1h

Zhang et al. also made an attempt to prepare temperature stable and high Q composite ceramic in low-temperature sinterable BaO-V₂O₅ binary system by co-firing mixtures of phase pure Ba₂V₂O₇ and Ba₃V₂O₈ [27]. They also found the coexistence of Ba₂V₂O₇ and Ba₃V₂O₈ at different sintering temperatures. According to them, the coexistence of Ba₂V₂O₇ and Ba₃V₂O₈ phases might be due to the different crystalline structures of these two phases and the different co-ordination between V⁵⁺, Ba²⁺ and O²⁻ in each crystal structure. Ba₃V₂O₈ has hexagonal structure where the V⁵⁺ ions are located inside tetrahedral [VO₄] units linked by six and ten-fold coordinated Ba²⁺ ions [28]. On the other hand, Ba₂V₂O₇ has triclinic structure with two unique divanadate groups that are repeated by b and c lattice translations to form sheets of divanadate groups parallel to (100) and are linked by four unique Ba²⁺ ions, which lie between themselves [29]. Therefore, the different crystal structures of Ba₂V₂O₇ and Ba₃V₂O₈ hinder the formation of solid solution between these two vanadate ceramics [27]. An attempt has also been made to replace Ba²⁺ with other alkaline earth cations, but all of them exhibited multiphase nature with respective orthovanadate and pyrovanadate analogues.

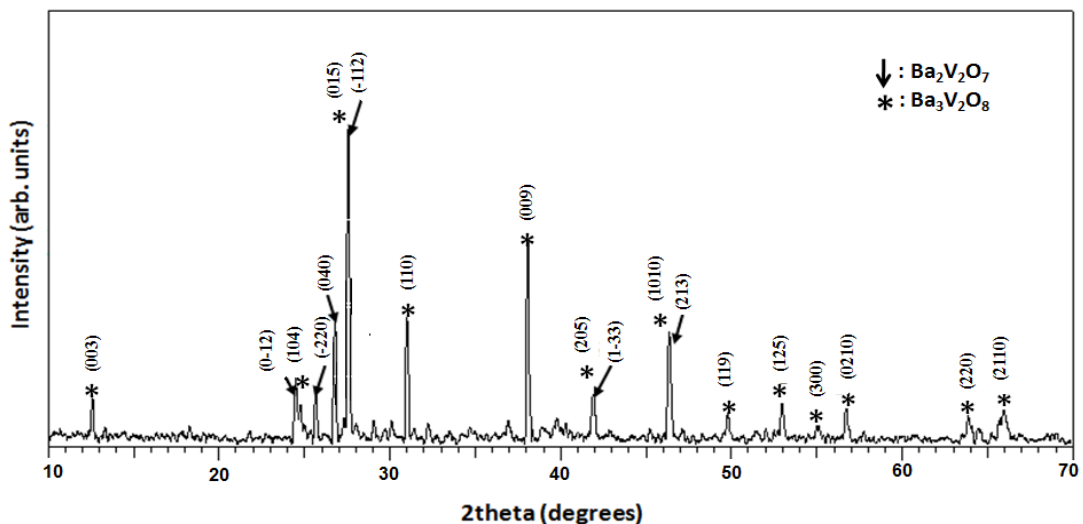


Figure 4.4 X-ray diffraction pattern of Ba₃V₂O₈-Ba₂V₂O₇ mixtures sintered at 900°C for 1h

4.3.2 Raman spectroscopic studies

Figure 4.5 shows the Raman spectra of $\text{Ba}_5\text{Nb}_{4-x}\text{V}_x\text{O}_{15}$ ($x=0-4$) ceramics. In the Raman spectrum of BN4 (Figure 4.5a), bands observed at 844 and 770 cm^{-1} are the symmetric stretching vibrations of NbO_6 octahedra, whereas asymmetric stretching vibration of NbO_6 octahedra is observed at 542 cm^{-1} . The vibrational modes observed at 681 cm^{-1} and 439 cm^{-1} are the symmetric and asymmetric bending vibrations of NbO_6 octahedra respectively [30]. When the vanadium concentration increased, the intensity of the Nb-O modes reduced considerably. On the other hand, strong vibrational mode is observed at 831 cm^{-1} in BN3V ceramic, which can be ascribed to the symmetric stretching vibration of $(\text{VO}_4)^{3-}$ vibrational units present in $\text{Ba}_3\text{V}_2\text{O}_8$. On increasing the vanadium concentration, the vibrational modes of $\text{Ba}_3\text{V}_2\text{O}_8$ become more prominent while the intensity of the vibrational modes of NbO_6 octahedra of $\text{Ba}_5\text{Nb}_4\text{O}_{15}$ reduced. The band assignments of BN4, BN3V, BN2V2, BNV3 and BV4 ceramics are compiled in Table 4.1. In the case of BV4, in addition to the vibrational modes of $\text{Ba}_3\text{V}_2\text{O}_8$, vibrational modes of $\text{Ba}_2\text{V}_2\text{O}_7$ are also observed. This result is in accordance with the X-ray diffraction studies of BV4 composition.

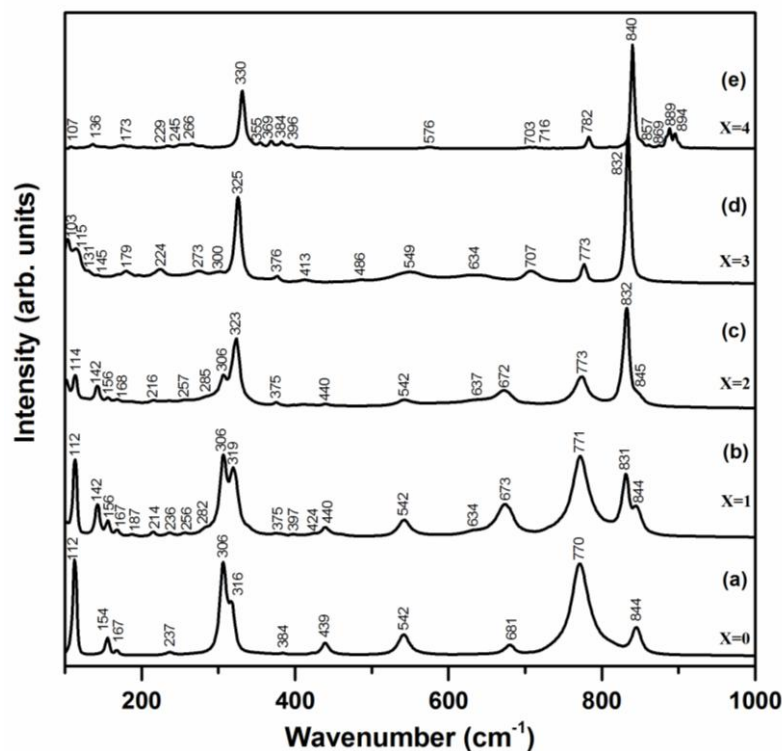


Figure 4.5 Raman spectra of $\text{Ba}_5\text{Nb}_{4-x}\text{V}_x\text{O}_{15}$ ($x=0-4$) ceramics

In order to study the crystal structure of 5BaO-2V₂O₅ in detail, Laser Raman Spectra of 5BaO-2V₂O₅, Ba₃V₂O₈ and Ba₂V₂O₇ have been recorded separately and the results are shown in Figure 4.6. It is reported that the structure of Ba₂V₂O₇ contains pyrovanadate (V₂O₇)⁴⁻ anions [31] whereas (VO₄)³⁻ groups are present in the structure of Ba₃V₂O₈ [32]. Hence, the internal vibrations of VO₃ groups and bridging V-O-V band of the pyrovanadate anions are expected in the Raman spectrum of Ba₂V₂O₇.

Strong vibrational modes observed in the Laser Raman spectrum of Ba₂V₂O₇ at 888 and 894 cm⁻¹ can be attributed to the symmetric stretching vibrations of end VO₃ groups. The stretching vibrations of bridging V-O-V bond is observed at 576 cm⁻¹ and bending vibrations are observed at 703 and 716 cm⁻¹. The vibrational features observed below 270 cm⁻¹ are attributed to external modes. On the other hand, vibrations corresponding to (VO₄)³⁻ molecular groups are seen in the Raman spectrum of Ba₃V₂O₈ ceramics. The symmetric stretching vibrations of (VO₄)³⁻ group is observed at 840 cm⁻¹ as a medium intense band. The symmetric and asymmetric bending vibrations are observed at 330 and 384 cm⁻¹ respectively (Figure 4.6). Interestingly, the vibrational features of both (VO₄)³⁻ and (V₂O₇)⁴⁻ groups are seen in the Raman spectrum of 5BaO-2V₂O₅, which is a clear indication of the co-existence of both Ba₃V₂O₈ and Ba₂V₂O₇ phases. No phases other than Ba₃V₂O₈ and Ba₂V₂O₇ are seen in the Raman spectrum of 5BaO-2V₂O₅ ceramics and the band assignments are given in Table 4.2.

Table 4.1: Raman mode assignments of BN4, BN3V, BN2V2, BNV3 and BV4 ceramics

BN4 (X=0)	BN3V (X=1)	BN2V (X=2)	BNV3 (X=3)	BV4 (X= 4)	Assignments
–	–	–	–	894 899 869 857	$\nu_s(\text{VO}_3)$
844	844	845	–	840	$\nu_s \text{NbO}_6$ $\nu_s(\text{VO}_4)^{3-}$
–	831	832	832	782	$\nu_s(\text{VO}_4)^{3-}$
770	771	773	773	–	$\nu_s \text{NbO}_6$
–	–	–	– 707	716 703	$\nu_{as}(\text{V-O-V})$
681	673 634	672 637	634	–	$\delta_s \text{NbO}_6$
–	–	–	–	576	$\nu_s(\text{V-O-V})$
542	542	542	549 486	–	$\nu_{as} \text{NbO}_6$
439	440 424	440	413	–	$\delta_{as} \text{NbO}_6$
384	397 375	375	376	396 384 369 355	$\delta(\text{VO}_3)$
316 306	319 306 282 256	323 306 285 257	325 300 273	330 266 245	$\delta_{as}(\text{VO}_4)^{3-}$
237	236 214 187	216	224 179	229 173	Lattice mode vibrations
167 154	167 156 142	168 156 142	145 131 115	136	
112	112	114	103	107	

ν_s – symmetric stretching, ν_{as} – asymmetric stretching, δ – asymmetric bending, δ_s – symmetric bending

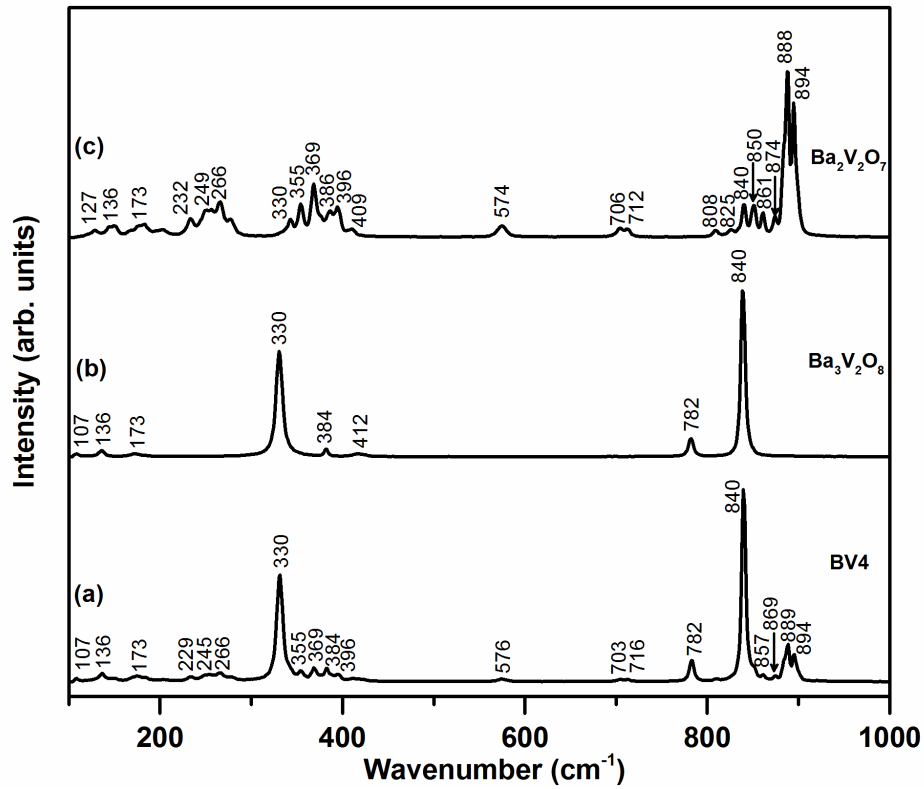


Figure 4.6 Raman spectra of (a) BV4 (b) Ba₃V₂O₈ and (c) Ba₂V₂O₇ ceramics

Table 4.2: Raman mode assignments of Ba₃V₂O₈, Ba₂V₂O₇ and BV4 ceramics

Ba ₃ V ₂ O ₈	Ba ₂ V ₂ O ₇	BV4	Assignments
–	894 888 874 861 850	894 889	$\nu_s(\text{VO}_3)$
840 782	840 825 808	840 782	$\nu_s(\text{VO}_4)^{3-}$
–	712 706	716 703	$\nu_{as}(\text{V-O-V})$
–	574 409 396	576 396	$\nu_s(\text{V-O-V})$
412 384	386 369 355	384 369 355	$\delta_{as}(\text{VO}_3)$
330	330	330	$\delta_s(\text{VO}_4)^{3-}$
173 136 107	266 249 232 173 136 127	266 245 229 173 136 107	Lattice mode vibrations

ν_s – symmetric stretching, ν_{as} – asymmetric stretching, δ_{as} – asymmetric bending, δ_s – symmetric bending

4.3.3 Morphological and dielectric studies

Figure 4.7 shows the SEM micrograph of Ba₅Nb_{4-x}V_xO₁₅ (x=0-4) ceramics sintered at optimum sintering temperatures. From the SEM pictures, it is clear that Ba₅Nb₄O₁₅ exhibits a well packed microstructure with elongated grains and the grain sizes range between 5-10 μm. As the vanadium content increases, the homogenous grain morphology changes for x=1 and 2 whereas well defined polygonal grains with average grain size of 1-2 μm become evident for x=3. It is inferred from the SEM images that the grain size decreases with increasing the vanadium content up to x=3. Dense microstructure with both polygonal and columnar grains are observed for BV4 ceramic with x=4. Polygonal grains having 1 to 3 μm size and columnar grains having 3-4 μm size are seen in the backscattered SEM picture of sintered BV4 ceramic. As per Zhang et al., Ba₃V₂O₈ and Ba₂V₂O₇ grains are difficult to distinguish

based on their morphology [27]. In order to further confirm this proposition, EDS analysis of BV4 sample was carried out (Figure 4.7e-g). EDS spot analysis confirms the existence of different types of grains in BV4 ceramic, which are obtained with different atomic% of Ba atoms. EDS mapping also confirms this hypothesis, since larger red grains are seen compared to columnar grains during mapping. The polygonal grains with higher atomic% of Ba could be $Ba_3V_2O_8$ phase rather than $Ba_2V_2O_7$ phase since Ba to V ratio is more (3:1) in former compared to 2:1 in later.

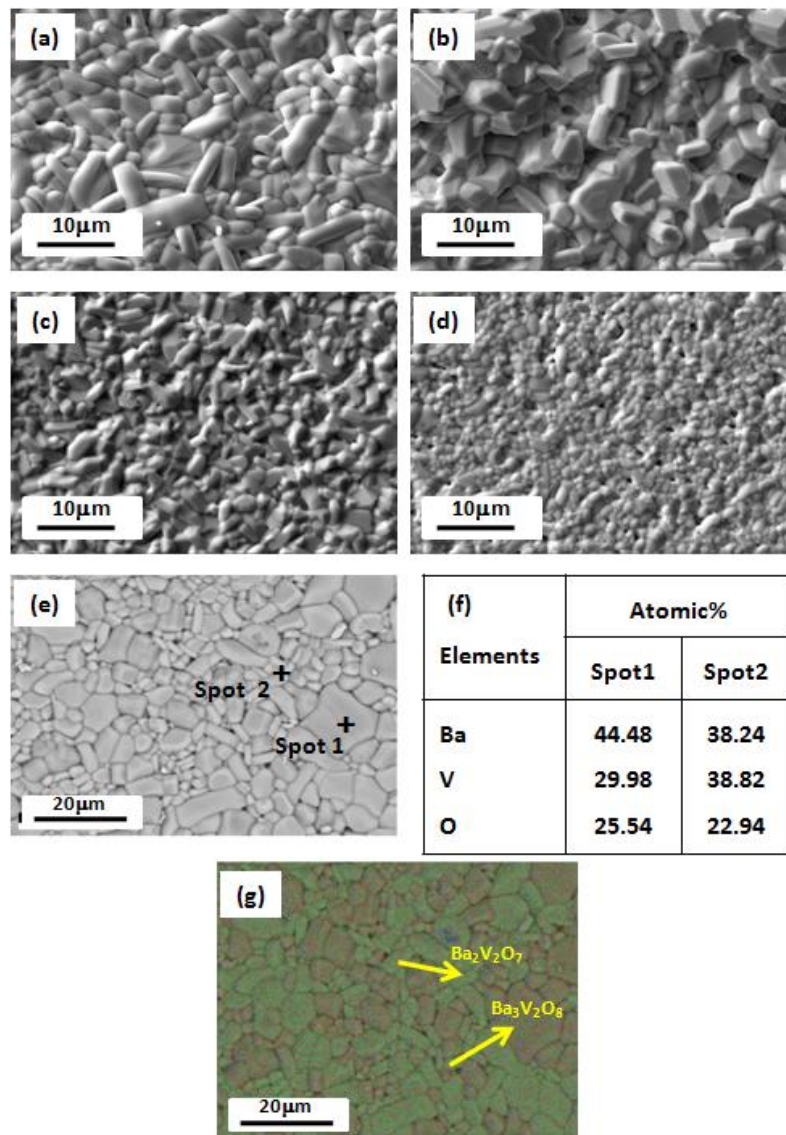


Figure 4.7 SEM pictures of (a) BN4 (b) BN3V (c) BN2V2 (d) BNV3 (e) backscattered SEM image of BV4 ceramic (f) EDS spot analysis result and (g) EDS mapping of BV4 ceramic sintered at optimum temperature

The shrinkage behavior of 5BaO-2V₂O₅ ceramic as a function of temperature is shown in Figure 4.8. It is clear from the figure that the shrinkage of BV4 green pellet starts around 600°C.

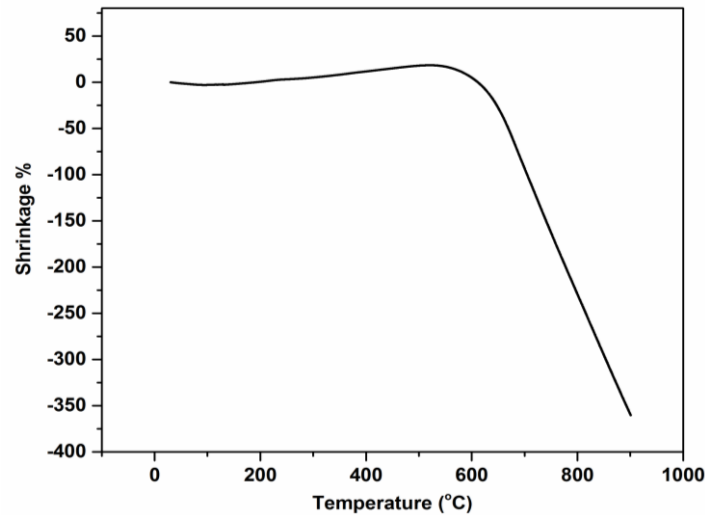


Figure 4.8 Shrinkage behavior of BV4 ceramic

Table 4.3 shows the sintering temperature, density and dielectric properties of Ba₅Nb_{4-x}V_xO₁₅ (x=0-4) ceramics sintered in the temperature range 900-1400°C. Among the five compositions studied, BN4, BN3V, BN2V2 and BV4 exhibit microwave dielectric properties, whereas BNV3 did not exhibit microwave dielectric properties. Hence, the dielectric constant of Ba₅Nb_{4-x}V_xO₁₅ (x=0-4) samples were also measured at 1 MHz. From Table 4.3, it is clear that as the vanadium content increases the sintering temperature, density and dielectric constant of the Ba₅Nb_{4-x}V_xO₁₅ ceramics decrease and this linear variation of density and dielectric constant of Ba₅Nb_{4-x}V_xO₁₅ (x=0-4) ceramics at 1 MHz is depicted in Figure 4.9. The decrease in dielectric constant and density can be attributed to the formation of Ba₃V₂O₈ phase having relatively low dielectric constant compared to Ba₅Nb₄O₁₅ ceramic.

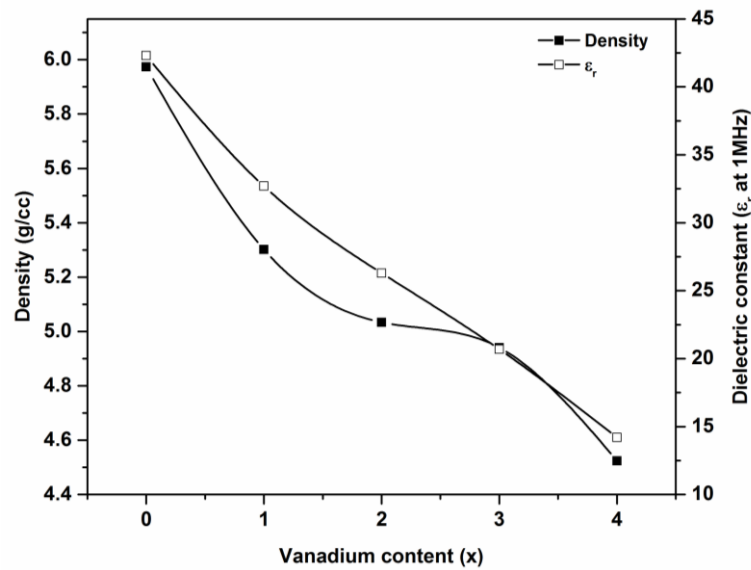


Figure 4.9 Variation of density and dielectric constant of $\text{Ba}_5\text{Nb}_{4-x}\text{V}_x\text{O}_{15}$ ceramics with respect to vanadium content (x) at 1MHz

BV4 ceramic was sintered in the 860-920°C temperature range to obtain optimum density. The variation of density and dielectric constant with sintering temperature of BV4 ceramic is shown in Figure 4.10. The maximum density and dielectric constant of the ceramic are obtained at a sintering temperature of 900°C for 1h. Further increase in temperature, both density and dielectric constant deteriorate. At optimum sintering temperature of 900°C for 1h, BV4 ceramic has an experimental density of 4.52 g/cc. The experimental density values obtained for $\text{Ba}_2\text{V}_2\text{O}_7$ and $\text{Ba}_3\text{V}_2\text{O}_8$ are 4.17 g/cc at 840°C for 1h and 4.31 g/cc at 1300°C for 1h respectively. The sintering temperature, density, dielectric constant, quality factor and temperature coefficient of resonant frequency of BV4 are compiled in Table 4.3.

Table 4.3: Sintering temperature, density, dielectric constant, quality factor and temperature coefficient of resonant frequency of $Ba_5Nb_{4-x}V_xO_{15}$ ($x = 0-4$), $Ba_2V_2O_7$ and $Ba_3V_2O_8$ ceramics

Compound	Sintering Temp. (°C)	Density (g/cc)	Low frequency data (Present study)		Microwave frequency data			Reference
			ϵ_r at 1MHz	$\tan\delta$ at 1MHz	ϵ_r	Qxf (GHz)	τ_f (ppm/°C)	
BN4	1400/3h	5.98	42.3	0.002	40	53,000	78	Ref. 16
BN3V	1240/2h	5.3	32.7	0.031	30.5	20,210	27.5	This work
BN2V2	1200/2h	5.03	26.3	0.008	23.3	34,798	60.5	This work
BNV3	1120/2h	4.94	20.7	0.005	*	*	*	This work
BV4	900/1h	4.52	14.2	0.012	12.1	26,790	7	This work
$Ba_2V_2O_7$	840/1h	4.17	11.87	0.055	9.6	30,315	-32	This work
$Ba_3V_2O_8$	1300/1h	4.31	13.3	0.094	12.3	52,197	41.6	This work

* No resonance

The dielectric properties of BV4 compacts are measured in the microwave frequency region by Hakki & Coleman post resonator method using a vector network analyzer. At optimum sintering temperature, BV4 ceramics exhibited a dielectric constant of 12.1 and quality factor of $\sim 26,790$ GHz. The temperature coefficient of resonant frequency is measured in the 30-100°C range for BV4 ceramics sintered in the 860-920°C temperature range and the average value is found to be ~ 7 ppm/°C. The stoichiometrically weighed and mixed powders of $\text{Ba}_3\text{V}_2\text{O}_8$ and $\text{Ba}_2\text{V}_2\text{O}_7$ ceramics are also well sintered at 900°C for 1h and exhibited a dielectric constant of 11.9 together with a quality factor of $\sim 24,540$ GHz and τ_f of 6 ppm/°C respectively.

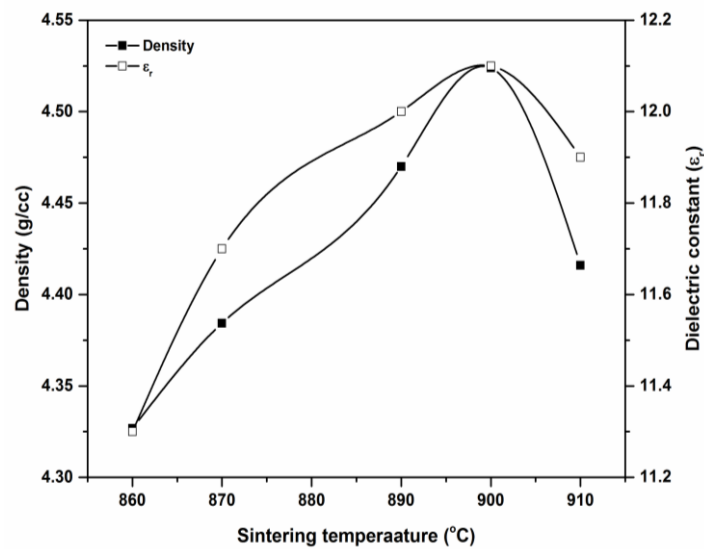


Figure 4.10 Variation of density and dielectric constant with sintering temperature of BV4 ceramic

In the present study, we obtained a dielectric constant of 9.6, unloaded quality factor of 2700 at 11.227983 GHz and $\tau_f = -32$ ppm/°C for $\text{Ba}_2\text{V}_2\text{O}_7$ ceramic and a dielectric constant of 12.3, unloaded quality factor of 4595 at 11.36089 GHz and $\tau_f = 41.6$ ppm/°C for $\text{Ba}_3\text{V}_2\text{O}_8$ ceramic respectively. The above results are reasonably in good agreement with the results reported by other researchers [33, 34]. As in the case of structural features, the microwave dielectric properties of BV4 also show resemblance with that of $\text{Ba}_3\text{V}_2\text{O}_8$. Both BV4 and $\text{Ba}_3\text{V}_2\text{O}_8$ ceramics have almost similar dielectric constant at microwave frequencies whereas the dielectric constant of $\text{Ba}_2\text{V}_2\text{O}_7$ is lower compared to other two compositions.

4.3.4 Compatibility studies

Even though, BV4 ceramic exists as a multiphase composition of $Ba_3V_2O_8$ and $Ba_2V_2O_7$ ceramics; it is well sintered at a sintering temperature of 900°C for 1h, and hence falls under the LTCC temperature range. For LTCC applications, BV4 ceramic should have chemical compatibility with silver electrode. Since there are published reports on the microwave dielectric properties and compatibility studies of ceramic composite systems for LTCC applications [35, 36], an attempt has been made to study the chemical compatibility of BV4 ceramic with silver. BV4 ceramic is co-fired with 20 wt% Ag powder at 900°C for 1h and the resultant sample is analyzed using X-ray diffraction and EDS analyses to ascertain the chemical interaction between the electrode material and BV4 composition. The X-ray diffraction pattern of BV4 ceramic co-fired with Ag at optimum sintering temperature of 900°C does not show any secondary phase formation other than $Ba_3V_2O_8$ and $Ba_2V_2O_7$ phases as a result of Ag addition (Figure 4.11). The silver peaks are observed separately which are marked with 'o' in the X-ray diffraction pattern of the co-fired sample. The planar SEM image of the BV4 ceramic co-fired with Ag powder at 900°C is given in Figures 4.12. The EDS analysis is carried out on both BV4 and Ag grains, which also did not show any chemical interaction between ceramic and metallic powder. Spot 1 in Figure 4.12 shows only the presence of Ag whereas Spot 2 represents the presence of BV4 ceramic without any inter-diffusion of Ag. The X-ray dot mapping of the co-fired BV4 sample is also done to further quantify the non-reactivity of Ag in the host matrix (Figure 4.13). The X-ray dot mapping result clearly shows the isolation of melted Ag particles in deep red color without any inter-diffusion in BV4 grains. Further, EDS line scan of the co-fired sample was carried out (Figure 4.14). From EDS line scan, it is clear that the Ag profile decreases sharply at the interface, which indicates that there is no inter-diffusion of Ag in to the ceramic grains, complementing the XRD and spot analyses results.

Although, the microwave dielectric properties of $Ba_2V_2O_7$ are previously studied, its chemical compatibility with metal electrode has been not reported yet. Hence, we performed the compatibility studies of barium pyrovanadate with Ag

powder. $Ba_2V_2O_7$ shows excellent chemical compatibility with Ag and hence can be used for LTCC applications.

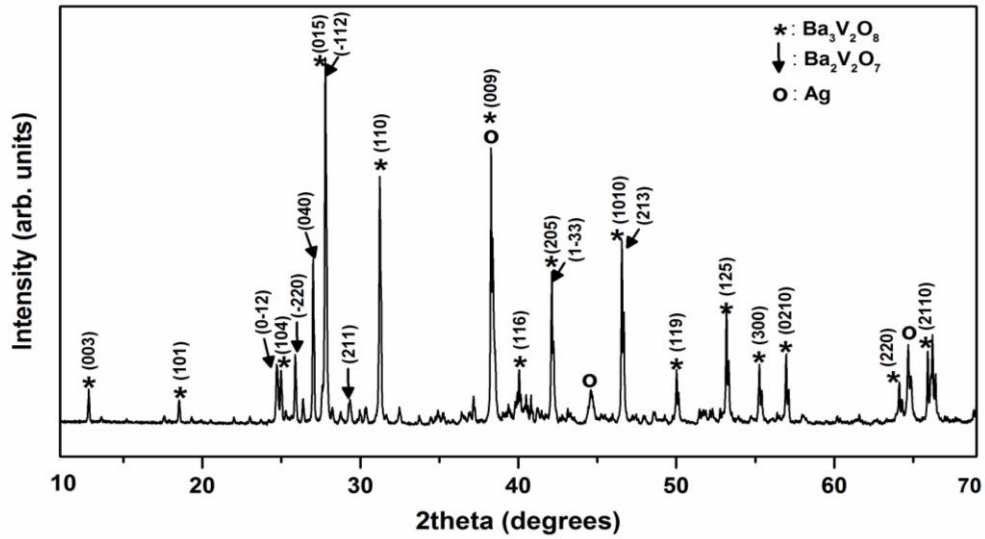


Figure 4.11 X-ray diffraction pattern of BV4 ceramic co-fired with 20 wt% Ag powder sintered at 900°C for 1h

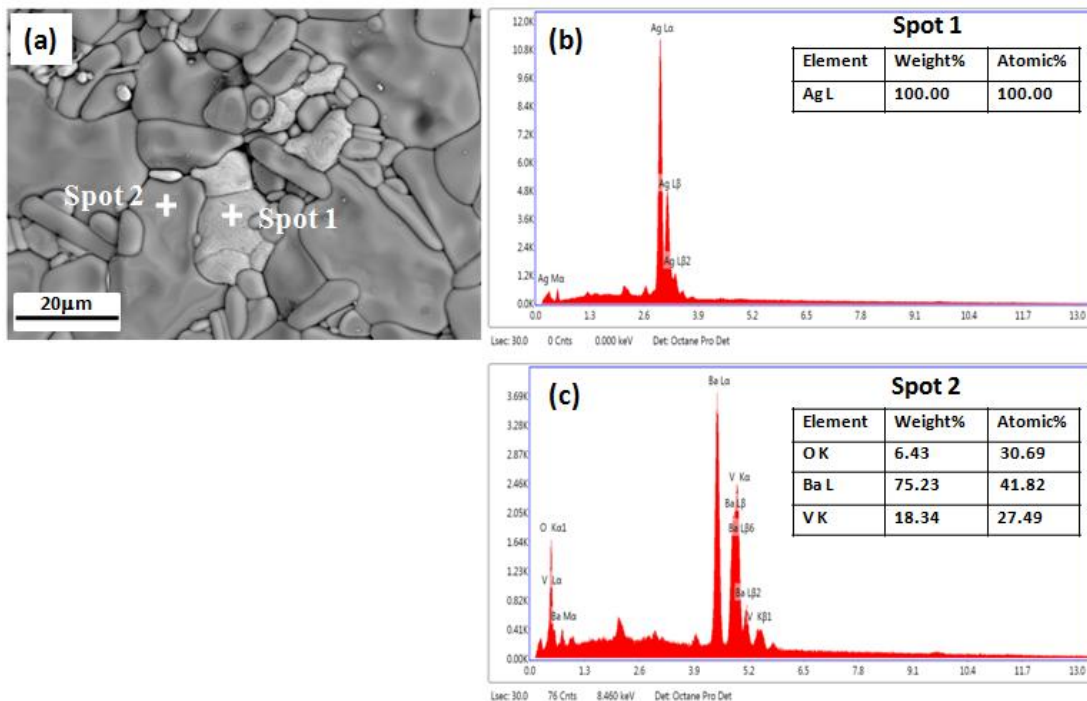


Figure 4.12 (a) SEM image of BV4 ceramic co-fired with 20 wt% Ag powder sintered at 900°C for 1h (b) EDS spectrum of Spot 1 (c) EDS spectrum of Spot 2

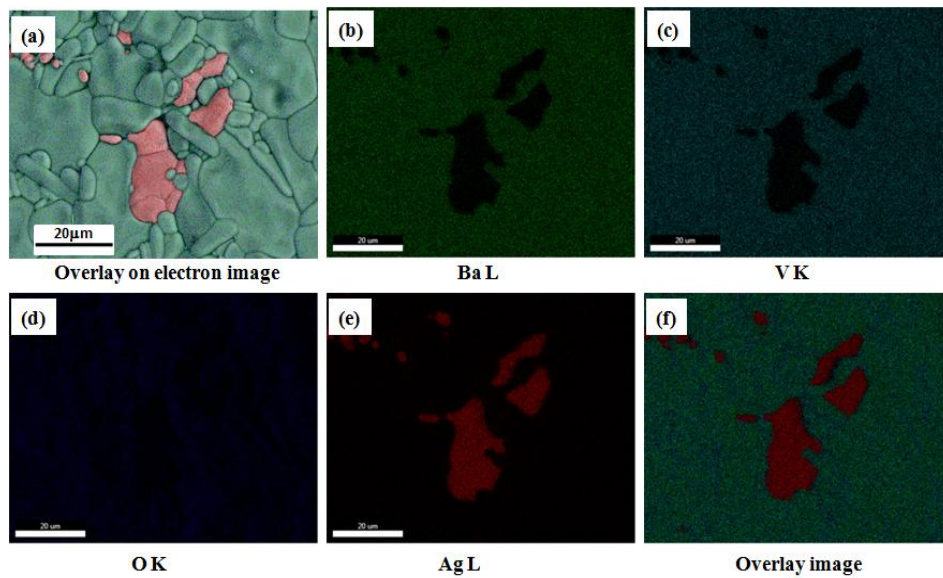


Figure 4.13 X-ray dot mapping image of BV4 ceramic co-fired with 20 wt% Ag powder sintered at 900°C for 1h [(a) Overlay on secondary electron image (b-e) elemental images (f) Overlay image]

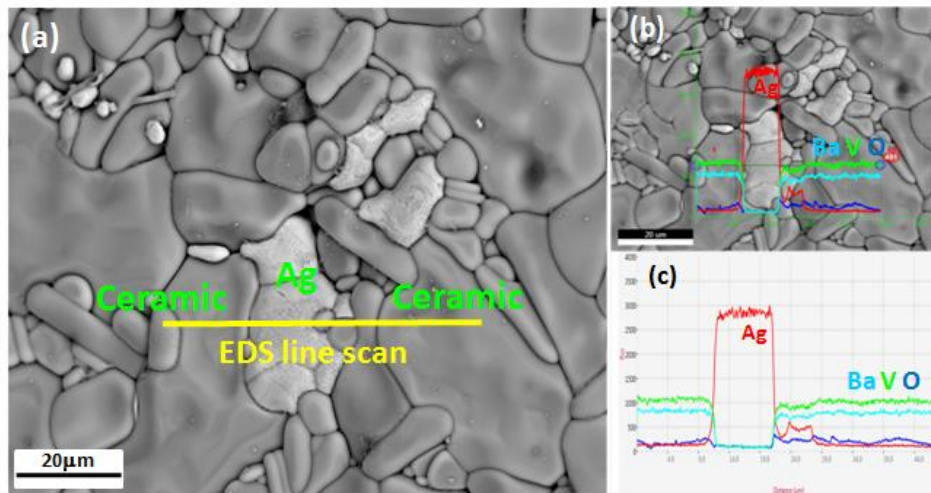


Figure 4.14 EDS line scan image of BV4 ceramic co-fired with 20 wt% Ag powder sintered at 900°C for 1h

4.4 Conclusions

The $Ba_5Nb_{4-x}V_xO_{15}$ ceramics ($x=0-4$) have been prepared through conventional solid state ceramic route. The powder X-ray diffraction studies reveal the existence of $Ba_3V_2O_8$ and $BaNb_2O_6$ as secondary phases in BN3V, BN2V2 and BNV3 ceramics, whereas the coexistence of hexagonal $Ba_3V_2O_8$ and triclinic $Ba_2V_2O_7$ phases are found in BV4. Laser Raman studies show that the structural

arrangement of BV4 ceramic is in close agreement with that of hexagonal $Ba_3V_2O_8$ phase. The SEM pictures of $Ba_5Nb_{4-x}V_xO_{15}$ ($x=0-3$) ceramics show dense microstructures and the grain size decreases with increasing the vanadium content. On the other hand, the SEM picture of BV4 has both polygonal and columnar grains. The sintering temperature, density and dielectric constant of $Ba_5Nb_{4-x}V_xO_{15}$ ($x=0-4$) ceramics decrease with increasing the vanadium content. The BV4 ceramic exhibits low dielectric constant ($\epsilon_r=12.1$), reasonably good quality factor ($Q_{xf}=26,790$ GHz) and low temperature coefficient of resonant frequency ($\tau_f \sim 7$ ppm/ $^{\circ}C$). The compatibility studies based on X-ray diffraction and EDS analyses confirm the chemical compatibility between BV4 ceramic and Ag powder.

References

- [1] M. Valant, D Suvorov, *Bol. Soc. Esp. Ceram.*, 43 [3] (2004) 634-639.
- [2] L. X. Pang, D. Zhou, *Mater. Lett.*, 64 [22] (2010) 2413- 2415.
- [3] M. Valant, D. Suvorve, *J. Am. Ceram. Soc.*, 83 [11] (2000) 2721-2729.
- [4] Y. Fang, A. Hu, Y. Gu, Y.J. Oh, *J. Eur. Ceram. Soc.* 23 [14] (2003) 2497-2502.
- [5] J. Takada, S. F. Wang, S. Yoshikawa, S. J. Jang, R. E. Newnham, *J. Am. Ceram. Soc.*, 77 [9] (1994) 2485-2488.
- [6] H. M. O'Bryan, J. Thomson, J. K. Plourde, *J. Am. Ceram. Soc.*, 57 [10] (1974) 450-453.
- [7] H. Sreemoolanadhan, M. T. Sebastian, *Mater. Res. Bull.*, 30 [6] (1995) 653-658.
- [8] C. L. Huang, M. H. Weng, *Mater. Chem. Phys.*, 71 [1] (2001) 17-22.
- [9] D. W. Kim, K. H. Ko, K. S. Hong, *J. Am. Ceram. Soc.*, 84 [6] (2001) 1286-1290.
- [10] C. L. Huang, K. H. Chiang, S. C. Chuang, *Mater. Res. Bull.*, 39[4-5] (2004) 629-636.
- [11] M. T. Sebastian, K. P. Surendran, *J. Eur. Ceram. Soc.*, 26 [10-11] (2006) 1791-1799.
- [12] L. Chai, M. A. Akbas, P. K Davies, J. B. Parise, *Mater. Res. Bull.* 32[9] (1997) 1261-1269.
- [13] C. T. Lee, C. T. Chen, C. Y. Huang, C. J. Wang, *Jpn. J. Appl. Phys.* 47 [6] (2008) 4634-4637.
- [14] C. Veneis, P. K. Davis, T. Negas, S. Bell, *Mater. Res. Bull.*, 31[5] (1996) 431-437.
- [15] I. N. Jawahar, P. Mohanan, M.T. Sebastian, *Mater. Lett.*, 57 [24-25] (2003) 4043-4048.
- [16] R. Ratheesh, M. T. Sebastian, P. Mohanan, M. E. Tobar, J. Hartnett, R. Woode, D.G. Blair, *Mater. Lett.*, 45 [5] (2000) 279-285.

- [17] H. Zhou, X. Chen, L. Fang, C. Hu, H. Wang, *J. Mater. Sci: Mater. Electron.*, 21 [9] (2010) 939-942.
- [18] D. W. Kim, J. R. Kim, S. H. Yoon, K. S. Hong, C. K. Kim, *J. Am. Ceram. Soc.*, 85 [11] (2002) 2759-2762.
- [19] D. W. Kim, K. S. Hong, C. S. Yoon, C. K. Kim, *J. Eur. Ceram. Soc.*, 23 [14] (2003) 2597-2601.
- [20] D. W. Kim, H. J. Youn, K. S. Hong, C. K. Kim, *Jpn. J. Appl. Phys.*, 41 (2002) 3812-3816.
- [21] F. Zhao, H. Zhuang, Z. Yue, J. Pei, Z. Gui, L. Li, *Mater. Lett.*, 61 [16] (2006) 3466-3468.
- [22] B. Mertens, Hk. Muller-Buschbaum, *Z. anorg. allg. Chem.*, 623 [7] (1997) 1061-1066.
- [23] C. L. Huang, M. H. Weng, C. C. Wu, *Jpn. J. Appl. Phys.*, 40 (2001) 698-702.
- [24] B. W. Hakki, P. D. Coleman, *IRE Trans. Microw. Theory Tech.*, 8 [4] (1960) 402-410.
- [25] J. Krupka, K. Derzakowski, B. Riddle, J. B. Jarvis, *Meas. Sci. Technol.*, 9 (1998) 1751-1756.
- [26] S. Pagola, G. Polla, G. Levya, M. T. Casais, J. A. Alonso, I. Rasines, R. E. Carbonio, *Mater. Sci. Forum.*, 228 (1996) 819-824.
- [27] C. Zhang, R. Zuo, *J. Alloys Compd.*, 622 (2015) 362-368.
- [28] P. Susse, M. J. Buerger, *Z. Kristallogr.*, 131 [1-6] (1970) 161-174.
- [29] F. C. Hawthorne, C. Calvo, *J. Solid State Chem.*, 26 [4] (1978) 345-355.
- [30] R. Ratheesh, H. Sreemoolanadhan, M. T. Sebastian, *J. Solid State Chem.*, 131 [1] (1997) 2-8.
- [31] I. L. Botto, E. J. Baran, J. C. Pedregosa, P. J. Aymonino, *Monatsh. Chem.*, 110 [4] (1979) 895-898.
- [32] C. S. Lim, *J. Ceram. Proc. Res.*, 13 [4] (2012) 432-436.
- [33] M. R. Joung, J.S. Kim, *J. Am. Ceram. Soc.*, 92 [12] (2009) 3092-3094.

- [34] R. Umemura, H. Ogawa, A. Yokoi, H. Ohsato, A. Kan, *J. Alloys Compd.*, 424 (2006) 388-393.
- [35] J. J. Bian, Y. M. Ding, *Mater. Res. Bull.*, 67 (2015) 245-250.
- [36] W. Wang, L. Li, S. Xiu, B. Shen, J. Zhai, *J. Alloys Compd.*, 639 (2015) 359-364.

5

Crystal Structure and Microwave Dielectric Properties of New Alkaline Earth Vanadate $A_4V_2O_9$ (A=Ba, Sr, Ca, Mg and Zn) Ceramics

- 4.1 Introduction
- 4.2 Experimental techniques
- 4.3 Results and discussion
- 4.4 Conclusions

Some of the contents of this chapter have published in

A. N. Unnimaya, E. K. Suresh, R. Ratheesh, Mater. Res. Bull., 88 (2017) 178-181

5.1 Introduction

Single phase materials reported in the BaO-V₂O₅ binary phase diagram viz. BaV₂O₆, Ba₂V₂O₇ and Ba₃V₂O₈ by Fotiev et al. [1] have been prepared and found useful for LTCC applications in previous chapters. The fourth single phase compound in the phase diagram, Ba₃V₄O₁₃ is reported as ULTCC material by our research group and the microwave dielectric properties of these stable compositions are given in Table 5.1 [2-5]. Interestingly, all these stable compositions are obtained with high mol% of BaO, in the range of 52-77 mol% [1]. On the other hand, metastable phases with low mol% of BaO, ie 10-14 mol% for BaV₁₂O₃₀ and 35-40 mol% for BaV₈O_{21-x} respectively are also reported by Fotiev et al. [1]. However, the existence of Ba₄V₂O₉ with higher mol% of BaO (> 77mol%), was not mentioned in the BaO-V₂O₅ binary phase diagram. Later, Golovkin and Kristallov reported the existence of Ba₄V₂O₉ ceramic with tetragonal crystal structure (ICDD Card No: 47-0114) in the BaO-V₂O₅ binary system [6]. However, to the best of our knowledge no reports are available on the dielectric properties of Ba₄V₂O₉ ceramic.

Table 5.1 Sintering temperature, density and dielectric properties of the stable compounds in the BaO-V₂O₅ phase diagram

Compound	Sintering Temp. (°C)	Density (g/cc)	ϵ_r	Qxf (GHz)	τ_f (ppm/°C)	Reference
BaV ₂ O ₆	550/1h	3.678	11.2	42,790	28.2	[2]
Ba ₂ V ₂ O ₇	900/10h	4.356	10.1	51,630	-26.5	[3]
Ba ₃ V ₂ O ₈	1600/5h	4.5	12.5	41,065	38.8	[4]
Ba ₃ V ₄ O ₁₃	600/1h	3.8	9.6	56,100	-42	[5]

Among the oxovanadates of general formula A₄V₂O₉, crystal structure of Zn₄V₂O₉ was well studied. Makarov et al. reported the existence of Zn₄V₂O₉ as a single phase compound in the ZnO-V₂O₅ system [7]. The ZnO-V₂O₅ binary system with Zn₄V₂O₉ as a single phase compound is reported by Kurzawa et al. which is shown in Figure 5.1 [8]. Later, the crystal structure is confirmed by Waburg and Muller [9].

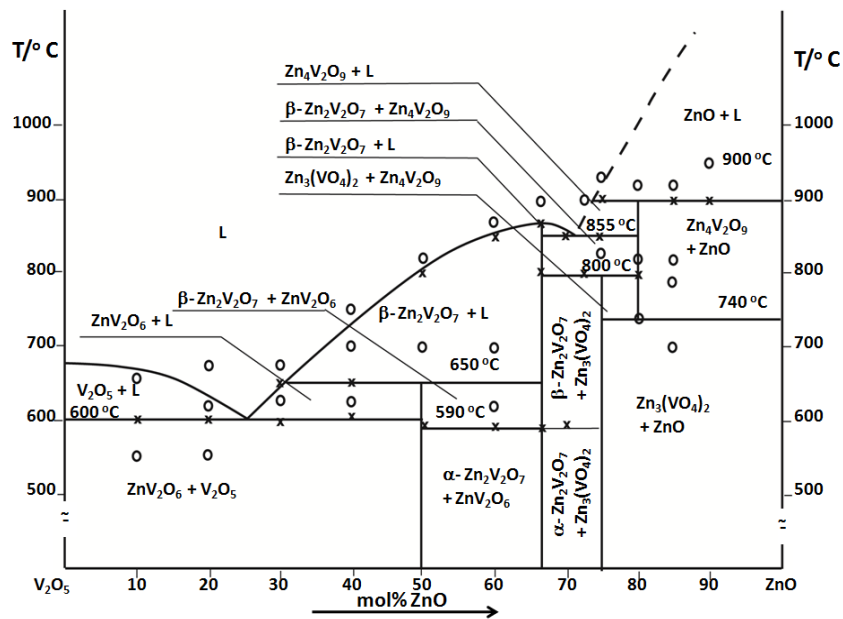


Figure 5.1 The ZnO-V₂O₅ phase diagram [Ref. 8]

According to Waburg and Muller, Zn₄V₂O₉ stands at the end of the ZnO-V₂O₅ system with isolated vanadium-oxygen polyhedra. The more zinc-rich compound Zn₄V₂O₉ has isolated vanadium, which is tetrahedrally coordinated [9]. The schematic representation of Zn₄V₂O₉ with hatched VO₄ tetrahedra is given in Figure 5.2.

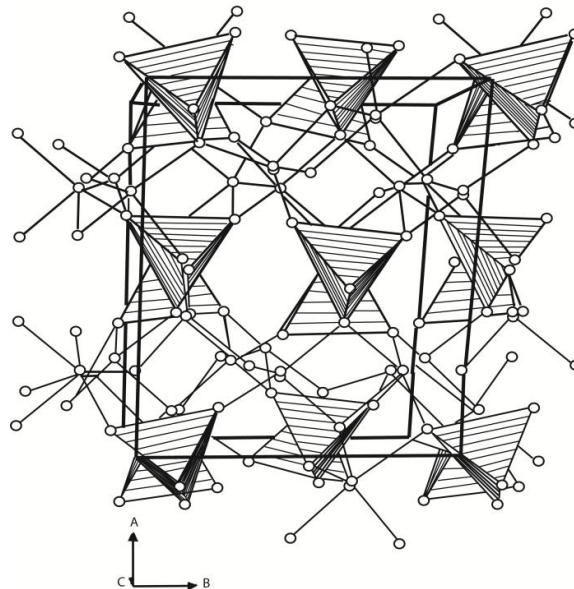


Figure 5.2 Schematic representation of the atomic order of Zn₄V₂O₉ along [001] [Ref. 9]

The SrO-V₂O₅ binary phase diagram reported by J. J. Brown (Figure 5.3) confirmed the existence of Sr₄V₂O₉ ceramic [10]. The strontium oxovanadate has a tendency to vaporize or possibly to decompose at higher temperatures (>1400°C) resulting SrO, which hydrate rapidly at room temperature. Recently, Zhu et al. carried out the luminescent studies of Sr₄V₂O₉ co-doped with Eu³⁺ and Ba²⁺ [11]. Also, there are published reports available on the existence of Ca₄V₂O₉ in the CaO-V₂O₅ system, which exhibits close resemblance with that of Ca₃V₂O₈ ceramic and decomposes incongruently at relatively higher temperature of 1365°C [12]. However, to the best of our knowledge, no reports are available on the phase formation of Mg₄V₂O₉ ceramic.

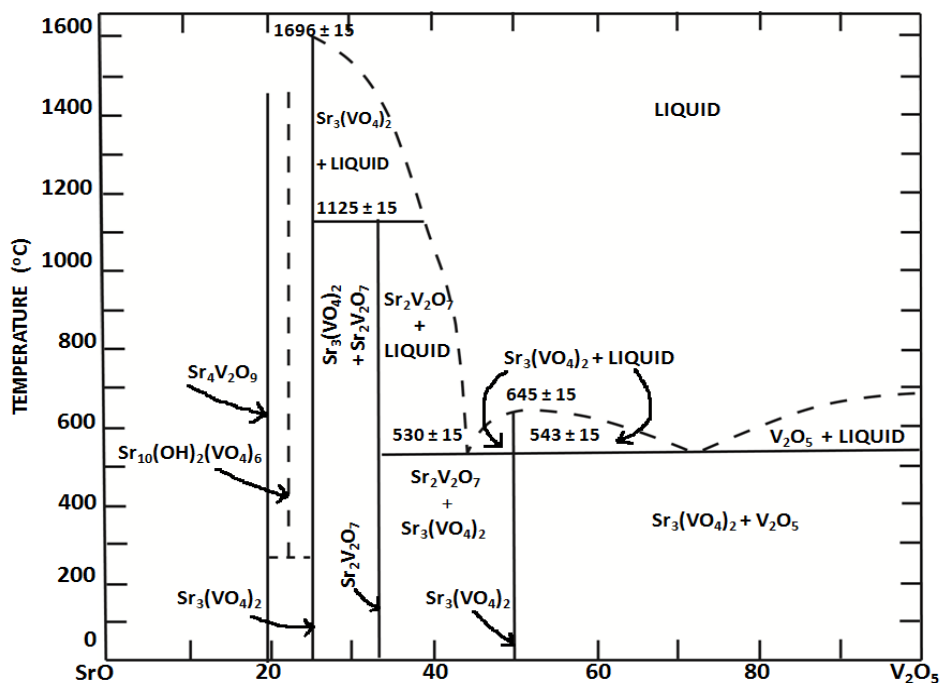


Figure 5.3 The SrO-V₂O₅ phase diagram [Ref. 10]

In the present work, a systematic study has been carried out on the structure and microwave dielectric properties of A₄V₂O₉ (A= Ba, Sr, Ca, Mg and Zn) ceramics with an objective to understand the existence of A₄V₂O₉ ceramics in the AO-V₂O₅ phase diagram. The chemical compatibility of microwave dielectric systems in the A₄V₂O₉ (A=Ba, Sr, Ca, Mg and Zn) ceramics has also been ascertained through X-ray diffraction and EDS analyses to identify their suitability for LTCC applications.

5.2 Experimental techniques

$A_4V_2O_9$ ceramics (A=Ba, Sr, Ca, Mg and Zn) were prepared by conventional solid state ceramic route. High purity oxides and carbonates such as $BaCO_3$ (Sigma Aldrich, 99%), $SrCO_3$ (Himedia, 99%), $CaCO_3$ (Sigma Aldrich, 99%), MgO (Sigma Aldrich, 99+ %), ZnO (Sigma Aldrich, 99%) and V_2O_5 (Sigma Aldrich, 99%) were used as starting materials. Stoichiometric amounts of the raw materials were weighed and wet mixed in distilled water for an hour in an agate mortar. The resultant slurry was dried at 100°C in a hot air oven, then ground well, and calcined at 600°C for an hour. The calcined powders were ground again and then mixed with 5 wt% polyvinyl alcohol (PVA) as binder and dried well. The granulated powders were pressed uniaxially in a 11 mm diameter tungsten carbide (WC) die by applying a pressure of 250 MPa in a hydraulic hand press. These cylindrical green compacts were sintered in a programmable furnace at various temperatures in the range 700-1250°C. The green compacts were fired at a rate of 5°C/min up to the sintering temperature and an intermediate soaking was given at 600°C for 30 min to expel the binder (PVA).

Phase purity of the $A_4V_2O_9$ samples were studied by powder X-ray diffraction (XRD) measurement using CuK_{α} radiation (Bruker 5005, Germany). The Raman spectra of the ceramic compositions under study were recorded using a Thermo Scientific DXR with Nd:YVO₄ DPSS laser of 532nm. In order to study the structural resemblance of $A_4V_2O_9$ ceramics with that of alkaline orthovanadates, $A_3V_2O_8$ (A=Ba, Sr, Ca, Mg and Zn) ceramics were also prepared through solid state ceramic route. All the prepared samples were calcined at 600°C for 1h. The sintering temperature of the samples was in the range of 700-1300°C. The surface morphology of the sintered samples was studied using scanning electron microscopy (Carl Zeiss, Model No: EVO18 Research, Germany). The low frequency measurements of the samples were carried out at 1 MHz using an impedance analyzer (Agilent, 4294A, Malaysia). The microwave dielectric properties were measured using a vector network analyzer (Agilent make PNA E8362B, Bayan Lepas, Malaysia). The dielectric constant and the unloaded quality factor of the samples were measured by Hakki and Coleman post resonator and resonant cavity methods respectively [13,

14]. The temperature coefficient of resonant frequency (τ_f) was also measured by noting the variation of TE_{01 δ} mode frequency with temperature in the range of 30-100°C.

5.3 Results and Discussion

5.3.1 X-ray diffraction studies

Figure 5.4 shows the X-ray diffraction patterns of A₄V₂O₉ ceramics sintered at different temperatures. Among A₄V₂O₉ (A= Ba, Sr, Ca, Mg and Zn) ceramics, the crystal structure of Ba₄V₂O₉ ceramic was studied by Golovkin and Kristallov [6]. The reported XRD pattern of Ba₄V₂O₉ (ICDD Card No: 47-0114) is only from 20 to 60° 2theta values. The XRD pattern of Ba₄V₂O₉ prepared in the present study is matching with the available ICDD pattern and indexed based on the same. Ba₄V₂O₉ ceramic crystallizes in the tetragonal structure with lattice parameters a=18.751, and c=18.091 Å. The calculated lattice parameters obtained for Ba₄V₂O₉ in the present study are, a=18.411 and c=18.353 Å, which show reasonably good agreement with the results reported by Golovkin and Kristallov [6].

The qualitative structural analysis of Sr₄V₂O₉ is reported by J. J. Brown without hkl values and other structural parameters like space group, theoretical density etc. [10]. The structural analysis of Ca₄V₂O₉ is reported by Y. Yuan and proposed that this composition has close resemblance with that of calcium orthovanadate [12]. In the present study also, XRD pattern of Ca₄V₂O₉ composition shows close resemblance with that of orthovanadate sample. Zn₄V₂O₉ ceramic crystallizes in the monoclinic system having P2₁ space group with lattice parameters a=10.488, b=8.198, c=9.682 Å and four number of molecules per unit cell (Z= 4) [9]. The XRD pattern of Zn₄V₂O₉ ceramic obtained in the present study closely matches with that of the available reports and hence indexed accordingly (ICDD Card N:-77-1757). The calculated lattice parameters of Zn₄V₂O₉ in the present study are; a=10.633, b=8.013 and c=9.601 Å which are in good agreement with the ICDD data.

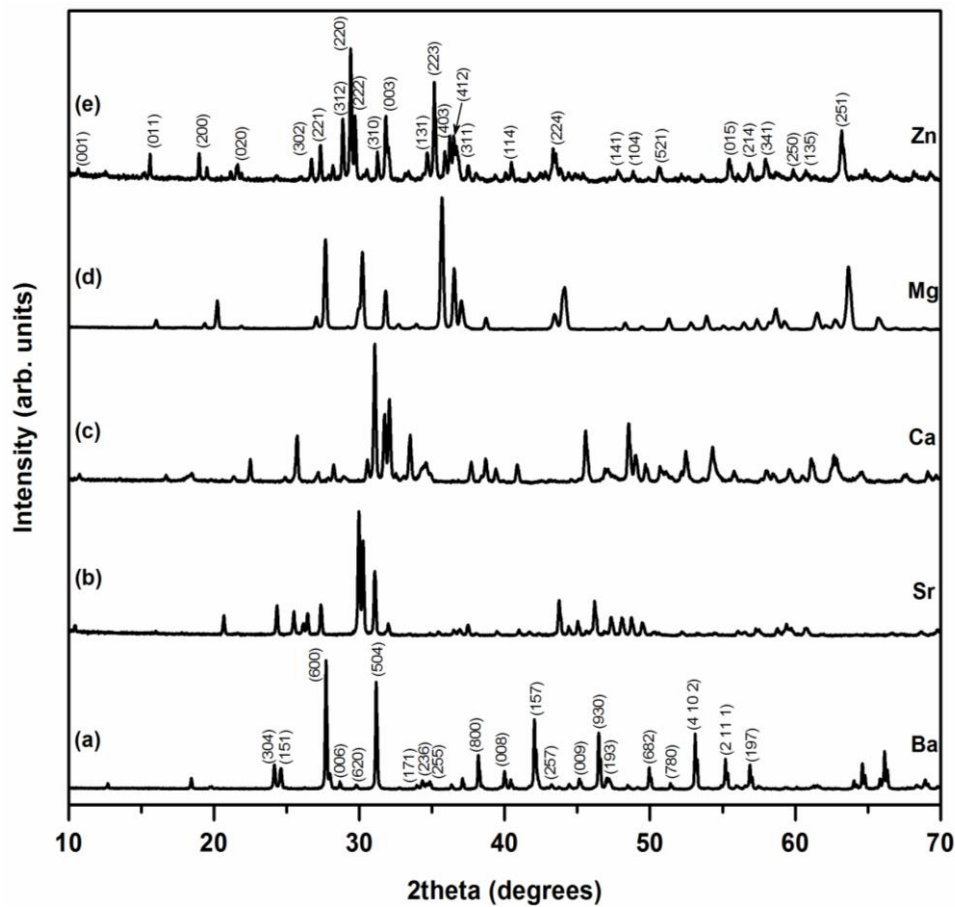


Figure 5.4 XRD patterns of $A_4V_2O_9$ ($A = \text{Ba, Sr, Ca, Mg and Zn}$) ceramics

Since there are reports on the structural resemblance of oxovanadate ceramics with that of orthovanadate ceramics, the X-ray diffraction patterns of $A_3V_2O_8$ ($A = \text{Ba, Sr, Ca, Mg and Zn}$) ceramics were also carried out to quantify the phase purity of the prepared oxovanadate ceramics. Figure 5.5 shows the XRD patterns of the orthovanadate samples and their crystal structures are already reported [15-19]. Orthovanadates with $A = \text{Ba and Sr}$ belong to the hexagonal crystal structure with $R\bar{3}m$ space group [15, 16]. $\text{Ca}_3\text{V}_2\text{O}_8$ also belongs to hexagonal crystal structure but with $R3c$ space group [17].

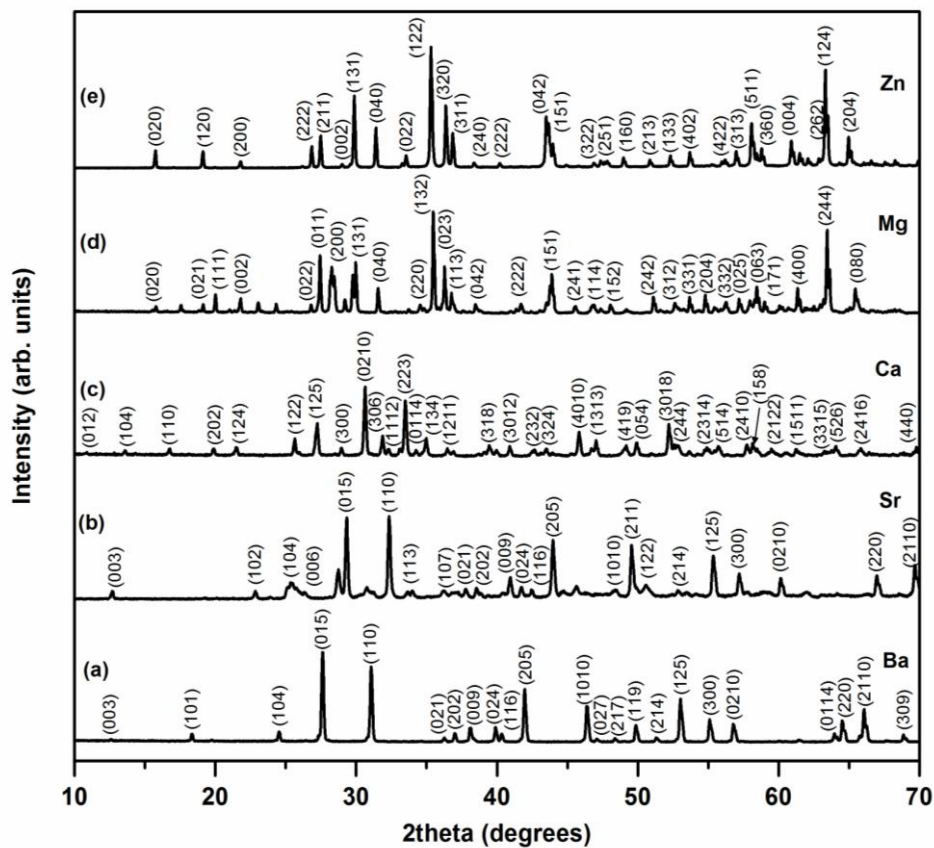


Figure 5.5 XRD patterns of $A_3V_2O_8$ (A = Ba, Sr, Ca, Mg and Zn) ceramics

Orthovanadates with alkaline earth elements having lower ionic radii such as magnesium and zinc crystallize in the orthorhombic space group $Cmca$ with $Z=4$ [18, 19]. The X-ray diffraction patterns of the orthovanadate samples in the present study are exactly match with the available ICDD patterns (ICDD Card No: 29-0211, 81-1844, 46-0756, 73-0207 and 34-0378) and hence indexed accordingly. Comparison of the available structural data of the oxovanadates and orthovanadates are compiled in Table 5.2. From the X-ray diffraction patterns and the available structural details of $A_3V_2O_8$ and $A_4V_2O_9$ samples, it is clear that oxovanadates have different crystal structure compared to that of orthovanadates.

Table 5.2 Comparison of the available structural details of the oxovanadate and orthovanadate ceramics

A ²⁺ ion	A ₃ V ₂ O ₈							Ref.
	Crystal structure	Calculated lattice parameters (Å)			Reported lattice parameters (Å)			
		a	b	c	a	b	c	
Ba	Hexagonal	5.755	5.755	21.27	5.762	5.762	21.29	15
Sr	Hexagonal	5.639	5.639	20.27	5.619	5.619	20.14	16
Ca	Hexagonal	10.671	10.671	37.576	10.809	10.809	38.0281	17
Mg	Orthorhombic	6.317	8.166	11.364	6.053	8.33	1.442	18
Zn	Orthorhombic	6.062	8.212	11.256	6.088	8.28	11.489	19
A ²⁺ ion	A ₄ V ₂ O ₉							Ref.
	Crystal structure	Calculated lattice parameters (Å)			Reported lattice parameters (Å)			
		a	b	c	a	b	c	
Ba	Tetragonal	18.411	18.411	18.353	18.751	18.751	18.091	6
Zn	Monoclinic	10.633	8.013	9.601	10.488	8.198	9.682	9

5.3.2 Raman spectroscopic studies

In order to study the structure of A₄V₂O₉ ceramics in detail, Raman spectroscopic studies of these compositions were carried out. Figure 5.6 shows the Raman spectra of A₄V₂O₉ ceramics and the corresponding band assignments are given in Table 5.3. The strong Raman bands observed in the internal mode region of Ba₄V₂O₉ at 832 cm⁻¹, 774 cm⁻¹ and 322 cm⁻¹ match with already reported Raman spectrum of Ba₃V₂O₈ ceramic [20]. The Raman spectra of both Ba₃V₂O₈ and Ba₄V₂O₉ show striking similarities in spite of the fact that the powder X-ray diffraction patterns of these compositions are entirely different with different crystal structures [6, 15]. Although the Raman spectrum of Ba₄V₂O₉ ceramic shows similarities with that of Ba₃V₂O₈ ceramics, other alkaline earth compositions in the A₄V₂O₉ ceramics (A= Sr, Ca, Mg and Zn) show remarkable changes in the Raman spectrum compared to A₃V₂O₈ analogues. The symmetry and molecular arrangements in A₃V₂O₈ ceramics have already been well studied and it is reported that most of these systems exhibit internal vibrations of (VO₄)³⁻ groups [20-25].

In order to confirm the difference in the Raman spectrum of A₄V₂O₉ from A₃V₂O₈ ceramics, Raman spectra of alkaline orthovanadate ceramics were also

recorded and the results are compared with that of $A_4V_2O_9$ systems (Figure 5.7 and Table 5.4). Symmetric stretching vibrations of $(VO_4)^{3-}$ tetrahedra are observed at 859 and 848 cm^{-1} for $Sr_3V_2O_8$ together with asymmetric stretching vibrations at 779 cm^{-1} whereas three symmetric stretching vibrations are appeared at 851, 830 and 807 cm^{-1} for $Sr_4V_2O_9$. The asymmetric stretching vibrations of $Sr_4V_2O_9$ are observed at 792 and 698 cm^{-1} . Similarly, the symmetric bending vibration of $Sr_3V_2O_8$ is observed at 326 cm^{-1} whereas two peaks are appeared at 356 and 343 cm^{-1} in the symmetric bending vibrations of $Sr_4V_2O_9$ composition. The more number of stretching and bending vibrations observed in the $Sr_4V_2O_9$ ceramic suggest a distorted VO_4 tetrahedral arrangement for this composition compared to $Sr_3V_2O_8$ analogue.

Similar changes are observed in the Raman spectrum of $Ca_4V_2O_9$ and $Mg_4V_2O_9$ ceramics. Symmetric stretching vibrations are appeared at 867, 828 and 800 cm^{-1} together with asymmetric stretching vibrations at 789 cm^{-1} for $Ca_4V_2O_9$ compared to $Ca_3V_2O_8$, where an additional symmetric stretching mode is observed at 926 cm^{-1} for $Ca_3V_2O_8$. Sharp stretching vibrations of $(VO_4)^{3-}$ are observed at 881 and 861 cm^{-1} along with shoulder peaks at 897 and 845 cm^{-1} for $Mg_3V_2O_8$. $Mg_4V_2O_9$ also has strong symmetric stretching vibrations at 859 and 823 cm^{-1} without any shoulder peaks. Asymmetric stretching vibrations of $(VO_4)^{3-}$ groups are observed at 793, 740 and 722 cm^{-1} for $Mg_3V_2O_8$ whereas only one peak is observed at 722 cm^{-1} for $Mg_4V_2O_9$ ceramic. Bending and lattice mode vibrations are almost similar for both $Mg_3V_2O_8$ and $Mg_4V_2O_9$ ceramics. Also, $Mg_4V_2O_9$ has less number of peaks compared to magnesium orthovanadate.

Strong symmetric stretching vibration is observed at 850 cm^{-1} for $Zn_3V_2O_8$ ceramic whereas more number of peaks is observed at 955, 910, 877, 861, 851, 820 and 807 cm^{-1} for $Zn_4V_2O_9$. However, both $Zn_3V_2O_8$ and $Zn_4V_2O_9$ have almost similar symmetric and asymmetric bending vibrations compared to other alkaline earth compositions. The lower symmetry and distortion of VO_4 tetrahedra may be the reason for the splitting of stretching modes in $Zn_4V_2O_9$ ceramics. As per the structural analysis, $Zn_3V_2O_8$ is composed of VO_4 tetrahedra with V-O bond lengths varying from 1.67Å to 1.79Å whereas the V-O bond length in VO_4 tetrahedra in $Zn_4V_2O_9$ varies from 1.65Å to 1.84Å.

Although there is not much difference in the V-O bond lengths in both the cases, the symmetric stretching vibrations of VO₄ tetrahedra in both cases are almost differ by 105 cm⁻¹. The wide variation in the symmetric stretching vibrations of VO₄ tetrahedra in Zn₃V₂O₈ and Zn₄V₂O₉ could be due to different structural environment.

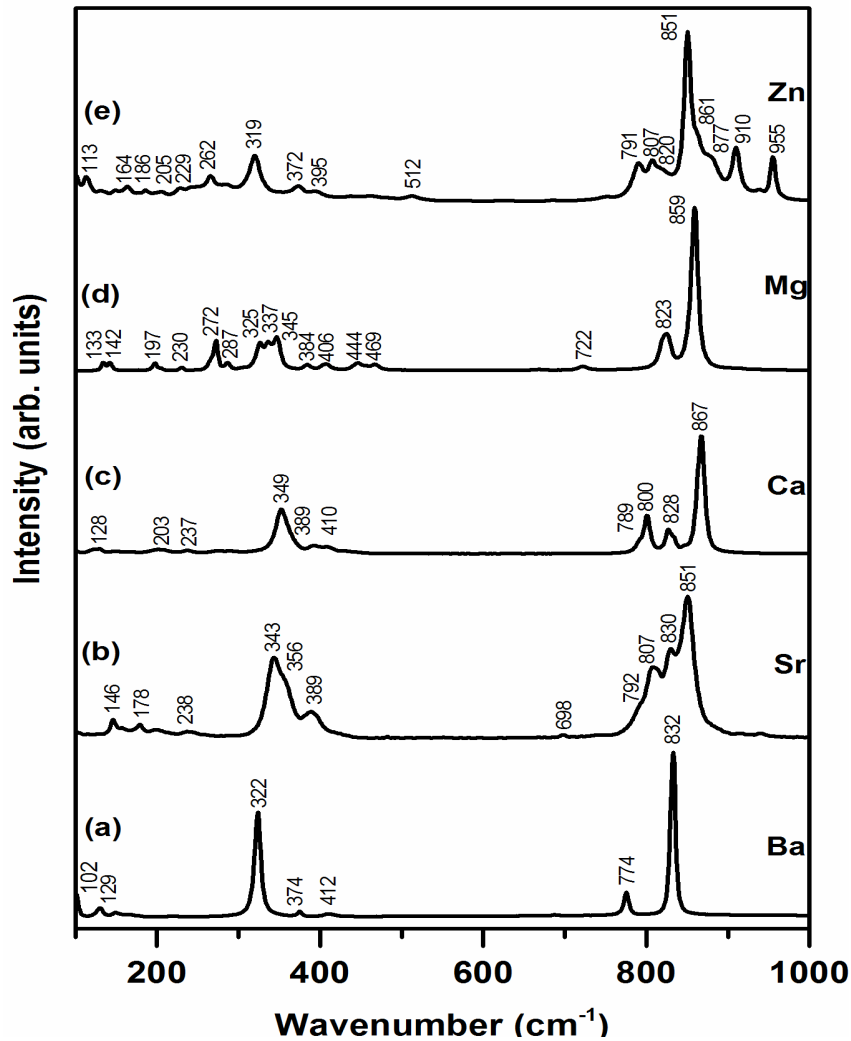


Figure 5.6 Raman spectra of A₄V₂O₉ (A= Ba, Sr, Ca, Mg and Zn) ceramics

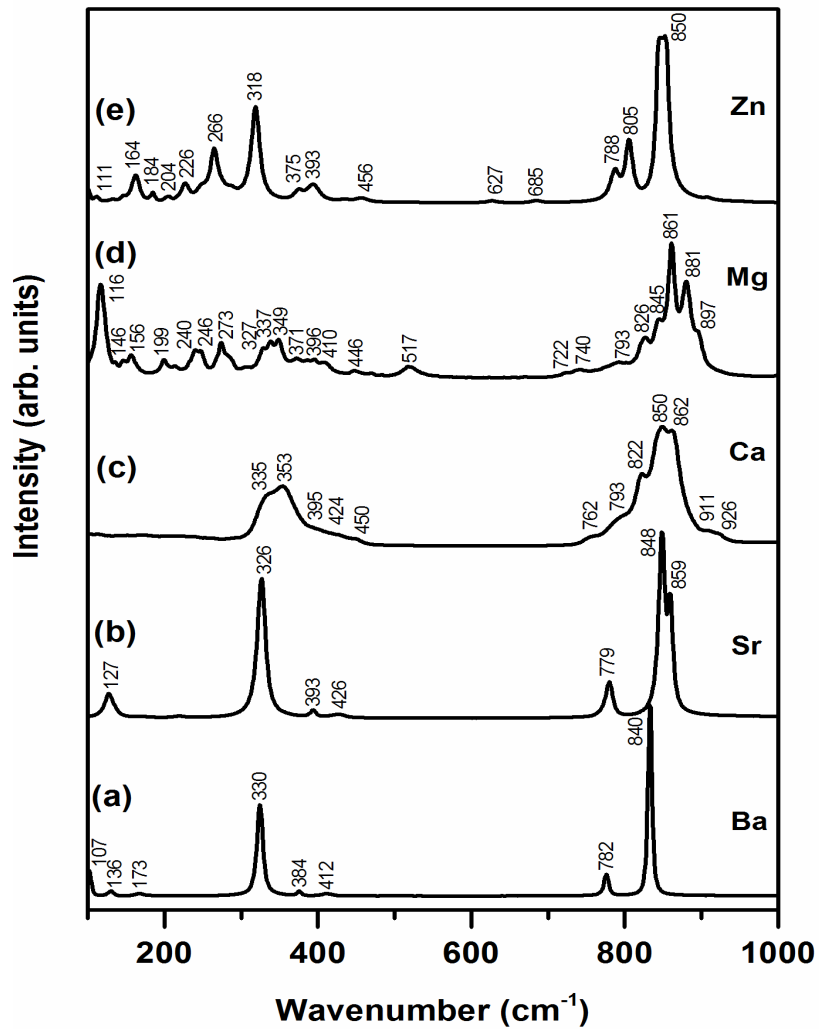


Figure 5.7 Raman spectra of $A_3V_2O_8$ (A= Ba, Sr, Ca, Mg and Zn) ceramics

Table 5.3 Raman mode assignments of $A_4V_2O_9$ (A=Ba, Sr, Ca, Mg and Zn) ceramics

$Ba_4V_2O_9$	$Sr_4V_2O_9$	$Ca_4V_2O_9$	$Mg_4V_2O_9$	$Zn_4V_2O_9$	Assignments
				955	$\nu_s (VO_4)^{3-}$
				910	
				877	
		867	859	861	
	851			851	
832	830	828	823	820	$\nu_s (VO_4)^{3-}$
	807	800		807	
774	792	789		791	
	698		722		
412		410	469	512	$\delta_{as} (VO_4)^{3-}$
374	389	389	444	395	
			406	372	
			384		$\delta_s (VO_4)^{3-}$
	356	349	345		
	343		337		
322			325	319	
			287	262	Lattice mode vibrations
			272	229	
	238	237	230	205	
		203	197	186	
129	178		142	164	
102	146	128	133	113	

ν_s – symmetric stretching, ν_{as} – asymmetric stretching, δ_{as} – asymmetric bending, δ_s – symmetric bending

Table 5.4 Raman mode assignments of $A_3V_2O_8$ (A=Ba, Sr, Ca, Mg and Zn) ceramics

$Ba_3V_2O_8$	$Sr_3V_2O_8$	$Ca_3V_2O_8$	$Mg_3V_2O_8$	$Zn_3V_2O_8$	Assignments
		926			$\nu_s (VO_4)^{3-}$
		911	897		
			881		
	859	862	861		
840	848	850	845	850	
		822	826	805	
782	779	793	793	788	$\nu_{as} (VO_4)^{3-}$
		762	740	685	
			722	627	
412	426	450	517	456	$\delta_{as} (VO_4)^{3-}$
384	393	424	446		
		395	410	393	
			396	375	
		353	371		
			349		
330	326	335	337		$\delta_s (VO_4)^{3-}$
			327	318	
			273	266	Lattice mode vibrations
			246	226	
			240	204	
			199	184	
173			156	164	
136	127		146		
107			116	111	

ν_s – symmetric stretching, ν_{as} – asymmetric stretching, δ_{as} – asymmetric bending, δ_s – symmetric bending

5.3.3 Morphological and dielectric studies

Figure 5.8 shows the SEM images of $A_4V_2O_9$ with $A = \text{Ba, Sr, Mg}$ and Zn ceramics sintered at optimum temperatures. $\text{Ba}_4\text{V}_2\text{O}_9$ ceramic has a porous microstructure with average grain size of $\sim 1 \mu\text{m}$ whereas $\text{Sr}_4\text{V}_2\text{O}_9$ has needle like grains along with polygonal grains. $\text{Mg}_4\text{V}_2\text{O}_9$ ceramic shows dense microstructure with polygonal grains with 1 to 3 μm size. $\text{Zn}_4\text{V}_2\text{O}_9$ ceramic also exhibits a dense microstructure with an average grain size of around 10 μm .

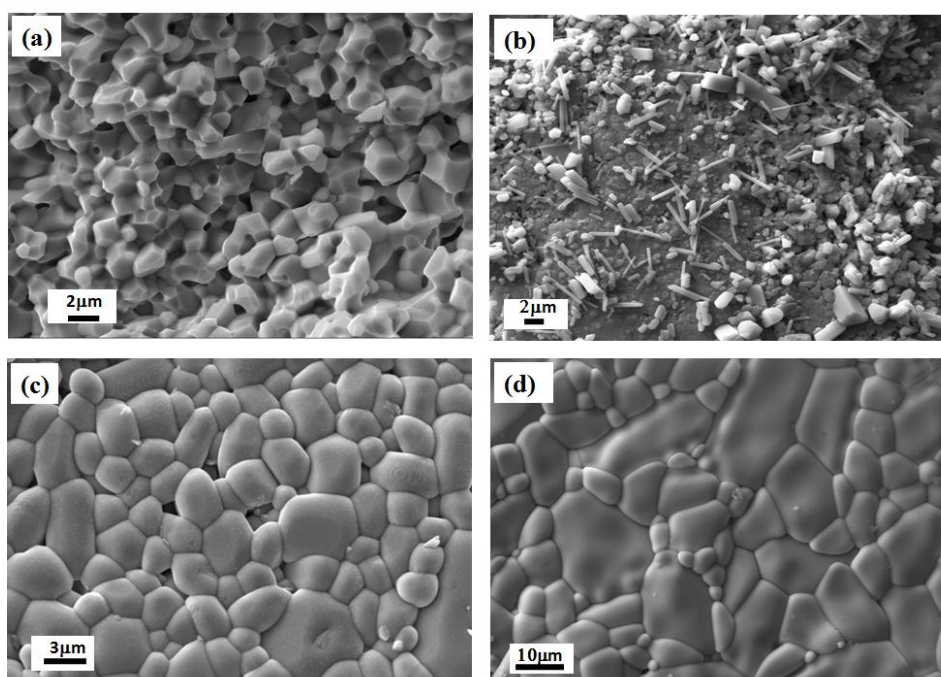


Figure 5.8 SEM images of (a) $\text{Ba}_4\text{V}_2\text{O}_9$ (b) $\text{Sr}_4\text{V}_2\text{O}_9$ (c) $\text{Mg}_4\text{V}_2\text{O}_9$ and (d) $\text{Zn}_4\text{V}_2\text{O}_9$ at optimum sintering temperatures

Table 5.5 shows the sintering temperature, density and dielectric properties of $A_4V_2O_9$ ceramics. $A_4V_2O_9$ ceramics with $A = \text{Ba, Sr, Mg}$ and Zn are well sintered below 950°C but $\text{Ca}_4\text{V}_2\text{O}_9$ exhibits a maximum density of 2.28 g/cc only even after sintering at 1250°C for 4h. The dielectric property measurement of this composition is not possible since the pellet crumbles within few hours after sintering. Among the $A_4V_2O_9$ samples studied, only $\text{Mg}_4\text{V}_2\text{O}_9$ ceramic shows microwave dielectric properties. It is clear from the Raman spectroscopic studies that $\text{Mg}_4\text{V}_2\text{O}_9$ has least distorted $(\text{VO}_4)^{3-}$ groups among $A_4V_2O_9$, which is a clear indication of structural ordering in this composition thereby resulting better microwave dielectric properties.

The optimum sintering temperature, density, dielectric constant and loss tangent of $A_4V_2O_9$ and $A_3V_2O_8$ samples at 1 MHz and GHz range are compiled in Table 5.5.

Table 5.5 Sintering temperature, density and dielectric properties of $A_4V_2O_9$ and $A_3V_2O_8$ (A=Ba, Sr, Ca, Mg, Zn) ceramics

Compound	Sintering Temp. (°C)	Density (g/cc)	Low frequency data (at 1MHz)		Microwave frequency data (GHz)			References
			ϵ_r	$\tan\delta$	ϵ_r	Qxf (GHz)	τ_f (ppm/°C)	
$Ba_4V_2O_9$	850/1h	4.35	11.44	0.14	*	*	*	<i>This work</i>
$Sr_4V_2O_9$	720/1h	3.77	11.16	0.003	*	*	*	<i>This work</i>
$Ca_4V_2O_9$	1250/4h	2.28	#	#	*	*	*	<i>This work</i>
$Mg_4V_2O_9$	940/1h	2.44	8.2	0.082	6.3	37,263	-43.5	<i>This work</i>
$Zn_4V_2O_9$	740/1h	4.14	18.16	0.1	*	*	*	<i>This work</i>
$Ba_3V_2O_8$	1600/5h	4.5	13.3	0.094	11	62,347	28.8	Ref. 4
$Sr_3V_2O_8$	1000/1h	3.91	26.72	0.414	*	*	*	<i>This work</i>
$Ca_3V_2O_8$	1100/1h	2.16	8.73	0.001	*	*	*	<i>This work</i>
$Mg_3V_2O_8$	950/50h	3.34	11.4	0.006	9.1	64,142	-93.2	Ref. 26
$Zn_3V_2O_8$	750/1h	4.2	16.17	0.053	*	*	*	<i>This work</i>

Measurement not possible, - No resonance

Figure 5.9 shows the variation of density and dielectric constant of $Mg_4V_2O_9$ ceramic sintered at different temperatures for 1h. Both density and dielectric constant show an increasing trend with sintering temperature up to 940°C. Further increase in sintering temperature deteriorates both density and dielectric constant of $Mg_4V_2O_9$ ceramics. At an optimum sintering temperature of 940°C for 1h, $Mg_4V_2O_9$ ceramic exhibits a maximum density of 2.44 g/cc together with a dielectric constant of 6.3 and Qxf of 37,263 GHz. Figure 5.10 shows the temperature variation of resonant frequency (τ_f) of $Mg_4V_2O_9$ ceramic sintered at 940°C for 1 h in the temperature range 30-100°C. The resonant frequency of $Mg_4V_2O_9$ ceramic shows a decreasing trend with increasing temperature and the sample exhibited a negative τ_f value of -43.5 ppm/°C.

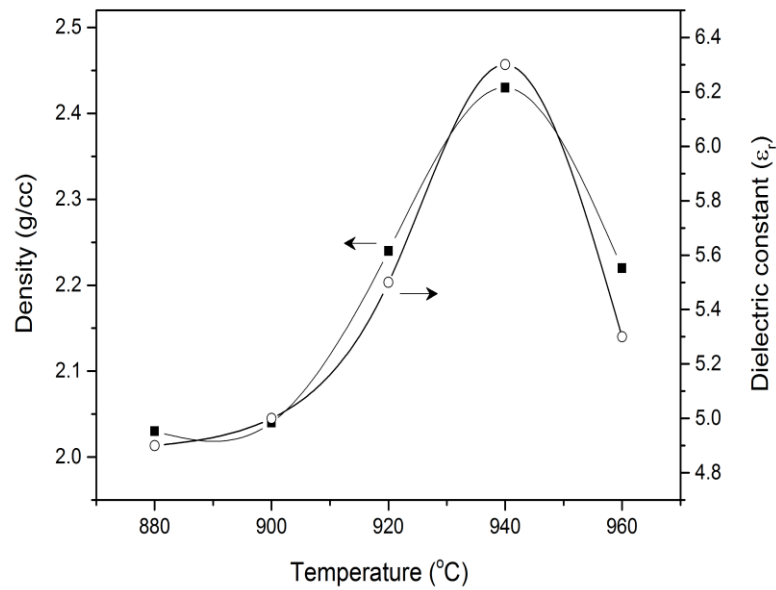


Figure 5.9 Variation of density and dielectric constant of $Mg_4V_2O_9$ ceramic with sintering temperature

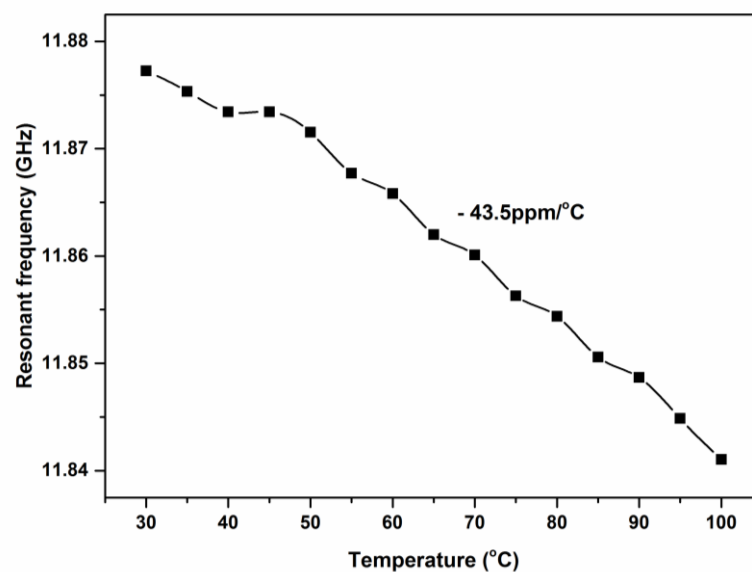


Figure 5.10 Temperature variation of resonant frequency of $Mg_4V_2O_9$ ceramic sintered at 940°C for 1h

It is interesting to note that $Zn_4V_2O_9$ sample shows highest dielectric constant at 1 MHz among the samples under study. The crystal structure of this composition has the most distorted $(VO_4)^{3-}$ groups, which is evident from the structural studies and the Raman bands are also observed at very high wavenumbers together with

splitting. The absence of microwave resonance in this composition can be attributed to the highly distorted $(VO_4)^{3-}$ groups.

5.3.4 Compatibility studies

In order to use $Mg_4V_2O_9$ ceramic for LTCC applications, chemical compatibility with metal electrode is an essential requirement. To evaluate the chemical compatibility, $Mg_4V_2O_9$ ceramic was co-fired with 20 wt% Ag powder at 900°C for 1h. The resultant XRD pattern is shown in Figure 5.11 and the pattern does not show any secondary phase formation. The silver peaks are observed separately and are marked with “o”.

Figure 5.12a shows the backscattered image of the co-fired $Mg_4V_2O_9$ ceramic on the planar surface. In order to quantify the compatibility of Ag with the $Mg_4V_2O_9$ composition, co-fired samples are subjected to EDS (energy dispersive spectroscopy) analysis (Figure 5.12 b and c). Spot 1 shows the segregation of melted Ag particles whereas Spot 2 represents well-formed grains of $Mg_4V_2O_9$ ceramic. It is clear from the EDS spectra that there is no inter-diffusion of Ag into $Mg_4V_2O_9$ phase. The X-ray dot mapping of the co-fired sample is also done to establish the non-reactivity of Ag in the host matrix (Figure 5.13). The X-ray dot mapping result clearly shows the isolation of melted Ag particles in deep red color without any inter-diffusion complementing the XRD and spot analyses results. Further, EDS line scan of the co-fired $Mg_4V_2O_9$ ceramic was carried out in order to quantify the XRD and spot analysis results (Figure 5.14). EDS line scan analysis reveals that the concentration of Ag particles sharply decreases at the Ag-ceramic interface clearly indicating that Ag particles are not diffused into the ceramic grains. In view of the above results, it can be inferred that the $Mg_4V_2O_9$ ceramic has excellent chemical compatibility with Ag electrode together with relatively good microwave dielectric properties and hence can be used for LTCC applications.

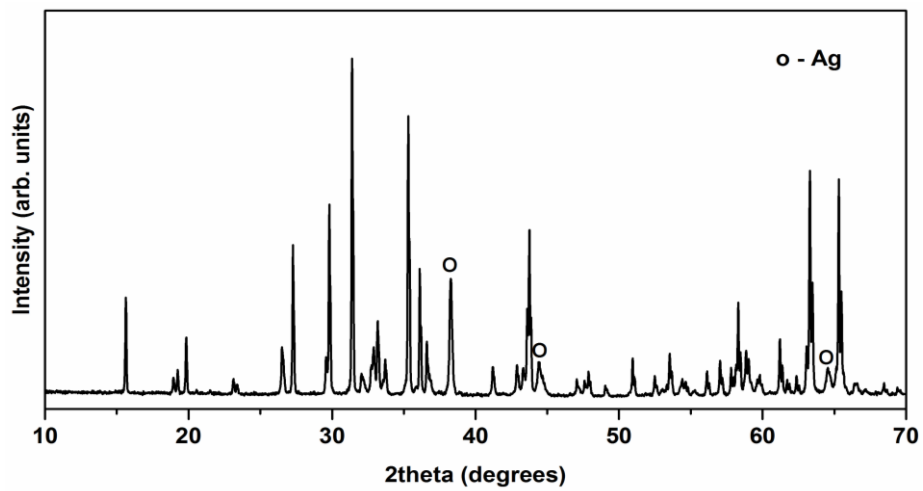


Figure 5.11 XRD pattern of $Mg_4V_2O_9 + 20 \text{ wt}\% \text{ Ag}$ ceramic sintered at 940°C for 1h

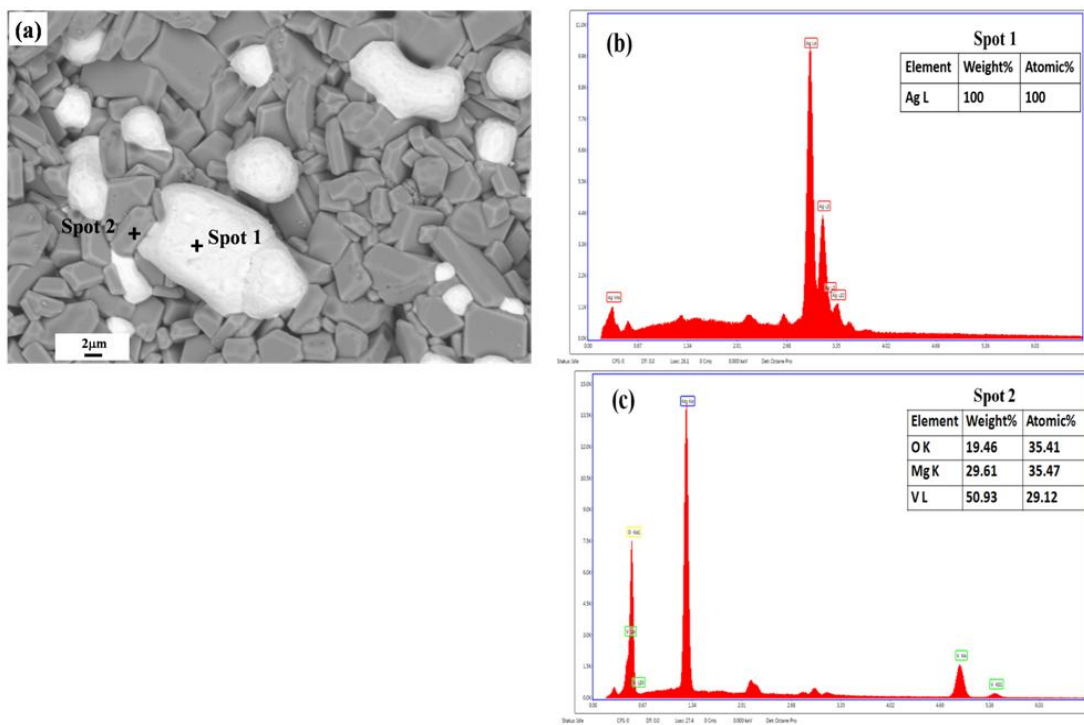


Figure 5.12 (a) Backscattered image of $Mg_4V_2O_9$ ceramic co-fired with 20 wt% Ag (b) EDS spectrum of spot 1 and (c) EDS spectrum of spot 2

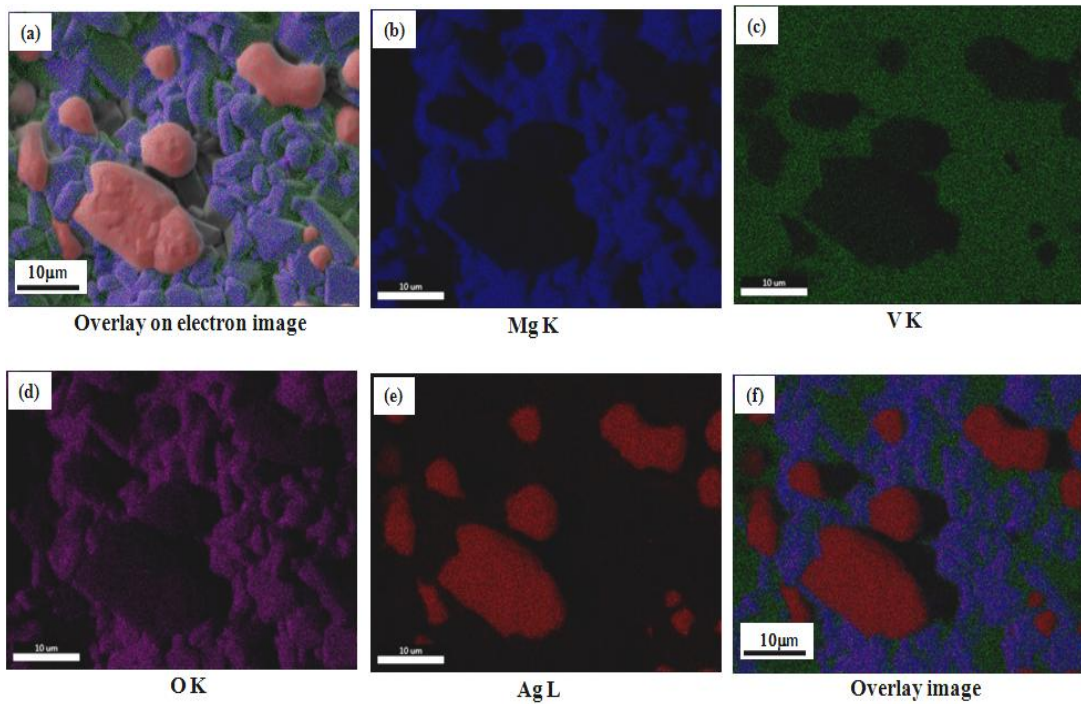


Figure 5.13 X-ray dot mapping of $Mg_4V_2O_9$ ceramic co-fired with 20 wt% Ag [(a) Overlay on secondary electron image (b-e) elemental images (f) overlay image]

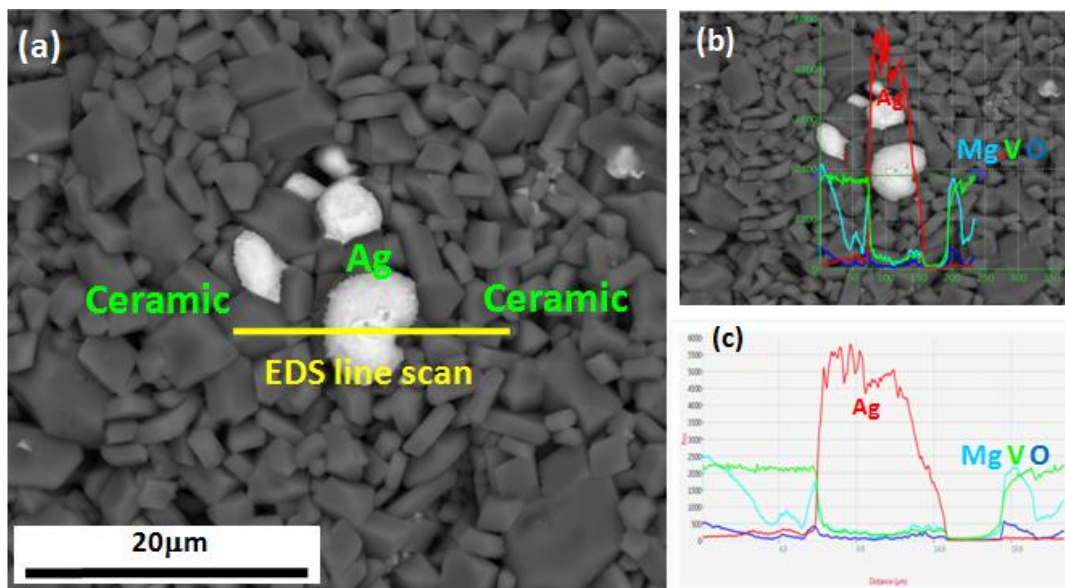


Figure 5.14 EDS line scan of $Mg_4V_2O_9$ ceramic co-fired with 20 wt% Ag

5.4 Conclusions

Alkaline earth vanadate $A_4V_2O_9$ ceramics with $A = \text{Ba, Sr, Ca, Mg and Zn}$ have been prepared through conventional solid state ceramic method. The phase purity of the samples was confirmed by powder X-ray diffraction technique. Raman spectroscopic studies validated the existence of $A_4V_2O_9$ ceramics in the $\text{AO-V}_2\text{O}_5$ binary system with $(\text{VO}_4)^{3-}$ vibrational groups. Distinct structural differences were observed in the Raman spectra of both oxovanadate and orthovanadate ceramics which support the formation of single phase materials in the phase diagram with high alkaline earth mol%. $\text{Mg}_4\text{V}_2\text{O}_9$ ceramic has been identified as a microwave ceramic material with phase purity for the first time. At optimum sintering temperature of 940°C for 1h, $\text{Mg}_4\text{V}_2\text{O}_9$ ceramic has a dielectric constant of 6.3, Q_{xf} of 37,263 GHz and a negative τ_f of $-43.5 \text{ ppm}/^\circ\text{C}$. The XRD and EDS analyses reveal good chemical compatibility between $\text{Mg}_4\text{V}_2\text{O}_9$ and Ag electrode. X-ray dot mapping of the co-fired $\text{Mg}_4\text{V}_2\text{O}_9$ ceramic also rule out the chemical interaction between $\text{Mg}_4\text{V}_2\text{O}_9$ and Ag powder. Present study shows that $\text{Mg}_4\text{V}_2\text{O}_9$ ceramic can be used as a suitable candidate material for LTCC applications.

References

- [1] A. A. Fotiev, V. V. Makarov, V. L. Volkov, L. L. Surat, *Russ. J. Inorg. Chem.*, 14 [4] (1969) 144-146.
- [2] A. N. Unnimaya, E. K. Suresh, R. Ratheesh, *Eur. J. Inorg. Chem.*, 2015 [2] (2015) 305–310.
- [3] M. R. Joung, J. S. Kim, M. E. Song, S. Nahm, *J. Am. Ceram. Soc.*, 92 [12] (2009) 3092–3094.
- [4] R. Umemura, H. Ogawa, A. Yoko, H. Ohsato, A. Kan, *J. Alloy. Compds.*, 424 [1-2] (2006) 388 – 393.
- [5] E. K. Suresh, A. N. Unnimaya, R. Ratheesh, *J. Am. Ceram. Soc.*, 97 [5] (2014) 1530-1533.
- [6] B. Golovkin, L. Kristallov, *Zh. Neorg. Khim.*, 35 (1990) 253-255.
- [7] V. A. Makarov, A. A. Fotieve, L. N. Srerbryakova, *Zh. Neorg. Khim.*, 16 (1971) 2849.
- [8] M. Kurzawa, I. Rychlowska-Himmel, M. Bosocka, A. Blonoska-Tabero, *J. Them. Anal. Cal.*, 64 (2001) 1113-1119.
- [9] M. Waburg, H. Muller-Buschbaum, *Monatsh. Chem.*, 117 (1986)131-138.
- [10] J. J. Brown, *J. Am. Ceram. Soc.*, 55 [10] (1972) 500-503.
- [11] Y. N. Zhu, G. H. Zheng, Z. X. Dai, L. Y. Zhang, Y. Q. Li, J. J. Mu, *Mater. Resear. Bull.*, 70 (2015) 222–228.
- [12] Y. Yuan, *Steel Res.*, 62 (1991) 60-65.
- [13] B. W. Hakki, P. D. Colcman, *IRE Trans. Microw. Theory Tech.*, 8 [4] (1960) 402-410.
- [14] J. Mazierska, M. V. Jacob, A. Harring, J. Krupka, P. Barnwell, T. Sims, *J. Eur. Ceram. Soc.*, 23 [14] (2003) 2611–2615.
- [15] P. Susse, M. J. Buerger, *Zeit. Kristallogr.*, 131 [1-6] (1970) 161-174.

- [16] W. C. Cabrera, H.G. Von Schnering, *Zeit. Kristallogr.*, 205 [1-2] (1993) 271–276.
- [17] R. Gopal, C. Calvo, *Zeit. Kristallogr.*, 137 [1-6] (1973) 67-85.
- [18] N. Krishnamachari, C. Calvo, *Can. J. Chem.*, 49 [10] (1971) 1629-1637.
- [19] R. Gopal and C. Calvo, *Can. J. Chem.*, 49 [18] (1971) 3056-3059.
- [20] A. N. Unnimaya, E. K. Suresh, J. Dhanya, R. Ratheesh, *J Mater Sci: Mater Electron.*, 25 [2] (2014) 1127–1131.
- [21] K. B. Shim, C. S. Lim, *J. Ceram. Proc. Research.*, 13 (2012) 291-295.
- [22] M. K. Ryu , J. G. Choi , G. H. Kim , S. Kojima , M. Takashige, M. S. Jang, *Ferroelectrics.*, 332 [1] (2006) 1-5.
- [23] A. Grzechnik, *Chem. Mater.*, 10 [4] (1998) 1034-1040.
- [24] G. Busca, G Ricchiardi, D. Siew Hew Sam, J. Volta, *J. Chem. Soc. Faraday Trans.*, 90 [8] (1994) 1161-1170.
- [25] S. Ni, X. Wang, G. Zhou, F. Yang, J. Wang, D. He, *J. Alloy. Compd.*, 491 [1-2] (2010) 378–381.
- [26] R. Umemura, H. Ogawa, H. Ohsato, A. Kan, A. Yokoi, *J. Eur. Ceram. Soc.*, 25 [12] (2005) 2865-2870.

6

Effect of A site Substitution on the Structure and Microwave Dielectric Properties of $A_4V_2O_9$ Ceramics

- 6.1 Introduction
- 6.2 Experimental techniques
- 6.3 Results and discussion
- 6.4 Conclusions

6.1 Introduction

Multilayer ceramics is one among the rapidly growing research areas, since it offers electronic devices with higher integration density, processing speed and circuit miniaturization. Among these parameters, miniaturization is the critical factor for device applications. In this context, low temperature co-fired ceramics (LTCC) attained considerable attention for the development of miniaturized devices for microwave/millimeter wave communication [1-4]. In chapter 5, detailed studies have been carried out to understand the structure and microwave dielectric properties of new alkaline earth $A_4V_2O_9$ (A= Ba, Sr, Ca, Mg and Zn) ceramics for LTCC applications. Among $A_4V_2O_9$ compositions studied, only $Mg_4V_2O_9$ exhibits microwave dielectric properties. It is inferred from the Raman spectroscopic studies that VO_4 tetrahedra is least distorted in magnesium oxovanadate compared to other alkaline earth analogues. Hence an attempt has been made in this chapter to partially substitute A site by R^{3+} (R= Bi, La, Nd, Y and Yb) ions with an objective to alter the crystal structure of $A_4V_2O_9$ ceramics and thereby improve their microwave dielectric properties.

The crystal structure of $Bi_2CaV_2O_9$ is well studied by Evans et al. in the Bi_2O_3 -CaO- V_2O_5 system [5]. Other single phase materials in this phase diagram are $BiCaVO_5$, $BiCa_2VO_6$, $BiCa_4V_3O_{13}$, $BiCa_9V_7O_{28}$ and $Bi_3Ca_9V_{11}O_{41}$ respectively [6-10]. Evans et al. reported that $Bi_2CaV_2O_9$ belongs to monoclinic crystal structure with $P2_1/n$ space group where A site is fully occupied by disordered mixtures of Bi and Ca. Eight of the nine oxygen atoms in the asymmetric unit forms VO_4 tetrahedron while the remaining oxygen atoms bond only to A site cations and has relatively short distances to Bi-rich sites A1 and A3 [5]. There are also published reports available on the crystal structure of $Bi_2SrV_2O_9$ compound. $Bi_2SrV_2O_9$ compound belongs to orthorhombic aurivillius-Bi-layered perovskite crystal structure with $A21am$ space group [11, 12]. However, to the best of our knowledge, there are no reports available on the phase formation and crystal structure of $Bi_2AV_2O_9$ ceramics with A= Ba, Mg and Zn.

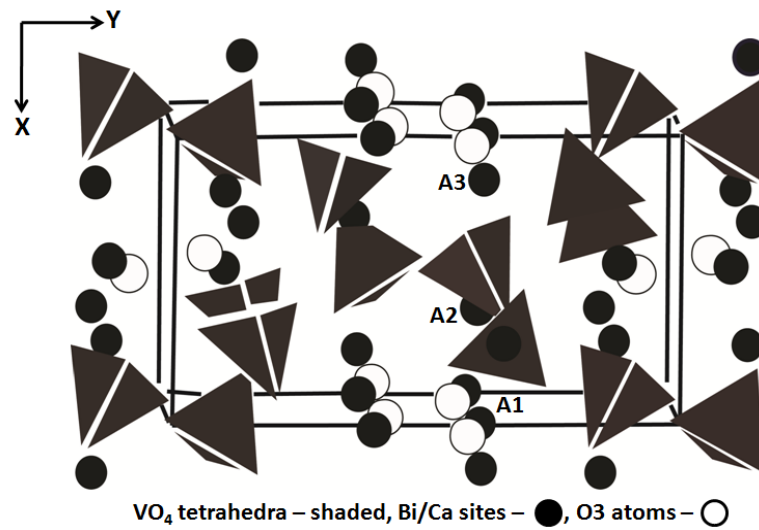


Figure 6.1 Structure of $\text{Bi}_2\text{CaV}_2\text{O}_9$ [Ref. 5]

In the present work, alkaline earth ions are substituted with Bi and R^{3+} ions in $\text{A}_4\text{V}_2\text{O}_9$ ceramics and the crystal structure and microwave dielectric properties of the resulting $\text{R}_2\text{AV}_2\text{O}_9$ (R= Bi, La, Nd, Y and Yb; A= Ba, Sr, Ca, Mg and Zn) ceramics are studied in detail.

6.2 Experimental techniques

$\text{R}_2\text{AV}_2\text{O}_9$ ceramics (R= Bi, La, Nd, Y and Yb; A= Ba, Sr, Ca, Mg and Zn) were prepared by conventional solid state ceramic route. High purity oxides and carbonates such as Bi_2O_3 (Himedia, 99%), La_2O_3 (Sigma Aldrich, 99%), Nd_2O_3 (Aldrich, 99.9%), Y_2O_3 (Star Rare Earth, 99.9%), Yb_2O_3 (Treibacher, 99.9%), BaCO_3 (Sigma Aldrich, 99%), SrCO_3 (Himedia, 99%), CaCO_3 (Sigma Aldrich, 99%), MgO (Sigma Aldrich, 99+ %), ZnO (Sigma Aldrich, 99%) and V_2O_5 (Sigma Aldrich, 99%) were used as starting materials. Stoichiometric amounts of the raw materials were weighed and wet mixed in distilled water for an hour in an agate mortar. The resultant slurry was dried at 100°C in a hot air oven, then ground well, and calcined at 600°C for an hour. The calcined powders were ground again and then mixed with 5 wt% polyvinyl alcohol (PVA) as binder and dried well. The granulated powders were pressed uniaxially in a 11 mm diameter tungsten carbide (WC) die by applying a uniaxial pressure of 250 MPa in a hydraulic hand press. These cylindrical green compacts were sintered in a programmable furnace at various temperatures in the range $650\text{--}800^\circ\text{C}$. The green compacts were fired at a rate of $5^\circ\text{C}/\text{min}$ up to the

sintering temperature and an intermediate soaking was given at 600°C for 30 min to expel the binder (PVA).

Phase purity of the $R_2AV_2O_9$ samples were studied by powder X-ray diffraction (XRD) measurement using CuK_{α} radiation (Bruker 5005, Germany). The Raman spectra of the $Bi_2AV_2O_9$ compositions under study were recorded using a Thermo Scientific DXR with Nd:YVO₄ DPSS laser of 532nm. The surface morphology of the sintered samples was studied using scanning electron microscopy (Carl Zeiss Model No- EVO18 Research, Germany). The low frequency measurements of the samples were carried out at 1 MHz using an impedance analyzer (Agilent, 4294A, Malaysia). The microwave dielectric properties were measured using a vector network analyzer (Agilent make PNA E8362B, Bayan Lepas, Malaysia). The dielectric constant and the unloaded quality factor of the samples were measured by Hakki and Coleman post resonator and resonant cavity methods respectively [13, 14]. The temperature coefficient of resonant frequency (τ_f) was also measured by noting the variation of $TE_{01\delta}$ mode frequency with temperature in the range of 30-100°C.

6.3 Results and discussion

6.3.1 X-ray diffraction studies

Figure 6.2 shows the X-ray diffraction patterns of sintered $Bi_2AV_2O_9$ samples. Among $Bi_2AV_2O_9$ (A= Ba, Sr, Ca, Mg and Zn) samples, detailed crystal structure study is available only for $Bi_2CaV_2O_9$ composition [5]. $Bi_2CaV_2O_9$ crystallizes in the monoclinic crystal structure with $P2_1/n$ space group having lattice parameters $a=7.096$, $b=12.4$, $c=9.397$ Å with four number of atoms per unit cell. The XRD pattern of $Bi_2CaV_2O_9$ obtained in the present study also matches with the Rietveld refined XRD pattern reported by Evans et al. [5]. Although structure paper is available for $Bi_2CaV_2O_9$ ceramic, indexing of the XRD pattern is not possible because of the non-availability of hkl planes in the published literature.

On the other hand, $Bi_2SrV_2O_9$ belongs to orthorhombic crystal structure with $A21am$ space group having lattice parameters $a=5.5195$, $b=5.5249$ and $c=25.2837$ Å respectively [11]. In addition to $Bi_2SrV_2O_9$ phase, small amount of $BiVO_4$ secondary phase is also observed in the present study although it was not found in the structural

studies by Elsbawy et al. [11]. In this case also indexing is not possible because of the non-availability of hkl planes in the structure paper.

Since crystal structure reports are not available for $Bi_2AV_2O_9$ with $A = Ba, Mg$ and Zn , the XRD patterns of $Bi_2AV_2O_9$ ($A = Ba, Mg$ and Zn) in the present study are compared with the probable phases in the $Bi_2O_3-V_2O_5$ and $Bi_2O_3-CaO-V_2O_5$ systems [15-17, 5-10]. The diffraction peaks corresponding to monoclinic $BiVO_4$ phase (ICDD No: 75-1867) are present in $Bi_2AV_2O_9$ ceramics where $A = Ba, Mg$ and Zn together with some additional peaks. It can be inferred from the solid solution of $Bi_2MgV_2O_9$ that $BiMgVO_5$ could be one of the probable phases present along with $BiVO_4$. Therefore, the X-ray diffraction pattern of the $Bi_2MgV_2O_9$ is compared with the $BiVO_4$ and $BiMgVO_5$ [18] phases and are marked with ‘*’ and ‘#’ respectively. Similarly secondary phases of $BiBaVO_5$ and $BiVO_4$ phases are seen in the XRD pattern of $Bi_2BaV_2O_9$ whereas $BiZnVO_5$ and $BiVO_4$ phases are observed in the XRD pattern of $Bi_2ZnV_2O_9$. From the above studies, it can be inferred that among the samples studied only $Bi_2CaV_2O_9$ exists as single phase.

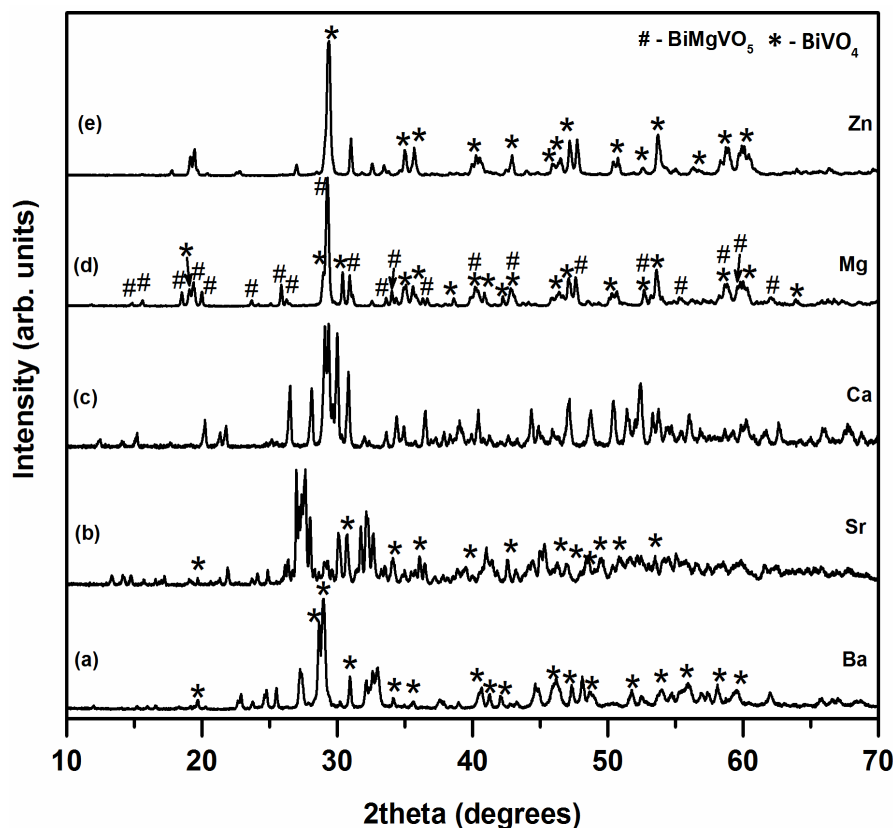


Figure 6.2 XRD patterns of $Bi_2AV_2O_9$ with $A = Ba, Sr, Ca, Mg$ and Zn ceramics

In order to further explore the possibility of arriving at single phase compositions, Bi^{3+} ions are replaced with rare earth ions with varying ionic radii and the resultant XRD patterns of the sintered $R_2AV_2O_9$ ($R = La, Nd, Y, Yb$; $A = Ba, Sr, Ca$) samples are given in Figures 6.3, 6.4 and 6.5. From the X-ray diffraction pattern of $La_2BaV_2O_9$ compound, it is clear that the partial substitution of A^{2+} ions with La^{3+} ions result multiphase compositions and the diffraction peaks corresponding to the monoclinic $LaVO_4$ phase (ICDD Card No: 70-0216) together with $LaBaVO_5$ phase.

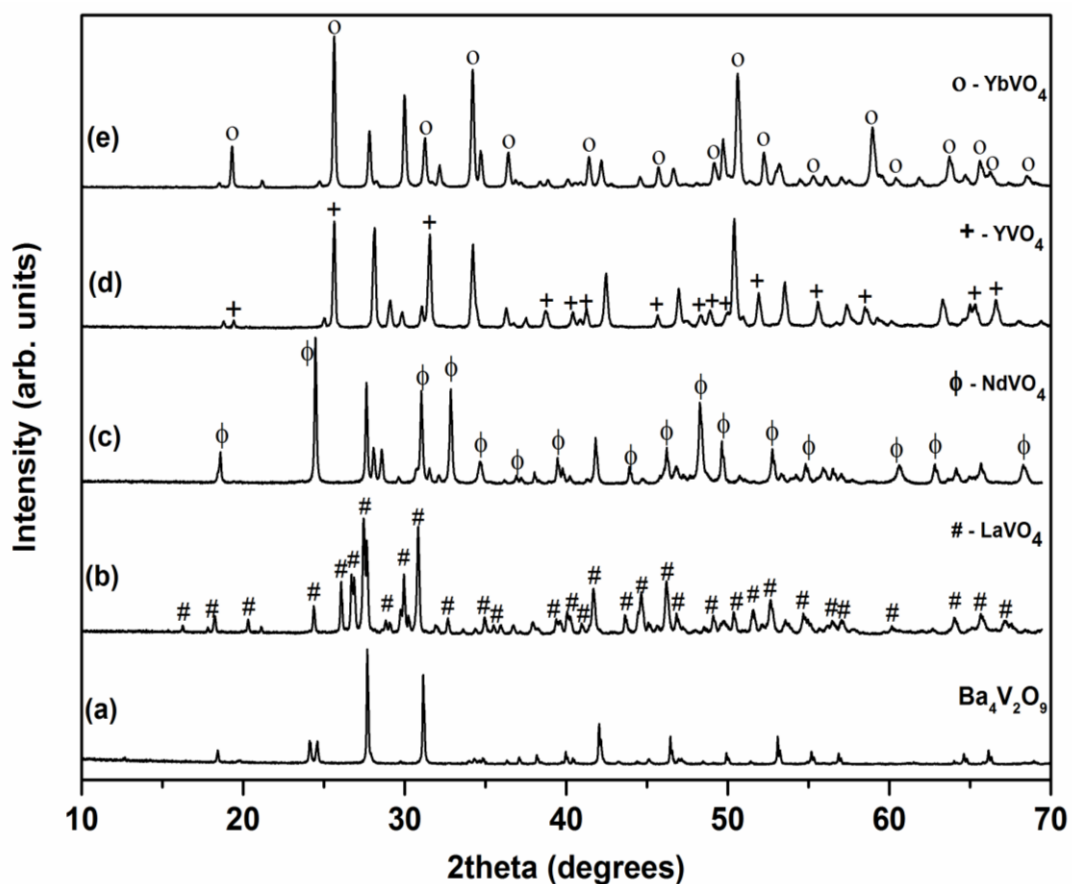


Figure 6.3 XRD patterns of $R_2BaV_2O_9$ ceramics with $R = La, Nd, Y$ and Yb

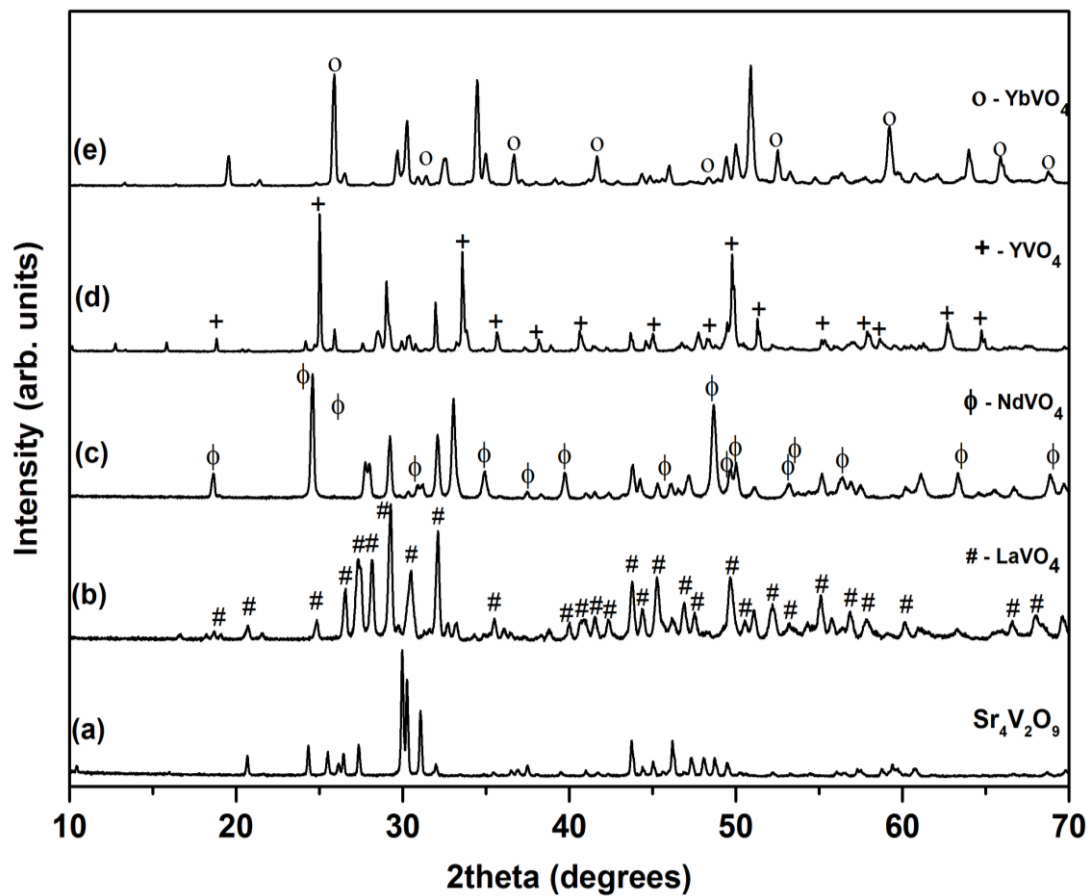


Figure 6.4 XRD patterns of $R_2SrV_2O_9$ ceramics with $R=La, Nd, Y$ and Yb

$R_2BaV_2O_9$ compounds with other rare earth elements ($R=Nd, Y$ and Yb) also exhibit multiphase nature and the obtained X-ray diffraction patterns comprising of RVO_4 and are marked separately with 'φ', '+' and 'o' respectively whereas the additional peaks could be that of $RAVO_5$ phases where $R=Nd, Y$ and $Yb, A=Ba, Sr$ and Ca . Since rare earth substitution in $A_4V_2O_9$ ($A=Ba, Sr$ and Ca) result multiphase $R_2AV_2O_9$ compositions, further detailed studies of $R_2AV_2O_9$ samples have not been carried out.

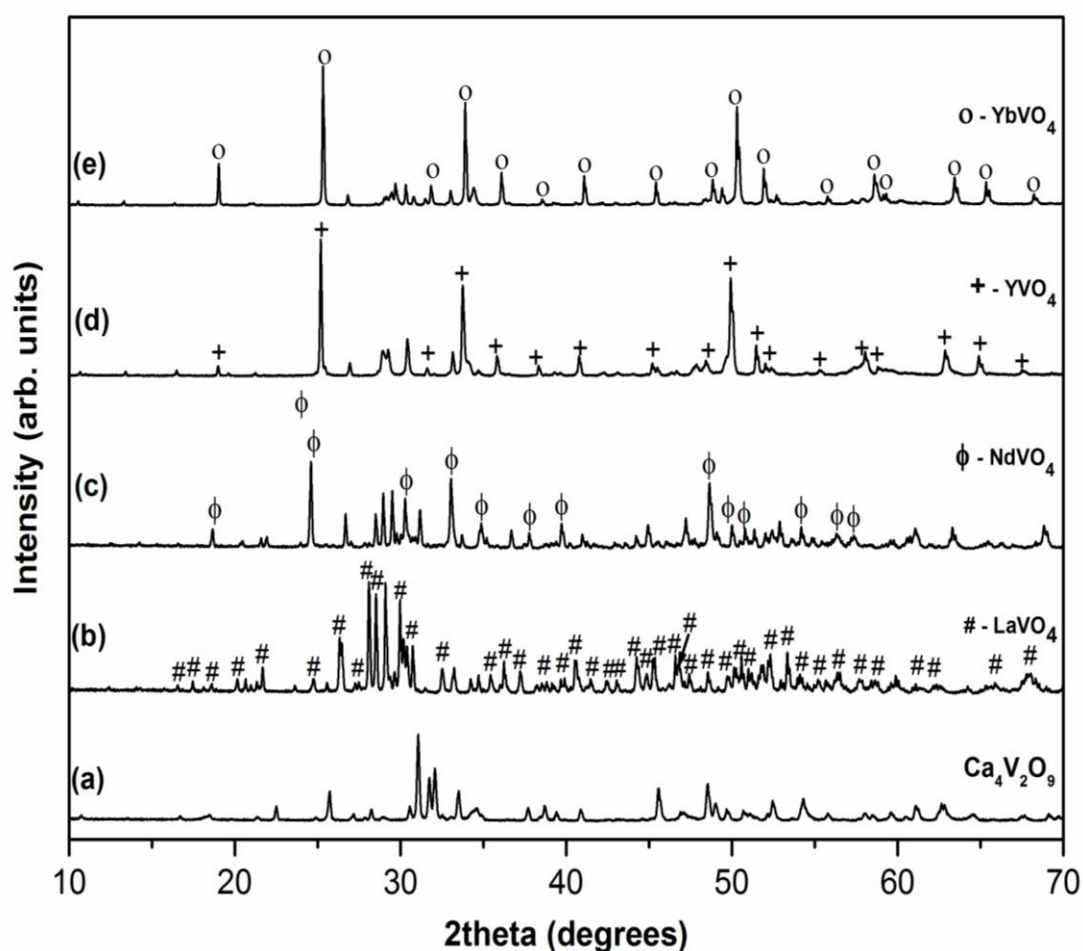


Figure 6.5 XRD patterns of $R_2CaV_2O_9$ ceramics with $R=La, Nd, Y$ and Yb

6.3.2 Raman spectroscopic studies

In order to study the effect of partial substitution of Bi^{3+} ions on the crystal structure of $A_4V_2O_9$ in detail, Raman spectra of $Bi_2AV_2O_9$ ($A= Ba, Sr, Ca, Mg$ and Zn) compositions were recorded and are compared with that of $A_4V_2O_9$ ($A= Ba, Sr, Ca, Mg$ and Zn) (Figure 6.6). As per the Raman spectroscopic studies carried out in Chapter 5, $A_4V_2O_9$ compounds have vibrational modes corresponding to distorted VO_4 tetrahedra and the modes are assigned based on that. Symmetric stretching vibrations of VO_4 tetrahedra are observed at 832 cm^{-1} for $Ba_4V_2O_9$ together with an asymmetric stretching vibration at 774 cm^{-1} . In the case of $Bi_2BaV_2O_9$ compound, the symmetric stretching vibrations are observed at $826, 864, 892$ and 927 cm^{-1} along with asymmetric stretching vibration at 745 cm^{-1} . According to Frost et al., the Raman spectrum of $BiVO_4$ exhibits intense Raman mode near 820 cm^{-1} which can

be assigned to the symmetric stretching mode of $(VO_4)^{3-}$ vibrational unit, and a weak asymmetric V–O stretching mode is observed at about 707 cm^{-1} . The symmetric and asymmetric bending modes of $BiVO_4$ are found at 366 and 325 cm^{-1} respectively [19]. Hence, the vibrational mode observed at 826 cm^{-1} could be attributed to the symmetric stretching vibration of VO_4 tetrahedra present in $BiVO_4$.

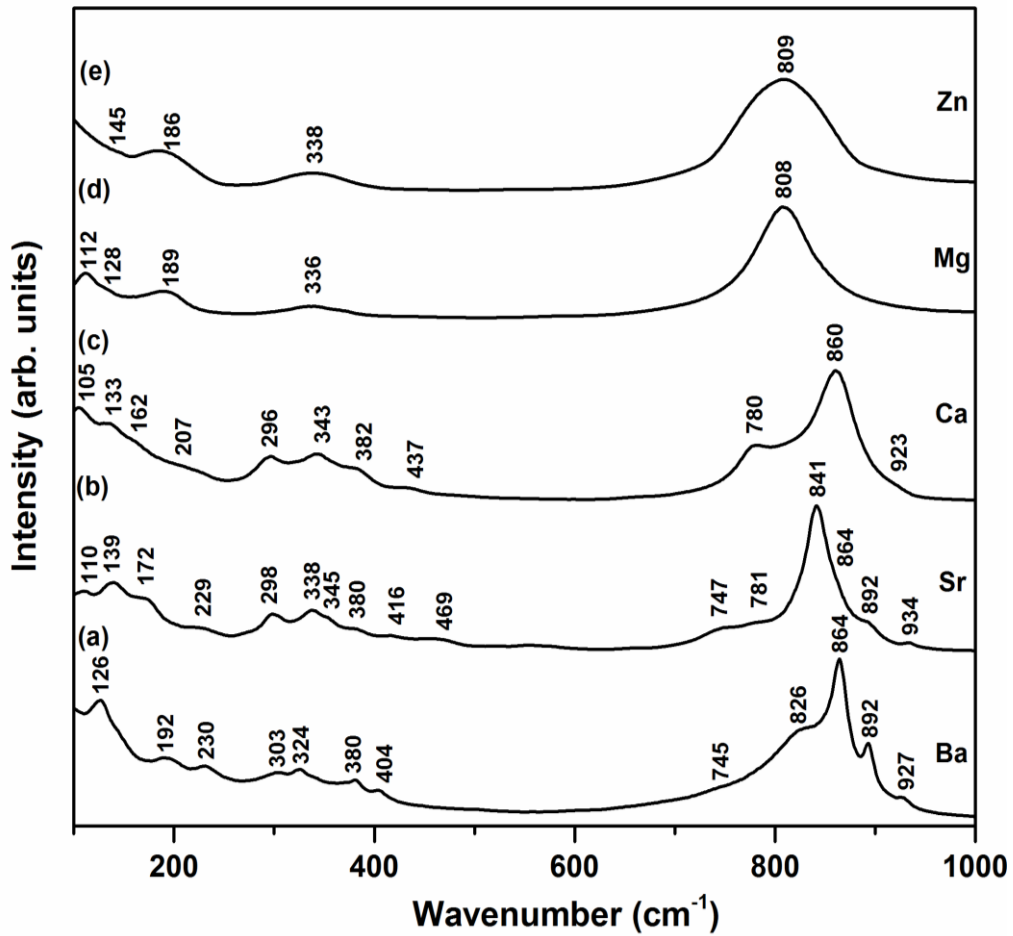


Figure 6.6 Raman spectra of $Bi_2AV_2O_9$ (A= Ba, Sr, Ca, Mg and Zn) ceramics

Table 6.1 Raman mode assignments of $Bi_2AV_2O_9$ (A= Ba, Sr, Ca, Mg and Zn) ceramics

$Bi_2BaV_2O_9$	$Bi_2SrV_2O_9$	$Bi_2CaV_2O_9$	$Bi_2MgV_2O_9$	$Bi_2ZnV_2O_9$	Assignments
927 892 864 826	934 892 864 841	923 860	 808	 809	$\nu_s(VO_4)^{3-}$
745	781 747	780			$\nu_{as}(VO_4)^{3-}$
404 380	469 416 380	437 382			$\delta_{as}(VO_4)^{3-}$
324	354 338	343	336	338	$\delta_s(VO_4)^{3-}$
303 230 192 126	298 172 139 110	296 207 162 133 105	 189 128 112	 186 145	Lattice mode vibrations

ν_s – symmetric stretching, ν_{as} – asymmetric stretching, δ_{as} – asymmetric bending, δ_s – symmetric bending

Symmetric stretching vibration of VO_4 tetrahedra are observed at 841, 864, 892 and 934 cm^{-1} for $Bi_2SrV_2O_9$ together with asymmetric stretching vibrations at 781 and 747 cm^{-1} whereas symmetric stretching vibrations of $Sr_4V_2O_9$ are observed at 851, 830 and 807 cm^{-1} together with asymmetric stretching vibration at 792 cm^{-1} . Symmetric stretching vibrations are appeared at 867, 828 and 800 cm^{-1} together with an asymmetric stretching mode at 789 cm^{-1} for $Ca_4V_2O_9$ whereas $Bi_2CaV_2O_9$ exhibits symmetric stretching vibration at 860 cm^{-1} along with a shoulder peak at 923 cm^{-1} . The mode at 780 cm^{-1} can be attributed to the asymmetric stretching vibration of VO_4 tetrahedral units. Unlike $Bi_2AV_2O_9$ with A= Ba, Sr and Ca samples, $Bi_2MgV_2O_9$ and $Bi_2ZnV_2O_9$ have less number of modes. Symmetric stretching vibrations of $Bi_2MgV_2O_9$ and $Bi_2ZnV_2O_9$ are observed at 808 and 809 cm^{-1} and the asymmetric bending modes are observed at 336 and 338 cm^{-1} , which can be attributed to the stretching and bending vibrations of VO_4 tetrahedral units present in $BiVO_4$. On the other hand, $Mg_4V_2O_9$ has strong symmetric stretching vibrations at 859 and 823 cm^{-1} and $Zn_4V_2O_9$ at 955, 910, 877, 861, 851, 820 and 807 cm^{-1} respectively.

6.3.3 Morphological and thermal studies

Typical backscattered electron images of sintered $Bi_2AV_2O_9$ with $A=Ba, Sr, Ca, Mg$ and Zn are given in Figure 6.7. It can be seen from the figure that separate dark and white grains are distributed in the sintered $Bi_2AV_2O_9$ ceramic samples with $A= Ba, Sr, Mg$ and Zn , which indicates the multiphase nature of these ceramics. It is also clearly evident from the SEM images that the average grain sizes of these samples are in the range of 1-2 μm . EDS analysis shows that the white grains are $BiVO_4$ and the dark grains belong to $BiBaVO_5$ (Figure 6.7a, f and g). The SEM and EDS analyses in the present study well support the results of XRD analysis given in Figure 6.2. On the other hand, $Bi_2CaV_2O_9$ ceramic exhibits a dense microstructure with polygonal grains with average grain size of 1 to 3 μm without any secondary phase (Figure 6.7c and h), which indicates the single phase nature of $Bi_2CaV_2O_9$ compound and this result is in agreement with the XRD and Raman results.

From the backscattered SEM images, it is found that only $Bi_2CaV_2O_9$ show single phase nature among the $Bi_2AV_2O_9$ ceramics, while other compounds exhibit multiphase nature. In order to further confirm the phase formation of $Bi_2CaV_2O_9$ ceramic, TGA-DSC of the composition was carried out using stoichiometrically mixed oxides and carbonates of the raw materials inside platinum crucible. The analysis was carried out at a heating rate of $5^\circ C/min$ in nitrogen atmosphere. The TGA-DSC results show that the $Bi_2CaV_2O_9$ phase formation is completed around $635^\circ C$ (Figure 6.8). A total weight loss of approximately 6.3% is observed, which can be attributed to the evaporation of CO_2 , and the value is comparable with the theoretical weight loss of 5.9%. This result shows good agreement with the single phase nature of $Bi_2CaV_2O_9$ phase observed in the XRD and SEM analyses.

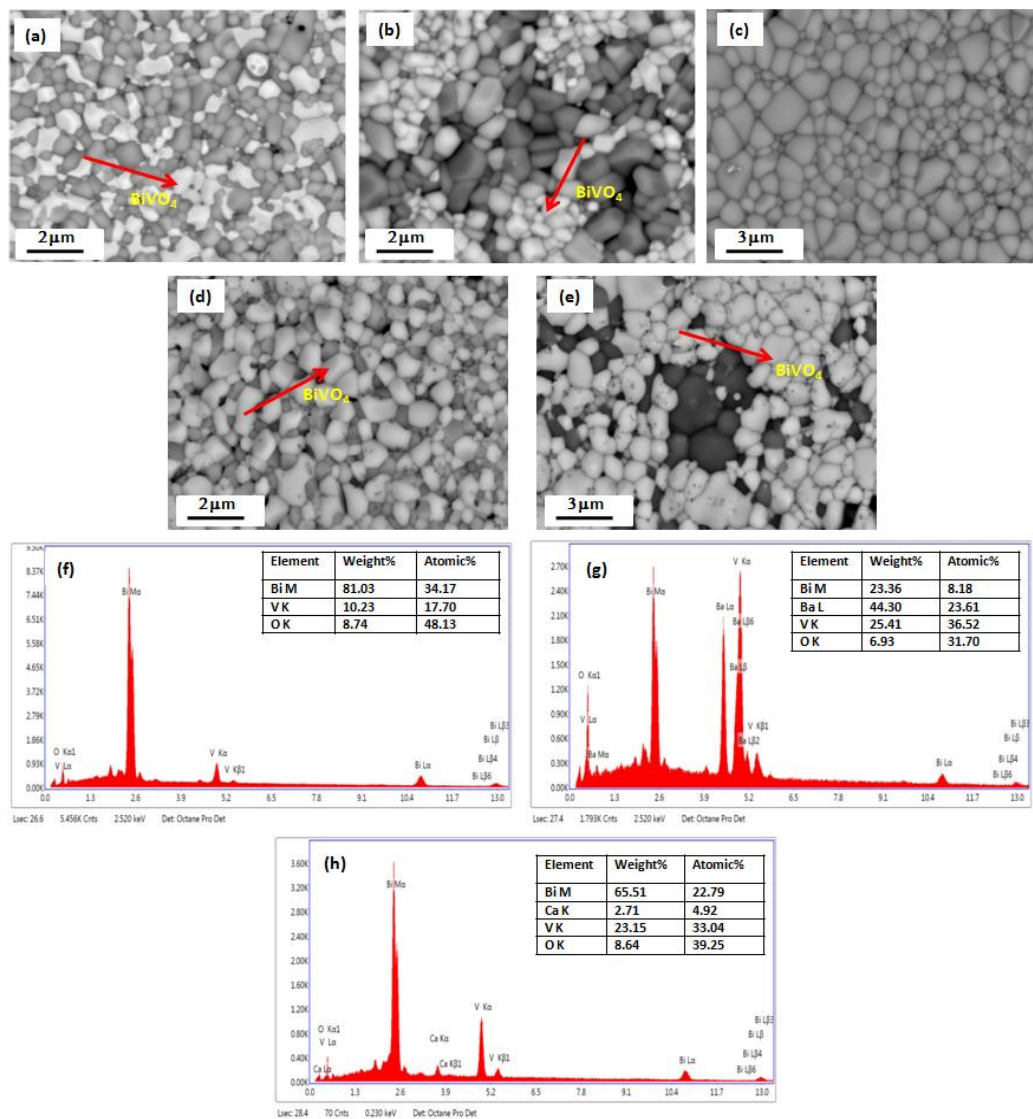


Figure 6.7 Backscattered SEM images of (a) $\text{Bi}_2\text{BaV}_2\text{O}_9$ (b) $\text{Bi}_2\text{SrV}_2\text{O}_9$ (c) $\text{Bi}_2\text{CaV}_2\text{O}_9$ (d) $\text{Bi}_2\text{MgV}_2\text{O}_9$ (e) $\text{Bi}_2\text{ZnV}_2\text{O}_9$, EDS spectra of (f) BiVO_4 (g) BiBaVO_5 and (h) $\text{Bi}_2\text{CaV}_2\text{O}_9$

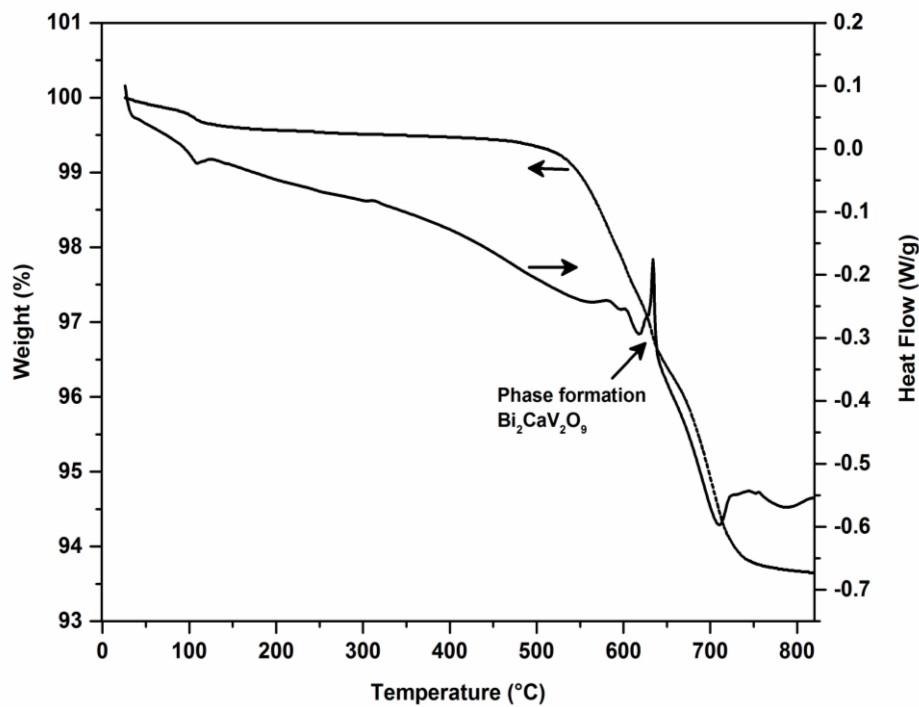


Figure 6.8 TGA-DSC curves of $\text{Bi}_2\text{O}_3\text{-CaO-V}_2\text{O}_5$ composition

6.3.4 Dielectric studies

Table 6.2 shows the sintering temperature, density and dielectric properties of $\text{Bi}_2\text{AV}_2\text{O}_9$ ($A = \text{Ba, Sr, Ca, Mg}$ and Zn) ceramics. $\text{Bi}_2\text{AV}_2\text{O}_9$ ceramics with $A = \text{Ba, Sr, Ca, Mg}$ and Zn are well sintered below 800°C for 1h. Among the $\text{Bi}_2\text{AV}_2\text{O}_9$ samples studied, $\text{Bi}_2\text{AV}_2\text{O}_9$ ceramics with $A = \text{Ca, Mg}$ and Zn show microwave dielectric properties. XRD and SEM analyses reveal that among $\text{Bi}_2\text{AV}_2\text{O}_9$, only $\text{Bi}_2\text{CaV}_2\text{O}_9$ shows single phase nature while other samples exhibit multiphase nature comprising of BiVO_4 and BiAVO_5 . Figure 6.9 shows the variation of density and dielectric constant of $\text{Bi}_2\text{CaV}_2\text{O}_9$ ceramic sintered at different temperatures for 1h. Both density and dielectric constant of $\text{Bi}_2\text{CaV}_2\text{O}_9$ ceramic show an increasing trend with sintering temperature up to 780°C . Further increase in sintering temperature deteriorates both density and dielectric constant of $\text{Bi}_2\text{CaV}_2\text{O}_9$ ceramic. At 780°C for 1h, single phase $\text{Bi}_2\text{CaV}_2\text{O}_9$ ceramic exhibits a maximum density of 5.2 g/cc together with a dielectric constant of 28.2 at 6.54065 GHz and Q_{xf} of $37,263 \text{ GHz}$. Figure 6.10 shows the temperature variation of resonant frequency (τ_f) of $\text{Bi}_2\text{CaV}_2\text{O}_9$ ceramic sintered at 780°C for 1h. The resonant frequency of $\text{Bi}_2\text{CaV}_2\text{O}_9$ ceramic

shows a decreasing trend with increasing temperature in the range 30-100°C and the sample exhibited a negative τ_f value of -46.1 ppm/°C.

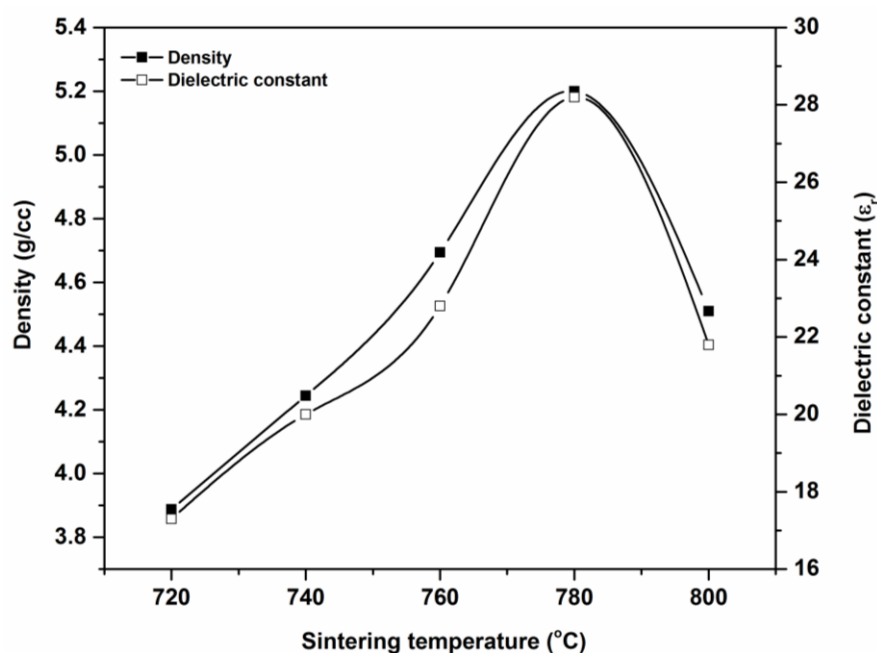


Figure 6.9 Variation of density and dielectric constant of $\text{Bi}_2\text{CaV}_2\text{O}_9$ ceramic as a function of sintering temperature at GHz

$\text{Bi}_2\text{AV}_2\text{O}_9$ with $A = \text{Mg}$ and Zn samples are well sintered at 740°C and 680°C for 1h respectively. $\text{Bi}_2\text{MgV}_2\text{O}_9$ ceramic has a dielectric constant of 34.2, Qxf of 28,400 GHz and τ_f of -15.3 ppm/°C whereas a dielectric constant of 35, Qxf of 20,000 GHz and τ_f of -190.2 ppm/°C are obtained for $\text{Bi}_2\text{ZnV}_2\text{O}_9$ ceramic. The microwave dielectric properties of BiVO_4 are already reported by Zhou et al. [20]. According to this report, BiVO_4 can be well sintered at 900°C and exhibits a relatively high dielectric constant $\epsilon_r = 68$, $\text{Qxf} = 6500\text{-}8000$ GHz and $\tau_f = -243$ to -260 ppm/°C. Among BiMgVO_5 and BiZnVO_5 ceramics, only BiMgVO_5 exhibits microwave dielectric properties. BiMgVO_5 is well sintered at 740°C for 1h and exhibits a dielectric constant of 22.4 at 7.291634 GHz, quality factor of 6870 GHz and τ_f of -130.5 ppm/°C. Although BiZnVO_5 is well sintered at 700°C, it did not show any resonance in the microwave frequency region. Hence, the relatively high dielectric constant obtained for $\text{Bi}_2\text{MgV}_2\text{O}_9$ and $\text{Bi}_2\text{ZnV}_2\text{O}_9$ ceramics compared to Ca may be due to the contribution from the higher dielectric constant of BiVO_4 phase.

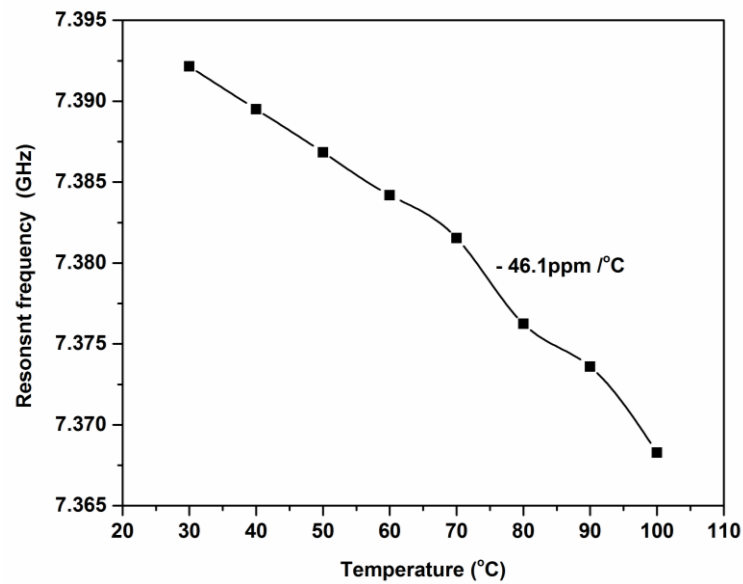


Figure 6.10 Variation of resonant frequency of $\text{Bi}_2\text{CaV}_2\text{O}_9$ ceramic as a function of temperature

In order to use $\text{Bi}_2\text{CaV}_2\text{O}_9$ ceramic for LTCC applications, chemical compatibility with metal electrode is very important. $\text{Bi}_2\text{CaV}_2\text{O}_9$ ceramic is co-fired with 20 wt% Ag powder at 780°C for 1h to evaluate the chemical compatibility. Interestingly, $\text{Bi}_2\text{CaV}_2\text{O}_9$ ceramic melts during co-firing as a result of reaction with Ag electrode. Hence, it is inferred that $\text{Bi}_2\text{CaV}_2\text{O}_9$ cannot be used for LTCC applications although it is having reasonably good microwave dielectric properties.

Table 6.2 Sintering temperature, density and dielectric properties of $\text{Bi}_2\text{AV}_2\text{O}_9$ (A=Ba, Sr, Ca, Mg, Zn) ceramics

A^{2+} ion	Sintering Temp. (°C)	Density (g/cc)	Low frequency data at 1MHz		Microwave frequency data (GHz)			Compatibility
			ϵ_r	$\tan\delta$	ϵ_r	Qxf (GHz)	τ_f (ppm/°C)	
Ba	780/1h	5.27	24.86	0.007	*	*	*	*
Sr	780/1h	5.6	33.01	0.002	*	*	*	*
Ca	780/1h	5.2	30.6	0.001	28.2	32,400	-46.1	No
Mg	740/1h	5.27	34.8	0.008	34.2	28,400	-15.3	No
Zn	680/1h	5.56	36.8	0.026	35	20,000	-190.2	No

*- No resonance

6.4 Conclusions

$Bi_2AV_2O_9$ ceramics with A= Ba, Sr, Ca, Mg and Zn have been prepared through conventional solid state ceramic route. X-ray diffraction and Raman studies confirm the multiphase nature for $Bi_2AV_2O_9$ ceramics with A= Ba, Sr, Mg and Zn except $Bi_2CaV_2O_9$. The rare earth substitution (R= La, Nd, Y and Yb) at A site did not result any single phase compositions. The existence of $(VO_4)^{3-}$ vibrational groups are confirmed in $Bi_2CaV_2O_9$ ceramics by Raman studies. The back scattered SEM images and TGA-DSC studies compliment the single phase nature of $Bi_2CaV_2O_9$ compound. Single phase $Bi_2CaV_2O_9$ ceramic sintered well at 780°C for 1h exhibits a maximum density of 5.2 g/cc together with a dielectric constant of 28.2, Qxf of 37,263 GHz and τ_f of -46.1 ppm/°C. Although $Bi_2MgV_2O_9$ and $Bi_2ZnV_2O_9$ ceramics exhibit microwave dielectric properties, they show multiphase nature comprising of $BiVO_4$ and $BiAVO_5$ (A= Mg and Zn) phases. $Bi_2CaV_2O_9$ ceramic melts during co-firing with Ag and hence it cannot be used for LTCC applications.

References

- [1] M. T. Sebastian, H. Jantunen, *Int. Mater. Rev.*, 53 [2] (2008) 57-90.
- [2] M. Valant, D. Suvorov, *J. Eur. Ceram. Soc.*, 24 [6] (2004) 1715-1719.
- [3] M. T. Sebastian, R. Ubic, H. Jantunen, *Int. Mater. Rev.*, 60 [7] (2015) 392-412.
- [4] D. Zhou, H. Wang, X. Yao, L. X. Pang, *J. Am. Ceram. Soc.*, 91 [10] (2008) 3419-3422.
- [5] J. S. O. Evans, A. W. Sleight, *Int. J. Inorg. Mater.*, 2 [4] (2000) 375-377.
- [6] J. Boje, H. M. Buschbaum, *Z. Anorg. Allg. Chem.*, 619 [3] (1993) 521-524.
- [7] I. Radosavljevic, J. S. O. Evans, A. W. Sleight, *J. Solid State Chem.*, 137 [1] (1998) 143-147.
- [8] J. Huang, A. W. Sleight, *J. Solid State Chem.*, 104 [1] (1993) 52-58.
- [9] J. S. O. Evans, J. Huang, A. W. Sleight, *J. Solid State Chem.*, 157 [2] (2001) 255-260.
- [10] I. Radosavljevic, J. A. K. Howard, A. W. Sleight, J. S. O. Evans, *J. Mater. Chem.*, 10 [9] (2000) 2091-2095.
- [11] K. M. Elsabawy, M. H. El-Newehy, *Der Chemica Sinica.*, 1 [1] (2010) 45-56.
- [12] K. M. Elsabawy, M. M. Abou-Sekkina, A. El-Maghraby, M. A. Asker, *Int. J. Inorg. Chem.*, (2012) 1-8.
- [13] B. W. Hakki, P. D. Coleman, *IRE Trans. Microw. Theory Tech.*, 8 [4] (1960) 402-410.
- [14] J. Mazierska, M. V. Jacob, A. Haring, J. Krupka, P. Barnwell, T. Sims, *J. Eur. Ceram. Soc.*, 23 [14] (2003) 2611-2615.
- [15] M. Touboul, C. Vachon, *Thermochim Acta.*, 133 (1988) 61-66.
- [16] C. K. Lee, D. C. Sinclair, A. R. West, *Solid State Ionics*, 62 [3-4] (1993) 193-198.

- [17] W. Wrobel, F. Krok, I. Abrahams, A. Kozanecka-Szmigel, M. Malys, S.C.S. Chan, J. R. Dygas, *Mater. Sci. Poland*, 24 (2006) 23-30.
- [18] S. Benmokhtar, A. El Jazouli, J. P. Chaminade, P. Gravereau, F. Guillen, D. de Waal, *J. Solid State Chem.*, 177 [11] (2004) 4175-4182.
- [19] R. L. Frost, D. A. Henry, M. L. Weier, W. Martens, *J. Raman Spectrosc.*, 37 [7] (2006) 722-732.
- [20] D. Zhou, L. X. Pang, J. Guo, Z. M. Qi, T. Shao, Q. P. Wang, H. D. Xie, X. Yao, C. A. Randall, *Inorg. Chem.*, 53 [2] (2014) 1048-1055.

7

Preparation and Characterization of $\text{Ba}_3\text{V}_2\text{O}_8$ Filled HDPE Composites and Design of Microstrip Patch Antennas

- 7.1 Introduction
- 7.2 Experimental techniques
- 7.3 Results and discussion
- 7.4 Conclusions

7.1 Introduction

Recent developments in microwave devices have witnessed revolutionary changes in the telecommunication and satellite communication sectors, which demands miniaturized electronic components with high performance. Integrated packaging technology offers miniaturized electronic components with higher circuit density and high speed signal transmission. In this context, ceramic filled polymer composites, especially the 0-3 type are potential candidates for microwave substrate applications because of their low cost, light weight, and robust nature. Also, polymer ceramic composites combine the electrical properties of ceramics and the mechanical flexibility, chemical stability and processing possibilities of polymers. The major advantages of ceramic filled polymer composites are their significant material properties such as dielectric constant, loss tangent, dimensional stability, heat dissipation etc. which can be tailored over a wide range by varying the filler content [1-4].

Polymer ceramic composites have huge application potential in various areas including high power solid state amplifiers, patch antennas, band pass filters etc. This fueled the search for new and improved polymer ceramic composite systems with excellent material properties in order to use them as cost effective substitutes for conventional ceramic substrates. Among the available soft substrates, PTFE is preferred as the most ideal host matrix for substrate applications because of its stable dielectric constant, extremely low loss tangent which is stable over a wide range of frequencies, good chemical resistance, dimensional stability and high operating temperature. The other properties of PTFE such as chemical inertness, low moisture absorption, high service temperature, superior electrical and mechanical properties etc. are also important for many microwave applications. However, high coefficient of thermal expansion ($\alpha_L \sim 109$ ppm/ $^{\circ}C$) is not desirable for microwave substrate applications although it has the lowest loss tangent among thermoplastics [2, 3, 5]. As results of this, efforts have been made to identify alternate polymer materials suitable for microwave substrate fabrication.

Polyethylene (PE) is a non-polar and semi-crystalline polymer with a melting point of $\sim 130^{\circ}C$ at which the plastic transforms to a completely amorphous state [6]. Polyethylene is formed by the heat and pressure treatment of ethylene, which

originate from methane gas. Crystalline regions in polyethylene are highly ordered, neatly folded, layered in parallel and densely packed molecular chains. This occurs only when the branching off the sides of the primary chains are smaller in number. High density polyethylene (HDPE) has greater proportion of crystalline region and hence large strength to density ratio. The density of HDPE varies from 0.93 to 0.97 g/cc, higher than the densities of other polyethylene materials such as medium-density polyethylene (MDPE) (0.93-0.94 g/cc) and low-density polyethylene (LDPE) (0.91-0.93 g/cc) [6, 7]. HDPE with fewer branches than MDPE or LDPE has greater density and greater strength since the size and size distribution of the crystalline regions are determinants of the tensile strength of the end product [6]. HDPE has excellent properties such as low dielectric constant ($\epsilon_r = 2.3$) and low loss tangent (10^{-4}) at 10 GHz, good chemical inertness and excellent insulating properties and as a result HDPE is extensively used as an engineering material [8, 9].

The effect of boron nitride content, particle size and thermal conductivity of HDPE/boron nitride composites have been studied by Zhou et al. [10]. Mechanical and thermal expansion properties of fiber reinforced HDPE composites have been studied by Huang et al. [11]. Also, the mechanical property studies of HDPE composites reinforced with wood flour, clay, carbon nanotube and hybrid organic fillers etc. have also been carried out by many researchers [12-15]. Even though the mechanical properties of reinforced HDPE composites are well studied, less attention has been paid to dielectric properties. Recently, dielectric properties of ceramic filled HDPE and epoxy composites have been reported by Subodh et al. [16]. The microwave dielectric, thermal and mechanical properties of CeO_2 filled HDPE composites prepared through powder processing technique was reported by Anjana et al. [17]. As per their reports, 0.4 volume fraction of CeO_2 loaded HDPE composite has an effective dielectric constant of 5.7 together with loss tangent of 0.0068 at 7 GHz.

Microwave substrates have gained considerable attention in the past few years especially for patch antenna design. The essential substrate requirement for the fabrication of patch antenna include low dielectric constant and dielectric loss, isotropic dielectric properties, good dimensional stability, low moisture absorption and good heat dissipation. Moreover, light weight, low cost and ease of fabrication are

the other critical factors that need to be taken in to account while selecting a substrate material for circuit fabrication. Conventional substrates such as polytetrafluoroethylene/ceramic, FR-4 glass epoxy, polybutadiene/ceramic etc. are used for the fabrication of microstrip patch antennas, but are not suitable for co-planar mounting [18]. Recently, Sarmah et al. developed TiO_2 filled low density polyethylene and polystyrene composites as potential substrates for microstrip patch antennas [19]. Gogoi et al. also reported linear low density polyethylene (LLDPE) as a flexible substrate with dielectric constant of 2.2 together with a low loss tangent of 0.0003 at 6GHz for antenna applications [20]. There is a renewed interest in developing novel flexible composite materials with stable dielectric properties not only for patch antenna design but also for variety of other microwave circuit applications.

Microwave dielectric ceramics based on low melting oxides such as vanadium, molybdenum etc. are usually used for LTCC applications. Nijesh et al. reported the microwave dielectric properties of $BaWO_4$ filled PTFE laminates for microwave substrate applications [21]. $BaWO_4$ was calcined at a temperature of 800°C for 4 hours to get the phase pure filler material. Among the vanadium based compositions investigated in the $BaO-V_2O_5$ binary system, hexagonal $Ba_3V_2O_8$ exhibits excellent microwave dielectric properties including high quality factor [22]. But it cannot be used for LTCC applications because of its high sintering temperature (1300°C for 1h). Hence, phase pure $Ba_3V_2O_8$ ceramics are prepared in the present study to use as particulate filler in the HDPE matrix. The HDPE/ $Ba_3V_2O_8$ composites are fabricated through dry milling followed by compression molding method with a view to use them as base substrates for microwave circuit design. The dielectric properties of the composites have been evaluated as a function of the volume fractions of the ceramic filler loading. In order to evaluate the applicability of HDPE/ $Ba_3V_2O_8$ composites, rectangular patch antenna design has been simulated using HFSS software and fabricated on optimum $Ba_3V_2O_8$ filled HDPE laminates through photolithographic technique. The end properties of the designed antenna are validated with simulated data.

7.2 Experimental

7.2.1 Preparation of phase pure $Ba_3V_2O_8$ filler

$Ba_3V_2O_8$ ceramic was prepared by conventional solid state ceramic route. High purity oxides and carbonates such as $BaCO_3$ (Sigma Aldrich, 99%) and V_2O_5 (Sigma Aldrich, 99%) were used as starting materials. Stoichiometric amounts of raw materials were weighed and wet mixed in distilled water for an hour in an agate mortar. The resultant slurry was dried at $100^\circ C$ in a hot air oven, ground well and calcined at $1100^\circ C$ for an hour. The phase formation of the ceramic filler was studied using powder X-ray diffraction (XRD) technique using CuK_α radiation (Bruker 5005, Germany). The morphology of the ceramic filler and composites were studied using scanning electron microscopy (Carl Zeiss, Model No: EVO18 Research, Germany).

7.2.2 Fabrication of HDPE/ $Ba_3V_2O_8$ composites

High density polyethylene (HDPE) powder and phase pure $Ba_3V_2O_8$ ceramic were used as the starting materials for the preparation of HDPE/ $Ba_3V_2O_8$ composites. HDPE fine powder was prepared from commercial grade HDPE granules supplied by Reliance Industries Limited, India. Fine HDPE powders were prepared by dissolving the commercially available HDPE granules in Xylene (95%, Merck) at a temperature of $130^\circ C$ along with continuous stirring using a magnetic/stirrer. The dissolved samples were taken out, dried and ground well. For the preparation of $Ba_3V_2O_8$ filled HDPE composites, both filler and polymer were weighed and dry mixed inside a polypropylene bottle for one hour. The HDPE/ $Ba_3V_2O_8$ composites were fabricated through compression molding method using a hydraulic laminating press. The optimized pressure and temperature used for the fabrication of the composites were 90 Kg/Cm^2 and $162^\circ C$ for 1h.

7.2.3 Theoretical Modeling

Composite systems are mixtures of two or more components and hence their effective dielectric constant will depend not only on the dielectric constant of the constituent components but also on their volume fraction, morphology, dispersion and the interaction between the phases [23]. The dielectric, thermal and mechanical properties of composites can be tailored by incorporating different ceramic fillers in

various proportions. For the same ceramic filler loading, the dielectric properties of the composites depend on the type of the polymer material used, dielectric properties of the polymer, the depolarization induced by the polymer on the effective dielectric constant of the composite system etc. Hence, the prediction of the effective dielectric constant of the heterogeneous systems from the dielectric constant and volume fraction of the individual components has significant importance for practical applications in the field of electronic packaging. Many theoretical models have been proposed so far for the prediction of the effective dielectric constant of the polymer ceramic composite systems and it has been found that the effective dielectric constant will lie in between the dielectric constant values of the individual components. The simplest equation is the volumetric law of mixing (Eq. 7.1 and 7.2), which can be used for predicting the dielectric constant of a biphasic system in common.

$$\varepsilon_f V_f + \varepsilon_m V_m = \varepsilon_c \quad (7.1)$$

$$\rho_f V_f + \rho_m V_m = \rho_c \quad (7.2)$$

In the above equation, ε_f , ε_m are the dielectric constant and V_f and V_m are the volume fractions of the ceramic filler and polymer matrix, respectively. There are a number of established mixing rules to predict the dielectric behavior of the composite systems. Among these, logarithmic law of mixing (Eq. 7.3) is the most commonly used relation, since it considers the composite as a random mixture of nearly spherical inclusions.

$$\log \varepsilon_c = V_f \log \varepsilon_f + V_m \log \varepsilon_m \quad (7.3)$$

Generally, the theoretical predictions based on Lichtnecker model (Eq. 7.3) are valid only for low filler contents and deviate more from the experimental values as the filler content increases. This is mainly due to the improper dispersion of the ceramic filler particles in the polymer matrix at higher filler contents and also by the porosity introduced in the composite systems. The dielectric constant of the composite also depends on the filler shape, size of the filler particles and the interface between ceramic and polymer [24]. A modified form of Lichtnecker equation (Eq. 7.4) with a fitting factor $k=0.3$ is also used for the theoretical

calculation of effective dielectric constant [24, 25], where the fitting factor k represents the interaction between the filler and matrix.

$$\log \varepsilon_c = \log \varepsilon_f + V_m (1 - k) \log \left(\frac{\varepsilon_m}{\varepsilon_f} \right) \quad (7.4)$$

$$\frac{\varepsilon_c - \varepsilon_m}{\varepsilon_c + 2\varepsilon_m} = V_f \frac{\varepsilon_f - \varepsilon_m}{\varepsilon_f + 2\varepsilon_m} \quad (7.5)$$

Compared to Lichtnecker model, Maxwell-Garnet model is an effective approach for the dielectric predictions (Eq. 7.5), where the particles are assumed to be embedded in the host polymer matrix. According to the Maxwell- Garnet model, the average cell has a cement topology with spherical inclusions surrounded by sufficient concentric layers of host matrix. In general, Maxwell Garnet equation matches with the experimental dielectric values only in the lower filling fraction of the ceramic [26]. The other commonly used theoretical models are given below.

Jayasundere-Smith Equation

$$\varepsilon_{eff} = \frac{\varepsilon_m (1 - V_f) + \varepsilon_f V_f \left[\frac{3\varepsilon_m}{\varepsilon_f + 2\varepsilon_m} \right] \left[\frac{1 + 3V_f (\varepsilon_f - \varepsilon_m)}{\varepsilon_f + 2\varepsilon_m} \right]}{1 - V_f + V_f \left[\frac{3\varepsilon_m}{\varepsilon_f + 2\varepsilon_m} \right] \left[\frac{1 + 3V_f (\varepsilon_f - \varepsilon_m)}{\varepsilon_f + 2\varepsilon_m} \right]} \quad (7.6)$$

Maxwell-Wagner-Sillars Equation

$$\varepsilon_{eff} = \varepsilon_m \frac{2\varepsilon_m + \varepsilon_f + 2V_f (\varepsilon_f - \varepsilon_m)}{2\varepsilon_m + \varepsilon_f - V_f (\varepsilon_f - \varepsilon_m)} \quad (7.7)$$

The Jayasundere-Smith equation is only valid for low volume fraction of filler since it considers the interactions between the neighboring spheres [27]. On the other hand, the Maxwell-Wagner-Sillars (MWS) equation is valid if the properties of the two phases of the composites are similar [24].

7.2.4 Fabrication of microstrip patch antenna

In order to fabricate microstrip patch antenna, optimum loaded HDPE/Ba₃V₂O₈ composite was copper cladded on both sides using 35 μm oxygen free copper foil through vacuum lamination process at a temperature of 112°C and pressure of 40 Kg/Cm² for 1h. The substrate material used for antenna fabrication should possess low dielectric loss in order to reduce the propagation delay and to

increase the signal speed. The antenna simulation studies are carried out using High Frequency Structure Simulator (HFSS) software based on Finite Element Method (FEM), which is the industry standard for simulating 3D full wave electromagnetic fields. At first, the possible simulation models of the antenna is developed using Ansys HFSS. The performance of the microstrip patch antenna depends on its dielectric constant and dimension of the substrate material. The operating frequency, radiation efficiency and return loss of the antenna are influenced by its operating frequency. For antenna fabrication, the design strategy of keeping minimum return loss at resonant frequencies as close as possible to achieve -10 dB return loss over the impedance bandwidth is adopted. For an efficient radiation, the practical width of the patch (W) and the length of the antenna (L) can be calculated by using the following equations.

$$W = \frac{1}{2f_r \sqrt{\mu_0 \epsilon_0}} \sqrt{\frac{2}{\epsilon_r + 1}} \quad (7.9)$$

$$L = \frac{1}{2\pi \sqrt{\epsilon_{eff}} \sqrt{\mu_0 \epsilon_0}} 2\Delta L \quad (7.10)$$

where

$$\epsilon_{eff} = \frac{\epsilon_r + 1}{2} + \frac{\epsilon_r - 1}{2\sqrt{1 + 12\frac{h}{W}}} \quad (7.11)$$

$$\text{and } \Delta L = \frac{(\epsilon_{eff} + 0.3)\left(\frac{W}{h} + 0.264\right)}{(\epsilon_{eff} - 0.258)\left(\frac{W}{h} + 0.8\right)} \times 0.412h \quad (7.12)$$

where λ is the wavelength, f_r is the resonant frequency, W is the width and L is the length of the patch, ΔL is the change in length of the patch due to the fringing of the electric field, h is the thickness of the substrate and ϵ_r is the dielectric constant of the substrate respectively. Then, width of 50 Ω microstrip transition line is calculated using the equation given below.

$$Z_o = \frac{120\pi}{\sqrt{\epsilon_{eff} \left(1.393 + \frac{w}{h} + \frac{2}{3} \ln\left(\frac{W}{h} + 1.444\right)\right)}} \quad (7.13)$$

where, w is the width of the feed line and $Z_o = 50 \Omega$. From these parameters, antenna structure is simulated using the structure simulation software corresponding to the

required operating frequency. The antenna geometry can be appropriately optimized for the desired impedance response. From the simulated results, the antenna parameters such as return loss, mutual coupling etc. are plotted as a function of frequency.

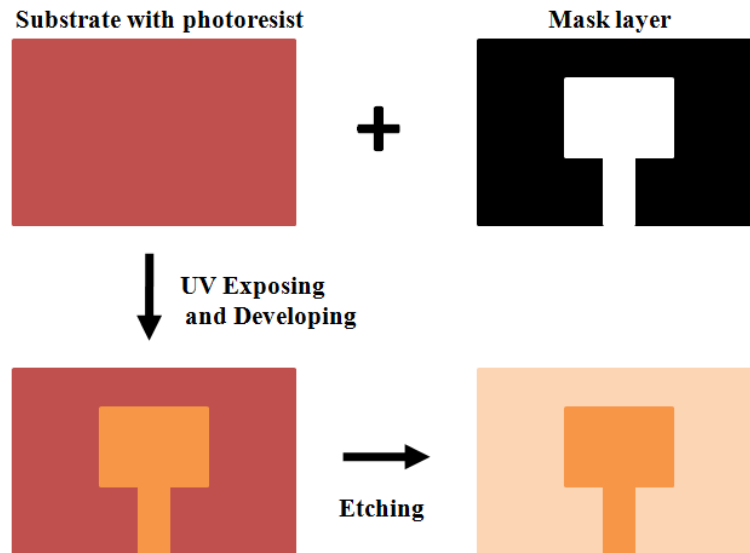


Figure 7.1 Photolithographic technique used for antenna fabrication

Photolithographic technique is used for the fabrication of patch antenna on copper cladded HDPE/ $Ba_3V_2O_8$ composite substrates. The negative mask of the antenna is prepared using Corel draw software followed by photoresist coating to avoid impurities. The photoresist coated substrate is exposed to UV light. Later, the UV exposed substrate is dipped in a developer solution, which hardens the photoresist in the exposed portion while removing the photoresist from the masked portions. Further, the unwanted copper portion from the substrate can be etched off using $FeCl_3$ solution to get the desired antenna geometry. The schematic diagram of photolithographic technique is given in Figure 7.1. The fabricated antenna is connected to a SMA connector for final testing.

7.2.5 Characterization techniques

Surface morphology and filler distribution in the composite samples were studied using a scanning electron microscope (Carl Zeiss, Model No: EVO18 Research, Germany). The low frequency dielectric measurements of the composite samples were carried out at 1 MHz using an impedance analyzer (Agilent, 4294A,

Malaysia). The temperature coefficient of dielectric constant of the composites was measured in the temperature range 30-100°C. Microwave characterization of HDPE/ $Ba_3V_2O_8$ composites was carried out using X-band waveguide cavity perturbation technique using a vector network analyzer (Agilent PNA E8362B, Bayan Lepas, Malaysia). The uncertainty in ϵ_r' and ϵ_r'' using waveguide cavity perturbation is estimated to be $\pm 2\%$ [28]. The coefficient of thermal expansion of the samples were studied in the temperature range 30-100°C using an EXSTAR 6000 model thermo mechanical analyzer (SII Nano technology INC., Japan). The ultimate tensile strength of HDPE/ $Ba_3V_2O_8$ composites was studied using a Universal Testing Machine (Shimadzu, AGS-1000G, Japan). The testing was carried at room temperature with a constant load of 500N and a drawing speed of 10 mm/min.

7.3 Results and discussion

7.3.1 X-ray diffraction studies of HDPE/ $Ba_3V_2O_8$ composites

Figure 7.2 represents the X-ray diffraction pattern of $Ba_3V_2O_8$ ceramic filler calcined at 1100°C for 1h. The phase purity of the ceramic filler is very important since it affects the effective dielectric properties of the composite system. It is reported that the crystal structure of $Ba_3V_2O_8$ is hexagonal with lattice parameters of $a=5.762 \text{ \AA}$ and $c=21.29 \text{ \AA}$ respectively [29]. The X-ray diffraction pattern of $Ba_3V_2O_8$ filler obtained in the present study exactly matches with that of the available ICDD data (ICDD Card No: 29-0211) and hence indexed based on the same.

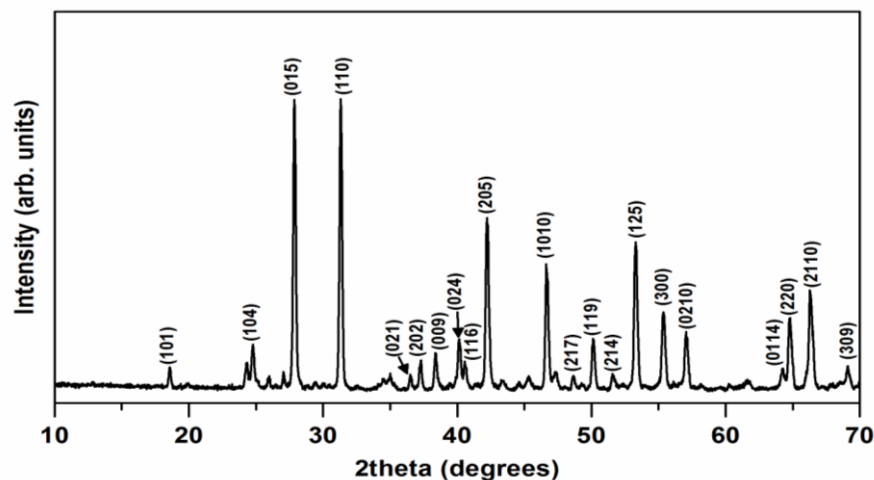


Figure 7.2 X-ray diffraction pattern of $Ba_3V_2O_8$ calcined at 1100°C for 1h

In order to study the chemical interaction between $Ba_3V_2O_8$ filler and HDPE polymer, X-ray diffraction studies of the $Ba_3V_2O_8$ filled HDPE composites were also carried out. X-ray diffraction patterns of pure HDPE and $Ba_3V_2O_8$ filled HDPE composites for different loading fractions are given in Figure 7.3. The strong crystalline peaks of HDPE is observed at 2theta angles $\sim 21^\circ$ and 24° , which is in good agreement with the XRD pattern of HDPE reported by Anjana et al. [17]. The diffraction peaks corresponding to $Ba_3V_2O_8$ filler are indexed based on the standard ICDD pattern. It can be seen from Figure 7.3 that the intensity of the $Ba_3V_2O_8$ diffraction peaks increases as the filler concentration increases and as a result the intensity of the HDPE peaks comes down. The appearance of diffraction peaks of the $Ba_3V_2O_8$ filler and HDPE separately in the X-ray diffraction pattern of the composite clearly indicates that there is no chemical interaction between the ceramic filler and polymer.

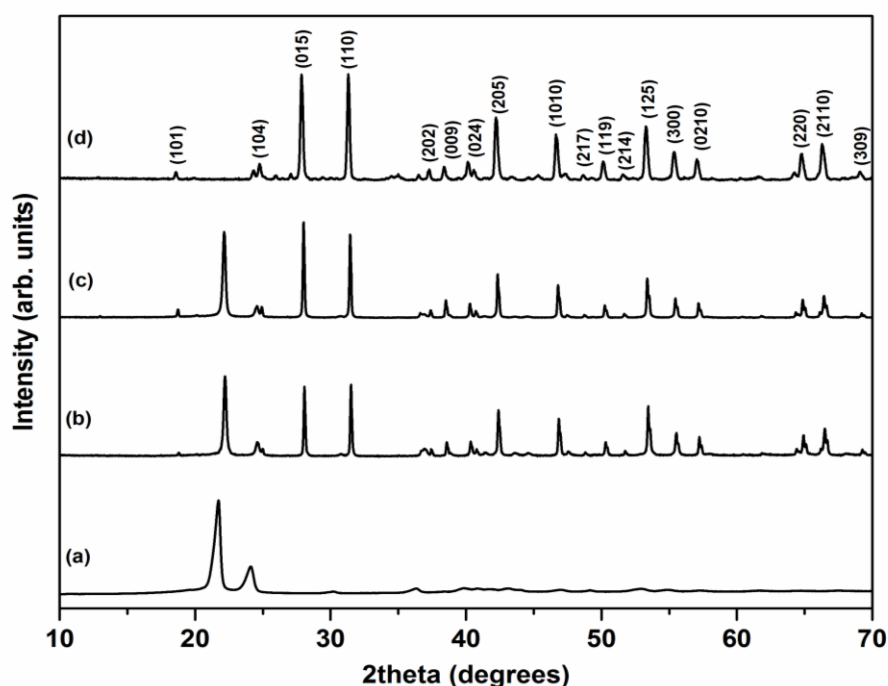


Figure 7.3 X-ray diffraction patterns of (a) Pure HDPE (b) HDPE+20 vol% $Ba_3V_2O_8$ (c) HDPE+40 vol% $Ba_3V_2O_8$ and (d) HDPE+60 vol% $Ba_3V_2O_8$

7.3.2 Density and dielectric properties of the composites

The dielectric properties of $Ba_3V_2O_8$ filled HDPE composites have been studied in the microwave frequency region using X-band cavity perturbation technique. The

starting materials used for the preparation of the composites in the present study, $Ba_3V_2O_8$ and HDPE have densities of 4.31 g/cc and 0.92 g/cc respectively. Both $Ba_3V_2O_8$ and HDPE have dielectric constants of 11.2 and 2.25 respectively in the X-band region. The variation of experimental density and dielectric constant of $Ba_3V_2O_8$ filled HDPE composites as a function of filler loading with an interval of 10 vol% is shown in Figure 7.4. Since $Ba_3V_2O_8$ has low dielectric constant and relatively low loss tangent, the $Ba_3V_2O_8$ filled HDPE composites are also expected to have low dielectric constant and loss tangent. It is clear from Figure 7.4 that both density and dielectric constant of the $Ba_3V_2O_8$ filled HDPE composites increases linearly with filler loading up to 50 vol%. This linear variation can be attributed to the increase in the total polarizability of the composites since both density and dielectric constant of the filler are greater than that of the polymer matrix. $Ba_3V_2O_8$ filled HDPE composite with a filler loading of 50 vol% has a density of 2.78 g/cc and a dielectric constant of 6.05. On the other hand, 60 vol % filler loaded composite sample has a density of 2.93 g/cc and a dielectric constant of 5.57. The higher density value of the composite at 60 vol% compared to 50 vol% is due to the relatively high density of the filler content. The decreasing trend observed for dielectric constant at 60 vol % of filler loading clearly indicates the presence of porosity in the composite system. From the above results, it can be inferred that the optimum $Ba_3V_2O_8$ loading in the HDPE matrix lies in between 50 and 60 vol%. Optimum filler loaded composites are very essential for reproducible microwave dielectric properties, low coefficient of linear thermal expansion, tight dielectric tolerance, low moisture absorption etc. In order to get optimum filler loading, fine tuning has been carried out by loading $Ba_3V_2O_8$ in 2 vol% intervals from 50 to 60 vol% and the results are shown in inset. It is clearly evident from the figure that both density and dielectric constant increase up to 54 vol% filler loading and beyond which both the properties decrease. From Figure 7.4, it is clear that both density and dielectric constant show almost linear variation at lower filler loading (<50 vol%) whereas a non-monotonic variation is observed at higher filler loadings. This may be due to the decrease in the polymer to ceramic connectivity at higher filler fractions. As per earlier reports, ceramic filler dispersed in the polymer matrix have interface regions which exhibit their own unique properties, different from that of the ceramic filler and polymer matrix, which also contribute to the non-monotonous

variation of dielectric constant at higher filler fractions [30]. Beyond 54 vol% filler loading both density and dielectric constant decreases due to the insufficiency of the polymer to encapsulate the filler. Hence, present study shows that the maximum filler loading possible in HDPE matrix for $Ba_3V_2O_8$ filler is 54 vol% with an effective dielectric constant of 6.3 at 9.32 GHz in the X-band region. The theoretical density and dielectric constant of the composites are found out using rule of mixtures (Eq.7.1 and 7.2) and the theoretical values are 3.22 g/cc and 7.08 respectively, which are greater than that of the experimental density and dielectric constant values.

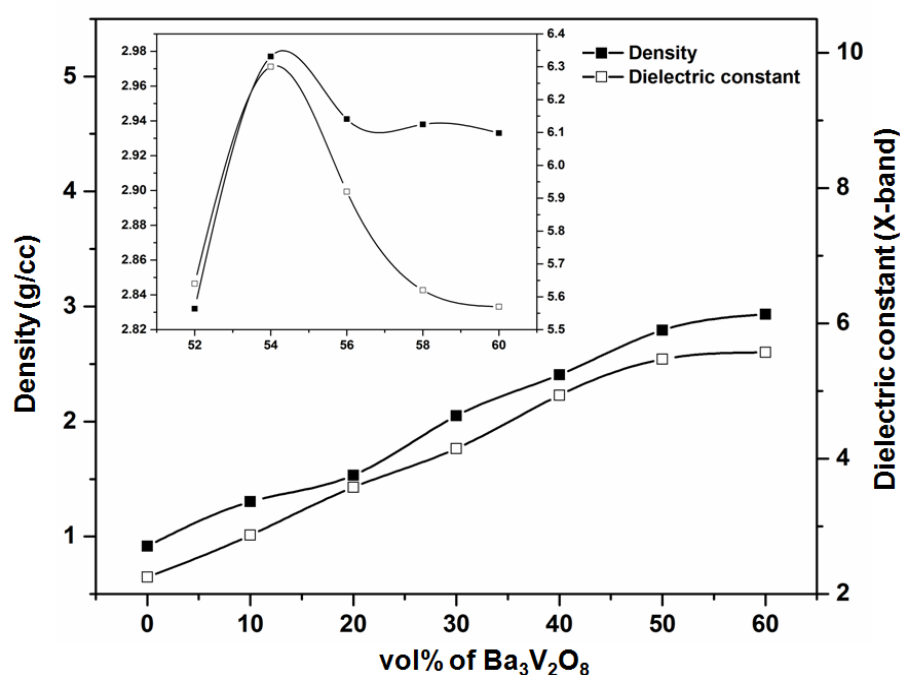


Figure 7.4 Variation of density and dielectric constant of HDPE/ $Ba_3V_2O_8$ as a function of filler loading. Fine tuning of density and dielectric constant of HDPE/ $Ba_3V_2O_8$ as a function of filler loading (Inset)

Variation of loss tangent of HDPE/ $Ba_3V_2O_8$ composites as a function of filler loading is depicted in Figure 7.5. The loss tangent shows an increasing trend with increasing $Ba_3V_2O_8$ content. At optimum filler loading of 54 vol%, HDPE/ $Ba_3V_2O_8$ composite exhibited a loss tangent of 0.004 at 9.32 GHz. A similar observation in loss tangent has been reported by Drishya et al. while loading $CaTiO_3$ in PP matrix [31]. The increasing trend of loss tangent at higher filler fractions is mainly contributed by the $Ba_3V_2O_8$ ceramic filler ($\tan \delta=0.094$) compared to the polymer ($\tan \delta=0.001$).

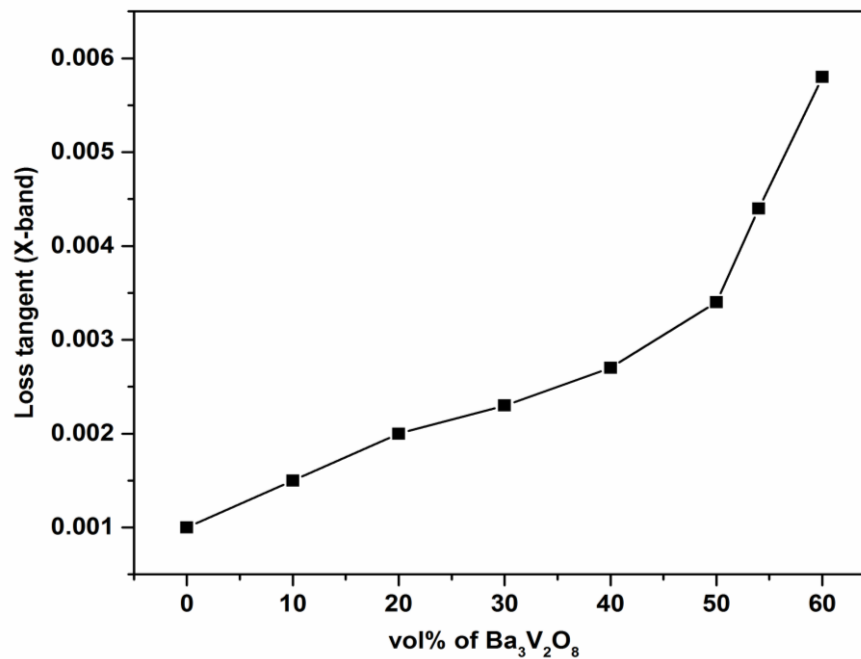


Figure 7.5 Variation of loss tangent of HDPE/ $Ba_3V_2O_8$ composites with filler loading at X-band

The dielectric constant values of HDPE/ $Ba_3V_2O_8$ composites measured at X-band region were compared with that measured at 1 MHz (Figure 7.6). From the figure, it is clear that dielectric constant measured at 1 MHz exhibits higher values compared to that measured at X-band region. This can be attributed to the presence of interface region in the polymer ceramic composites which contributes to interface polarization at 1 MHz region. Whereas, ionic polarization is more dominant at X-band region compared to other polarization mechanisms. Similar observations are reported in rutile filled PTFE composites by Rajesh et al. [32].

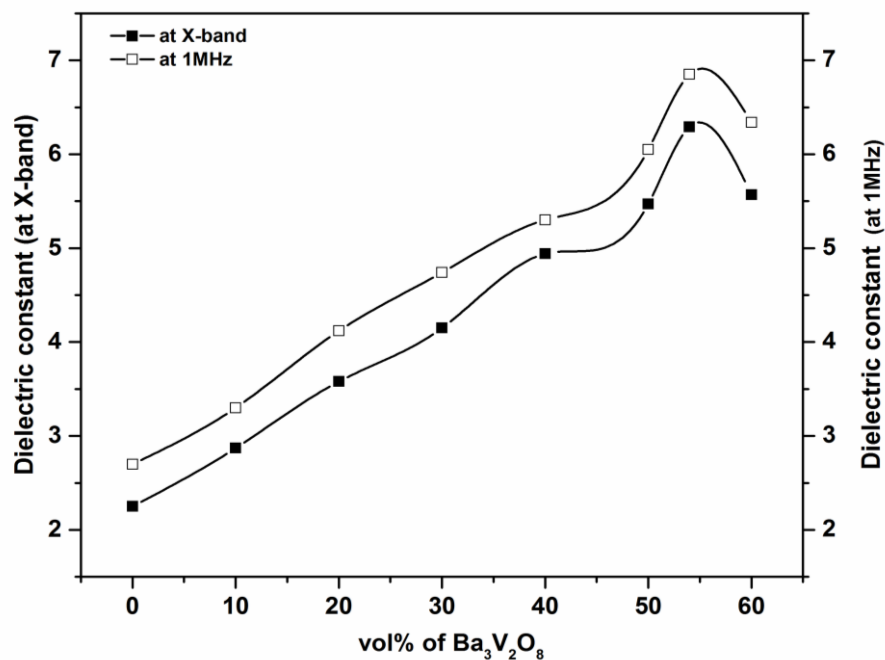


Figure 7.6 Comparison of dielectric constant of HDPE/ $Ba_3V_2O_8$ composites measured at X-band and 1MHz

Temperature coefficient of dielectric constant (τ_{er}) is an important parameter for composite systems, since it affects the operating frequency of the substrate while used for outdoor applications. τ_{er} of $Ba_3V_2O_8$ filled HDPE composites are measured in the temperature range of 30-100°C and the results are given in Figure 7.7. The τ_{er} of HDPE and $Ba_3V_2O_8$ are -52 ppm/°C and -92 ppm/°C respectively. From Figure 7.7, it can be seen that τ_{er} decreases in the negative direction with increase in the $Ba_3V_2O_8$ content and the optimum loaded (54 vol%) composite has a τ_{er} of -498 ppm/°C.

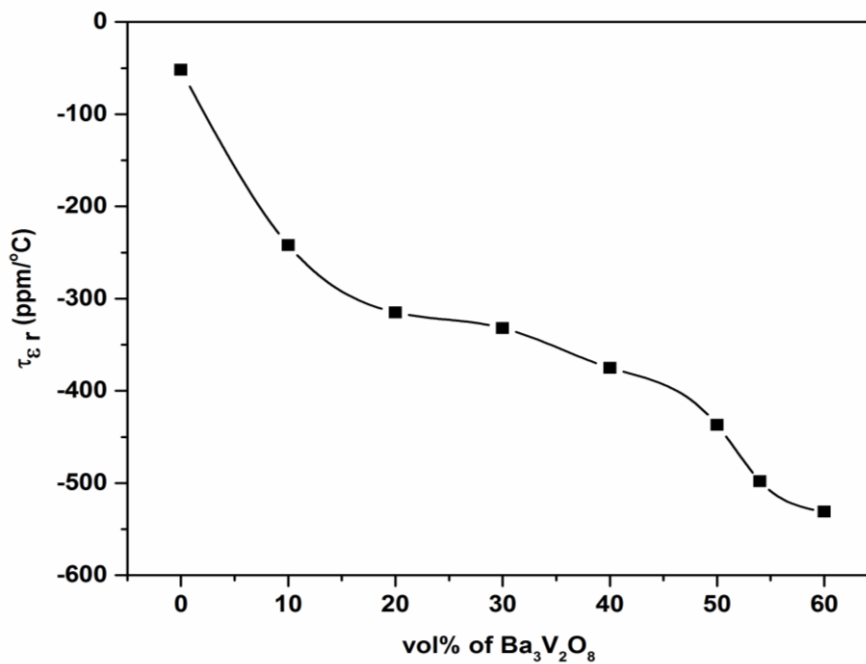


Figure 7.7 Variation of temperature coefficient of dielectric constant with respect to filler loading

Comparison with theoretical modeling

Dielectric constant values of the $Ba_3V_2O_8$ filled HDPE composites have been determined using various theoretical modeling approaches viz. Lichtnecker, Maxwell Garnet, Maxwell Wagner-Silalrs (MWS) and Jayasundere Smith models. Figure 7.8 shows the comparison of experimental dielectric constant values with the dielectric constant obtained from various theoretical approaches. The dielectric constant obtained from MWS model exhibits better correlation with the experimental values, while other theoretical approaches show more deviation from the experimental values. Hence, MWS model can be used as an effective approach to predict the dielectric constant of $Ba_3V_2O_8$ filled HDPE composites.

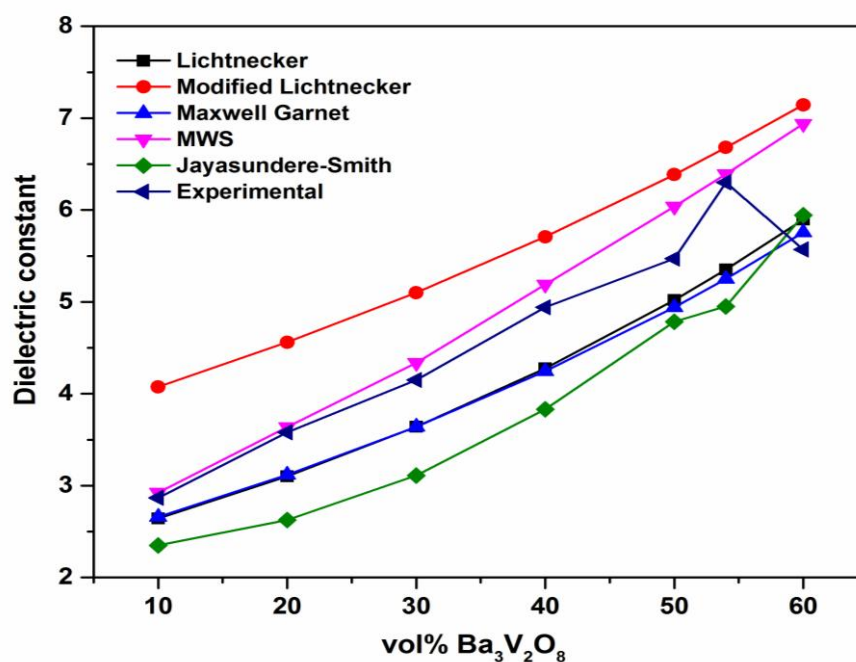


Figure 7.8 Comparison of experimental dielectric constant with different theoretical models

7.3.3 Morphology of the composites

Surface morphology of the ceramic filler and filler distribution in the HDPE matrix were studied using scanning electron microscopic techniques. The SEM micrograph of the $Ba_3V_2O_8$ filler used in the present study is given in Figure 7.9a which shows polygonal morphology. Typical SEM micrographs of the planar and cross-sectional surfaces of 52, 54 and 56 vol% $Ba_3V_2O_8$ filled HDPE composites are given in Figure 7.9b-d. Nearly pore free and homogeneous distribution of filler in the HDPE matrix can be seen from the planar SEM micrograph of 52 and 54 vol% filled composites, whereas aggregation of $Ba_3V_2O_8$ filler is observed for 56 vol% filled composite, which in turn result slight amount of porosity. This may be due to the enhanced ceramic to ceramic connectivity beyond the percolation threshold, where the composite loses its 0-3 connectivity. It is clear from the planar SEM micrograph that $Ba_3V_2O_8$ particles are observed to be distributed uniformly in the HDPE matrix. Further, the cross-sectional micrograph of the 54 vol% loaded composite given in Figure 7.9e reveals the uniform distribution of filler materials throughout the polymer matrix. Such a uniform distribution of ceramic filler is essential for polymer ceramic composites to avoid dielectric anisotropy.

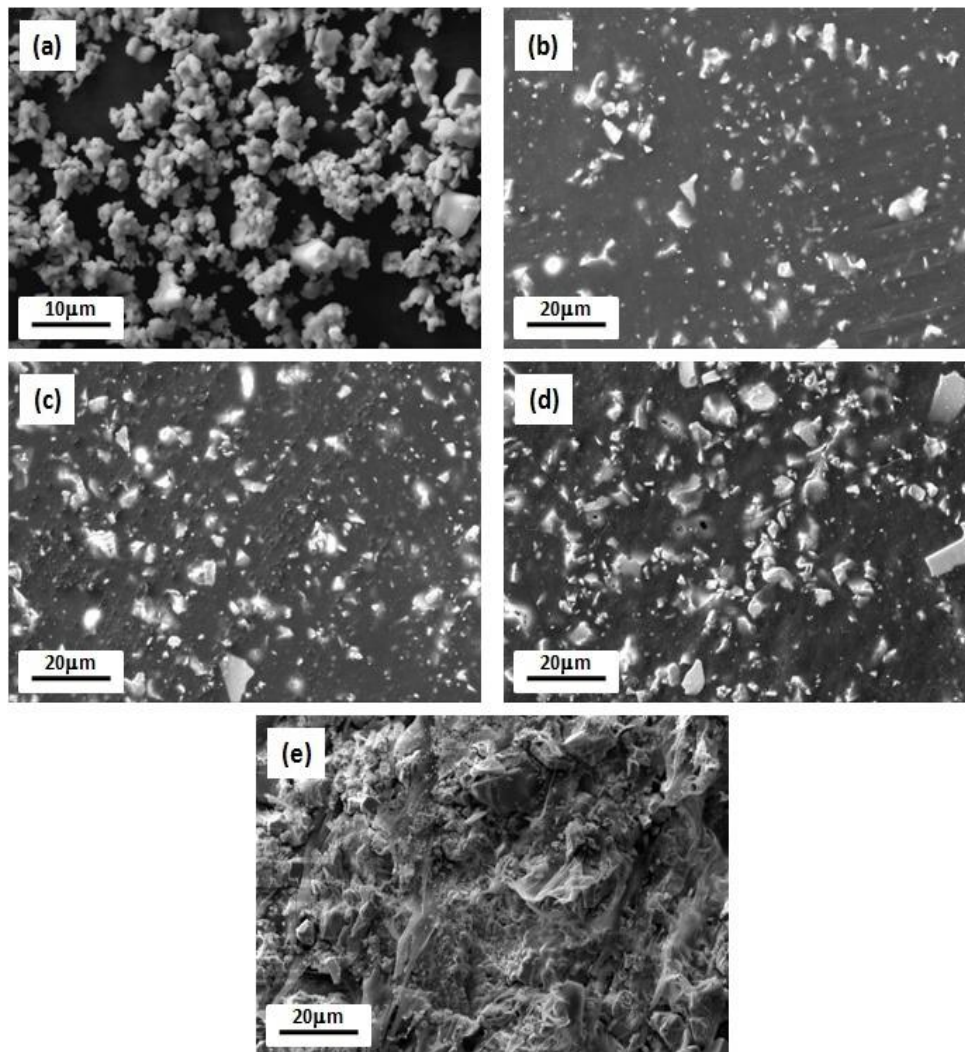


Figure 7.9 SEM micrographs of (a) $Ba_3V_2O_8$ filler (b) 52 vol% (c) 54 vol% (d) 56 vol % and (e) cross section of 54 vol% $Ba_3V_2O_8$ filled HDPE composites

7.3.4 Coefficient of linear thermal expansion (CTE)

In addition to dielectric properties, coefficient of linear thermal expansion (CTE) of $Ba_3V_2O_8$ filled HDPE composites is also measured at different filler loadings and the variation of CTE of HDPE/ $Ba_3V_2O_8$ composites with filler fraction is depicted in Figure 7.10. Pure HDPE has a linear thermal expansion coefficient of ~ 230 ppm/ $^{\circ}C$ in the 30-230 $^{\circ}C$ temperature range [17, 33]. From Figure 7.10, it is clear that the CTE values come down with the increasing amount of $Ba_3V_2O_8$ filler. During thermal excursion, the polymer matrix in the composite expands more than the ceramic filler and if the interfaces in the composites are capable to transmit these stresses, the expansion will be less [34, 35]. Also at higher filler loading, the

entanglement of the polymer with the filler restricts the linear expansion of the polymer composites. HDPE/ $Ba_3V_2O_8$ composite exhibited a CTE of 138 ppm/°C for an optimum filler loading of 54 vol%.

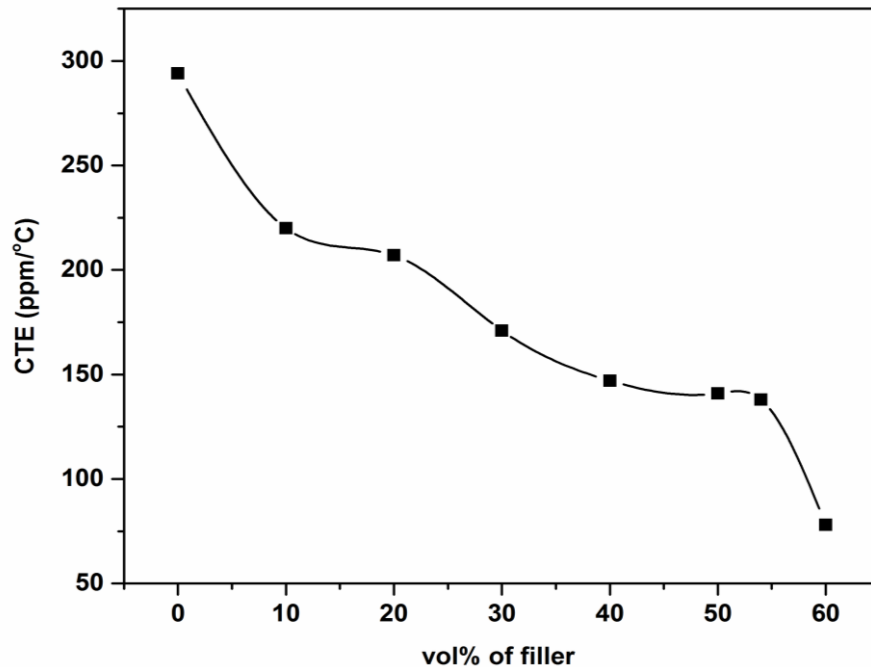


Figure 7.10 Variation of CTE as a function of filler loading in HDPE/ $Ba_3V_2O_8$ composites

7.3.5 Ultimate tensile strength (UTS)

The mechanical properties can also affect the performance of the microwave substrates. HDPE has an ultimate tensile strength of 20.04 MPa [36]. Because of this, HDPE behaves like a yielding material under tension. Figure 7.11 shows the variation of mechanical strength of $Ba_3V_2O_8$ filled HDPE composites as a function of filler loading. It can be clearly seen from Figure 7.11 that pristine HDPE has the highest tensile strength and the addition of ceramic filler in to HDPE matrix changes it to brittle nature near to the optimum filler loading. At optimum filler loading of 54 vol%, HDPE/ $Ba_3V_2O_8$ composite exhibits an ultimate tensile strength of 5.5 MPa. The reduction in mechanical properties of the ceramic filled HDPE composite can be due to the presence of porosity in the composites with higher volume fractions of the filler.

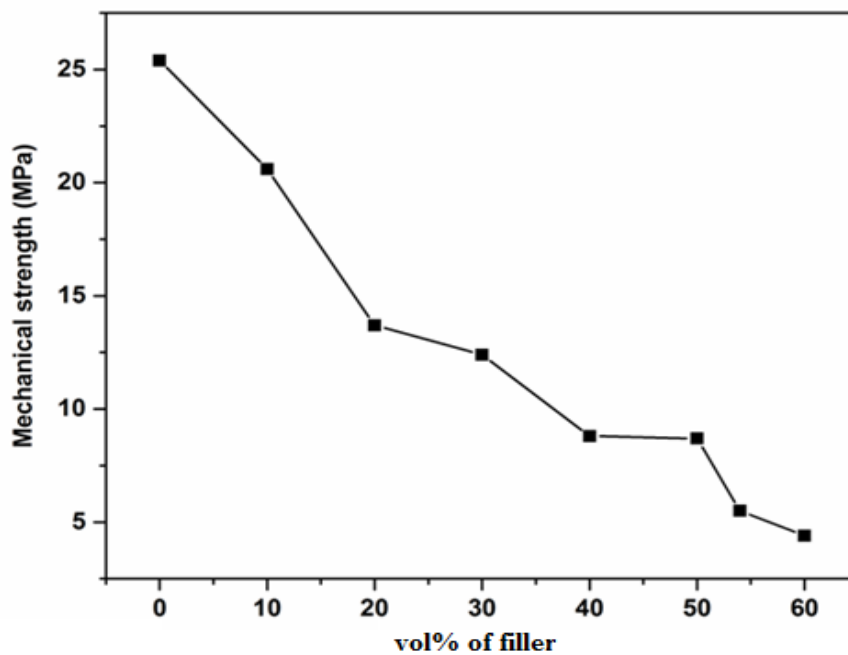


Figure 7.11 Variation of ultimate tensile strength of HDPE/ $Ba_3V_2O_8$ composites as a function of filler loading

7.3.6 Microstrip patch antenna measurements

The simulated models of the antennas are developed in Ansys HFSS software by specifying the coordinates for each point of the structure along with appropriate material specifications and the results are given in Figure 7.12. Lumped ports are assigned to excite the antennas. The frequency sweep is set over a desired range of frequencies before the simulations are commenced. The return loss is plotted as a function of frequency from the simulated results. Based on the simulation results, microstrip patch antenna is fabricated out of HDPE/ $Ba_3V_2O_8$ substrate having a dielectric constant of 6.3 and loss tangent of 0.004 through photolithographic technique. The fabricated antennas are fed by a 50Ω SMA connector and the photographs of the fabricated antennas are shown in Figure 7.13. Using copper clad substrates having dielectric constant of 6.3 and dielectric thickness of 1.6mm, the simulation studies are carried out to arrive at a microstrip patch antenna having an operating frequency of 2.45 GHz. This frequency is selected since it falls under industrial, scientific and medical (ISM) radio bands. The dielectric thickness

was varied from 1.6 mm to 0.8 mm for obtaining patch antenna design, which can work at 5 GHz retaining the same dielectric constant for the substrate.

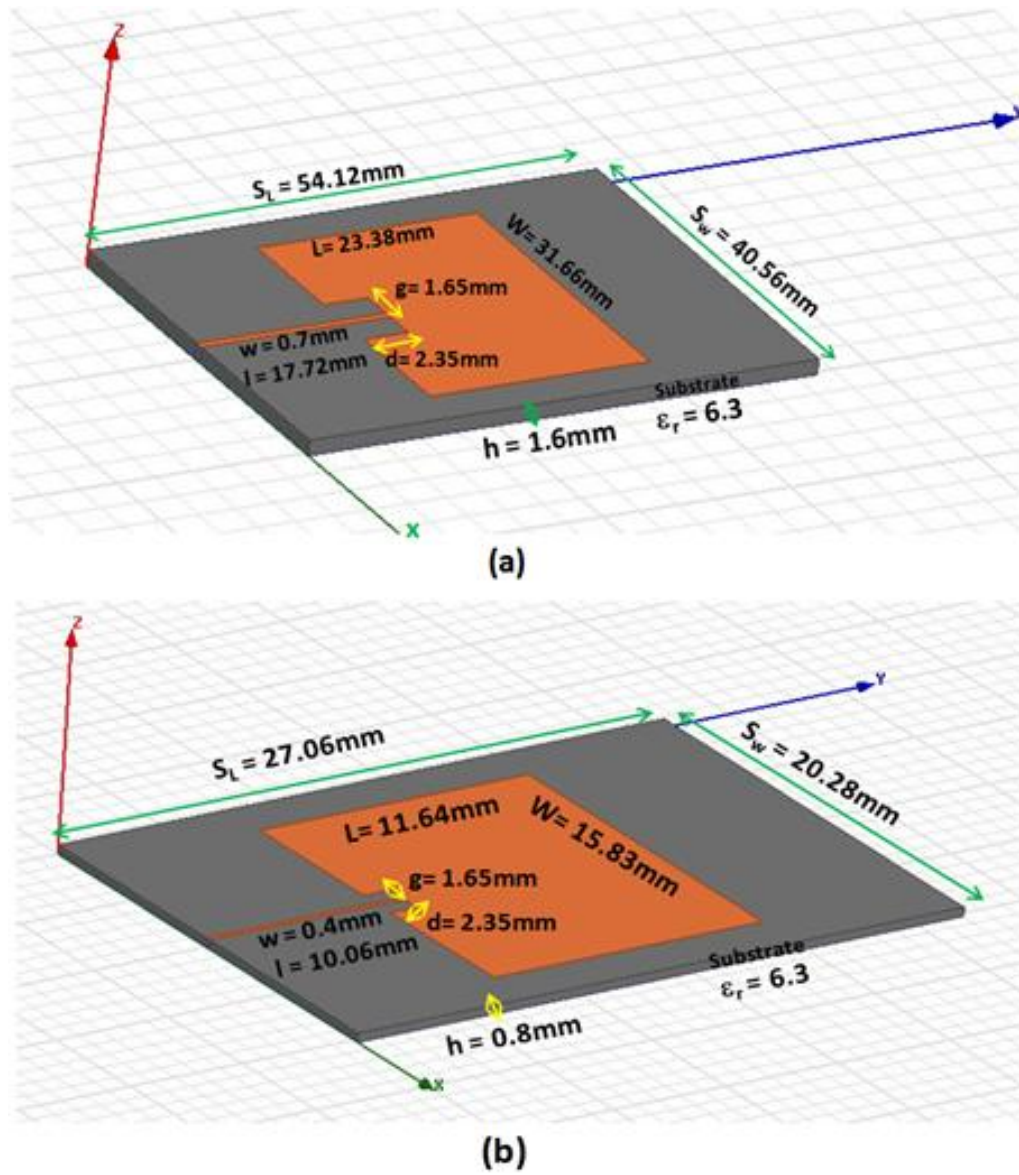


Figure 7.12 Simulated structures of microstrip patch antennas with substrates of (a) 1.6mm and (b) 0.8mm thickness

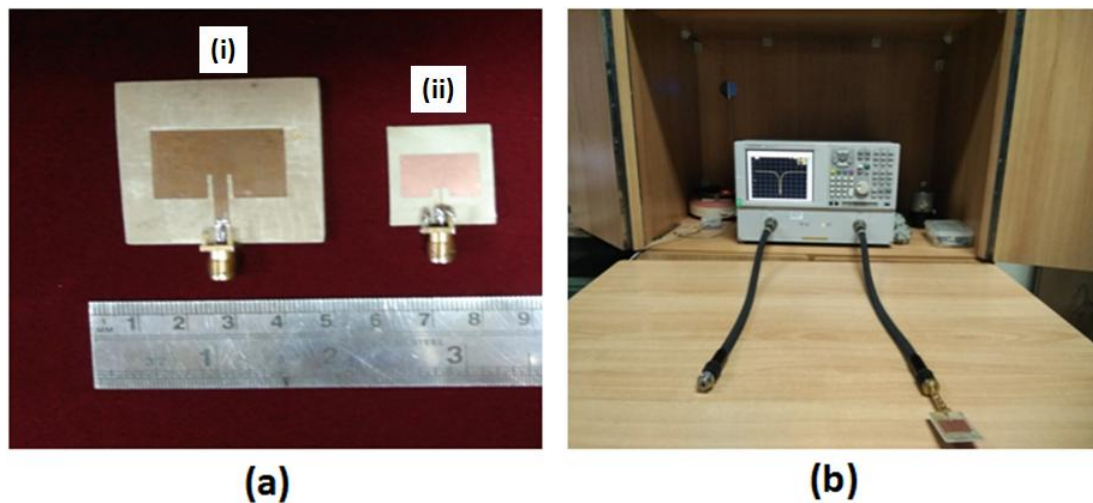
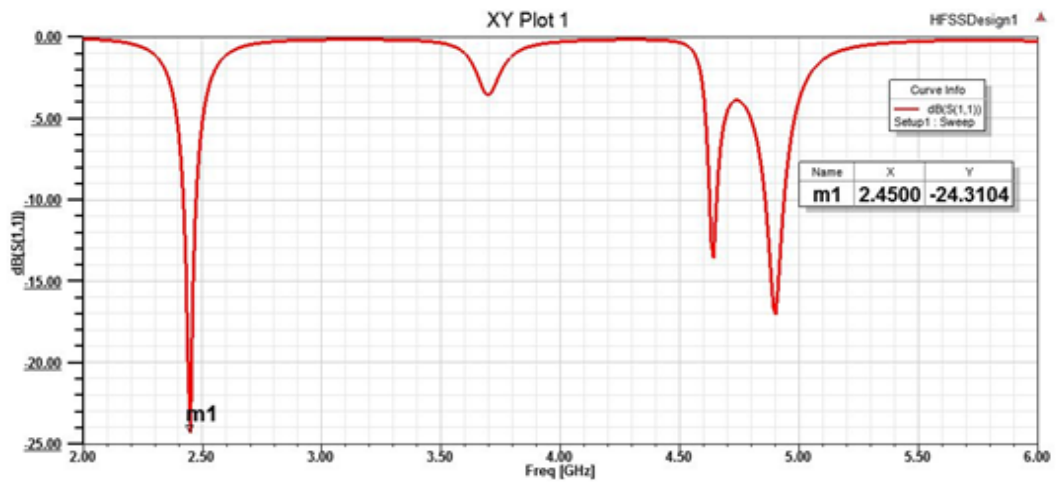
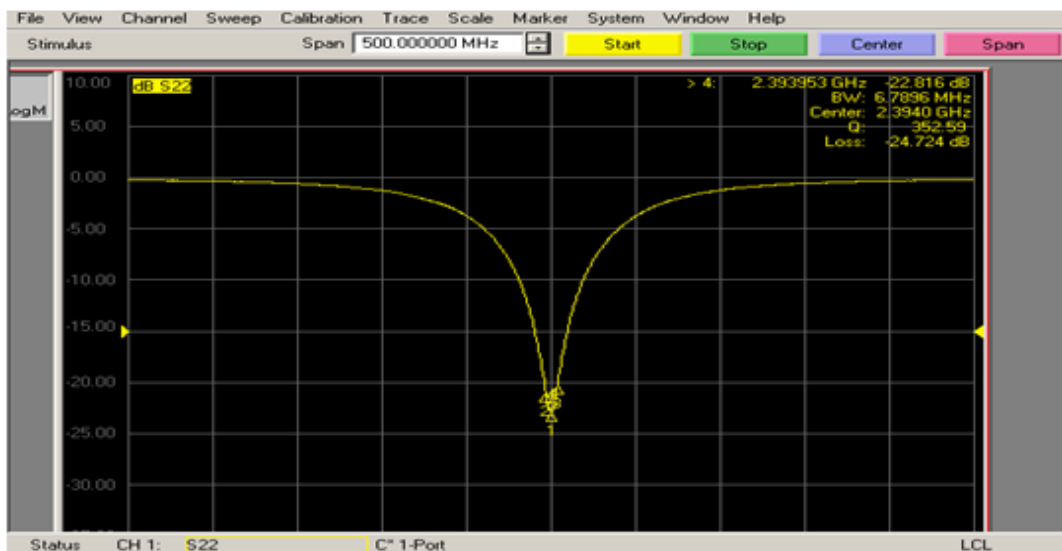


Figure 7.13 (a) Microstrip patch antenna fabricated for (i) 2.45GHz and (ii) 5GHz (b) Measurement setup for microstrip patch antenna using vector network analyzer

Return loss of the antennas can be measured using a vector network analyzer in the 10 MHz to 20 GHz range. Vector network analyzer is composed of RF source and multiple measurement receivers and is specifically designed to measure the forward and reverse reflection and transmission responses (S-parameters) of RF components. The simulated and measured reflection coefficients of the microstrip patch antennas are shown in Figures 7.14 and 7.15. The microstrip patch antenna fabricated using HDPE/ $Ba_3V_2O_8$ substrate with 1.6 mm thickness exhibited an operating frequency of 2.39 GHz, bandwidth of 6.7896 MHz and an insertion loss of -24.724 dB. While the patch antenna fabricated with 0.8 mm thickness of HDPE/ $Ba_3V_2O_8$ substrate exhibited an operating frequency of 5.257095 GHz with bandwidth of 51.99 MHz and an insertion loss of -12.737 dB. The differences between the simulated and measured performances of the antennas at lower frequencies are mainly due to the back current flowing through the outer surface of the feeding cable [37, 38].

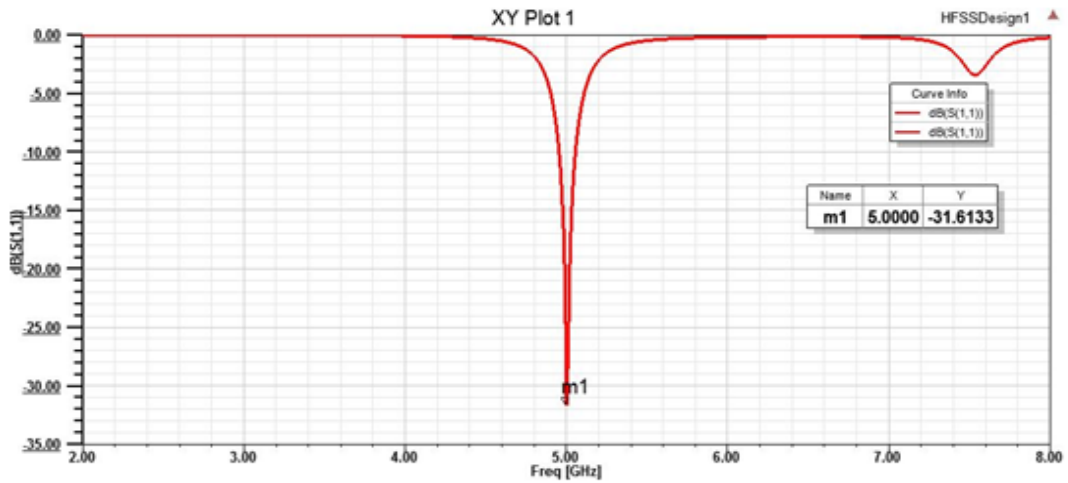


(a)

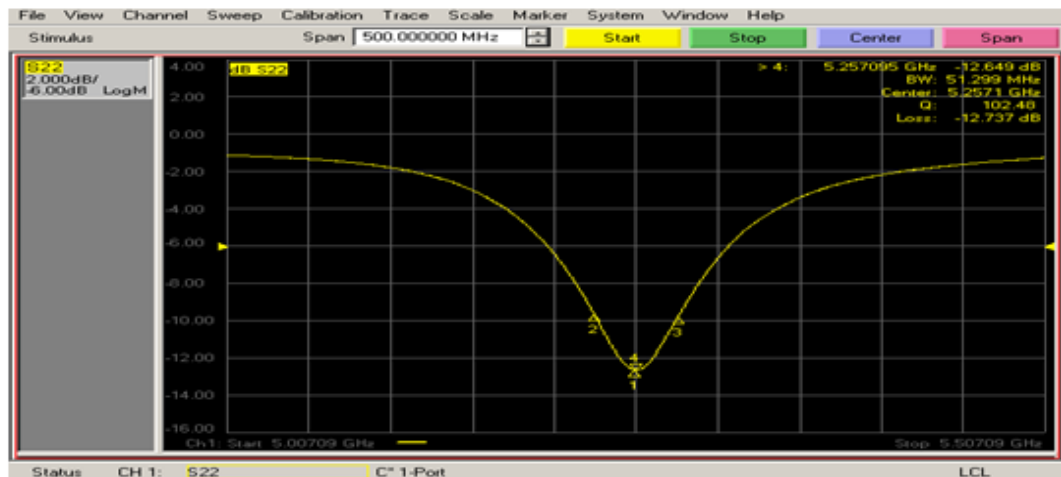


(b)

Figure 7.14 (a) Simulated and (b) measured return loss characteristics of the patch antenna at 2.45 GHz for $\epsilon_r=6.3$ and $\tan\delta=0.004$



(a)



(b)

Figure 7.15 (a) Simulated and (b) measured return loss characteristics of the patch antenna at 5 GHz for $\epsilon_r=6.3$ and $\tan\delta=0.004$

7. 4 Conclusions

HDPE/ $Ba_3V_2O_8$ composites have been prepared at different loading fractions through dry mixing and compression molding techniques. X-ray diffraction and SEM studies confirm that there is no chemical interaction takes place while inorganic $Ba_3V_2O_8$ filler is incorporated in the HDPE matrix. The density and dielectric constant of the $Ba_3V_2O_8$ filled HDPE composites exhibit an increasing trend up to 54 vol%, and thereafter both the properties deteriorates. At optimum filler loading of 54 vol%, HDPE/ $Ba_3V_2O_8$ composite exhibits a dielectric constant of 6.3 and loss tangent of 0.004 in the X-band frequency region. Various theoretical modeling techniques have been employed to predict the dielectric constant of the composite samples and the results are compared with that of experimental results. Temperature coefficient of dielectric constant ($\tau_{\epsilon r}$), coefficient of thermal expansion (CTE) and ultimate tensile strength of the HDPE/ $Ba_3V_2O_8$ composites decrease with respect to filler loading. High Frequency Structure Simulator (HFSS) is effectively used to simulate and predict the end properties of microstrip patch antenna designs operating at 2.45 GHz and 5 GHz frequencies based on material parameters. Microstrip patch antennas have been fabricated on copper cladded HDPE/ $Ba_3V_2O_8$ substrates through photolithographic technique based on simulation results. Measured results of the microstrip patch antennas are in good agreement with simulated data and exhibited excellent microwave response in terms of bandwidth and insertion loss. Present study shows that HDPE/ $Ba_3V_2O_8$ composites are ideal substrate materials for microstrip antenna design.

References

- [1] D. D. L. Chung, *Composite materials: Functional materials for modern technologies*, Springer (2003).
- [2] T. S. Laverghetta, *Microwave materials and fabrication techniques*, Artech House (1984).
- [3] K. P. Murali, S. Rajesh, K. Stanly Jacob, Om Prakash, A. R. Kulkarni, R. Ratheesh, *J Mater Sci: Mater Electron.*, 21 [2] (2010) 192-198.
- [4] V. S. Nisa, S. Rajesh, K. P. Murali, V. Priyadarshini, S. N. Potty, R. Ratheesh, *Comp. Sci. Technol.*, 68 [1] (2008) 106-112.
- [5] D. N. Light, J. R. Wilcox, *IEEE Trans. Compon. Pack. Technol. A.*, 18 [1] (1995) 118-126.
- [6] A. J. Bur, *Polymer.*, 26 [7] (1985) 963-977.
- [7] Gabriel, L.H., History and physical chemistry of HDPE, available at: https://plasticpipe.org/pdf/chapter-1_history_physical_chemistry_hdpe.pdf
- [8] A. Peacock, *Handbook of Polyethylene: Structures, Properties, and Applications*, CRC Press, (2000).
- [9] K. Seeger, *IEEE Trans. Microw. Theory Tech.*, 39 [2] (1991) 352-354.
- [10] W. Zhou, S. Qi, Q. An, H. Zhao, N. Liu, *Mater. Res. Bull.*, 42 [10] (2007) 1863-1867.
- [11] R. Huang, X. Xu, S. Lee, Y. Zhang, B. J. Kim, Q. Wu, *Materials.*, 6 [9] (2013) 4122-4138.
- [12] K. B. Adhikary, S. Pang, M. P. Staiger, *Compos.Part B.Eng.*, 39 [5] (2008) 807-815.
- [13] W. Tang, M. H. Santare, S. G. Advani, *Carbon.*, 41 [14] (2003) 2779-2785.
- [14] G. Lu, W. Wang, S. Shen, *Mater. Sci. Medzg.*, 20 [4] (2014) 464.
- [15] O. E. Gouda, S. F. Mahmoud, A. A. El-Gendy, A. S. Haiba, *Indonesian Journal of Electrical Engineering*, 12 [12] (2014) 7987-7995.

- [16] G. Subodh, V. Deepu, P. Mohanan, M.T. Sebastian, *Appl. Phys. Lett.*, 95 [6] (2009) 062903 (1-3).
- [17] P. S. Anjana, V. Deepu, S. Uma, P. Mohanan, J. Philip, M.T. Sebastian, *J. Polym. Sci. B Polym. Phys.*, 48 [9] (2010) 998-1008
- [18] J. R. James, P. S. Hall, *Handbook of microstrip antenna*, Peter Peregrinus Ltd. (1989).
- [19] D. Sarmah, J. R. Deka, S. Bhattacharyya, N. S. Bhattacharyya, *J. Electron. Mat.*, 39 [10] (2010) 2359-2365.
- [20] P. J. Gogoi, S. B. Bhattacharyya, N. S. Bhattacharyya, *J. Electron. Mat.*, 44 [4] (2015) 1071-1080.
- [21] N. K James, S. Rajesh, K.P Murali, K.S. Jacob, R. Ratheesh, *J. Mater. Sci. Mater. Electron.*, 21 [12] (2010) 1255-1261.
- [22] A. N. Unnimaya, E. K. Suresh, J. Dhanya, R. Ratheesh, *J. Mater.Sci. Mater. Electron.*, 25 [2] (2014) 1127-1131.
- [23] M. Roy, J. K. Nelson, R. K. MacCrone, L. S. Schadler, C. W. Reed, R. Keefe, W. Zenger, *IEEE Trans. Dielectr. Electr. Insul.*, 24 [4] (2005) 629-643.
- [24] M. T. Sebastian, H. Jantunen, *Int. J. Appl. Ceram. Technol.*, 7 [4] (2010) 415-434.
- [25] S. Thomas, V. Deepu, S. Uma, P. Mohanan, J. Phlip, M. T. Sebastian, *Mater. Sci. Eng. B.*, 163 [2] (2009) 67-75.
- [26] Y. Rao, J. Qu, T. Marinis, C. P. Wong, *IEEE Trans. Comp. Pack. Technol.*, 23 [4] (2000) 680-683.
- [27] N. Jayasundere, B. V. Smith, *J. Appl. Phys.*, 73 [5] (1993) 2462-2466.
- [28] D. C. Dube, M. T. Lanagan, J. H. Kim, and S. J. Jang, *J. Appl. Phys.*, 63 [7] (1988) 2466–2468.
- [29] P. Susse, M. J. Buerger, *Zeitschrift fur Kristallographie.*, 131 [1-6] (1970) 161-174.
- [30] S. Rajesh, K. P. Murali, R. Ratheesh, *Appl. Phys. A.*, 104 [1] (2011) 159-164.

- [31] V. Drishya, A. N. Unnimaya, R. Naveenraj, E. K. Suresh, R. Ratheesh, *Int. J. Appl. Ceram. Technol.*, 13 [5] (2016) 810-815.
- [32] S. Rajesh, K. P. Murali, V. Priyadarsini, S. N. Potty, R. Ratheesh, *Mater. Sci. Eng. B.*, 163 [1] (2009) 1-7.
- [33] K. M. Gupta, *Engineering materials: Research, applications and advances*, Taylor & Francis Group, LLC (2015).
- [34] L. Holliday, J. Robinson, *J. Mater. Sci.*, 8 [3] (1973) 301-311.
- [35] C. Y. Ho, R. E. Taylor, ASM International (1998).
- [36] S. Fiaz, A. Anis, M. Luqman, S. M. Al Zahrani, *Polym. Compos.*, 37 [1] (2016) 5-13.
- [37] L. Liu, S. W. Cheung, Y. F. Weng, T.I. Yuk, Cable effects on measuring small planar UWB monopole antennas, *Ultra Wideband Current Status and Future Trends*, (2012) 273-294.
- [38] L. Liu, Y. F. Weng, S. W. Cheung, T. I. Yuk, L. J. Foged, Modeling of cable for measurements of small monopole antennas, *IEEE Antennas & Propagation Conference*, November (2011) 1-4.

8

Summary and Scope of Future Work

8.1 Summary

8.2 Future work

8.1 Summary

The wide spread development of wireless communication sector necessitated the utilization of operating frequency from microwave to millimeter wave range for the transmission of large quantity of information with high speed. The demand for low cost, high volume and miniaturized circuit fabrication has led to the evolution of integrated technologies. In this context, low temperature co-fired ceramics (LTCC) play a decisive role as the base material for development of miniaturized circuits, which involves co-firing of dielectric and highly conductive metal electrodes. In order to avoid the difficulties in the processing of glass-ceramic based systems, which are currently being used for LTCC applications, glass-free ceramic systems are preferred owing to their less phase complexity, superior dielectric properties, excellent chemical compatibility with metal electrode etc. Further reduction in the sintering temperature leads to a new area of ultra-low temperature co-fired ceramics (ULTCC) which offer considerable energy savings, less processing time, integration with semiconductors and co-firing with cheap metal electrodes.

The work presented in this thesis establishes the structure-property correlations of alkaline earth compounds in the AO-V₂O₅ systems (A= Ba, Sr, Ca, Mg and Zn) with an objective to use them as suitable candidate materials for LTCC and ULTCC applications. It also includes the preparation, characterization and properties of polymer ceramic composites based on barium orthovanadate, which is having the highest sintering temperature (1300°C) among the alkaline earth vanadates. The simulation, fabrication and characterization of patch antennas fabricated using Ba₃V₂O₈ filled HDPE composite were also presented.

8.1.1 Alkaline earth vanadate systems

The single phase compositions in the well-known BaO-V₂O₅ phase diagram have been explored to study their suitability as base materials for low temperature co-fired ceramics (LTCC) and ultra-low temperature co-fired ceramics (ULTCC) technologies at microwave frequencies. The phase formation, crystal structure, microwave dielectric properties, thermal properties and chemical compatibility with metal electrodes were investigated. The crystal structure of alkaline earth vanadate

materials can be classified as meta, pyro, ortho and oxovanadates based on the presence of V-O polyhedra. Conventional solid state ceramic reaction yielded single phase alkaline earth metavanadates. Among metavanadates, BaV_2O_6 and SrV_2O_6 belong to orthorhombic crystal structure with $C222$ space group having VO_4 tetrahedral units whereas monoclinic crystal structures are obtained for CaV_2O_6 , MgV_2O_6 and ZnV_2O_6 ceramics. Although calcium, magnesium and zinc metavanadates have same crystal structure and space group, both magnesium and zinc are having VO_6 octahedral networks in the unit cell whereas VO_5 trigonal bipyramids are seen in the unit cell of calcium metavanadate. Among the metavanadates studied, only BaV_2O_6 and CaV_2O_6 exhibited microwave dielectric properties. BaV_2O_6 exhibits a dielectric constant of 11.2, Q_{xf} of 42,790 GHz and τ_f of 28.2 ppm/°C whereas CaV_2O_6 ceramic has a dielectric constant of 8.7, Q_{xf} of 60,310 GHz and τ_f of -50.7 ppm/°C. Theoretical dielectric constant values of metavanadates have been calculated using ionic polarizability concepts and were compared with experimental results. Interestingly, CaV_2O_6 ceramic exhibits relatively high quality factor value of 73,120 GHz at 660°C as a result of better structural ordering. Barium and calcium metavanadates show low coefficient of linear thermal expansion (α_L) of 10 and 9.7 ppm/°C respectively, which are at par with commercial LTCC compositions. Both BaV_2O_6 and CaV_2O_6 ceramics exhibit excellent chemical compatibility with Al electrode and hence can be used for ULTCC applications.

The effect of vanadium substitution on the structure and microwave dielectric properties of $\text{Ba}_5\text{Nb}_4\text{O}_{15}$ ceramic was investigated to ascertain the possibility of existence of $\text{Ba}_5\text{V}_4\text{O}_{15}$ in the $\text{BaO-V}_2\text{O}_5$ phase diagram. The complete substitution of niobium by vanadium results a multiphase composition comprising of $\text{Ba}_2\text{V}_2\text{O}_7$ and $\text{Ba}_3\text{V}_2\text{O}_8$ phases and hence ruled out the possibility of existence of $\text{Ba}_5\text{V}_4\text{O}_{15}$ in the $\text{BaO-V}_2\text{O}_5$ binary phase diagram. Even though $5\text{BaO-2V}_2\text{O}_5$ is formed as a multiphase composition, it exhibits excellent microwave dielectric properties especially very low τ_f together with good chemical compatibility. $\text{Ba}_2\text{V}_2\text{O}_7$ and $\text{Ba}_3\text{V}_2\text{O}_8$ phases have temperature coefficient of resonant frequency (τ_f) with opposite signs and present study demonstrates that near zero τ_f LTCC material can be

arrived at by using appropriate amounts of barium pyro and orthovanadates. Replacing Ba with other alkaline earth elements also result analogous pyro and orthovanadate mixtures and hence ruled out the possibility of existence of single phase materials in the $5\text{AO}-2\text{V}_2\text{O}_5$ system.

As per the $\text{BaO}-\text{V}_2\text{O}_5$ phase diagram reported by Fotiev et al., existence of single phase compositions with higher BaO mol% ($>77\text{mol}\%$) was not mentioned. However, crystal structure of barium oxovanadates having BaO mol% $>77\%$ were reported later by other researchers. In the present work, detailed studies have been carried out to understand the structure of alkaline earth oxovanadates, their sintering properties, difference in the microwave dielectric properties of oxovanadate and orthovanadate families etc. Both XRD and Raman studies confirm distinct structural features for both ortho and oxovanadates. Among oxovanadates, only $\text{Mg}_4\text{V}_2\text{O}_9$ exhibits resonance in the microwave frequency region with a dielectric constant of 6.3, Qxf of 37,263 GHz and a negative τ_f of $-43.5\text{ ppm}/^\circ\text{C}$, due to structural ordering, which is evident from Raman studies. $\text{Mg}_4\text{V}_2\text{O}_9$ ceramic exhibits excellent chemical compatibility with Ag electrode and hence can be used as a suitable candidate material for LTCC applications. Present study affirms the possibility of existence of $\text{Ba}_4\text{V}_2\text{O}_9$ phase in the $\text{BaO}-\text{V}_2\text{O}_5$ phase diagram (Figure 8.1).

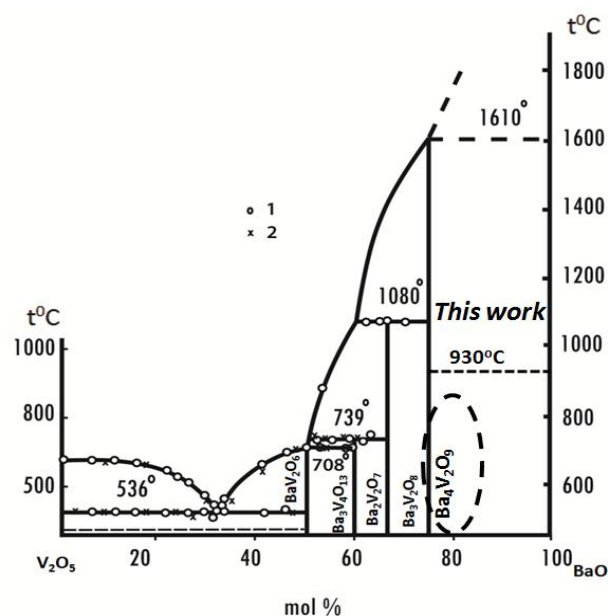


Figure 8.1 Modified $\text{BaO}-\text{V}_2\text{O}_5$ phase diagram

It is clear from the above results that the structural distortion could be one of the main reasons for non-resonance of most of the alkaline earth oxovanadates. In order to reduce the structural distortion of oxovanadates, partial substitution of Bi in the A site of $A_4V_2O_9$ samples has been attempted. Except $Bi_2CaV_2O_9$, all other compositions exhibit multiphase nature comprising of $BiVO_4$ and $BiAVO_5$ phases. The single phase formation of $Bi_2CaV_2O_9$ is further confirmed by TGA-DSC, laser Raman and EDS analyses. The well sintered $Bi_2CaV_2O_9$ exhibits a dielectric constant of 28.2, Qxf of 37,263 GHz and τ_f of -46.1 ppm/°C. Both $Bi_2MgV_2O_9$ and $Bi_2ZnV_2O_9$ also exhibited microwave dielectric properties although they are multiphase in nature. $Bi_2MgV_2O_9$ exhibits a dielectric constant of 34.2, Qxf of 28,400 GHz and τ_f of -15.3 ppm/°C whereas $Bi_2ZnV_2O_9$ has a dielectric constant of 35, Qxf of 20,000 GHz and τ_f of -190.2 ppm/°C. The high dielectric values of $Bi_2MgV_2O_9$ and $Bi_2ZnV_2O_9$ could be due to the relatively high dielectric constant of $BiVO_4$ secondary phase. Unlike other alkaline earth vanadates studied in the present work, $Bi_2CaV_2O_9$ melts during co-firing with Ag electrode and hence cannot be used for LTCC applications. The identified single phase LTCC and ULTCC compositions in the $AO-V_2O_5$ (A= Ba, Sr, Ca, Mg and Zn) system along with their microwave dielectric properties are compiled in Table 8.1.

Table 8.1 Identified LTCC and ULTCC single phase compositions in the $AO-V_2O_5$ (A= Ba, Sr, Ca, Mg and Zn) system

Compound	Sintering temp. (°C/1h)	Microwave dielectric properties			Chemical compatibility	Application
		ϵ_r	Qxf(GHz)	τ_f (ppm/°C)		
BaV_2O_6	550	11.2	42,790	28.2	Al	ULTCC
CaV_2O_6	680	8.7	60,310	-50.7	Al	ULTCC
$Ba_3V_4O_{13}$	600	9.6	56,100	-42	Al	ULTCC
$Ba_2V_2O_7$	840	9.6	30,315	-32	Ag	LTCC
$Mg_4V_2O_9$	940	6.3	37,263	43.5	Ag	LTCC

$Ba_3V_2O_8$ cannot be used for LTCC applications in spite of having excellent microwave dielectric properties owing to its relatively high sintering temperature (1300°C). In order to utilize excellent microwave dielectric properties of $Ba_3V_2O_8$, this composition has been used as particulate filler in the HDPE matrix through dry milling followed by compression molding techniques with a view to fabricate planar

and dimensionally stable base substrates for microwave circuit applications. At optimum filler loading of 54 Vol%, Ba₃V₂O₈ filled HDPE composite exhibited a dielectric constant of 6.3 and loss tangent of 0.004 at 9.32 GHz. Theoretical modeling of Ba₃V₂O₈ filled HDPE composite has been done and it was found that Maxwell-Wagner-Sillars model showed better correlation with the experimental values compared to other theoretical models.

8.1.2 Microstrip patch antenna

In order to ascertain the usefulness of Ba₃V₂O₈ filled HDPE composite, rectangular patch antenna design working at Industrial Scientific and Medical band frequency (2.45 GHz) has been simulated using High Frequency Structure Simulator (HFSS) software and fabricated through photolithographic technique. The end performance of the developed composite material has also been studied at higher frequencies (5 GHz). The operating frequency, insertion loss and band width of the fabricated patch antennas have been compared with the simulated data. The fabricated rectangular patch antennas exhibited excellent microwave dielectric properties in terms of low insertion loss and higher band width.

8.2 Future work

In general, microwave circuits consist of fundamental devices such as filters, antennas, power dividers, couplers etc. for the transfer of electromagnetic energy in the form of propagating waves from one point to another with minimum loss. Because of this, microwave devices are designed as guiding structures like microstrip lines since they are low cost, simple in construction and possess higher integrity with surface mounted components. The critical parameters for microwave devices using microstrip lines are width, thickness and conductivity of the microstrip line, dielectric constant, loss tangent and dielectric thickness of the substrate material.

Even though microstrip lines are easy and cost effective to fabricate, it cannot be used at higher frequencies such as millimeter wave because of the transmission and radiation losses. These disadvantages of microstrip lines can be easily overcome by the use of substrate integrated waveguide (SIW) structures. SIWs are integrated waveguide like structures fabricated by metal filled via-hole arrays in a dielectric

substrate where the ground planes are interconnected and hence can be miniaturized into small packages called as system in package (SiP). These miniaturized and cost effective packages can be fabricated either on printed circuit boards (PCB) or low temperature co-fired ceramics (LTCC) by making non-planar rectangular waveguide in the planar form.

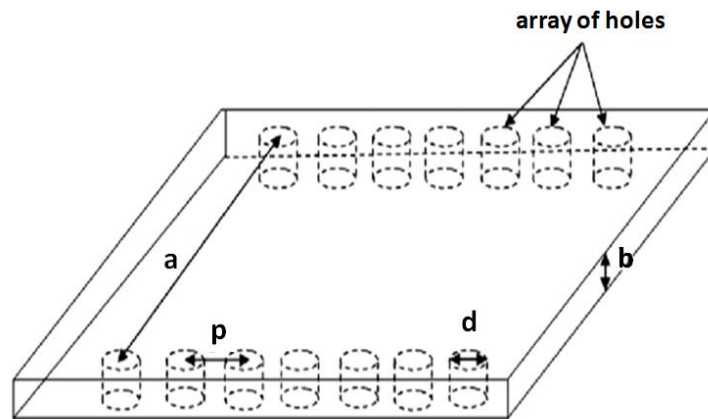


Figure 8.2 Schematic of a substrate integrated waveguide (SIW)

The width of a SIW can be calculated using the formula

$$a = a_d + \frac{d^2}{0.95p}$$

where, a_d is the width of the dielectric filled waveguide at cut off frequency f_c ($f_c = c/2a_d$, where c is the speed of light), d is the diameter of the vias and p is the centre to centre separation between the vias. SIW structures exhibit similar propagation characteristics as that of a classical rectangular waveguide at higher frequencies. SIW structures have various advantages over conventional metallic waveguides such as high power handling capability, self-consistent electrical shielding and the flexibility of determining the cut off frequency f_c . The most significant advantage of SIW technology is the possibility of integration of active and passive components and even antennas on the same substrate. Since SIW circuits offer high quality factor, they can be considered as an excellent candidates for the integration of high density millimeter wave circuits. In view of the above, it is proposed to carry out future work in SIW technology since it offers compact size, low cost, low interference due to shielding etc.